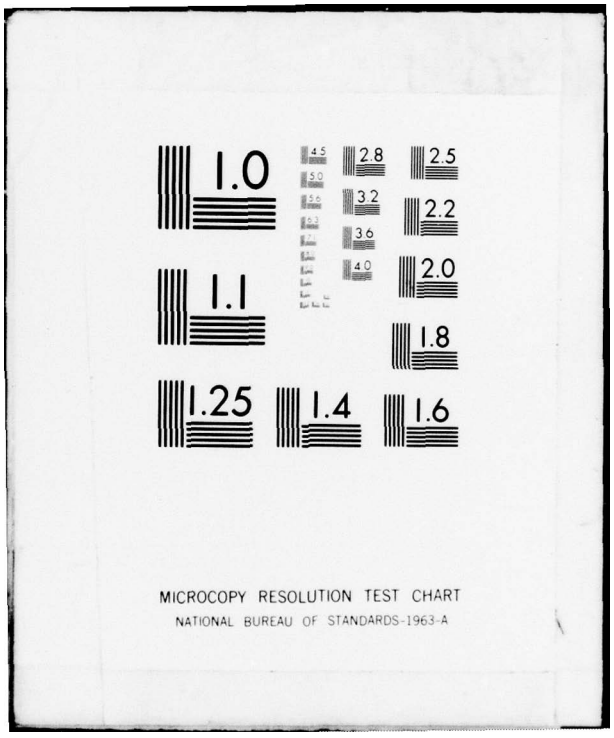
AD-A080 094 AUBURN UNIV ALA ENGINEERING EXPERIMENT STATION F/G 20/3
SINGULARITIES, COUPLING COEFFICIENTS, AND MODE VECTORS FOR A TH--ETC(U)
DEC 79 T H SHUMPERT AFOSR-79-0017
UNCLASSIFIED AFOSR-TR-80-0013 NL

1 OF 2
AD A080094




1.0
1.1
1.25
1.4
1.6
1.8
2.0
2.2
2.5
2.8
3.2
3.6
4.0
4.5
5.0
5.6
6.3
MICROCOPY RESOLUTION TEST CHART
NATIONAL BUREAU OF STANDARDS-1963-A

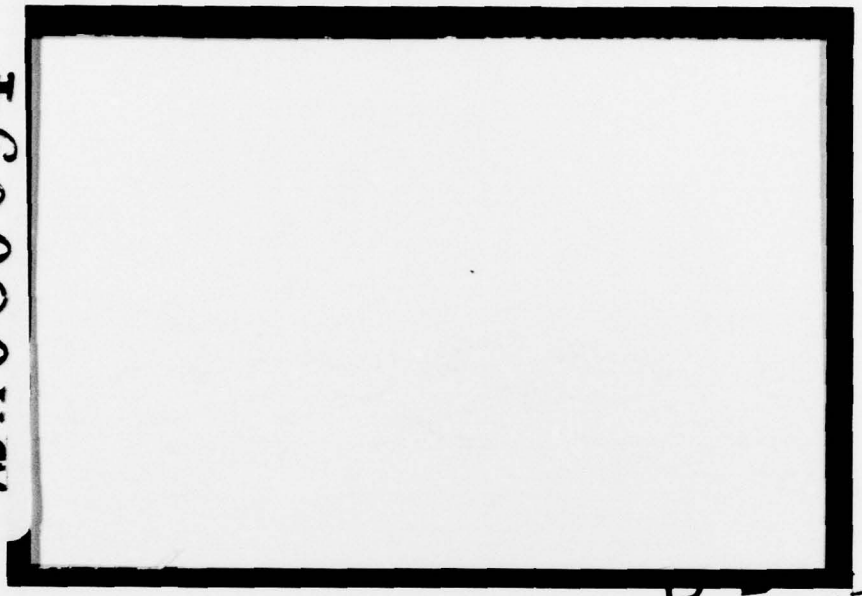
AFOSR-TR- 80-0013

ELECTRICAL

12

ENGINEERING

AD A080094





DDC FILE COPY

JAN 30 1980

Approved for public release;
distribution unlimited.

ENGINEERING EXPERIMENT STATION

AUBURN UNIVERSITY

AUBURN, ALABAMA

80 1 29 073

(12)

FINAL REPORT

SINGULARITIES, COUPLING COEFFICIENTS, AND MODE VECTORS FOR A THIN WIRE SCATTERER PARALLEL TO A LOSSY GROUND

Prepared by

T. H. Shumpert
Project Leader

LEVEL II

15 December 1979

DDC
RECEIVED
JAN 30 1980
E

Grant No. AFOSR-79-0017

Air Force Office of Scientific Research

Bolling AFB, D.C. 20332

AIR FORCE OFFICE OF SCIENTIFIC RESEARCH (AFSC)
NOTICE OF TRANSMITTAL TO DDC
This technical report has been reviewed and is approved for public release IAW AFR 190-12 (7b).
Distribution is unlimited.
A. D. BLOSE
Technical Information Officer

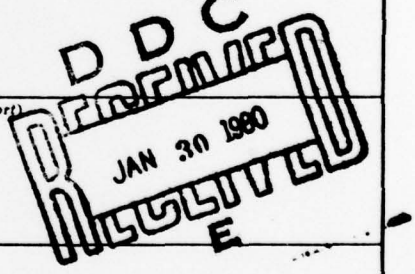
UNCLASSIFIED

SECURITY CLASSIFICATION OF THIS PAGE (When Data Entered)

REPORT DOCUMENTATION PAGE	READ INSTRUCTIONS BEFORE COMPLETING FORM
1. REPORT NUMBER: AFOSR-TR-80-0013	2. GOVT ACCESSION NO. / 3. RECIPIENT'S CATALOG NUMBER
4. TITLE (and Subtitle): SINGULARITIES, COUPLING COEFFICIENTS, AND MODE VECTORS FOR A THIN WIRE SCATTERER PARALLEL TO A LOSSY GROUND.	5. TYPE OF REPORT & PERIOD COVERED: Final rept.,
	6. PERFORMING ORG. REPORT NUMBER
7. AUTHOR(s): T. H. Shumpert	8. CONTRACT OR GRANT NUMBER(s): AFOSR 79-0017
9. PERFORMING ORGANIZATION NAME AND ADDRESS: Engineering Experiment Station, Auburn University, Auburn, AL	10. PROGRAM ELEMENT, PROJECT, TASK AREA & WORK UNIT NUMBERS: 61102F / 2301/A3
11. CONTROLLING OFFICE NAME AND ADDRESS: AFOSR/NP, Bolling AFB, Bldg. 410, Wash DC 20332	12. REPORT DATE: Dec 1979
	13. NUMBER OF PAGES: 155
14. MONITORING AGENCY NAME & ADDRESS (if different from Controlling Office)	15. SECURITY CLASS. (of this report): unclassified
	15a. DECLASSIFICATION/DOWNGRADING SCHEDULE

16. DISTRIBUTION STATEMENT (of this Report)

Approved for public release; distribution unlimited.



17. DISTRIBUTION STATEMENT (of the abstract entered in Block 20, if different from Report)

18. SUPPLEMENTARY NOTES

19. KEY WORDS (Continue on reverse side if necessary and identify by block number)

20. ABSTRACT (Continue on reverse side if necessary and identify by block number)

The Singularity Expansion Method (SEM) coupled with the reflection coefficient approximation seems to be an appropriate technique for analyzing a cylindrical scatterer over a finitely conducting ground. Pole locations of the cylinder over perfect ground calculated by investigators were found to be identical to those calculated in this analysis when the ground conductivity is large. Also, when the ground conductivity is reduced with the relative permittivity held at unity, calculated pole locations agree with those of the free space problem. These facts add credence to the reflection coefficient technique. In general,

it is found that displacement of the singularities from their free space position is a function of discontinuity in the ground plane. The mechanism for discontinuity is seen to be somewhat immaterial. Mode vectors corresponding to first layer singularities show littler or no dependence on the paramters of the problem.

FOREWORD

This report is the Final Technical Report of a study being conducted by the Electrical Engineering Department under the auspices of the Engineering Experiment Station of Auburn University. This technical report is submitted toward fulfillment of the requirements prescribed in AFOSR Grant No. AFOSR-79-0017.

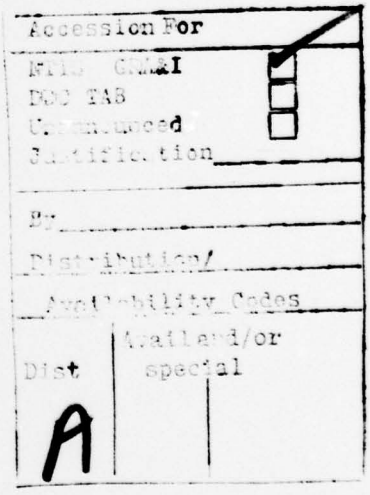


TABLE OF CONTENTS

LIST OF TABLES iii

LIST OF FIGURES iv

I. INTRODUCTION 1

II. THEORY 2

Integro-differential Equation
Application of the Method of Moments
Alternate Formulation for the Secondary Scattered Electric Field
Application of the Singularity Expansion Method
Approximations and Limitations Imposed

III. NUMERICAL RESULTS 29

IV. CONCLUSIONS 138

REFERENCES 140

LIST OF FIGURES

2- 1. System Geometry. 3

2- 2. Vertically polarized total incident and transmitted electromagnetic excitation 8

2- 3. Moment method partitioning of geometry 13

3- 1. Location of the resonances of a thin wire scatterer in free space 43

3- 2. Location of the singularities of the thin wire scatterer above a perfectly conducting ground plane. 44

3- 3. Trajectory of singularity γ_{11} for the case of a thin wire over a perfectly conducting ground. 45

3- 4. Trajectory of fundamental self-resonant singularity, γ_{11}, as a function of spacing, h/ℓ, and conductivity, σ. The relative permittivity, ε_R, is held at one. 46

3- 5. Trajectory of fundamental self-resonant singularity, γ_{11}, as a function of spacing, h/ℓ, and conductivity, σ. The relative permittivity, ε_R, is held at five. 47

3- 6. Trajectory of fundamental self-resonant singularity, γ_{11}, as a function of spacing, h/ℓ, and conductivity, σ. The relative permittivity is held at fifteen. 48

3- 7. Trajectory of fundamental self-resonant singularity, γ_{11}, as a function of spacing, h/ℓ, and conductivity, σ. The relative permittivity is held at one hundred. 49

3- 8. Trajectory of second self-resonant singularity, γ_{12}, as a function of spacing, h/ℓ, and conductivity, σ. The relative permittivity is held at one. 50

3- 9. Trajectory of second self-resonant singularity, γ_{12}, as a function of spacing, h/ℓ, and conductivity, σ. The relative permittivity is held at fifteen. 51

3-10. Trajectory of third self-resonant singularity, γ_{13}, as a function of spacing, h/ℓ, and conductivity, σ. The relative permittivity is held at one. 52

3-11. Trajectory of third self-resonant singularity, γ_{13}, as a function of spacing, h/ℓ, and conductivity, σ. The relative permittivity is held at fifteen. 53

3-12. Trajectory of fourth self-resonant singularity, γ_{14}, as a function of spacing, h/ℓ, and conductivity, σ. The relative permittivity is held at one. 54

3-13. Trajectory of fourth self-resonant singularity, γ_{14}, as a function of spacing, h/ℓ, and conductivity, σ. The relative permittivity is held at fifteen. 55

3-14. Trajectory of fifth self-resonant singularity, γ_{15}, as a function of spacing, h/ℓ, and conductivity, σ. The relative permittivity is held at one. 56

3-15. Trajectory of fifth self-resonant singularity, γ_{15}, as a function of spacing, h/ℓ, and conductivity, σ. The relative permittivity is held at fifteen 57

3-16. Plot of the percent change of the fundamental damping constant relative to the free space damping constant, shown as a function of permittivity, $\varepsilon_R\varepsilon_o$, and conductivity, σ, for fixed spacing, $h/\ell = 0.25$ 58

3-17. Plot of the percent change of the fundamental resonant frequency relative to the free space resonant frequency, shown as a function of permittivity, $\varepsilon_R\varepsilon_o$, and conductivity, σ, for fixed spacing, $h/\ell = 0.25$. 59

3-18. Plot of the percent change of the fundamental damping constant relative to the free space damping constant, shown as a function of permittivity, $\varepsilon_R\varepsilon_o$, and conductivity, σ, for fixed spacing, $h/\ell = 0.50$. 60

3-19. Plot of the percent change of the fundamental resonant frequency relative to the free space resonant frequency, shown as a function of permittivity, $\varepsilon_R\varepsilon_o$, and conductivity, σ, for fixed spacing, $h/\ell = 0.50$. 61

3-20. Plot of the percent change of the fundamental damping constant relative to the free space damping constant, shown as a function of permittivity, $\varepsilon_R\varepsilon_o$, and conductivity, σ, for fixed spacing, $h/\ell = 0.75$. 62

3-21. Plot of the percent change of the fundamental resonant frequency relative to the free space resonant frequency, shown as a function of permittivity, $\varepsilon_R\varepsilon_o$, and conductivity, σ, for fixed spacing, $h/\ell = 0.75$. 63

3-22. Plot of the percent change of the fundamental damping constant relative to the free space damping constant, shown as a function of permittivity, $\varepsilon_R\varepsilon_o$, and conductivity, σ, for fixed spacing, $h/\ell = 1.0$ 64

3-23. Plot of the percent change of the fundamental resonant frequency relative to the free space resonant frequency, shown as a function of permittivity, $\varepsilon_R\varepsilon_o$, and conductivity, σ, for fixed spacing, $h/\ell = 1.0$ 65

3-24. Real and imaginary part of normalized natural modal current distribution for resonant frequencies γ_{11}, γ_{12}, γ_{13}, $h/\ell = 0.5$, $\varepsilon_R = 1.0$, $\sigma = 120.0$, $\Omega = 10.6$. 66

3-25. Real and imaginary part of normalized natural modal current distributions for resonant frequencies γ_{14} and γ_{15}, $h/\ell = 0.5$, $\varepsilon_R = 1.0$, $\sigma = 120.0$, $\Omega = 10.6$. 67

3-26. Coupling coefficient for fundamental self-resonant singularity, γ_{11}, as a function of conductivity, σ, and incident angle θ. The scatterer height-to-length ratio, h/ℓ, is 0.25, and the relative permittivity, ε_R, is unity 69

3-27. Coupling coefficient for fundamental self-resonant singularity, γ_{11}, as a function of conductivity, σ, and incident angle θ. The scatterer height-to-length ratio, h/ℓ, is 0.50, and the relative permittivity, ε_R, is unity 70

3-28. Coupling coefficient for fundamental self-resonant singularity, γ_{11}, as a function of conductivity, σ, and incident angle θ. The scatterer height-to-length ratio, h/ℓ, is 0.75, and the relative permittivity, ε_R, is unity 71

3-29. Coupling coefficient for fundamental self-resonant singularity, γ_{11}, as a function of conductivity, σ, and incident angle θ. The scatterer height-to-length ratio, h/ℓ, is 1.00, and the relative permittivity, ε_R, is unity 72

3-30. Coupling coefficient for fundamental self-resonant singularity, γ_{11}, as a function of conductivity, σ, and incident angle θ. the scatterer height-to-length ratio, h/ℓ, is 1.25, and the relative permittivity, ε_R, is unity 73

3-31. Coupling coefficient for fundamental self-resonant singularity, γ_{11}, as a function of conductivity, σ, and incident angle θ. The scatterer height-to-length ratio, h/ℓ, is 1.50, and the relative permittivity, ε_R, is unity 74

3-32. Real part of coupling coefficient for fundamental self-resonant singularity, γ_{11}, as a function of scatterer height-to-length ratio, h/ℓ, and incident angle θ. The ground conductivity, σ, is 120.0, and the relative permittivity, ε_R, is unity 76

3-33. Imaginary part of coupling coefficient for fundamental self-resonant singularity, γ_{11}, as a function of scatterer height-to-length ratio, h/ℓ, and incident angle θ. The ground conductivity, σ, is 120.0, and the relative permittivity, ε_R, is unity . . 77

3-34. Coupling coefficient for fundamental self-resonant singularity, γ_{11}, as a function of the ground plane relative permittivity, ε_R, and incident angle θ. The scatterer height-to-length ratio, h/ℓ, is 0.25, and the conductivity, σ, is 120.0 78

3-35. Coupling coefficient for fundamental self-resonant singularity, γ_{11}, as a function of the ground plane relative permittivity, ε_R, and incident angle θ. The scatterer height-to-length ratio, h/ℓ, is 0.25, and the conductivity, σ, is 0.12 79

3-36. Coupling coefficient for fundamental self-resonant singularity, γ_{11}, as a function of the ground plane relative permittivity, ε_R, and incident angle θ. The scatterer height-to-length ratio, h/ℓ, is 0.25, and the conductivity, σ, is 0.00012 80

3-37. Coupling coefficient for fundamental self-resonant singularity, γ_{11}, as a function of the ground plane relative permittivity, ε_R, and incident angle θ. The scatterer height-to-length ratio, h/ℓ, is 0.75, and the conductivity, σ, is 120.0 81

3-38. Coupling coefficient for fundamental self-resonant singularity, γ_{11}, as a function of the ground plane relative permittivity, ε_R, and incident angle θ. The scatterer height-to-length ratio, h/ℓ, is 0.75, and the conductivity, σ, is 0.12 82

3.39. Coupling coefficient for fundamental self-resonant singularity, γ_{11}, as a function of the ground plane relative permittivity, ε_R, and incident angle θ. The scatterer height-to-length ratio, h/ℓ, is 0.75, and the conductivity, σ, is 0.00012 83

3-40. Coupling coefficient for fundamental self-resonant singularity, γ_{11}, as a function of the ground plane relative permittivity, ε_R, and incident angle θ. The scatterer height-to-length ratio, h/ℓ, is 1.25, and the conductivity, σ, is 120.0 84

3-41. Coupling coefficient for fundamental self-resonant singularity, γ_{11}, as a function of the ground plane relative permittivity, ε_R, and incident angle θ. The scatterer height-to-length ratio, h/ℓ, is 1.25, and the conductivity, σ, is 0.12 85

3-42. Coupling coefficient for fundamental self-resonant singularity, γ_{11}, as a function of the ground plane relative permittivity, ε_R, and incident angle θ. The scatterer height-to-length ratio, h/ℓ, is 1.25, and the conductivity, σ, is 0.00012 86

3-43. Coupling coefficient for second self-resonant singularity, γ_{12}, as a function of conductivity, σ, and incident angle θ. The scatterer height-to-length ratio, h/ℓ, is 0.20, and the relative permittivity, ε_R, is unity 87

3-44. Coupling coefficient for second self-resonant singularity, γ_{12}, as a function of conductivity, σ, and incident angle θ. The scatterer height-to-length ratio, h/ℓ, is 0.40, and the relative permittivity, ε_R, is unity 88

3-45. Coupling coefficient for second self-resonant singularity, γ_{12}, as a function of conductivity, σ, and incident angle θ. The scatterer height-to-length ratio, h/ℓ, is 0.60, and the relative permittivity, ε_R, is unity 89

3-46. Coupling coefficient for second self-resonant singularity, γ_{12}, as a function of conductivity, σ, and incident angle θ. The scatterer height-to-length ratio, h/ℓ, is 0.80, and the relative permittivity, ε_R, is unity 90

3-47. Coupling coefficient for second self-resonant singularity, γ_{12}, as a function of conductivity, σ, and incident angle θ. The scatterer height-to-length ratio, h/ℓ, is 1.0, and the relative permittivity, ε_R, is unity 91

3-48. Real part of coupling coefficient for second self-resonant singularity, γ_{12}, as a function of scatterer height-to-length ratio, h/ℓ, and incident angle θ. The ground conductivity, σ, is 120.0, and the relative permittivity, ε_R, is unity 93

3-49. Imaginary part of coupling coefficient for second self-resonant singularity, γ_{12}, as a function of scatterer height-to-length ratio, h/ℓ, and incident angle θ. The ground conductivity, σ, is 120.0, and the relative permittivity, ε_R, is unity 94

3-50. Real part of coupling coefficient for second self-resonant singularity, γ_{12}, as a function of scatterer height-to-length ratio, h/ℓ, and incident angle θ. The ground conductivity, σ, is 0.12, and the relative permittivity, ε_R, is unity 95

3-51. Imaginary part of coupling coefficient for second self-resonant singularity, γ_{12}, as a function of scatterer height-to-length ratio, h/ℓ, and incident angle θ. The ground conductivity, σ, is 0.12, and the relative permittivity, ε_R, is unity 96

3-52. Coupling coefficient for second self-resonant singularity, γ_{12}, as a function of the ground plane relative permittivity, ε_R, and incident angle θ. The scatterer height-to-length ratio, h/ℓ, is 0.20, and the conductivity, σ, is 120.0 97

3-53. Coupling coefficient for second self-resonant singularity, γ_{12}, as a function of the ground plane relative permittivity, ε_R, and incident angle θ. The scatterer height-to-length ratio, h/ℓ, is 0.20, and the conductivity, σ, is 0.12 98

3-54. Coupling coefficient for second self-resonant singularity, γ_{12}, as a function of the ground plane relative permittivity, ε_R, and incident angle θ. The scatterer height-to-length ratio, h/ℓ, is 0.20, and the conductivity, σ, is 0.00012 99

3-55. Coupling coefficient for second self-resonant singularity, γ_{12}, as a function of the ground plane relative permittivity, ε_R, and incident angle θ. The scatterer height-to-length ratio, h/ℓ, is 0.40, and the conductivity, σ, is 120.0 100

3-56. Coupling coefficient for second self-resonant singularity, γ_{12}, as a function of the ground plane relative permittivity, ε_R, and incident angle θ. The scatterer height-to-length ratio, h/ℓ, is 0.40, and the conductivity, σ, is 0.12 101

3-57. Coupling coefficient for second self-resonant singularity, γ_{12}, as a function of the ground plane relative permittivity, ε_R, and incident angle θ. The scatterer height-to-length ratio, h/ℓ, is 0.40, and the conductivity, σ, is 0.00012 102

3-58. Coupling coefficient for second self-resonant singularity, γ_{12}, as a function of the ground plane relative permittivity, ε_R, and incident angle θ. The scatterer height-to-length ratio, h/ℓ, is 0.60, and the conductivity, σ, is 120.0 103

3-59. Coupling coefficient for second self-resonant singularity, γ_{12}, as a function of the ground plane relative permittivity, ε_R, and incident angle θ. The scatterer height-to-length ratio, h/ℓ, is 0.60, and the conductivity, σ, is 0.12 104

3-60. Coupling coefficient for second self-resonant singularity, γ_{12}, as a function of the ground plane relative permittivity, ε_R, and incident angle θ. The scatterer height-to-length ratio, h/ℓ, is 0.60, and the conductivity, σ, is 0.00012 105

3-61. Coupling coefficient for second self-resonant singularity, γ_{12}, as a function of the ground plane relative permittivity, ε_R, and incident angle θ. The scatterer height-to-length ratio, h/ℓ, is 0.80, and the conductivity, σ, is 120.0 106

3-62. Coupling coefficient for second self-resonant singularity, γ_{12}, as a function of the ground plane relative permittivity, ε_R, and incident angle θ. The scatterer height-to-length ratio, h/ℓ, is 0.80, and the conductivity, σ, is 0.12 107

3-63. Coupling coefficient for second self-resonant singularity, γ_{12}, as a function of the ground plane relative permittivity, ε_R, and incident angle θ. The scatterer height-to-length ratio, h/ℓ, is 0.80, and the conductivity, σ, is 0.00012 108

3-64. Coupling coefficient for second self-resonant singularity, γ_{12}, as a function of the ground plane relative permittivity, ε_R, and incident angle θ. The scatterer height-to-length ratio, h/ℓ, is 1.0, and the conductivity, σ, is 120.0 109

3-65. Coupling coefficient for second self-resonant singularity, γ_{12}, as a function of the ground plane relative permittivity, ε_R, and incident angle θ. The scatterer height-to-length ratio, h/ℓ, is 1.0, and the conductivity, σ, is 0.12 110

3-66. Coupling coefficient for second self-resonant singularity, γ_{12}, as a function of the ground plane relative permittivity, ε_R, and incident angle θ. The scatterer height-to-length ratio, h/ℓ, is 1.0, and the conductivity, σ, is 0.00012 111

3-67. Coupling coefficient for third self-resonant singularity, γ_{13}, as a function of conductivity, σ and incident angle θ. The scatterer height-to-length ratio, h/ℓ, is 0.10, and the relative permittivity, ε_R, is unity 112

3-68. Coupling coefficient for third self-resonant singularity, γ_{13}, as a function of conductivity, σ, and incident angle θ. The scatterer height-to-length ratio, h/ℓ, is 0.20, and the relative permittivity, ε_R, is unity 113

3-69. Coupling coefficient for third self-resonant singularity, γ_{13}, as a function of conductivity, σ, and incident angle θ. The scatterer height-to-length ratio, h/ℓ, is 0.30, and the relative permittivity, ε_R, is unity 114

3-70. Coupling coefficient for third self-resonant singularity, γ_{13}, as a function of conductivity, σ, and incident angle θ. The scatterer height-to-length ratio, h/ℓ, is 0.40, and the relative permittivity, ε_R, is unity 115

3-71. Coupling coefficient for third self-resonant singularity, γ_{13}, as a function of conductivity, σ, and incident angle θ. The scatterer height-to-length ratio, h/ℓ, is 0.50, and the relative permittivity, ε_R, is unity 116

3-72. Real part of coupling coefficient for third self-resonant singularity, γ_{13}, as a function of scatterer height-to-length ratio, h/ℓ, and incident angle θ. The ground conductivity, σ, is 120.0, and the relative permittivity, ε_R, is unity 118

3-73. Imaginary part of coupling coefficient for third self-resonant singularity, γ_{13}, as a function of scatterer height-to-length ratio, h/ℓ, and incident angle θ. The ground conductivity, σ, is 120.0, and the relative permittivity, ε_R, is unity 119

3-74. Real part of coupling coefficient for third self-resonant singularity, γ_{13}, as a function of scatterer height-to-length ratio, h/ℓ, and incident angle θ. The ground conductivity, σ, is 0.12, and the relative permittivity, ε_R, is unity 120

3-75. Imaginary part of coupling coefficient for third self-resonant singularity, γ_{13}, as a function of scatterer height-to-length ratio, h/ℓ, and incident angle θ. The ground conductivity, σ, is 0.12, and the relative permittivity, ε_R, is unity 121

3-76. Coupling coefficient for third self-resonant singularity, γ_{13}, as a function of the ground plane relative permittivity, ε_R, and incident angle θ. The scatterer height-to-length ratio, h/ℓ, is 0.10, and the conductivity, σ, is 120.0 122

3-77. Coupling coefficient for third self-resonant singularity, γ_{13}, as a function of the ground plane relative permittivity, ε_R, and incident angle θ. The scatterer height-to-length ratio, h/ℓ, is 0.10, and the conductivity, σ, is 0.12 123

3-78. Coupling coefficient for third self-resonant singularity, γ_{13}, as a function of the ground plane relative permittivity, ε_R, and incident angle θ. The scatterer height-to-length ratio, h/ℓ, is 0.10, and the conductivity, σ, is 0.00012 124

3-79. Coupling coefficient for third self-resonant singularity, γ_{13}, as a function of the ground plane relative permittivity, ε_R, and incident angle θ. The scatterer height-to-length ratio, h/ℓ, is 0.20, and the conductivity, σ, is 120.0 125

3-80. Coupling coefficient for third self-resonant singularity, γ_{13}, as a function of the ground plane relative permittivity, ε_R, and incident angle θ. The scatterer height-to-length ratio, h/ℓ, is 0.20, and the conductivity, σ, is 0.12 126

3-81. Coupling coefficient for third self-resonant singularity, γ_{13}, as a function of the ground plane relative permittivity, ε_R, and incident angle θ. The scatterer height-to-length ratio, h/ℓ, is 0.20, and the conductivity, σ, is 0.00012 127

3-82. Coupling coefficient for third self-resonant singularity, γ_{13}, as a function of the ground plane relative permittivity, ε_R, and incident angle θ. The scatterer height-to-length ratio, h/ℓ, is 0.30, and the conductivity, σ, is 120.0 128

3-83. Coupling coefficient for third self-resonant singularity, γ_{13}, as a function of the ground plane relative permittivity, ε_R, and incident angle θ. The scatterer height-to-length ratio, h/ℓ, is 0.30, and the conductivity, σ, is 0.12 129

3-84. Coupling coefficient for third self-resonant singularity, γ_{13}, as a function of the ground plane relative permittivity, ε_R, and incident angle θ. The scatterer height-to-length ratio, h/ℓ, is 0.30, and the conductivity, σ, is 0.00012 130

3-85. Coupling coefficient for third self-resonant singularity, γ_{13}, as a function of the ground plane relative permittivity, ε_R, and incident angle θ. The scatterer height-to-length ratio, h/ℓ, is 0.40, and the conductivity, σ, is 120.0 131

3-86. Coupling coefficient for third self-resonant singularity, γ_{13}, as a function of the ground plane relative permittivity, ε_R, and incident angle θ. The scatterer height-to-length ratio, h/ℓ, is 0.40, and the conductivity, σ, is 0.12 132

3-87. Coupling coefficient for third self-resonant singularity, γ_{13}, as a function of the ground plane relative permittivity, ε_R, and incident angle θ. The scatterer height-to-length ratio, h/ℓ, is 0.40, and the conductivity, σ, is 0.00012 133

3-88. Coupling coefficient for third self-resonant singulatiry, γ_{13}, as a function of the ground plane relative permittivity, ε_R, h/ℓ, is 0.50, and the conductivity, σ, is 120.0 134

3-89. Coupling coefficient for third self-resonant singularity, γ_{13}, as a function of the ground plane relative permittivity, ε_R, h/ℓ, is 0.50, and the conductivity, σ, is 0.12 135

3-90. Coupling coefficient for third self-resonant singularity, γ_{13}, as a function of the ground plane relative permittivity, ε_R, h/ℓ, is 0.50, and the conductivity, σ, is 0.00012 136

LIST OF TABLES

3- 1. Predicted angle of incidence for maximum coupling using the "standing wave analogy." The table applies to Figure 3-26 through 3-31 for large conductivity, (σ = 120.0), and unity permittivity, (ε_R = 1.0) . . . . . .

3- 2. Predicted angle of incidence for maximum coupling using the "standing wave analogy." The table applies to Figure 3-43 through 3-47 for large conductivity, (σ = 120.0), and unity permittivity, (ε_R = 1.0) . . . . . .

3- 3. Predicted angle of incidence for maximum coupling using the "standing wave analogy." The table applies to Figures 3-67 through 3-71 for large conductivity, (σ = 120.0), and unity permittivity, (ε_R = 1.0) . . . . . .

I. INTRODUCTION

Previous investigators have studied the interactions of thin cylinders in free space [1], and thin cylinders over perfectly conducting ground [2] with an electromagnetic step plane wave. This study will present in an approximate manner the interaction of a thin cylinder over a finitely conducting ground with an electromagnetic step plane wave. Analysis will be conducted using the Singularity Expansion Method (SEM).

Current induced by the incident field on the cylinder surface is approximated by an axially directed filamentary current on the cylinder axis. Boundary conditions are applied only to the axial component of the incident electromagnetic field on the wire axis. The above "thin-wire" assumptions are valid provided the length of the cylinder is much greater than its radius, and the cylinder is many radii away from the ground plane [3].

The scattered field reflected from the ground plane is scaled by the complex Fresnel reflection coefficient for the appropriate angle of incidence and polarization involved. Since the Fresnel reflection coefficient is strictly valid only for plane wave incidence, the scattered field must approximate a plane wave at the free space-lossy ground interface. In a study by Sarkar and Strait [4] it was shown that the above method, termed "reflection method" gave results in the real frequency domain within 10% of the exact Sommerfeld formulation for a horizontal electric dipole as long as the dipole was at least $(0.25\lambda/\sqrt{\varepsilon_R})$ from the ground plane. Speed of computation is an inherent advantage when using the reflection method.

II. THEORY

Integro-Differential Equation

The system defined by Figure 1 is composed of a thin cylinder over an imperfectly conducting ground plane and the incident electromagnetic radiation. As shown, the cylinder is of length ℓ, radius a, and height h above the ground plane. The imperfectly conducting nonmagnetic, $\mu = \mu_o$, ground plane is characterized by its conductivity σ, and permittivity, $\varepsilon = \varepsilon_R \varepsilon_o$. The incident plane wave is vertically polarized and propagates at an angle θ with respect to the normal.

Currents will be induced on the cylinder by the incident field and by reflection of the incident field from the ground plane. These induced currents will reradiate in the presence of the imperfectly conducting ground producing a primary and secondary scattered field. Primary scattered radiation is that part of the current induced field which propagates directly from the scatterer surface to observation point. Secondary scattered radiation reflects from the ground plane before reaching the observation point, and therefore must be scaled by the complex Fresnel reflection coefficient for the appropriate angle of incidence and polarization involved. The total scattered field consist of the sum of the primary and scaled secondary parts.

The primary scattered electric field is related to the currents that produced it through a magnetic vector potential and appropriate differential operators. This relation may be written as

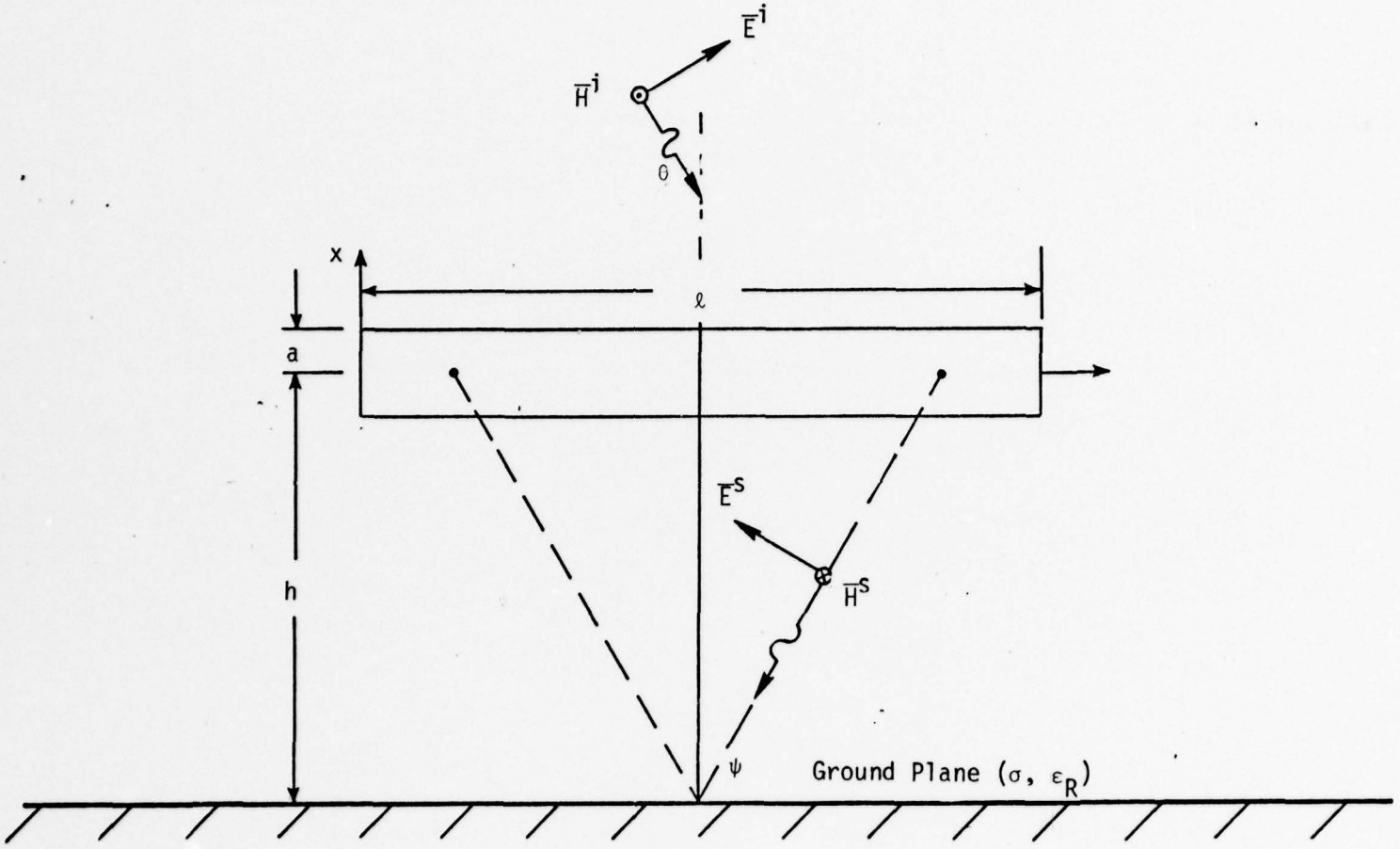


Figure 2-1. System Geometry

$$\bar{E}^p = -\mu_o s\bar{A}^p + \bar{\nabla}(\bar{\nabla} \cdot \bar{A}^p)/s\varepsilon_o \tag{2.1}$$

= primary scattered electric field

where $$\bar{A}^p = \frac{1}{4\pi}\int_0^{2\pi}\int_0^{\ell} \bar{K}(\bar{r}',s)\,\frac{e^{-\gamma|r-r'|^p}}{|\bar{r}-\bar{r}'|^p}\,ds' \tag{2.2}$$

= primary magnetic vector potential

$\bar{K}(\bar{r}',s)$ = surface current density

$\nabla = \hat{u}_x \frac{\partial}{\partial x} + \hat{u}_y \frac{\partial}{\partial y} + \hat{u}_z \frac{\partial}{\partial z}$ = vector operator

$r' = \hat{u}_x x' + \hat{u}_y y' + \hat{u}_z z'$ = source vector

$|\bar{r}-\bar{r}'|^p$ = direct distance from source point to observation point

$s = \sigma + j\omega$ = complex frequency variable

$\gamma = s/c$, c = speed of light in free space.

Use of the complex frequency variable s in the above equations implies that the Maxwell equations have been Laplace transformed.

Secondary scattered electric radiation may also be written in terms of a magnetic vector potential as

$$\bar{E}^s = -\mu_o s\bar{A}^s + \nabla(\nabla \cdot \bar{A}^s)/s\varepsilon_o \tag{2.3}$$

= secondary scattered electric field

where $$\bar{A}^s = \frac{1}{4\pi}\int_0^{2\pi}\int_0^{\ell} \bar{K}(\bar{r}',s)\,\frac{e^{-\gamma|\bar{r}-\bar{r}'|^s}}{|\bar{r}-\bar{r}'|^s}\,ds' \qquad (2.4)$$

= secondary magnetic vector potential

$|\bar{r}-\bar{r}'|^s$ = distance from source point to ground plane to observation point.

All other terms in (2.3) and (2.4) have been previously defined.

With surface currents on the cylinder approximated by a z-directed filamentary current on the cylinder axis, the primary and secondary magnetic vector potentials of (2.2) and (2.4) reduce to

$$A_z^p = \frac{1}{4\pi}\int_0^{\ell} I(z',s)\,\frac{e^{-\gamma|\bar{r}-\bar{r}'|^p}}{|\bar{r}-\bar{r}'|^p}\,dz' \qquad (2.5)$$

$$A_z^s = \frac{1}{4\pi}\int_0^{\ell} I(z',s)\,\frac{e^{-\gamma|\bar{r}-\bar{r}'|^s}}{|\bar{r}-\bar{r}'|^s}\,dz' \quad . \qquad (2.6)$$

Locate the observation point on the cylinder surface, then

$$|\bar{r}-\bar{r}'|^p = r_1 = [(z-z')^2 + a^2]^{\frac{1}{2}} \qquad (2.7)$$

and $$|\bar{r}-\bar{r}'|^s = r_2 = [(z-z')^2 + (2h+a)^2]^{\frac{1}{2}} \quad . \qquad (2.8)$$

An expression for the primary scattered electric field in terms of the unknown induced currents may be formed by substituting (2.5) into (2.1), the result is

$$E_z^p(z,s) = \left(-\mu_o s + \frac{1}{s\varepsilon_o}\,\frac{\partial^2}{\partial z^2}\right)\,\frac{1}{4\pi}\int_0^{\ell} I(z',s)\,\frac{e^{-\gamma r_1}}{r_1}\,dz' \,. \qquad (2.9)$$

A similar expression for secondary scattered electric radiation may be formed by substituting (2.2) into (2.3) with the result

$$E_z^s(z,s) = \left(-\mu_o s + \frac{1}{s\varepsilon_o}\frac{\partial^2}{\partial z^2}\right)\frac{1}{4\pi}\int_o^{\ell} I(z',s)\,\frac{e^{-\gamma r_2}}{r_2}\,dz' \quad . \quad (2.10)$$

As stated, the total scattered field consists of the sum of the primary and scaled secondary parts, that is

$$\begin{aligned} E_z^{tot}(z,s) &= E_z^p(z,s) - R_v^{\psi}E_z^s(z,s) \\ &= \left(-\mu_o s + \frac{1}{s\varepsilon_o}\frac{\partial^2}{\partial z^2}\right)\frac{1}{4\pi}\int_o^{\ell} I(z',s)\,\frac{e^{-\gamma r_1}}{r_1}\,dz' \qquad (2.11) \\ &\quad - R_v^{\psi}\left(-\mu_o s + \frac{1}{s\varepsilon_o}\frac{\partial^2}{\partial z^2}\right)\frac{1}{4\pi}\int_o^{\ell} I(z',s)\,\frac{e^{-\gamma r_2}}{r_2}\,dz' \quad . \end{aligned}$$

The complex Fresnel reflection coefficient for vertical polarization, i.e. (R_v^{ψ}) is used in (2.11) to scale the z-directed secondary electric field, and is defined as

$$R_v^{\psi} = \frac{(\varepsilon_R + X)\sin\psi - [(\varepsilon_R + X) - \cos^2\psi]^{\frac{1}{2}}}{(\varepsilon_R + X)\sin\psi + [(\varepsilon_R + X) - \cos^2\psi]^{\frac{1}{2}}} \qquad (2.12)$$

where $X = 120\pi\sigma/\gamma$, $\gamma = s/c$.

This expression utilizes Jordon's [5] definition of the plane wave reflection coefficient for vertical polarization. As pointed out by a previous investigator [6], the minus sign in (2.11) comes from Jordon's assumed positive directions of electric fields for the incident and reflected waves [5]. Note that ψ in (2.12) is the angle formed by the

secondary scattered incident ray and the ground plane. It is a function of source and field point position as depicted by Figure 2-1.

In Figure 2-2 is shown the vertically polarized total incident and transmitted electromagnetic excitation. At the free-space lossy ground interface the tangential components of the total incident field must equal the tangential components of the transmitted field. This condition is equivalent to requiring normal wave impedances to be continuous at the interface [7], thus

$$Z_x^i = \frac{E_z^i}{H_y^i} = -Z_x^t = \frac{E_z^t}{H_y^t} \text{ at } x = -h \tag{2.13}$$

where

Z_x^i = x-directed wave impedance in free space region

$$E_z^i = E_o^i(s) \sin\theta_i \left[e^{-\gamma(-x \sin\theta_i + z \cos\theta_i)} - \Gamma e^{-\gamma(x \sin\theta_i + z \cos\theta_i)}\right] \tag{2.14}$$

= total z-directed incident electric field

$$H_y^i = E_o^i(s)/\eta_1 \left[e^{-\gamma(-x \sin\theta_i + z \cos\theta_i)} + \Gamma e^{-\gamma(x \sin\theta_i + z \cos\theta_i)}\right] \tag{2.15}$$

= total y-directed incident magnetic field

Z_x^t = x-directed wave impedance in lossy region

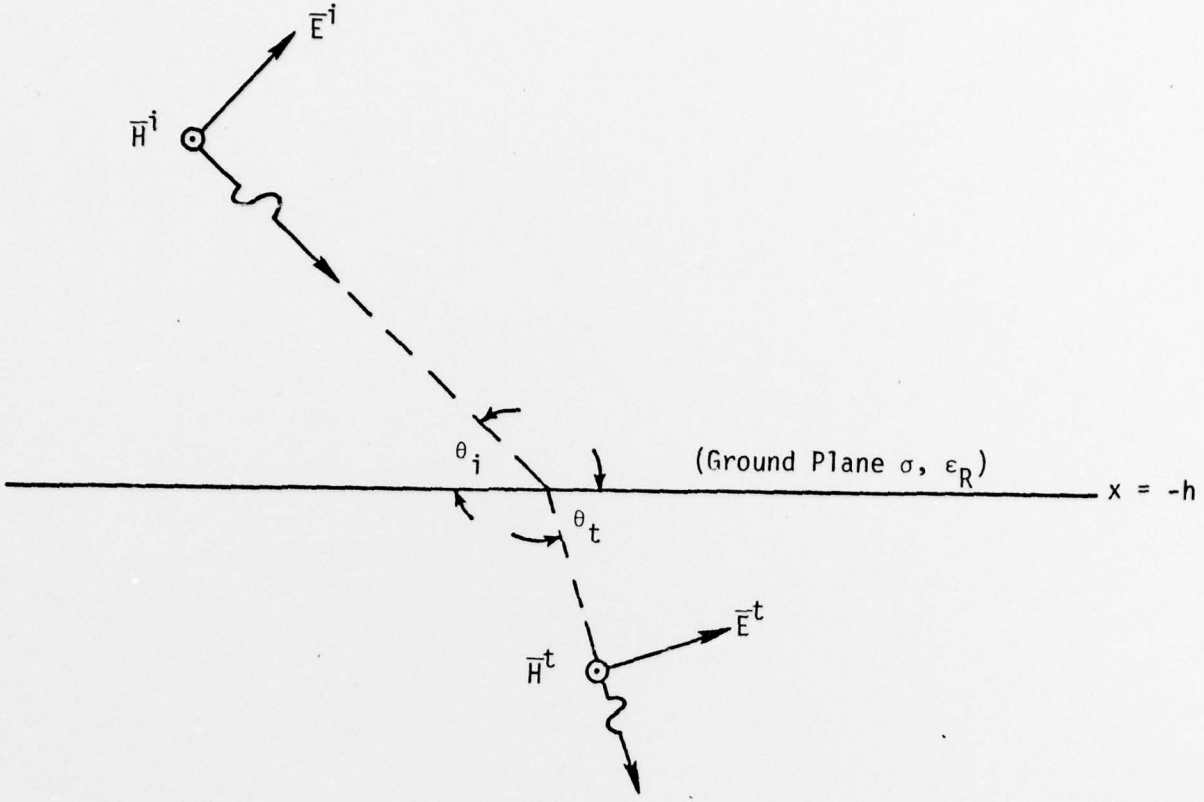


Figure 2-2. Vertically polarized total incident and transmitted electromagnetic excitation.

$$E_z^t = E_o^t(s)\,\sin\theta_t\, e^{-\gamma_2(-x\,\sin\theta_t + z\,\cos\theta_t)} \qquad (2.16)$$

= z-directed transmitted electric field

$$H_y^t = E_o^t(s)/\eta_2\, e^{-\gamma_2(-x\,\sin\theta_t + z\,\cos\theta_t)} \qquad (2.17)$$

= y-directed transmitted magnetic field

η_1 = intrinsic impedance of free space

η_2 = intrinsic impedance of conducting earth

γ_2 = complex propagation number of conducting earth

and Γ is the reflection coefficient to be determined. Note that the total incident field consists of the direct electromagnetic excitation plus its reflection from the ground plane. The principal of direction cosines has been used in the development of (2.14) through (2.17). Substituting the field expressions into (2.13), and simplifying the result, gives

$$\Gamma = e^{-\gamma 2h\sin\theta_i}\,\frac{\eta_1\,\sin\theta_i - \eta_2\,\sin\theta_t}{\eta_1\,\sin\theta_i + \eta_2\,\sin\theta_t} \qquad . \qquad (2.18)$$

Through the application of Snell's law of refraction (2.18) may be written

$$\Gamma = e^{-\gamma 2h\sin\theta}\,\frac{(\varepsilon_R+X)\,\sin\theta - [(\varepsilon_R+X)-\cos^2\theta]^{\frac{1}{2}}}{(\varepsilon_R+X)\,\sin\theta + [(\varepsilon_R+X)-\cos^2\theta]^{\frac{1}{2}}}$$

$$= e^{-\gamma 2h\sin\theta}\,R_v^\theta \qquad . \qquad (2.19)$$

Equation (2.19) differs from (2.12) only by the exponential factor and angular dependence of R_v. The total z-directed incident electric field may now be obtained by substituting (2.19) into (2.14) with the result

$$E_z^i = E_o^i(s) \sin\theta \left[e^{-\gamma(-x \sin\theta + z \cos\theta)} - R_v^\theta \right.$$

$$\left. e^{-\gamma(2h \sin\theta + x \sin\theta + z \cos\theta)} \right] . \qquad (2.20)$$

To insure uniqueness the total z-directed scattered electric field must cancel the total z-directed incident electric field on the cylinder axis, therefore

$$E_z^i \Big|_{x=o} = - E_z^{tot}(z,s) \Big|_{x=o} \qquad . \qquad (2.21)$$

Evaluating the z-directed scattered and incident fields on the cylinder axis rather than on the surface is an appropriate thin wire assumption. Using (2.11) and (2.20) in (2.21) and applying the above discussed thin wire assumption, (2.21) becomes

$$E_o^i(s) \sin\theta \left[e^{-\gamma z \cos\theta} - R_v^\theta \, e^{-\gamma(z \cos\theta + 2h \sin\theta)}\right]$$

$$= (\mu_o s - \frac{1}{s\epsilon_o} \frac{\partial^2}{\partial z^2}) \frac{1}{4\pi} \int_o^\ell I(z',s) \frac{e^{-\gamma r_1}}{r_1} dz'$$

$$- R_v^\psi (\mu_o s - \frac{1}{s\epsilon_o} \frac{\partial^2}{\partial z^2}) \frac{1}{4\pi} \int_o^\ell I(z',s) \frac{e^{-\gamma r_2}}{r_2} dz' \qquad . \qquad (2.22)$$

Define

$$F^p(z,z',s) = \frac{e^{-\gamma r_1}}{r_1} = \text{primary Green's function} \qquad (2.23)$$

$$F^s(z,z',s) = \frac{e^{-\gamma r_2}}{r_2} = \text{secondary Green's function} \qquad (2.24)$$

where

$$r_1 = [(z-z')^2 + a^2]^{\frac{1}{2}}$$

$$r_2 = [(z-z')^2 + (2h+a)^2]^{\frac{1}{2}}$$

and since

$$\frac{1}{4\pi}(-4\pi\varepsilon_o s)\left(\mu_o s - \frac{1}{s\varepsilon_o}\frac{\partial^2}{\partial z^2}\right) = \left(\frac{\partial^2}{\partial z^2} - \gamma^2\right) \quad . \qquad (2.25)$$

the integro-differential equation to be solved for the unknown induced currents is

$$(-4\pi\varepsilon_o s)\, E_o^i(s) \sin\theta \left[e^{-\gamma z \cos\theta} - R_v^\theta\, e^{-\gamma(z\cos\theta + 2h\sin\theta)}\right]$$

$$= \left(\frac{\partial^2}{\partial z^2} - \gamma^2\right) \int_0^\ell I(z',s)\, F^s(z,z',s)\, dz'$$

$$- R_v^\psi \left(\frac{\partial^2}{\partial z^2} - \gamma^2\right) \int_0^\ell I(z',s)\, R^s(z,z',s)\, dz' \qquad (2.26)$$

Application of the Method of Moments

The purpose of this section is to reduce the integro-differential equation, (2.26), to a form suitable for numerical solution. The technique by which this may be accomplished is known as the method of moments [8].

Generally, the method of moments may be used to solve an inhomogeneous equation

$$L(f) = g \qquad (2.27)$$

where L is a linear operator, g is known, and f is to be determined. The unknown f is expanded in a series of functions as

$$f = \sum_n \alpha_n f_n \tag{2.28}$$

where the f_n are called basis functions and the α_n are constants. Using the linearity of L and (2.28), (2.27) may be written

$$\sum_n \alpha_n L(f_n) = g \tag{2.29}$$

Next a set of testing functions is defined, w_1, w_2, w_3 ..., and the inner product of (2.29) with each w_m formed, yielding

$$\sum_n \alpha_n \langle w_m, L(f_n) \rangle = \langle w_m, g \rangle \tag{2.30}$$

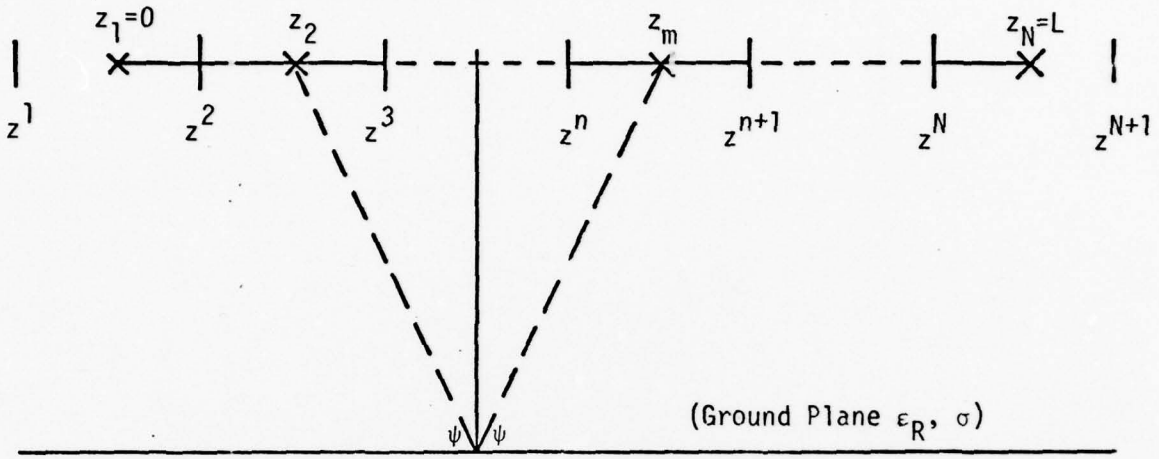
$n = 1, 2, 3, \ldots$

$m = 1, 2, 3, \ldots$

Equation (2.30) is a matrix equation which may be solved using standard numerical techniques.

For the problem at hand, a geometric interpretation of the method of moments may be forwarded. Let the thin wire be broken into segments, with the induced current on each segment assumed to be constant. See Figure 2-3. This is equivalent to expanding the current in a set of pulse functions as

$$I(z',s) = \sum_n \alpha_n(s)\, I_n(z') \tag{2.31}$$



\- "Thin Wire"

| Subsection Ends

x Match Points

$z_n = (m-1)\Delta$ (Match Points) m = 1, 2, ... N

$z^n = (n-3/2)\Delta$ (Subsection Ends) n = 1, 2, ... N+1

$\Delta = \ell/(N-1)$ Length of Zones

N = Number of Subsections

Figure 2-3. Moment Method Partitioning of Geometry

where

$\alpha_n(s)$ = unknown coefficient of constant current in the n^{th} subsection.

and $$I_n(z') = \begin{cases} 1 \text{ for } z^n < z < z^{n+1} \\ 0 \text{ elsewhere } n = 2, 3, \ldots N-1 \end{cases} \quad . \tag{2.32}$$

At wire ends the boundary condition of zero current may be satisfied by defining

$$I(o) = I(\ell) = 0 \quad . \tag{2.33}$$

Actually, this condition is automatically met by allowing the two end subsections to extend past the end of the scatterer. Using a pulse function expansion of the unknown induced current allows the integration in (2.26) to be approximated by a sum of integrations over N segments. Thus,

$$(-4\pi\varepsilon_o s)\, E_o^i(s) \sin\theta \left[e^{-\gamma z \cos\theta} - R_v^\theta\, e^{-\gamma(z\cos\theta + 2h\sin\theta)}\right]$$

$$= \sum_n \alpha_n(s) \int_{z^n}^{z^{n+1}} \left(\frac{\partial^2}{\partial z^2} - \gamma^2\right) F^p(z,z',s)\, dz' \tag{2.34}$$

$$- R_v^\psi \sum_n \alpha_n(s) \int_{z^n}^{z^{n+1}} \left(\frac{\partial^2}{\partial z^2} - \gamma^2\right) F^s(z,z',s)\, dz'$$

where

$$\Delta = \ell/(N-1) = \text{length of a zone} \tag{2.35}$$

N = number of subsections or zones

$z^n = (n - 3/2)\Delta \quad n = 1, 2, \ldots N+1$

= subsection ends.

A set of testing functions may now be defined as

$$\delta(z-z_m) = \begin{cases} 1 & z=z_m \\ 0 & z \neq z_m \end{cases} \tag{2.36}$$

where $z_m = (m-1)\Delta \quad m = 1, 2, \ldots N$. (2.37)

Now by forming the inner product of (2.34) with each of the delta functions of (2.36), and approximating the differentiation in (2.34) by finite differences, that is

$$\frac{d^2F}{dz^2} \simeq \frac{1}{(\Delta z)^2} [F(z+\Delta z) - 2F(z) + F(z-\Delta z)] \tag{2.38}$$

the integro-differential equation becomes

$$(-4\pi\varepsilon_o s)\, E_o^i(s) \sin\theta \left[e^{-\gamma z_m \cos\theta} - R_v^\theta\, e^{-\gamma(z_m \cos\theta + 2h \sin\theta)}\right]$$

$$= \sum_n \alpha_n(s) \frac{1}{\Delta^2} \left\{\left[\int_{z_n}^{z_{n+1}} F^p(z_{m+1},z',s) - (\gamma^2\Delta^2+2)F^p(z_m,z',s)\right.\right.$$

$$\left. + F^p(z_{m-1},z',s)\, dz'\right] - R_v^\psi \left[\int_{z_n}^{z_{n+1}} F^s(z_{m+1},z',s)\right.$$

$$\left.\left. -(\gamma^2\Delta^2+2)\, F^s(z_m,z',s) + F^s(z_{m-1},z',s)\, dz'\right]\right\}$$

$n = 2, 3, \ldots N-1$

$m = 2, 3, \ldots N-1.$ (2.39)

Equation (2.39) is a set of linear algebraic equations, and may be placed in the form of a matrix equation,

$$\bar{V}(s) = \bar{\bar{Z}}(s)\ \bar{I}(s), \tag{2.40}$$

where a single bar represents a column matrix or vector and double bars indicate a square matrix. Define the matrices as

$\bar{V}(s)$ = the source vector = $[v_m]$,

where

v_m = the matrix elements of $\bar{V}(s)$

$$= (-4\pi\varepsilon_o s)\ E_o^i(s)\ \sin\theta\ [e^{-\gamma z_m \cos\theta} - R_v^\theta\ e^{-\gamma(z_m \cos\theta + 2h \sin\theta)}] \tag{2.41}$$

$$m = 2, 3, \ldots N-1$$

$\bar{I}(s)$ = the response vector = $[i_n]$

where

i_n = the matrix elements of $\bar{I}(s)$

= α_n, unknown coefficients of constant current in the n^{th} zone (2.42)

$$n = 2, 3, \ldots N-1;$$

$\bar{\bar{Z}}(s)$ = the impedance matrix = $[z_{mn}]$,

where z_{mn} = the matrix elements of $\bar{\bar{Z}}(s)$

$$z_{mn} = \frac{1}{\Delta^2} \{[\int_{z_n}^{z^{n+1}} F^p(z_{m+1},z',s) - (\gamma^2\Delta^2+2)\, F^p(z_m,z',s) + F^p(z_{m-1},z',s)\, dz'] - R_v^{\psi} [\int_{z_n}^{z^{n+1}} F^s(z_{m+1},z',s) - (\gamma^2\Delta^2+2)\, F^s(z_m,z',s) + F^s(z_{m-1},z',s)\, dz']\}$$

$$n = 2, 3, \ldots N-1$$

$$m = 2, 3, \ldots N-1 \qquad (2.43)$$

The unwieldy appearance of (2.43) may be improved by defining two functions

$$H^p_{m,n}(z_m,s) = \int_{z_n}^{z^{n+1}} F^p(z_m,z',s)\, dz' \qquad (2.44)$$

$$H^s_{m,n}(z_m,s) = \int_{z_n}^{z^{n+1}} F^s(z_m,z',s)\, dz' \qquad (2.45)$$

with $$F^p(z_m,z',s) = \frac{e^{-\gamma[(z_m-z')^2 + a^2]^{\frac{1}{2}}}}{[(z_m-z')^2 + a^2]^{\frac{1}{2}}} \qquad (2.46)$$

$$F^s(z_m,z',s) = \frac{e^{-\gamma[(z_m-z')^2 + (2h+a)^2]^{\frac{1}{2}}}}{[(z_m-z')^2 + (2h+a)^2]^{\frac{1}{2}}} \qquad (2.47)$$

Now (2.43) may be redefined as

$$z_{mn} = \frac{1}{\Delta^2} \{H^p_{m,n}(z_{m+1},s) - (\gamma^2\Delta^2+2)H^p_{m,n}(z_m,s) + H^p_{m,n}(z_{m-1},s) - R_v^{\psi} [H^s_{m,n}(z_{m+1},s) - (\gamma^2\Delta^2+2)H^s_{m,n}(z_m,s) + H^s_{m,n}(z_{m-1},s)]\} \quad \begin{matrix} n = 2, 3, \ldots N-1 \\ m = 2, 3, \ldots N-1 \end{matrix} \qquad (2.48)$$

Alternate Formulation for the Secondary Scattered Electric Field

As pointed out by Shumpert [9], an alternate formulation for the secondary scattered electric field is derivable by using the exact expression for the electric field produced by a constant current element. Using (2.11) in (2.21) gives

$$-E_z^i = E_z^p(z,s) - R_v^{\psi} E_z^s(z,s) \tag{2.49}$$

where $E_z^p(z,s)$ and $R_v^{\psi} E_z^s(z,s)$ are the primary and scaled secondary scattered electric fields on the cylinder surface respectively, due to the unknown induced current. Since the wire scatterer has been segmented as shown in Figure 2-3, and the current induced on each segment assumed constant, it follows that the secondary scattered electric field will be merely the sum of the fields caused by each individual constant current element. The exact electric field due to a constant current element has been given by Harrington [7]. Applying the principles discussed above, and using Harrington's expression for a constant current element, the secondary scattered electric field may be written

$$E_z^s(z,s) = \frac{Z_o \Delta}{2\pi} \sum_{n=2}^{N-1}{}' \alpha_n e^{-\gamma r_{mn}} \left[\left(\frac{1}{r_{mn}^2} + \frac{1}{\gamma r_{mn}^3}\right) \cos^2\psi_{mn} \right.$$

$$\left. + \frac{1}{2}\left(\frac{\gamma}{r_{mn}} + \frac{1}{r_{mn}^2} + \frac{1}{\gamma r_{mn}^3}\right) \sin^2\psi_{mn}\right] \tag{2.50}$$

where

$$Z_o = (\mu_o/\varepsilon_o)^{\frac{1}{2}} = 120\pi$$

$$\Delta = \ell/(N-1)$$

$$r_{mn} = \{(2h)^2 + [\Delta(m-n)]^2\}^{\frac{1}{2}}$$

$$\cos\psi_{mn} = (m-n)\Delta/r_{mn}$$

$$\sin\psi_{mn} = 2h/r_{mn}$$

$$m = 2, 3, \ldots N-1$$

$$n = 2, 3, \ldots N-1 \quad .$$

From (2.9) we have

$$E_z^p(z',s) = \frac{Z_o}{4\pi\gamma\Delta^2}\,\alpha_n \sum_{n=2}^{N-1} \Big[H_{m,n}^p(z_{m+1},s) - (\gamma^2\Delta^2+2)\,H_{m,n}^p(z_m,s) + H_{m,n}^p(z_{m-1},s)\Big]$$

$$m = 2, 3, \ldots N-1 \quad . \qquad (2.51)$$

Using these expressions for the scattered fields in (2.49) the matrix elements of (2.48) may be redefined as

$$Z_{m,n} = \frac{1}{\Delta^2}\,[H_{m,n}^p(z_{n+1},s) - (\gamma^2\Delta^2+2)\,H_{m,n}^p(z_n,s) + H_{m,n}^p(z_{n-1},s)] - R_v^{\psi} 2\Delta\gamma\, e^{-\gamma r_{mn}} \Big[\Big(\frac{1}{r_{mn}^2} + \frac{1}{\gamma r_{mn}^3}\Big)\cos^2\psi_{mn} + \frac{1}{2}\Big(\frac{\gamma}{r_{mn}} + \frac{1}{r_{mn}^2} + \frac{1}{\gamma r_{mn}^3}\Big)\sin^2\psi_{mn}\Big] \qquad (2.52)$$

$$m = 2, 3, \ldots N-1$$

$$n = 2, 3, \ldots N-1 \quad .$$

The obvious utility of the alternate expression for z_{mn} is that an integration has been replaced by an algebraic expression, and thus numerical evaluation time reduced.

Application of the Singularity Expansion Method

The Singularity Expansion Method (SEM) formalized by Baum [10-11], and applied by many others, allows one to treat a distributed system, such as the one at hand, in a manner similar to that used in classical circuit theory. In circuit theory the time domain response of a linear circuit excited by an arbitrary waveform may be determined by knowledge of the location of any singularities of the response function as well as the corresponding residues [1]. In the case of a distributed system there are an infinite number of singularities, and associated with each is a natural modal current distribution. For any arbitrary excitation, i.e., incident electromagnetic radiation, one need only determine how much of each natural modal current has been excited [12]. This is determined by the coupling coefficient associated with the given singularity.

The solution of (2.40) is

$$\bar{I}(s) = \bar{\bar{Z}}^{-1}(s)\,\bar{V}(s) = \bar{\bar{Y}}(s)\,\bar{V}(s) \qquad (2.53)$$

$\bar{\bar{Y}}(s)$ = the inverse of the system impedance matrix

$= [y_{mn}]$

where

y_{mn} = the matrix elements of $\bar{\bar{Y}}(s)$.

Elements of the inverse matrix may be written

$$y_{mn} = \frac{(-1)^{m+n} \Delta_{nm}(s)}{\Delta(s)} \qquad (2.54)$$

where $\Delta_{nm}(s)$ is a minor determinant of $Z(s)$ formed by deleting the n^{th} row and the m^{th} column, and $\Delta(s)$ is the determinant of $Z(s)$. Examination of (2.54) indicates that the poles of the response function $I(s)$, are the zeros of $\Delta(s)$. The poles have been termed the system natural resonant frequencies. Now writing the unknown current in a partial fraction expansion, one obtains

$$\bar{I}(s) = \bar{\bar{Y}}(s)\, \bar{V}(s) = \sum_i \frac{\bar{\bar{Y}}_i^r}{(s-s_i)}\, \bar{V}(s) \qquad . \qquad (2.55)$$

In (2.55) s_i is the i^{th} natural resonant frequency and $\bar{\bar{Y}}_i^r$ the corresponding residue, defined as

$$\bar{\bar{Y}}_i^r = \lim_{s \to s_i} [(s-s_i)\, \bar{\bar{Y}}(s)] \qquad . \qquad (2.56)$$

Using the circuit theory analogy, certain information about the system natural resonant frequencies may be inferred. First, the resonances must occur in the left-hand portion of the complex plane to insure a decaying response. The poles must occur in conjugate pairs to produce a real time domain current, and since the scatterer has a finite quality factor, no poles may reside on the $j\omega$ axis. Furthermore, it is assumed, but without proof, that the poles are all simple [1]. This has been found to be the case in many exactly solvable geometries.

The system residue matrix at the pole $s=s_\alpha$, $\bar{\bar{Y}}_\alpha^r$, has been shown to

be a dyadic [13], [14]; that is, it is proportional to the outer product of two n dimensional vectors

$$\overline{\overline{Y}}^{r}_{\alpha} = \beta_{\alpha} \overline{\nu}_{\alpha} \overline{C}^{t}_{\alpha} \tag{2.57}$$

where

$\overline{\nu}_{\alpha}$ = natural mode vector

$\overline{C}^{t}_{\alpha}$ = transpose of coupling vector

and

β_{α} = proportionality constant.

The natural mode vector is a solution to the equation

$$\overline{\overline{Z}}(s_{\alpha})\ \overline{\nu}_{\alpha} = \overline{0} \tag{2.58}$$

and the coupling vector satisfies the equation

$$\overline{\overline{Z}}^{t}(s_{\alpha})\ \overline{C}_{\alpha} = 0 \tag{2.59}$$

where

$\overline{\overline{Z}}^{t}(s_{\alpha})$ = transpose of $\overline{\overline{Z}}(s_{\alpha})$.

In this problem the system impedance matrix is symmetric, that is

$$\overline{\overline{Z}}^{t}(s_{\alpha}) = \overline{\overline{Z}}(s_{\alpha}) \tag{2.60}$$

so the natural mode vector and the coupling vector are identical,

$$\overline{\nu}_{\alpha} = \overline{C}_{\alpha} \tag{2.61}$$

and therefore, (2.57) may be written

$$\overline{\overline{Y}}^{r}_{\alpha} = \beta_{\alpha} \overline{\nu}_{\alpha} \overline{\nu}^{t}_{\alpha} \tag{2.62}$$

where

$$\bar{\nu}_\alpha^t = \text{transpose of } \bar{\nu}_\alpha \quad .$$

Let the natural mode vector be normalized such that its maximum element is real and equal to unity,

$$\bar{\nu}_{\alpha_o} = \bar{\nu}_\alpha \text{ normalized} \quad . \tag{2.63}$$

Now the residue matrix becomes

$$\bar{\bar{Y}}_\alpha^r = \beta_\alpha \bar{\nu}_{\alpha_o} \bar{\nu}_{\alpha_o}^t \tag{2.64}$$

Note that the proportionality constant β_α is not the same as in (2.62), but no confusion should result since it has not yet been defined.

Several methods are available for calculating the proportionality constant β_α. The method presented here is simple and requires a minimum of computation time. From (2.64) it is evident that

$$\begin{aligned} (y_\alpha^r)_{ii} &= \beta_\alpha \{(\nu_\alpha)_i\}_o \{(\nu_\alpha)_i\}_o \\ &= \beta_\alpha \{(\nu_\alpha)_i\}_o^2 \end{aligned} \tag{2.65}$$

where

$(y_\alpha^r)_{ii}$ = an element from the i^{th} row and i^{th} column of the system residue matrix evaluated at the singularity s_α

$\{(\nu_\alpha)_i\}$ = an element from the i^{th} row of the natural mode vector corresponding to the singularity s_α

and therefore,

$$\beta_\alpha = \frac{(y_\alpha^r)_{ii}}{\{(\nu_\alpha)_i\}_o^2} \quad . \tag{2.66}$$

The ij^{th} element of the system residue matrix at the pole s_α may be found using (2.54) and (2.56)

$$(y_\alpha^r)_{ij} = \lim_{s\to s_\alpha} (s-s_\alpha)(y_\alpha)_{ij}$$

$$= \lim_{s\to s_\alpha} \frac{(s-s_\alpha)(-1)^{i+j}\ \Delta_{ij}(s_\alpha)}{\Delta(s)} \tag{2.67}$$

so that finally,

$$\beta_\alpha = \lim_{s\to s_\alpha} \frac{(s-s_\alpha)(-1)^{i+j}\ \Delta_{ij}(s_\alpha)}{\{(\nu_\alpha)_i\}_o^2\ \Delta(s)} \quad . \tag{2.68}$$

Expressing the residue matrix as in (2.64) allows one to write the response vector of (2.55) in the form

$$I(s) = \sum_\alpha \beta_\alpha \bar{\nu}_{\alpha_o} \bar{\nu}_{\alpha_o}^t \frac{V(s)}{(s-s_\alpha)} \tag{2.69}$$

or equivalently as

$$I(s) = \sum_\alpha \beta_\alpha \bar{\nu}_{\alpha_o} \bar{C}_{\alpha_o}^t \frac{V(s)}{(s-s_\alpha)} \tag{2.70}$$

since by (2.61)

$$\bar{\nu}_{\alpha_o} = \bar{C}_{\alpha_o} = \text{normalized coupling vector} \quad .$$

In (2.70) the scalar product of the normalized coupling vector $C^t_{\alpha_o}$, and the incident field vector V(s) occurs, multiplied by the proportionality constant β_α. This quantity has been defined by Baum [14], as the coupling coefficient c_α at the singularity $s=s_\alpha$, so

$$c_\alpha = \beta_\alpha C^t_{\alpha_o} [V_o(s_\alpha)] \quad . \qquad (2.71)$$

As stated, the coupling coefficient determines how much of each natural modal current distribution, (i.e. natural mode vector) will be used in calculating the response vector I(s). It is a function of the incident angle θ, ground parameters, (conductivity σ, and permittivity, $\varepsilon_R\varepsilon_o$) and the particular singularity at which it is calculated. The response vector may now be written in terms of the coupling coefficient as

$$I(s) = \sum_\alpha \frac{c_\alpha \bar{\nu}_{\alpha_o}}{(s-s_\alpha)} \quad . \qquad (2.72)$$

Consideration of (2.72) will show that the complex natural frequencies, and natural mode vectors are not a function of the angle of incidence of the electromagnetic excitation, only the coupling coefficient. Therefore, once these quantities have been determined for a particular geometry the response function for any incident field is easily found.

Time domain currents may be found by using the Laplace inversion formula, thus

$$\bar{i}(t) = \frac{1}{2\pi j} \int_{C_b} \frac{c_\alpha \nu_{\alpha_o} e^{st}}{(s-s_\alpha)} ds \qquad (2.73)$$

where C_b is the Bromwich contour.

Approximations and Limitations Imposed

The validity of any analysis is a function of the approximations used in its construction. This section will discuss the limitations imposed by the approximations used in this analysis.

The assumptions and approximations are as follows:

a) Current is assumed to flow only in the direction of the wire axis.

b) Boundary conditions are applied only to the axial component of the electromagnetic field.

c) The surface current density is approximated by a filament of current on the wire axis.

d) End caps on the cylinder are ignored.

e) The moment method is an approximate numerical solution.

f) The reflection method is an approximate technique.

For a finite length cylinder the axially directed incident field excites both an axially and circumferentially directly current [15-18]. However, the axial component of the current is much more significant than the circumferential component provided the length of the cylinder is much greater than its radius. Therefore, the first two approximations are valid for thin cylinders. Replacing the surface currents with filamentary currents on the wire axis is valid provided the circumferential variation of the surface currents is uniform [3]. This will be the case if the cylinder is thin and located many radii away from the ground plane. The scattered field contributed by currents induced on the ends of the cylinder will be negligible provided the cross-sectional area of the cylinder

is small, $a<<\lambda$. In applying the moment method, the number of zones into which the scatterer is divided must be increased as the frequency of analysis increases. For an acceptable solution, ten zones per half wavelength may be used. Thus, one may conclude that this analysis is not applicable for high frequencies.

The term "ground wave" applies to energy propagated over paths near the earth's surface [5]. It is convenient to divide the ground wave into a "space wave" and "surface wave". The space wave is made up of direct and ground-reflected energy. The surface wave is that energy which is guided along the earth's surface, in much the same manner as an electromagnetic wave is guided by a transmission line.

Sommerfeld [19], was the first to treat radiation from a vertical dipole over a finitely conducting earth. In this original discussion, Sommerfeld stated that it was possible to divide the ground wave strength into two parts, a space wave and a surface wave. Norton [20], later expressed the fields for an electric dipole above a finitely conducting earth in a form which clearly showed this separation into space and surface waves. As pointed out by Jordon [5], when the dipole is located far from the earth the space wave becomes the total ground wave. But as the dipole nears the earth additional terms must be taken into account in order to form the total reflected field. These terms are the ones which account for the surface wave.

A comparative numerical study of several methods for analyzing a vertical thin wire antenna over a finitely conducting ground plane was done in a dissertation by Jerry McCannon [21]. In this work the

reflection method was found to give answers within 1 to 2 percent of the exact solution when the height of the dipole was greater than 3/8 λ.

As stated in the introduction, it was found that the reflection method for the horizontal dipole produced results within 10% of the exact Sommerfeld formulation if

$$h > (0.25/\sqrt{\varepsilon_R})\lambda \tag{2.73}$$

where

h = height of the dipole above ground

ε_R = relative permittivity of ground

λ = free space wavelength.

For an average relative permittivity of 15 the dipole must be located at a height greater than $h = .065\lambda$.

In short, the reflection method used in this analysis gives good results provided the scatterer is not brought into close proximity of the ground plane.

III. Numerical Results

A computer code has been written to determine specific SEM parameters (i.e., the system resonances and corresponding natural modal current distributions). These parameters are a function of scatterer height-to-length ratio, length-to-radius ratio, ground conductivity and relative permittivity.

Before presenting the results of this work, a brief review of two other closely related problems is in order.

Tesche [1] treated the case of a cylindrical scatterer in free space. The exterior natural resonances of this problem occur in layers in the complex plane and may be described by $\gamma_{\ell,n}$ where "ℓ" denotes the layer of the pole and "n" the pole within the layer. These free space resonances are repeated in Figure 3-1. Singularities located with an "x" have natural modal current distributions which are even functions about the scatterer midpoint; those located with a dot have odd modal distributions. Note that the imaginary part, $\omega\ell/c$, of the singularities in the first layer occurs at approximately an integer multiple of π, or at a point where the length of the cylinder is resonant (i.e., $\ell=n\lambda/2$). First layer resonances are of greatest importance in calculating induced currents since their position in the complex plane is nearest the imaginary axis. In the free space problem pole locations are a function only of cylinder length-to-radius ratio. As the radius of the structure is increased, the poles move away from the imaginary axis indicating that

more damping is introduced. A commonly used shape parameter is defined by

$$\Omega = 2\ln(\ell/a) \tag{3.1}$$

All the figures in this work are for a shape parameter of 10.6 (ℓ/a=200).

The problem of a thin cylinder over a perfectly conducting ground plane has been treated by Shumpert [9]. Singularities in this problem are a function of scatterer height-to-length ratio as well as length-to-radius ratio. When the cylinder is half its length above the perfectly conducting ground plane, the poles will be oriented as shown in Figure 3-2. Comparison of this figure with Figure 3-1 indicates that the critical resonances, those along the imaginary axis, are only slightly displaced from their free space counterpart. Figure 3-3 displays the movement of singularity γ_{11} as the scatterer recedes from the ground plane. As shown, this pole spirals about the free space location until a pole from another layer takes its place. That is, the original pole, γ_{11}, leaves the spiral path and begins to approach the origin while the new pole takes up the spiral trajectory left by the original pole. This pole makes only a partial revolution about the free space location before it, too, is replaced by a new pole. It is interesting to note that each of these singularities have similar modal current distributions. First layer singularities are associated with the length of the scatterer, as in the free space case. Singularities in the other layers have been associated with scatterer-ground plane interactions.

Let us now consider the problem of a thin cylinder over a finitely

conducting ground plane. Figure 3-4 shows the movement of singularity γ_{11} in the complex plane as several system parameters are varied. The outer dashed spiral through the points labeled "A" is the trajectory of pole γ_{11} as the scatterer is brought near the ground plane; the conductivity is held constant at $\sigma = 1.2 \times 10^{2}$ along this curve. A conductivity of this value corresponds to a very good earth, that is, the ground plane may be considered perfectly conducting. Therefore, this spiral is seen to be identical with the trajectory of γ_{11} presented in Figure 3-3. For each value of h/ℓ, the conductivity is varied from $\sigma = 1.2 \times 10^{2}$, point "A" on the dashed curve, to $\sigma = 1.2 \times 10^{-4}$, point "G", intermediate values are shown at points "B" through "F". The value $\sigma = 1.2 \times 10^{-3}$ and $\sigma = 1.2 \times 10^{-2}$ at points "E" and "F" respectively correspond to typical values of conductivity for normal terrain. Let the paths traversed by the pole for a given value of h/ℓ be called the inner spirals. It is seen that each inner spiral, corresponding to a given value of h/ℓ, converges to point "G" as the conductivity of the ground is reduced, this result is to be expected since "G" is the location of γ_{11} for free space conditions. When the pole is displaced from position "G" along one of the inner spirals more energy is being reflected from the ground plane. As σ becomes very large, points "A", all the incident energy is reflected, and the problem becomes that of a cylindrical scatterer over a perfectly conducting ground plane. Figure 3-5 is also a plot of γ_{11} as the value of h/ℓ and σ vary, the relative permittivity is held at five. Unlike Figure 3-4, point "G" is not the same in the limiting case of small σ, but rather each inner spiral

converges to some point along an inner dashed spiral. Although the conductivity becomes small, the ground plane is still somewhat reflective since the relative permittivity is held at five. Next consider Figures 3-6 and 3-7 where the relative permittivity is held at fifteen and one hundred, respectively. Again, as the conductivity is reduced, the paths followed by the singularity for a given value of h/ℓ converges to an inner spiral. The points along these inner spirals are displaced from the free space pole position in proportion to the relative permittivity of the ground.

Some insight into the behavior of the system singularities may be obtained by considering their origin. As stated, the singularities in the complex plane are the zeros of the determinant of the system impedance matrix. Therefore, as the impedance elements vary so will the position of a given pole. The impedance elements for this problem may be expressed as

$$z_{mn} = z^{f}_{mn} - R^{\psi}_{v} z^{i}_{mn} \tag{3.2}$$

where

z^{f}_{mn} = matrix elements of the free space problem

z^{i}_{mn} = matrix elements due to image terms in the perfect ground problem

and

$$R^{\psi}_{v} = \frac{(\varepsilon_R + X)\sin\psi - [(\varepsilon_R + X) - \cos^2\psi]^{\frac{1}{2}}}{(\varepsilon_R + X)\sin\psi + [(\varepsilon_R + X) - \cos^2\psi]^{\frac{1}{2}}} \tag{3.3}$$

ε_R = relative permittivity of earth

$X = 120\pi\sigma/\gamma$, σ = conductivity of earth.

From (3.2) it is apparent that when the reflection coefficient is very small the impedance elements will be the elements of the free space problem, and thus the singularity locations will be those of Figure 3-1. This condition will be met when the relative permittivity of the earth is unity and the term "X" in (3.3) is much less than one. When the Fresnel reflection coefficient is near unity the impedance elements will be those of the perfect ground case, and the singularity locations will be those of Figure 3-2. This occurs when either the term "X" or the relative permittivity of the earth is large. Note that the size of the term "X" is proportional to the conductivity of the earth and inversely proportional to the frequency of the particular singularity under consideration. Thus for higher order poles the ground conductivity must be larger to produce a perfectly conducting earth than for lower order poles. In short, displacement of a singularity from its free space position is a function of the magnitude of discontinuity in the ground plane whether it be produced by the conductivity or relative permittivity.

Trajectories of first layer singularities γ_{12}, γ_{13}, γ_{14}, and γ_{15} are presented in Figures 3-8 through 3-15. As the system parameters vary, these singularities behave similarly to the fundamental resonance discussed above.

Figures 3-16 through 3-26 were constructed in order to determine the percent change in the fundamental damping constant, $(R_e\gamma_{11})$, relative to

the free space damping constant, ($R_e\gamma_o$), and the percent change in the fundamental resonant frequency, ($Im\gamma_{11}$), relative to the free space resonant frequency, ($Im\gamma_o$). This data, taken from the trajectories of Figures 3-4 through 3-11 is presented as a function of conductivity with the relative permittivity and height of the scatterer above the ground plane as parameters. Note that although the percent change in damping constant can be quite large, the resonant frequency changes no more than ±5%. This result supports the proposition that first layer resonances are associated with the scatterer itself not the scatterer-ground plane interactions.

The real and imaginary part of the natural modal current distributions for resonant frequencies γ_{11}, γ_{12}, γ_{13}, γ_{14} and γ_{15} are shown in Figures 3-24 and 3-25. These distributions are, of course, influenced by ground characteristics and scatterer height-to-length ratio, but numerical results show that these influences are relatively minor. One should also observe that the imaginary part of the mode vectors is at least an order of magnitude less than the real part indicating that the mode function is approximately a real function of position.

Coupling coefficients associated with singularities γ_{11}, γ_{12}, and γ_{13} are shown in Figures 3-26 through 3-90. In each of these figures, the coupling coefficient, normalized such that its maximum magnitude is equal to unity, is plotted as function of the angle of incidence of the electromagnetic excitation, ie (the angle θ shown in Figure 2-1). In addition, the curves are presented with either scatterer height-to-length ratio, or ground conductivity, or ground relative permittivity as a parameter.

Figures 3-26 to 3-31 present coupling coefficients for fundamental self-resonant singularity γ_{11} at scatterer height-to-length ratios of 0.25, 0.50, 0.75, 1.0, 1.25, and 1.50 respectively. In each of these figures, the relative permittivity, ε_R, is held at unity, while the curves in a given figure correspond to ground conductivities of σ=120.0, σ=0.12, and σ=0.00012. When σ=0.00012 and ε_R=1.0, the coupling coefficient remains the same regardless of the scatterer height-to-length ratio; an expected result since the ground plane has vanished and "free space" conditions prevail. For the "free space" case, the coupling coefficient has its maximum value at broadside incidence, ie (θ=90°), a result which agrees with previous investigation [1]. One observes that the coupling coefficient does not differ greatly from the "free space" case, Figures 3-26 and 3-27, even when the ground conductivity is high, σ=120.0, as long as the scatterer is within approximately 1/4 wavelength of the ground plane. In Figures 3-28 through 3-31, the coupling coefficients for σ=0.12 and 120.0 begin to differ significantly from the free space case. With a height-to-length ratio of 0.75 and σ=120.0, see Figure 3-28, maximum coupling occurs at 75°, and for a height-to-length ratio of 1.00 and σ=120.0, see Figure 3-29, maximum coupling occurs at 45°. Now when σ=120.0 and the scatterer height-to-length ratio is 1.25 and 1.50 in Figures 3-30 and 3-31 respectively, the coupling coefficient again maximizes at θ=90°.

One might logically ask, for a fixed scatterer geometry and ground parameters, what angle of incidence will produce maximum coupling?

First consider the simple case of a time harmonic plane wave obliquely incident on a perfectly conducting half-space. If the normal to the half-space is in the x-direction, and if the incident electric vector is parallel to the plane of incidence, (vertical polarization), then the sum of the incident and reflected waves will produce a standing wave in the x-direction whose electric vector is parallel to the perfectly conducting ground plane. Defining α as the angle formed by the incident ray and the ground plane, the magnitude of this standing wave will be proportional to $\sin[\beta x \sin\alpha] \quad \sin\alpha$, where $\beta = \frac{2\pi}{\lambda}$, λ the free-space wavelength, and x is the perpendicular distance from the ground plane. Now let us immerse a "thin-wire" in this standing wave with its axis parallel to the electric field at a fixed number of free-space wavelengths above the ground plane. What incident angle α will produce a maximum standing wave at the position of the thin wire? It will occur at the angle α that maximizes $\sin[\beta x \sin\alpha] \sin\alpha$, which occurs when either $\cos\alpha=0$ or $\tan[\beta x \sin\alpha] + \beta x \sin\alpha = 0$.

Returning to the scatterer-ground plane problem with the above discussion in mind, will afford some interesting results. Table 3-1 predicts the angle θ that results in maximum coupling for a given scatterer height when the ground plane is nearly perfectly conducting, (σ=120.0). For Figures 3-26 and 3-27 where the scatterer is 0.11 and 0.22 wavelengths above the ground plane, the table predicts maximum coupling to occur at broadside incidence. From Figure 3-28, maximum coupling occurs at θ=75°; for this case the table predicts a value between 73.0° and 73.5°. The difference in the predicted value and

the value in the figure is probably due to numerical evaluation of the coupling coefficient at 5° intervals. Using the standing wave analogy, see Table 3-1, one would expect the coupling coefficient to maximize for $42.0° < \theta < 42.5°$ in Figure 3-29. In the figure, the maximum occurs at 45°. Figure 3-30 indicates peak coupling at $\theta = 90°$, a value which is predicted by the table. Although the table also predicts a maximum at approximately 33°, as can be seen from Figure 3-30, there is a relative extrema in the magnitude of the coupling coefficient at this angle. Generally, the discussion applicable to Figure 3-30 applies as well to Figure 3-31.

Figures 3-32 and 3-33 display the angular variation in the real and imaginary part of the coupling coefficient for the fundamental resonance with the scatterer height-to-length ratio as a parameter. For these figures, the conductivity is large, $\sigma = 120.0$, and the relative permittivity is one, $\epsilon_R = 1.0$. Note that although the information contained in these figures is redundant, (see Figures 3-26 through 3-31), there inclusion provides ready visualization of the variation in coupling coefficient with scatterer height-to-length ratio.

Figures 3-34 through 3-42 show variation in the coupling coefficient for γ_{11} with the relative permittivity as a parameter.

In Figures 3-34, 3-35 and 3-36, the scatterer height-to-length ratio is held at 0.25, while the conductivity σ is respectively 120.0, 0.12, and 0.00012. In each of these figures, the coupling coefficient, (real and imaginary part), is plotted for a ground relative permittivity, ϵ_R,

of 1.0, 15.0, and 100.0. As can be seen from Figure 3-34, when the ground conductivity is large, σ=120.0, there is no variation in the coupling ccefficient as the ground permittivity is varied. This result can be explained as follows. As previously discussed, the singularity location relative to its free space position is a function of the discontinuity at the free space-lossy ground plane interface. Although the ground relative permittivity for conditions depicted in Figure 3-34 varies greatly, the conductivity remains large, producing a large discontinuity in the ground plane. Thus, the position of γ_{11} in the complex plane will be constant. Since the coupling coefficient is strongly dependant on singularity location, (see Equation 2.71), it too will be constant. In Figure 3-35, the conductivity σ is 0.12. Since this is still a relatively large value of conductivity only a slight variation in the coupling coefficient is produced by varying the relative permittivity. In Figure 3-36, the greatest variation in the coupling coefficient with relative permittivity is observed. The conductivity for this case is essentially zero and, therefore, the discontinuity in the lossy ground-free space interface is controlled by the relative permittivity.

Figures 3-37 through 3-39 and Figures 3-40 through 3-42 contain plots of the variation in coupling coefficient with relative permittivity for scatterer height-to-length ratios of 0.75 and 1.25 respectively. The interpretation of these figures is similar to that given for Figures 3-34 through 3-36.

The coupling coefficients associated with the second self-resonant singularity, γ_{12}, are shown in Figures 3-43 through 3-66.

The coupling coefficients corresponding to the second self-resonant singularity locations "A", "D", "G" of Figure 3-8 are shown in Figures 3-43 to 3-47. Table 3-2 predicts possible angles of maximum coupling for these figures using the "standing wave analogy". From the first row in the table, it is seen that there is no angle θ between 0 and 90 degrees that satisfies the equation TAN[βhSINθ] + βhSINθ=0. The reason for this is that $0 \leq \beta h \sin\theta \leq 1.38$ for $0° < \theta < 90°$ and thus TAN[βhSINθ] will be positive. However, as always, a relative extrema is predicted at θ=90°, an expected result considering the fact that all the coupling coefficients are even functions about θ=90°. That is, one would expect the same amount of coupling at say θ=95° as at θ=85°. From Figures 3-44 and 3-45 maximum coupling occurs at 50 and 35 degrees respectively, values that are predicted reasonably well by Table 3-2. Using the "standing wave analogy" one would expect peak coupling to occur for an incident angle of approximately 22 or 67 degrees for the coupling coefficient in Figure 3-46. From the figure peak coupling occurs at 65°, with a relative extrema in the magnitude of the coupling coefficient occuring at approximately 22 degrees. Results from the last row of the table agree reasonably well with the corresponding figure.

Variations in the real and imaginary part of the coupling coefficient for the second self-resonant singularity, γ_{12}, as a function of spacing, h/ℓ, are shown in Figures 3-48 through 3-51. In each of these figures, the relative permittivity is one. The conductivity in Figures 3-48 and

3-49 is large, σ=120.0, while for Figures 3-50 and 3-51 the conductivity is 0.12.

Figures 3-52 through 3-66 are plots of the coupling coefficients for singularity γ_{12} with the relative permittivity of the ground plane as a parameter. Coupling coefficients in these figures are for singularity positions "A", "D", and "G" in Figure 3-8, and positions "A", "D", and "F" in Figure 3-9. As before, when the ground conductivity is large, the coupling coefficient is insensitive to changes in the relative permittivity (see Figures 3-52, 3-55, 3-58, 3-61, and 3-64). The largest variation in the coupling coefficient with relative permittivity is noticed in Figure 3-54, 3-57, 3-60, 3-63, and 3-66, a result indicative of the large difference in position of points "G" and "F" in Figures 3-8 and 3-9.

In Figures 3-67 through 3-90 are presented the coupling coefficient for the third self-resonant singularity, γ_{13}.

Figures 3-67 through 3-71 present the angular variation in the coupling coefficient for singularity positions "A", "D", and "G" in Figure 3-10. Table 3-3 predicts possible angles of maximum coupling for these figures using the "standing wave analogy". From Figures 3-67 and 3-68 maximum coupling for perfect ground (σ=120.0) occurs at 45 degrees and as always, a relative extrema in the magnitude of the coupling coefficient occurs at 90 degrees. Of course, the extrema at 90° is predicted by Table 3-3, the maximum at 45°, however, is not since $\beta h \mathrm{SIN}\theta < \pi/2$ when $h/\ell < 0.2$. It is also interesting to note that unlike the corresponding figures for γ_{12} and γ_{13} in Figures 3-67 and 3-68 the

coupling coefficient for σ=0.12 (real and imaginary part) corresponds more closely to the "free space" coefficient than to the "perfect ground" coupling coefficient. This result can be explained by noting that for higher order poles the ground conductivity must be larger to produce a perfectly conducting earth than for lower order poles. Next, consider Figure 3-69, for the high conductivity case maximum coupling occurs at θ=40 degrees; using the "standing wave analogy" one would expect peak coupling to occur at approximately 50 degrees. The mechanism for this error is not known. For Figures 3-70 and 3-71 Table 3-3 again predicts relatively accurately the angle of maximum coupling.

Figures 3-72 through 3-75 show variation in the real and imaginary part of the coupling coefficient for the third self-resonant singularity with the scatterer height-to-length ratio as a parameter. In Figures 3-72 and 3-73 the conductivity is 120.0 and the relative permittivity is one. In Figures 3-74 and 3-75, the conductivity is 0.12 and the relative permittivity is one.

Figures 3-76 to 3-90 show variation in the coupling coefficient for γ_{11} with the relative permittivity as a parameter. In each of these figures, the conductivity and scatterer height-to-length ratio are held constant. Explanation of the behavior of the coupling coefficients in these figures is similar to that given for Figures 3-34 through 3-42.

For the wire scatterer in free space, the coupling coefficient for the third singularity at an incident angle of 70 degrees was shown by Tesche [1] to be zero. Note from Figures 3-67 through 3-90 that a nul

in the coupling coefficient occurs at 70° independant of the ground parameter and scatterer height-to-length ratio.

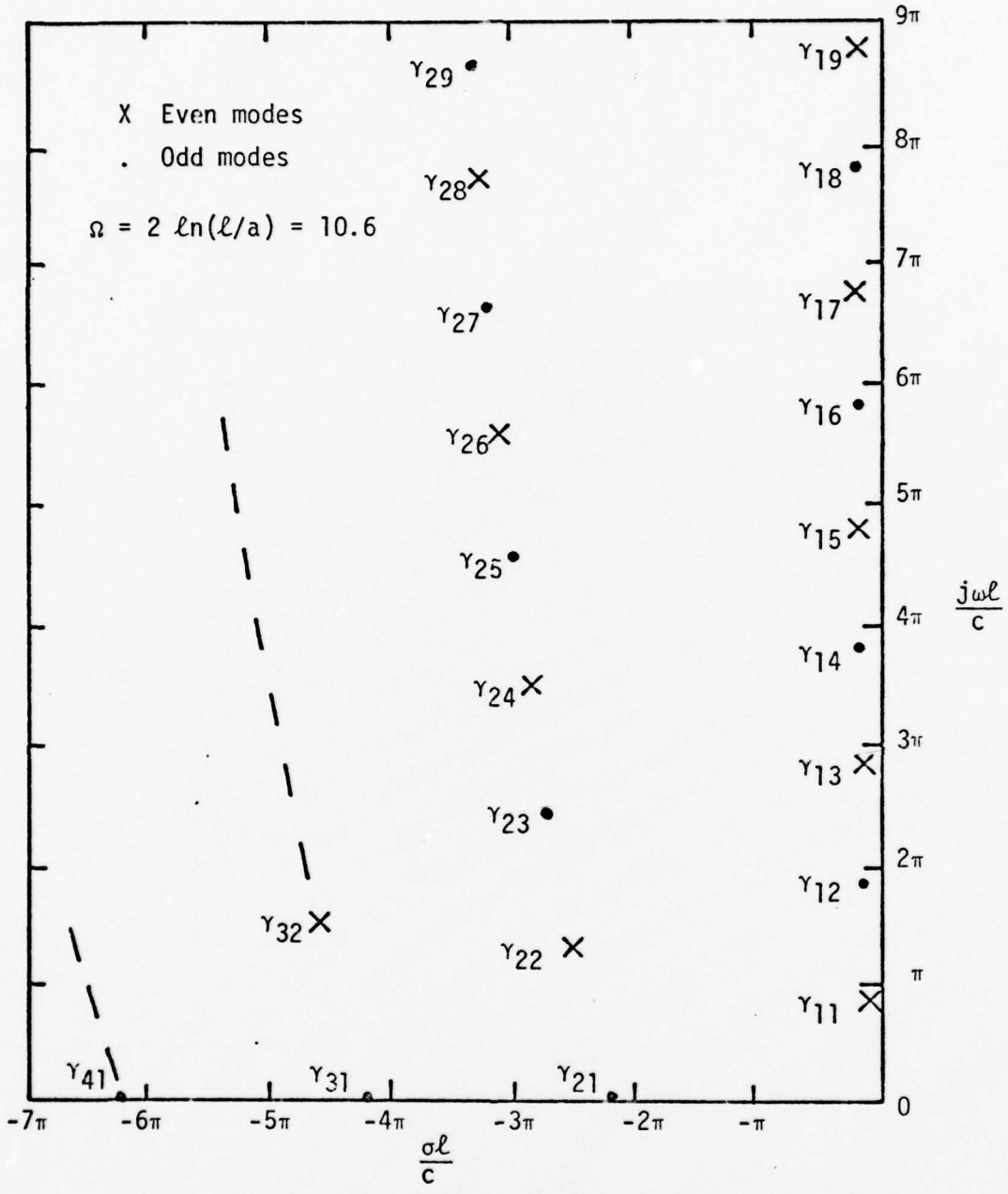


Figure 3-1. Location of the resonances of a thin-wire scatterer in free space.

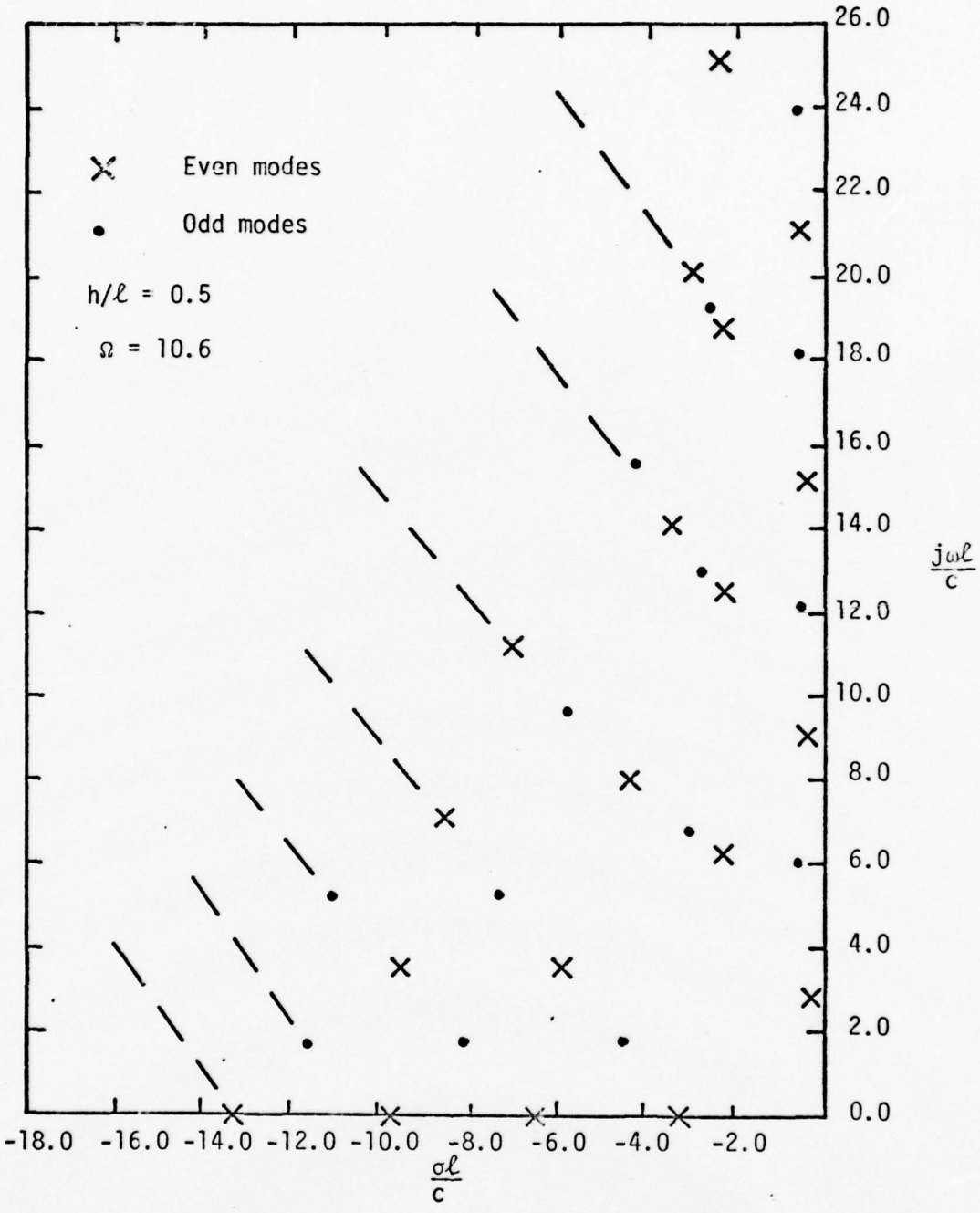


Figure 3-2. Location of the singularities of the thin-wire scatterer above a perfectly conducting ground plane.

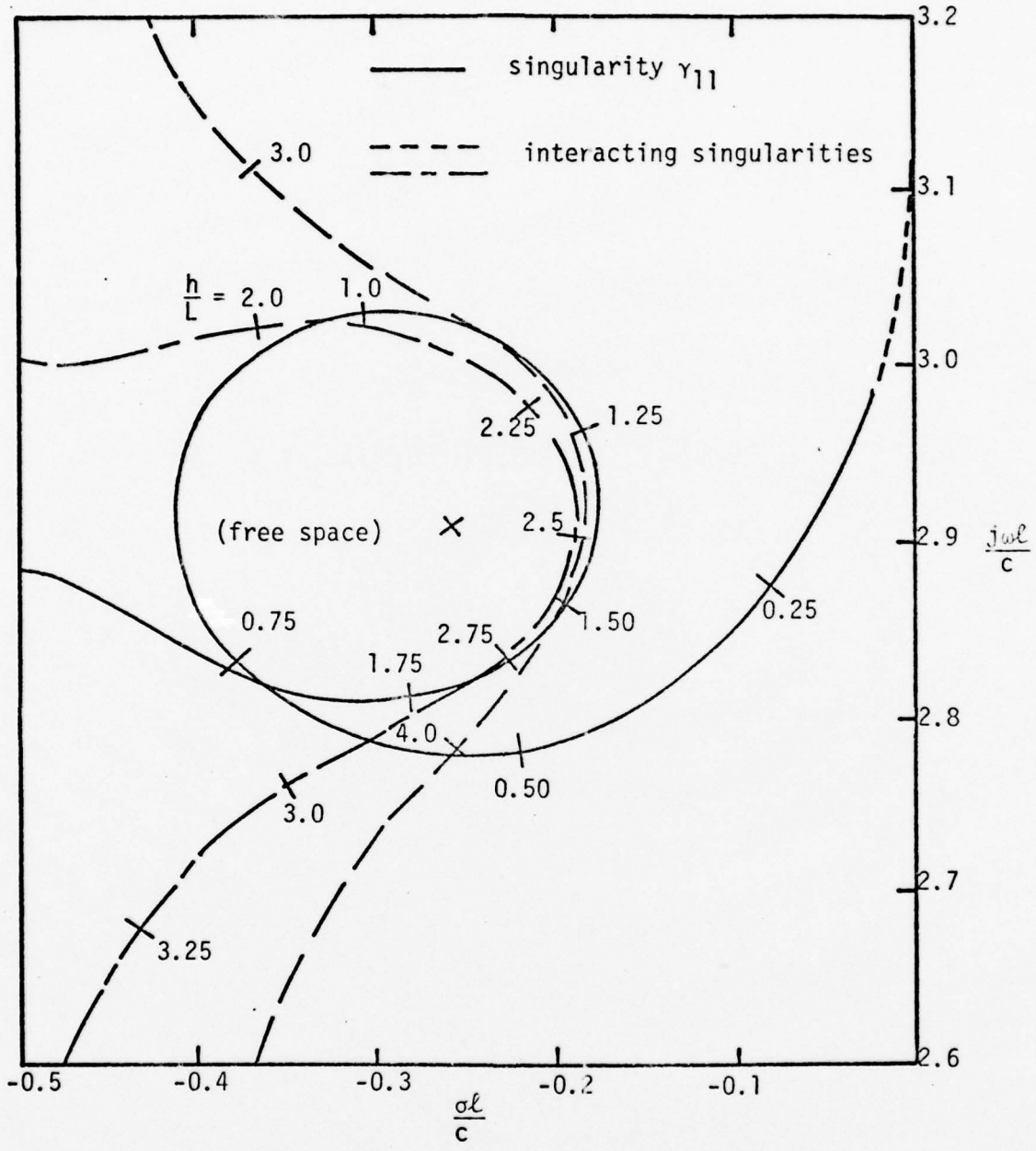


Figure 3-3. Trajectory of singularity γ_{11} for the case of a thin wire over a perfectly conducting ground.

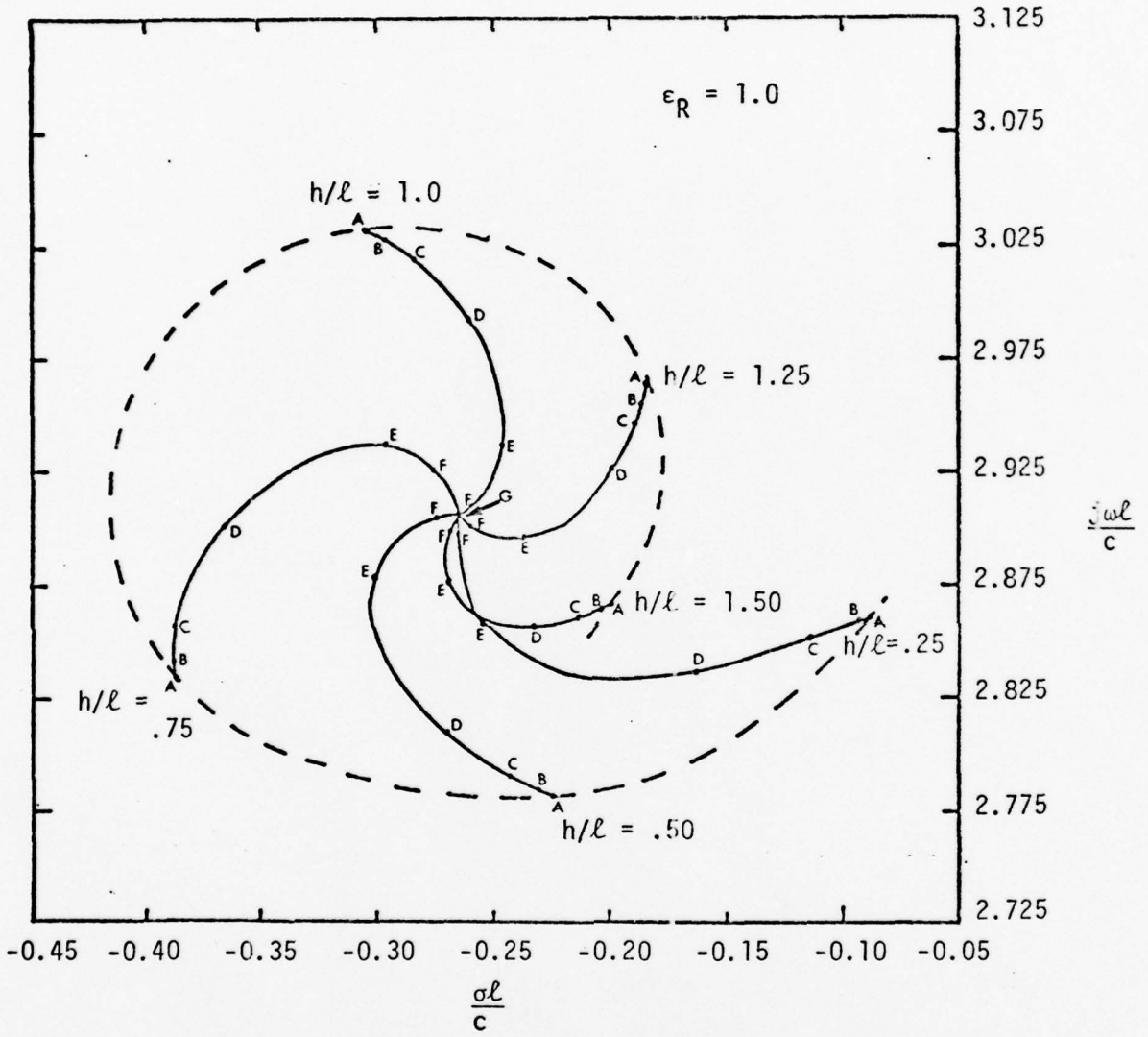


Figure 3-4. Trajectory of fundamental self-resonant singularity, γ_{11}, as a function of spacing, h/ℓ, and conductivity, σ. The relative permittivity, ε_R, is held at one.

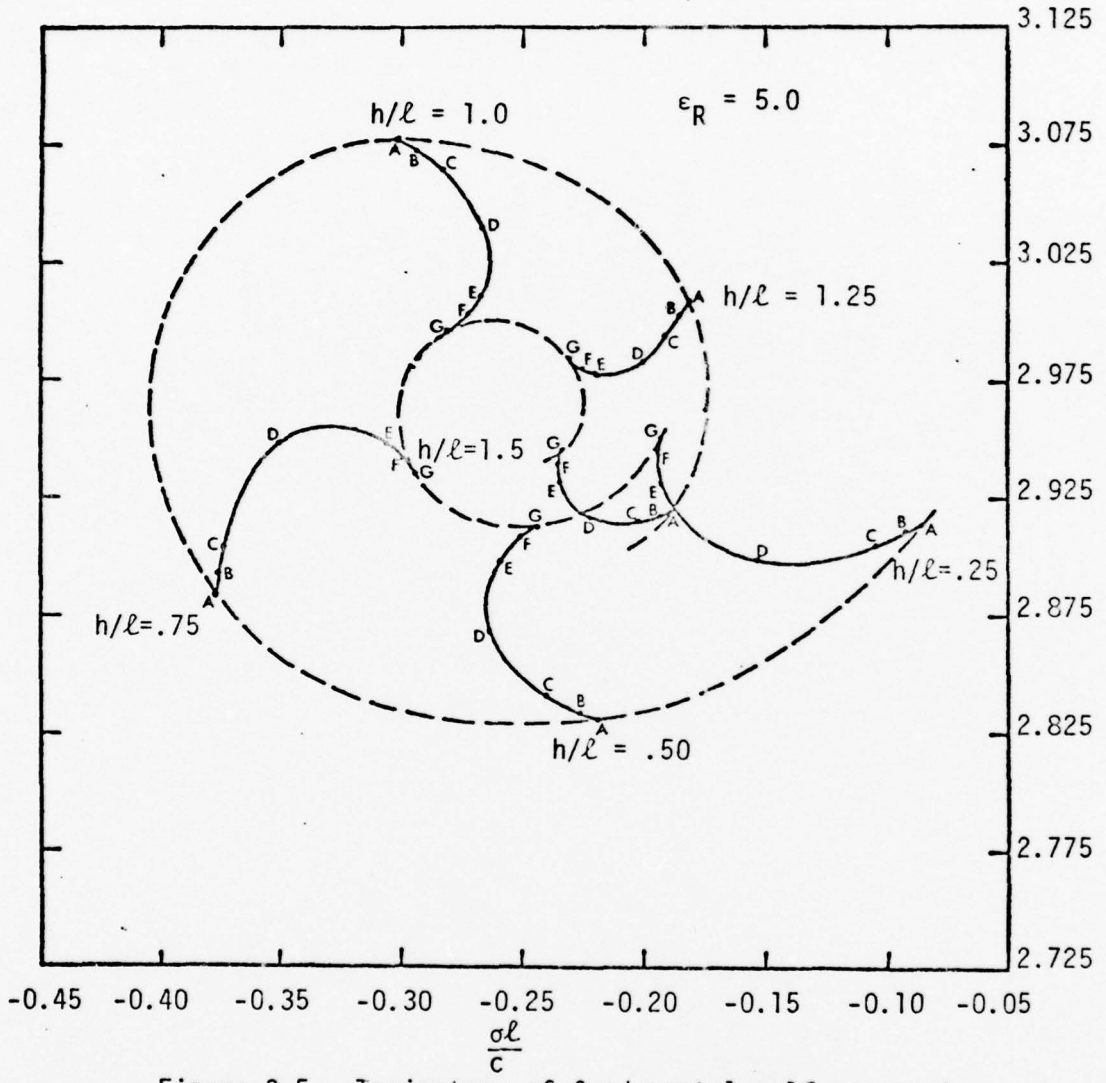


Figure 3-5. Trajectory of fundamental self-resonant singularity, γ_{11}, as a function of spacing, h/ℓ, and conductivity, σ. The relative permittivity, ε_R, is held at five.

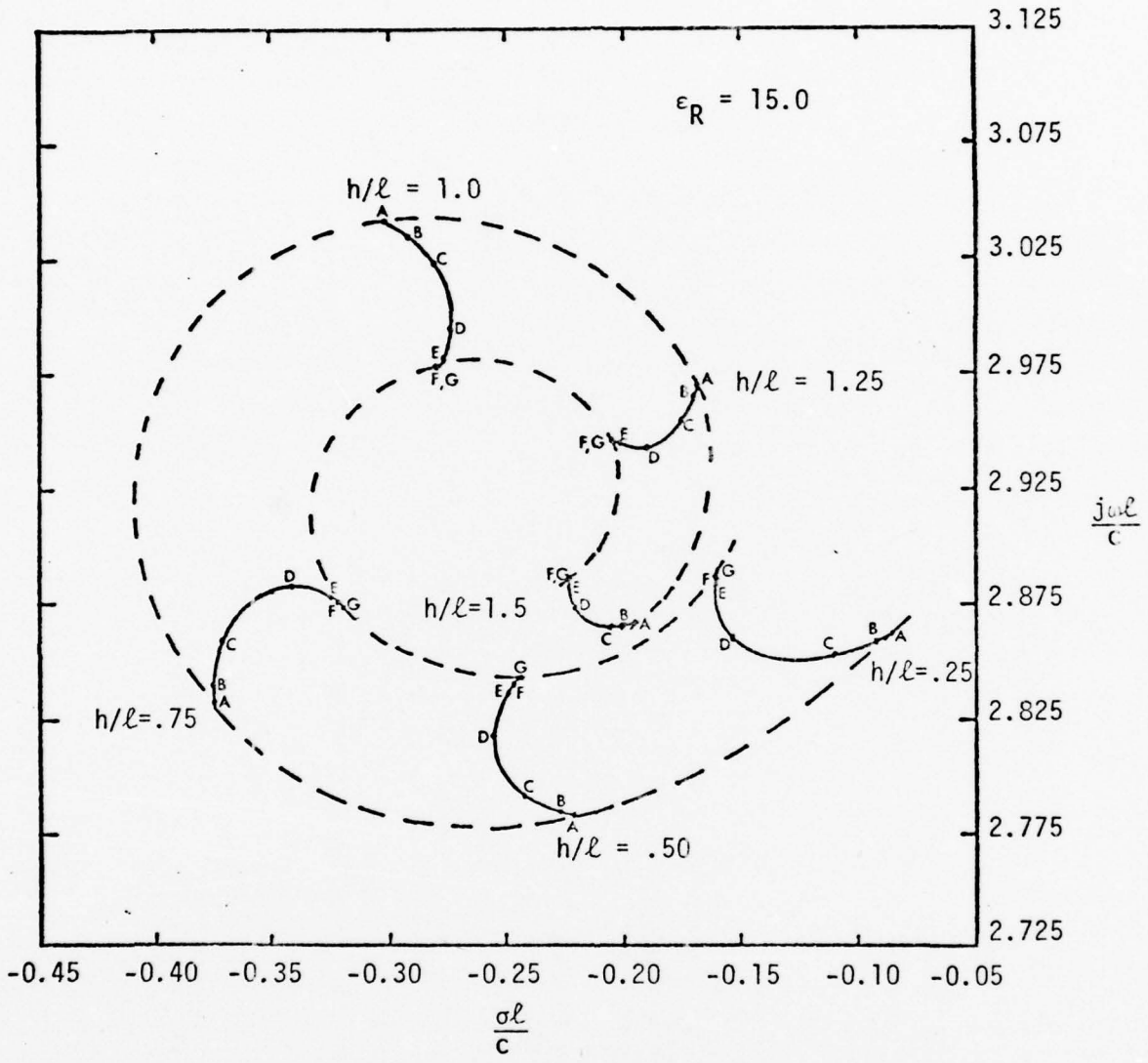


Figure 3-6. Trajectory of fundamental self-resonant singularity, γ_{11}, as a function of spacing, h/ℓ, and conductivity, σ. The relative permittivity is held at fifteen.

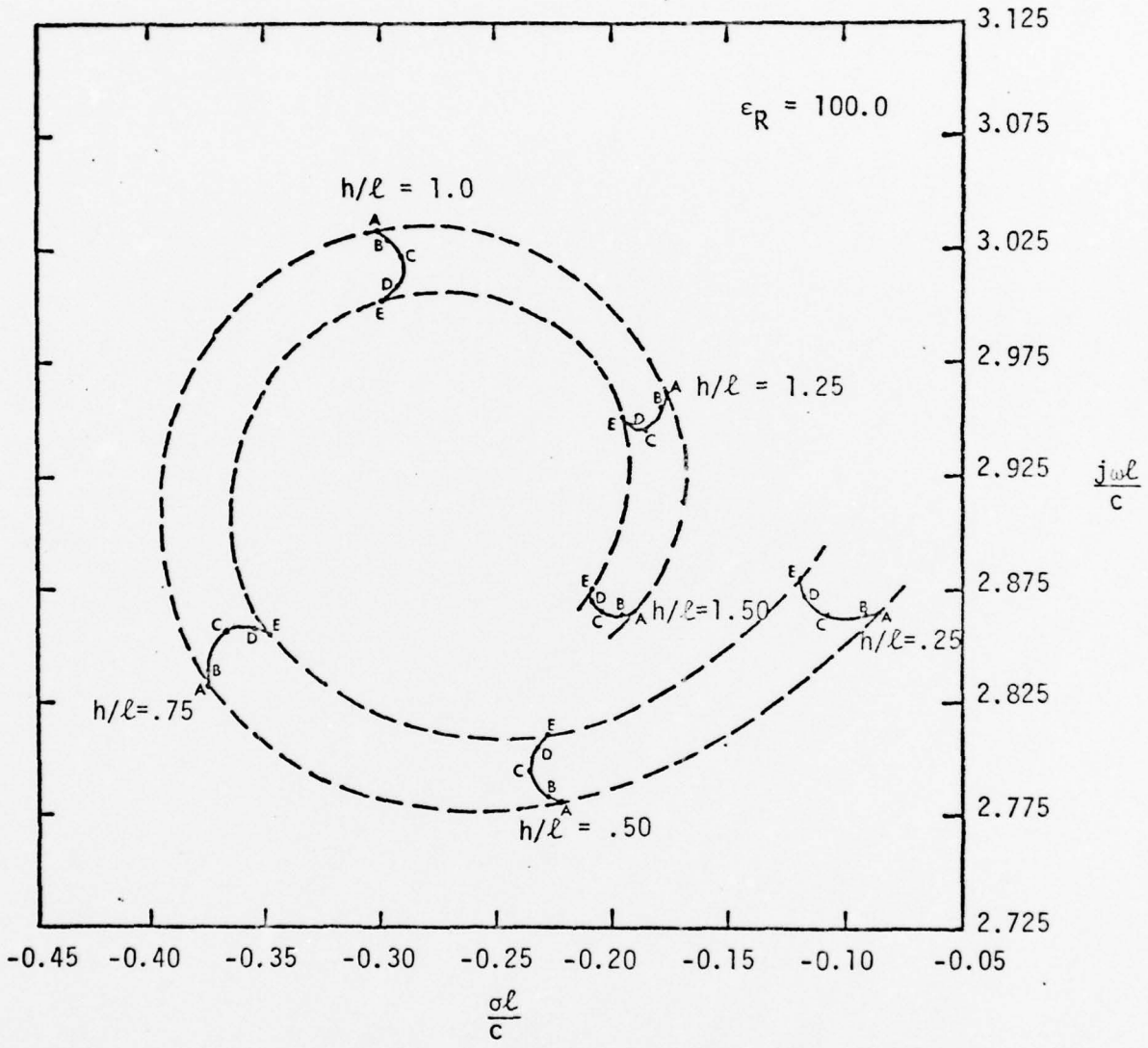


Figure 3-7. Trajectory of fundamental self-resonant singularity, γ_{11}, as a function of spacing, h/ℓ, and conductivity, σ. The relative permittivity is held at one hundred.

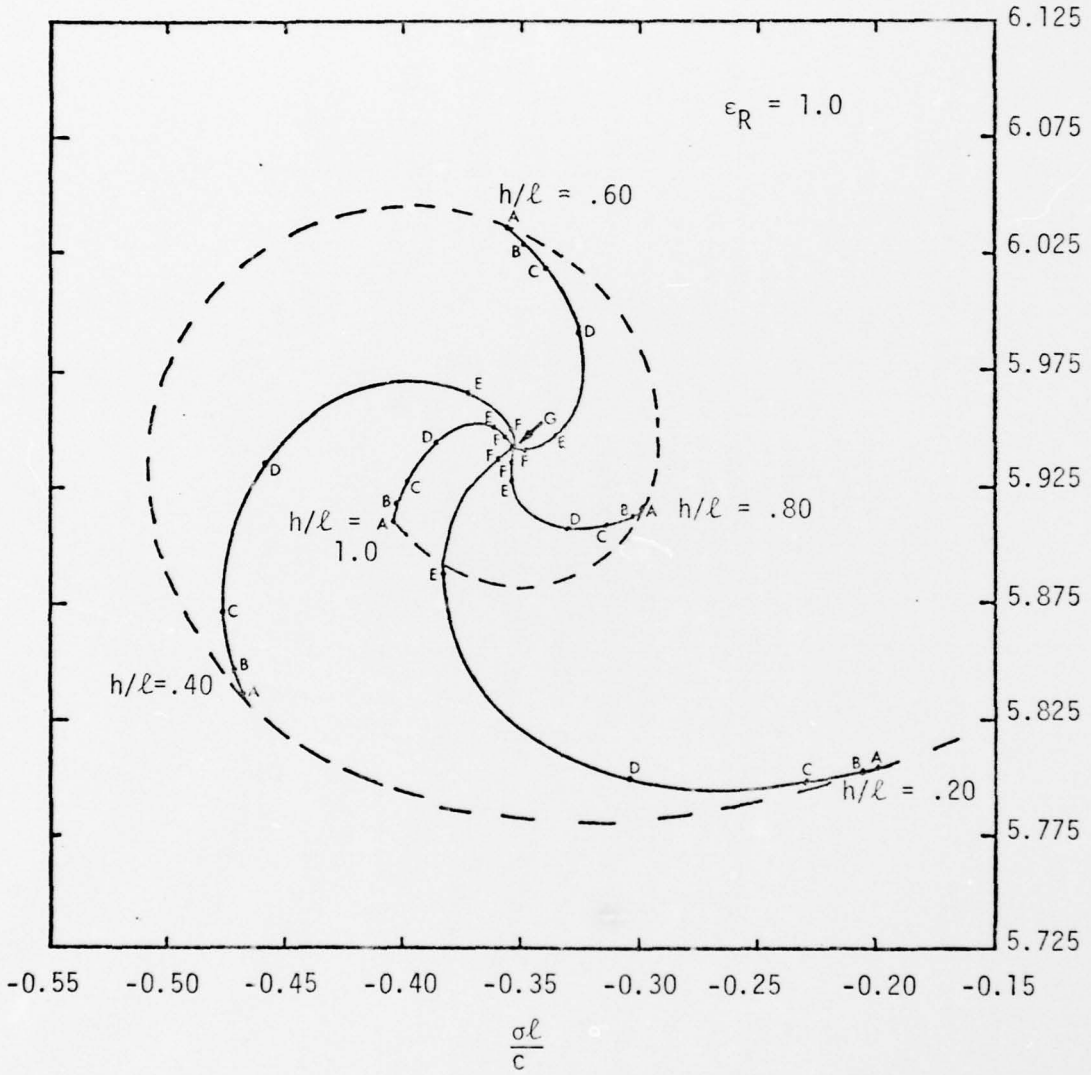


Figure 3-8. Trajectory of second self-resonant singularity, γ_{12}, as a function of spacing, h/ℓ, and conductivity, σ. The relative permittivity is held at one.

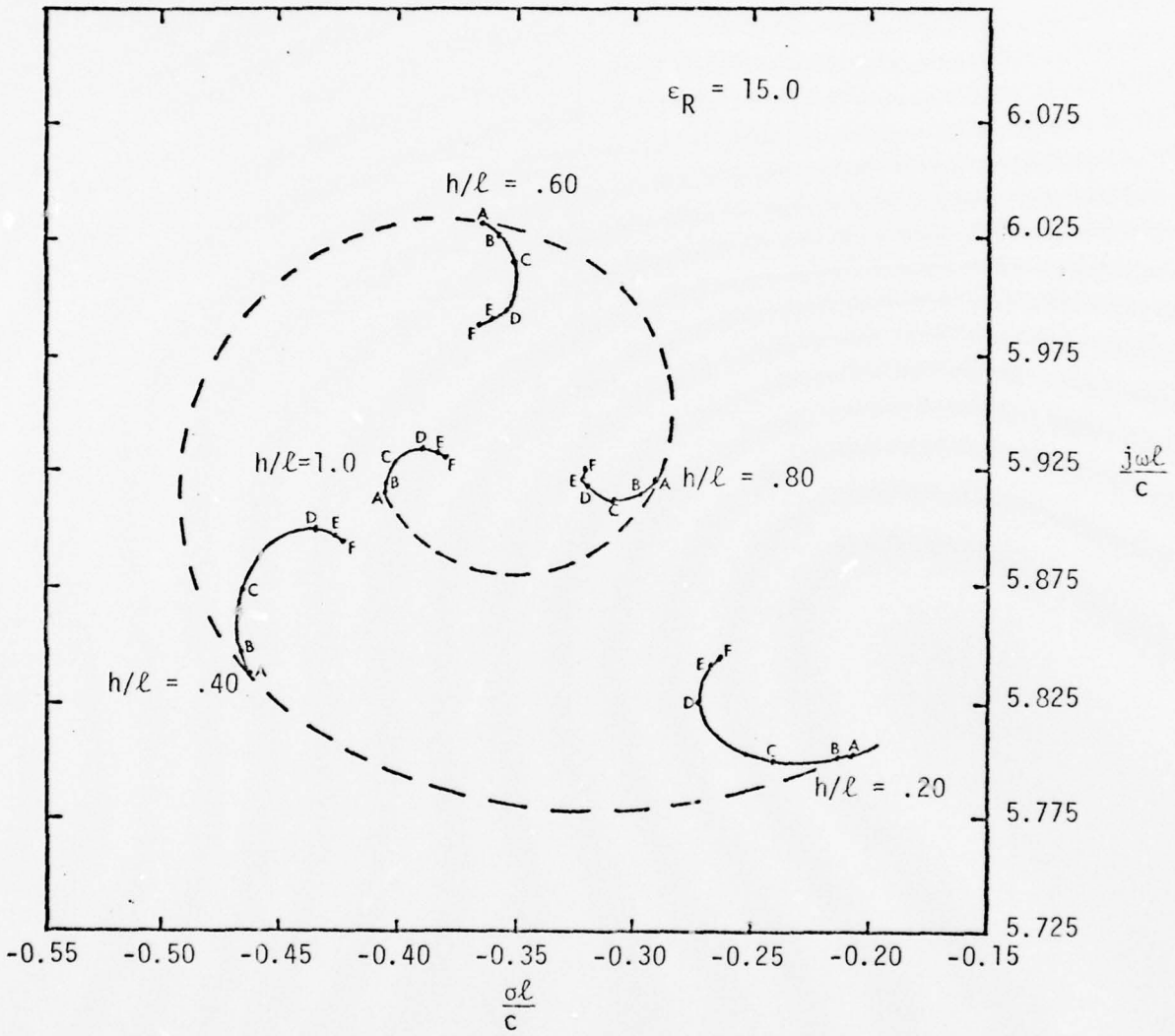


Figure 3-9. Trajectory of second self-resonant singularity, γ_{12}, as a function of spacing, h/ℓ, and conductivity, σ. The relative permittivity is held at fifteen.

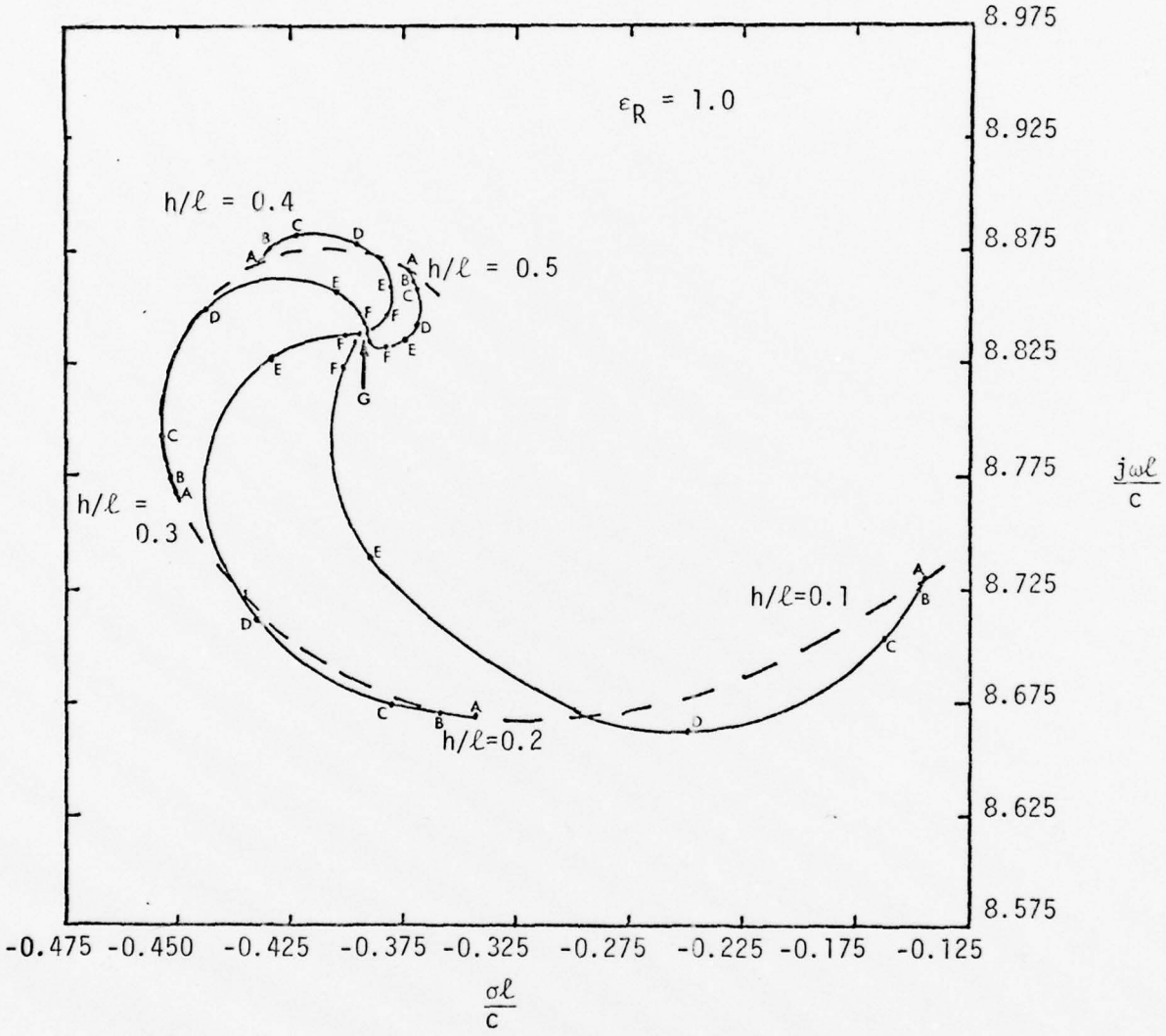


Figure 3-10. Trajectory of third self-resonant singularity, γ_{13}, as a function of spacing, h/ℓ, and conductivity, σ. The relative permittivity is held at one.

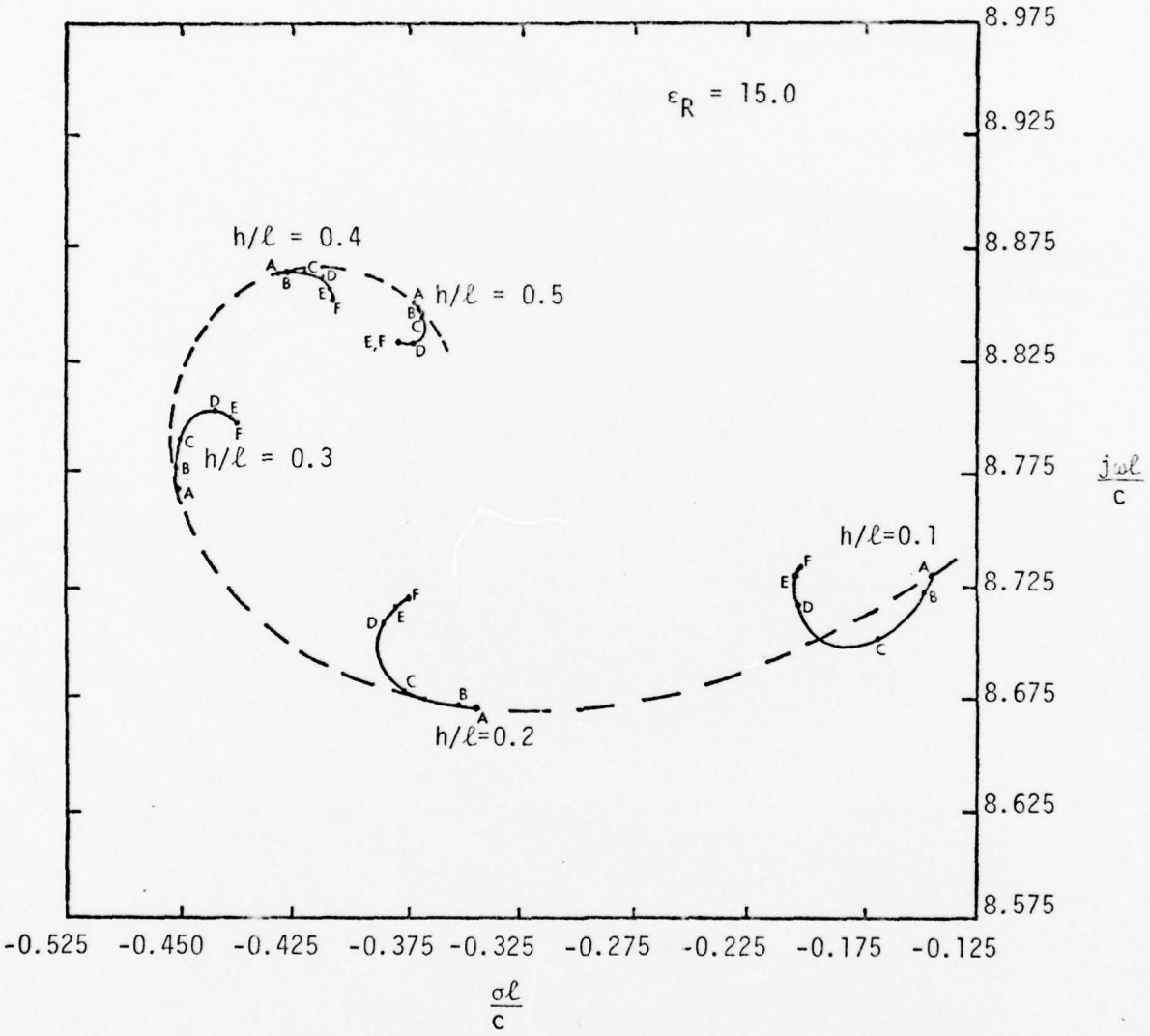


Figure 3-11. Trajectory of third self-resonant singularity, γ_{13}, as a function of spacing, h/ℓ, and conductivity, σ. The relative permittivity is held at fifteen.

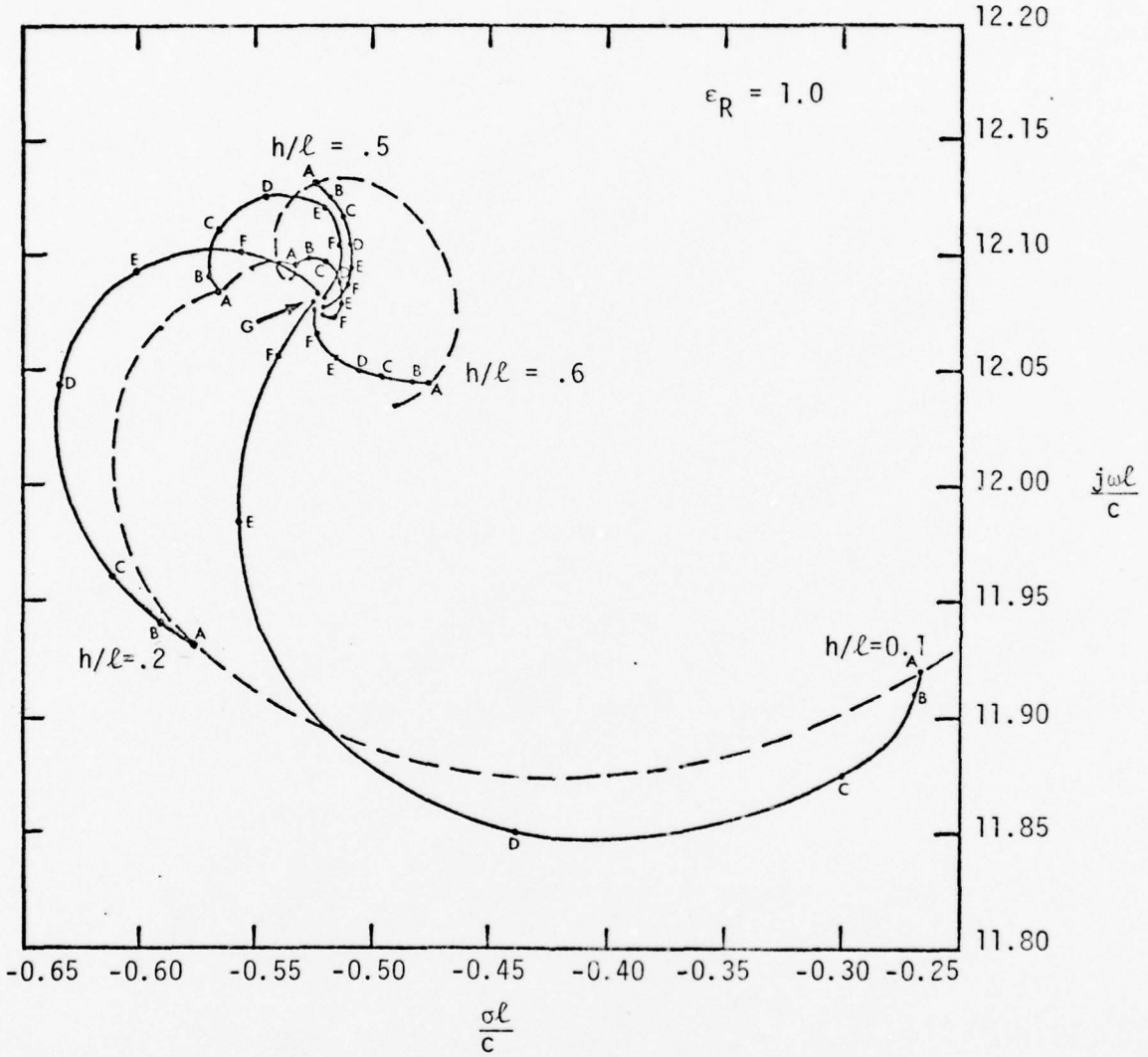


Figure 3-12. Trajectory of fourth self-resonant singularity, γ_{14}, as a function of spacing, h/ℓ, and conductivity, σ. The relative permittivity is held at one.

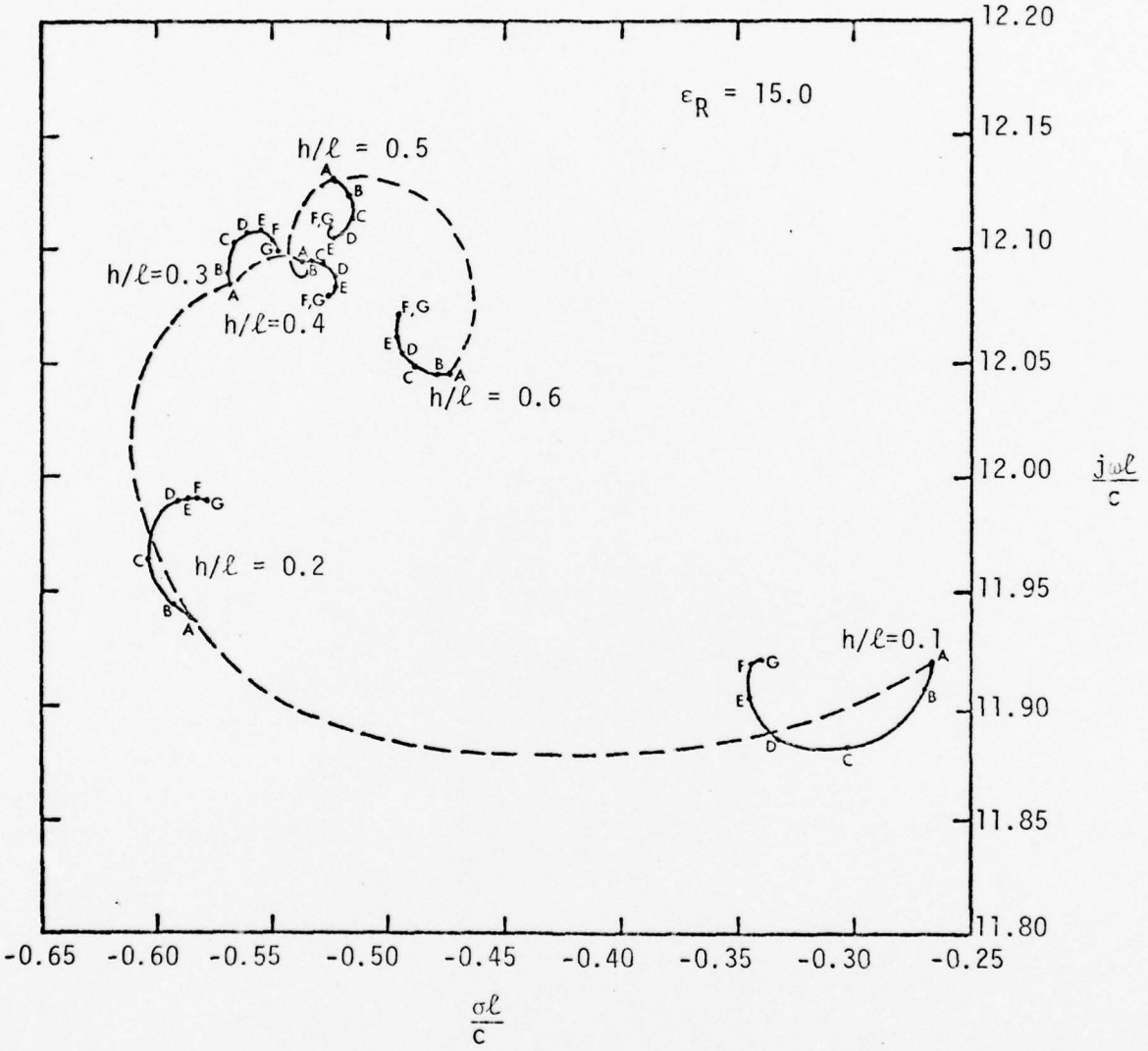


Figure 3-13. Trajectory of fourth self-resonant singularity, γ_{14}, as a function of spacing, h/ℓ, and conductivity, σ. The relative permittivity is held at fifteen.

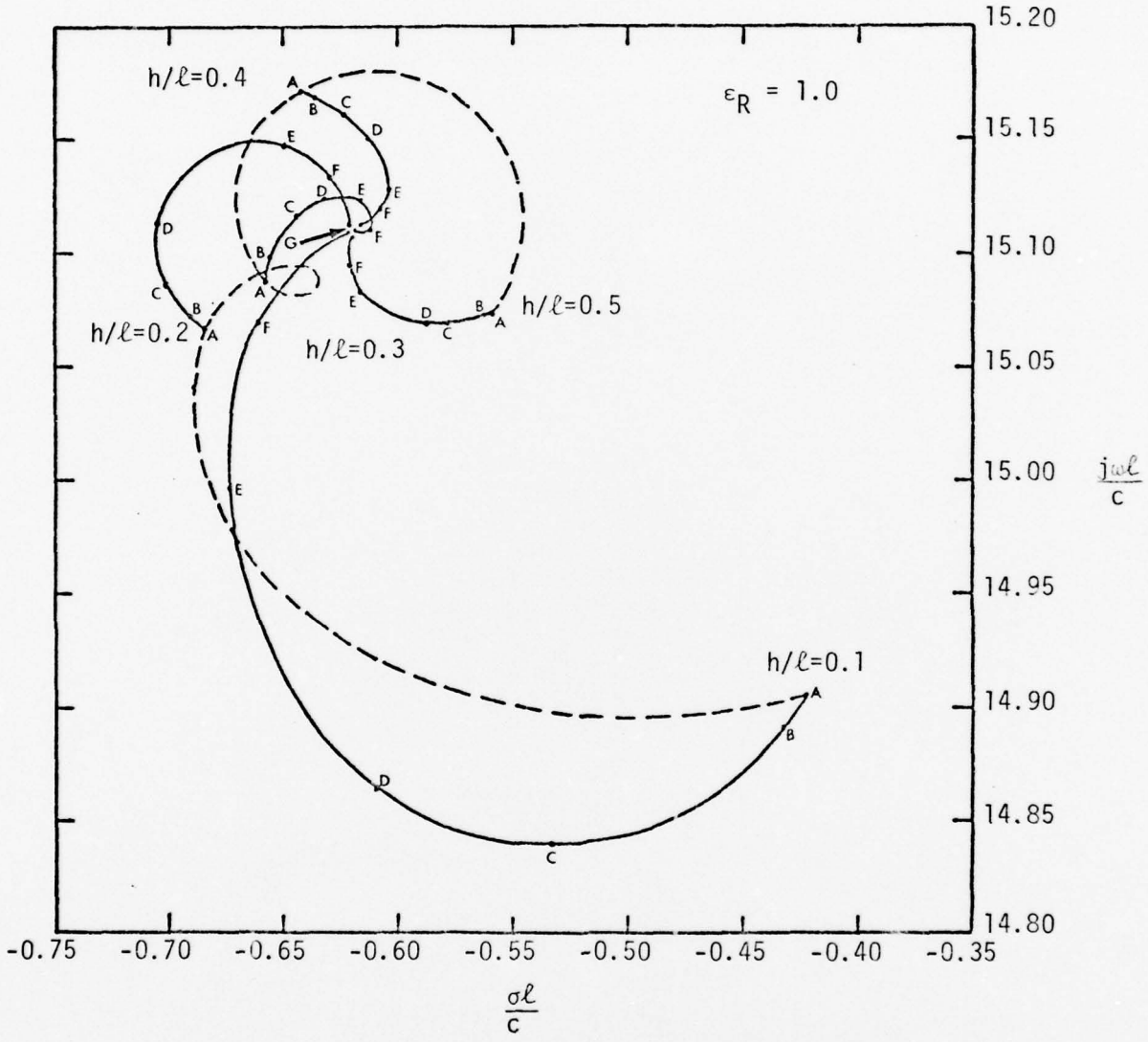


Figure 3-14. Trajectory of fifth self-resonant singularity, γ_{15}, as a function of spacing, h/ℓ, and conductivity, σ. The relative permittivity is held at one.

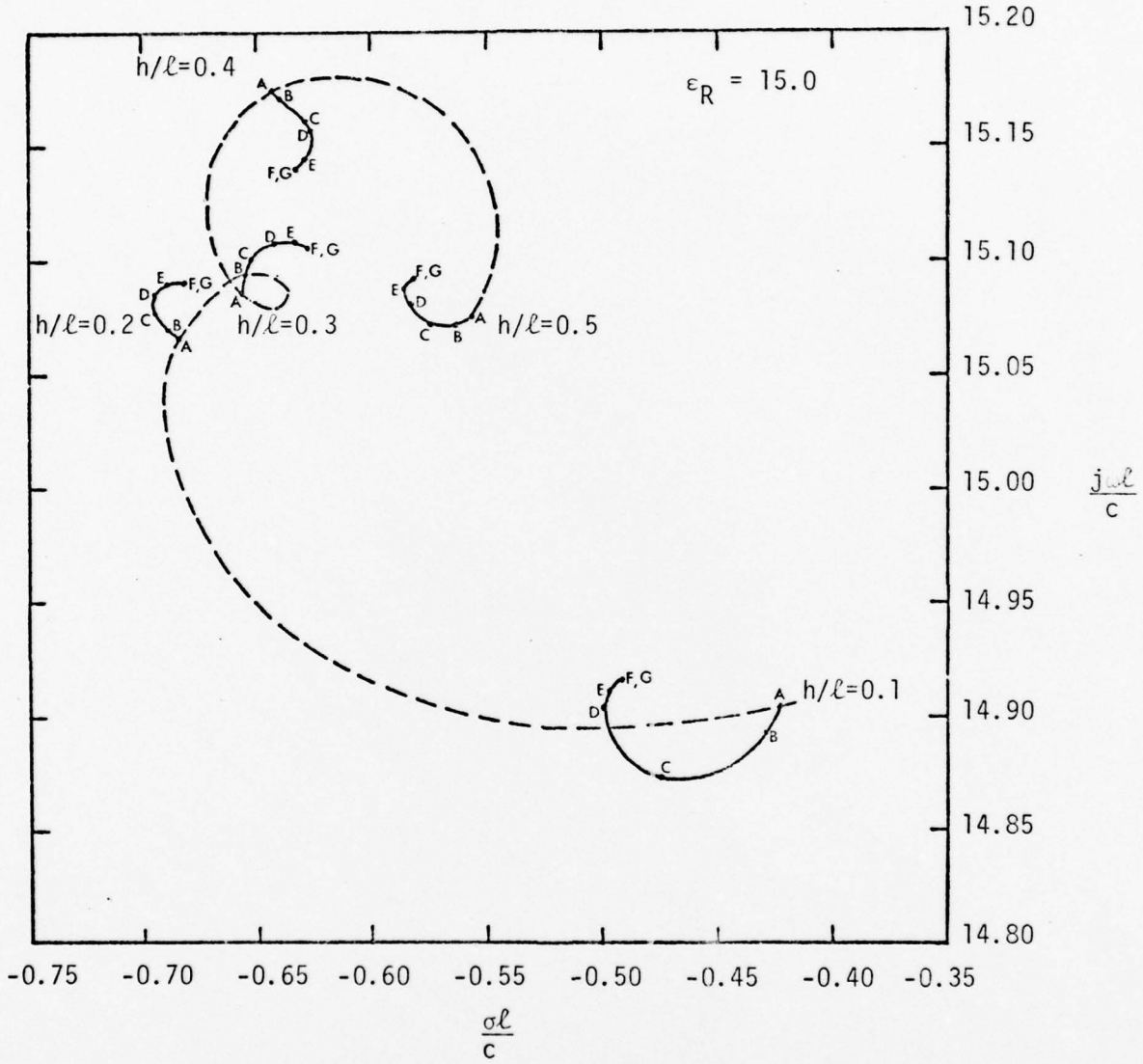


Figure 3-15. Trajectory of fifth self-resonant singularity, γ_{15}, as a function of spacing, h/ℓ, and conductivity, σ. The relative permittivity is held at fifteen.

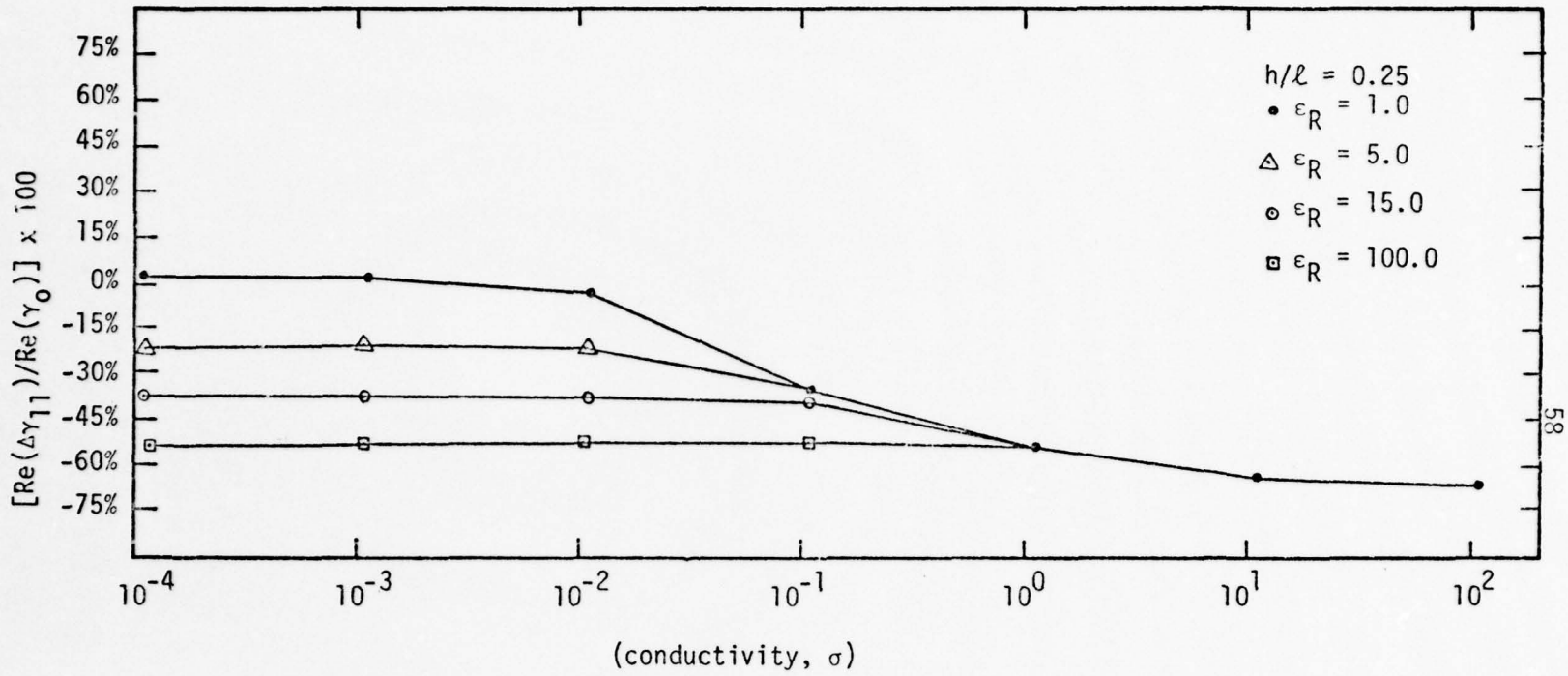


Figure 3-16. Plot of the percent change of the fundamental damping constant relative to the free space damping constant, shown as a function of permittivity, $\varepsilon_R\varepsilon_o$, and conductivity, σ, for fixed spacing, $h/\ell = 0.25$.

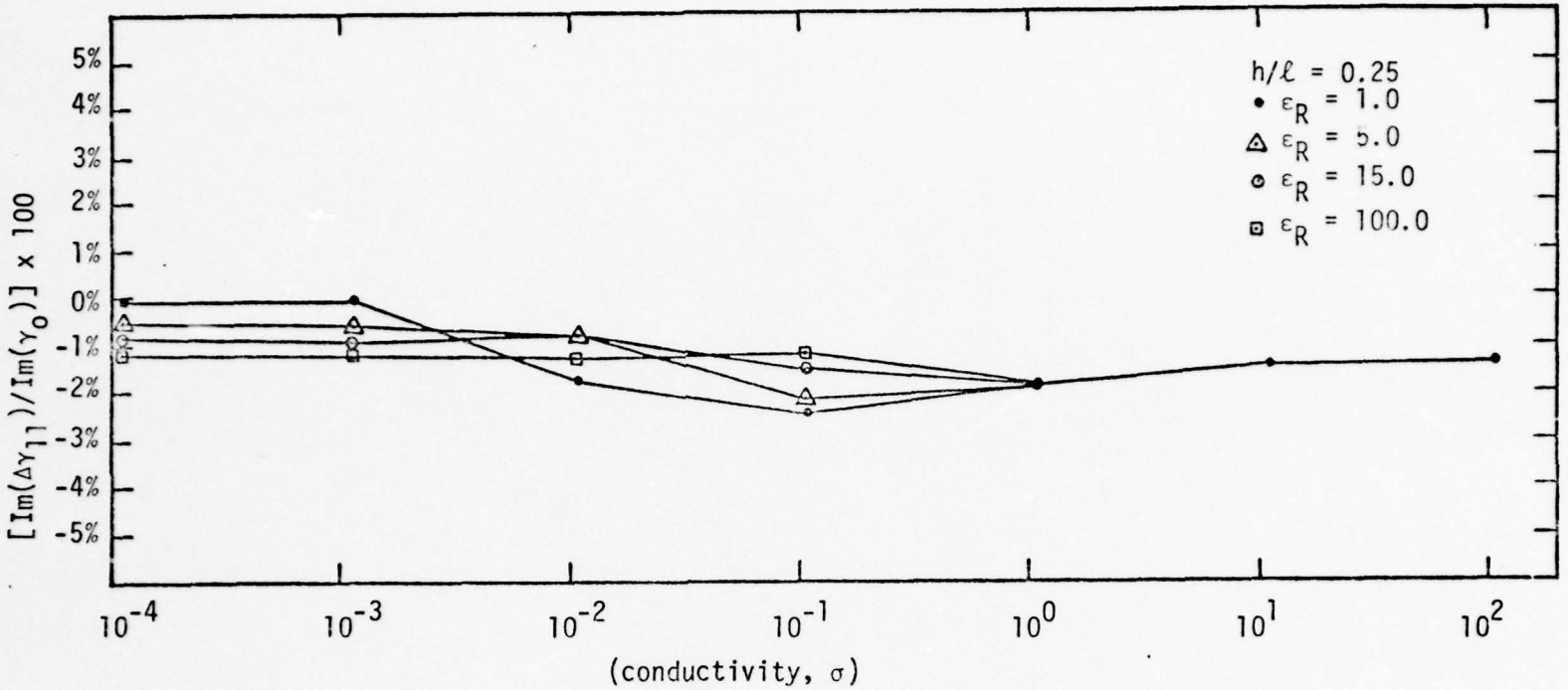


Figure 3-17. Plot of the percent change of the fundamental resonant frequency relative to the free space resonant frequency, shown as a function of permittivity, $\varepsilon_R\varepsilon_o$, and conductivity, σ, for fixed spacing, $h/\ell = 0.25$.

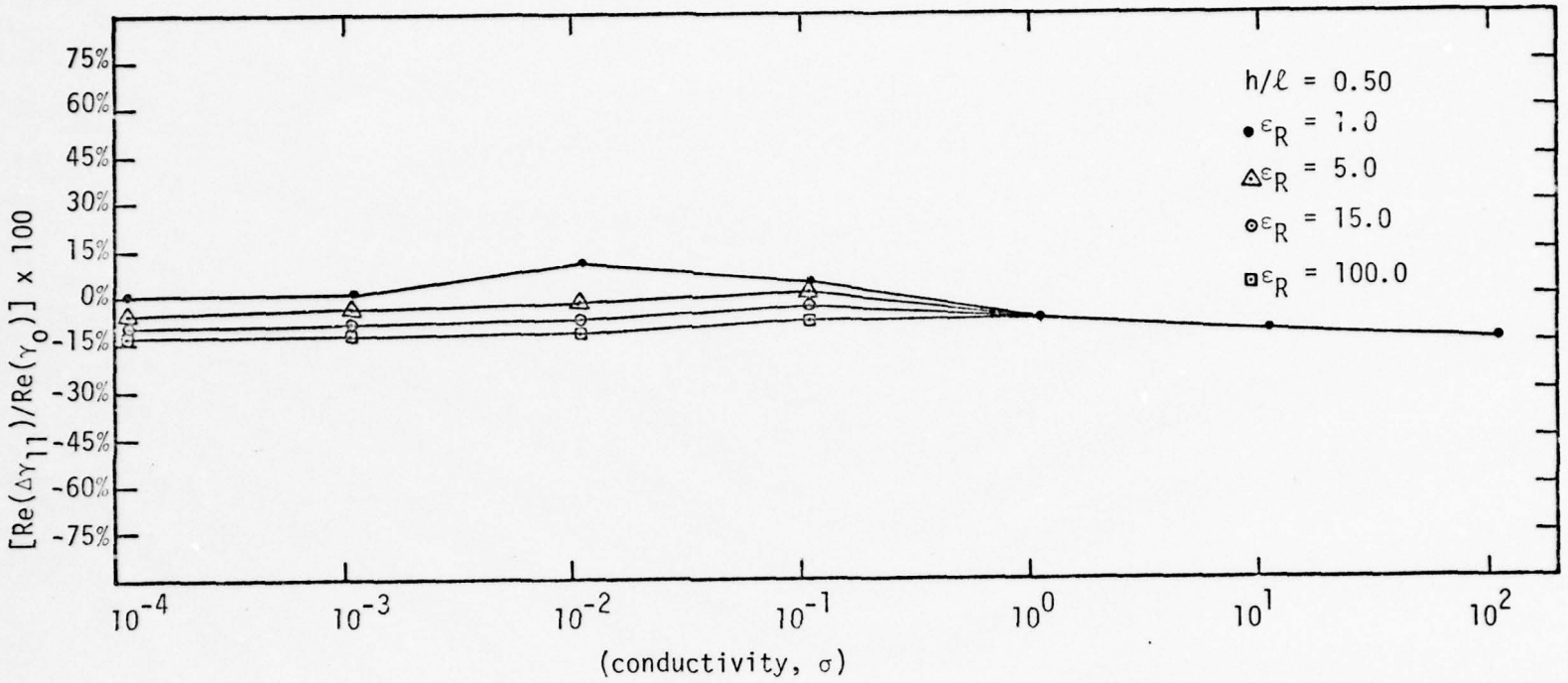


Figure 3-18. Plot of the percent change of the fundamental damping constant relative to the free space damping constant, shown as a function of permittivity, $\varepsilon_R\varepsilon_o$, and conductivity, σ, for fixed spacing, $h/\ell = 0.50$.

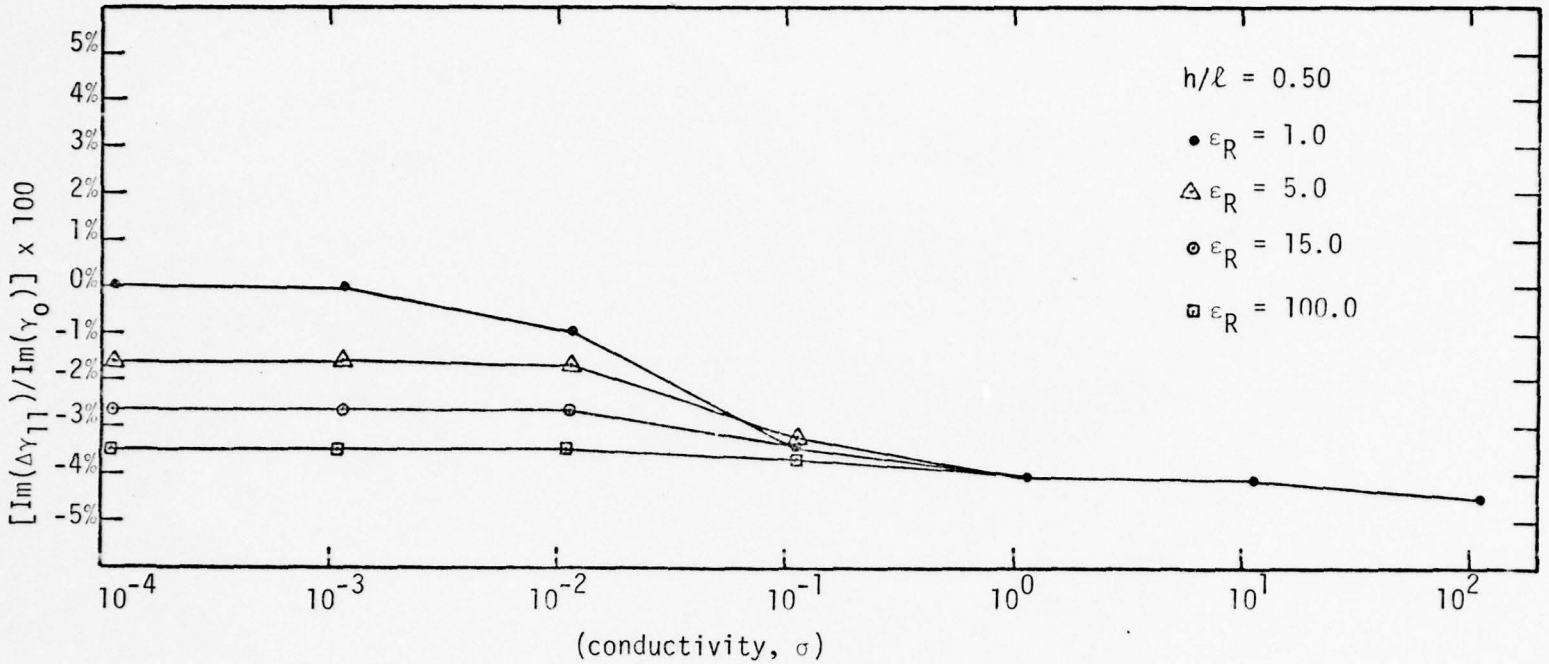


Figure 3-19. Plot of the percent change of the fundamental resonant frequency relative to the free space resonant frequency, shown as a function of permittivity, $\varepsilon_R\varepsilon_o$, and conductivity, σ, for fixed spacing, $h/\ell = 0.50$.

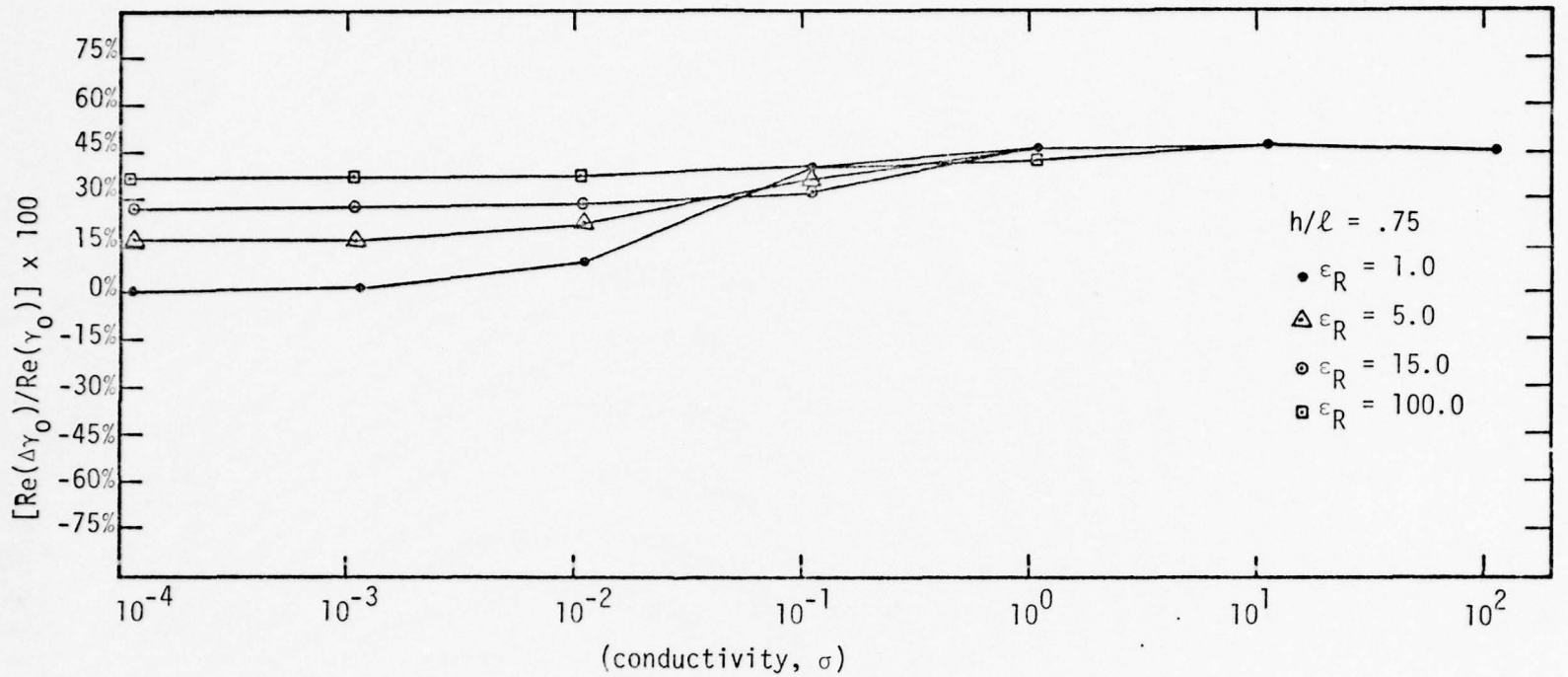


Figure 3-20. Plot of the percent change of the fundamental damping constant relative to the free space damping constant, shown as a function of permittivity, $\varepsilon_R\varepsilon_o$, and conductivity, σ, for fixed spacing, $h/\ell = 0.75$.

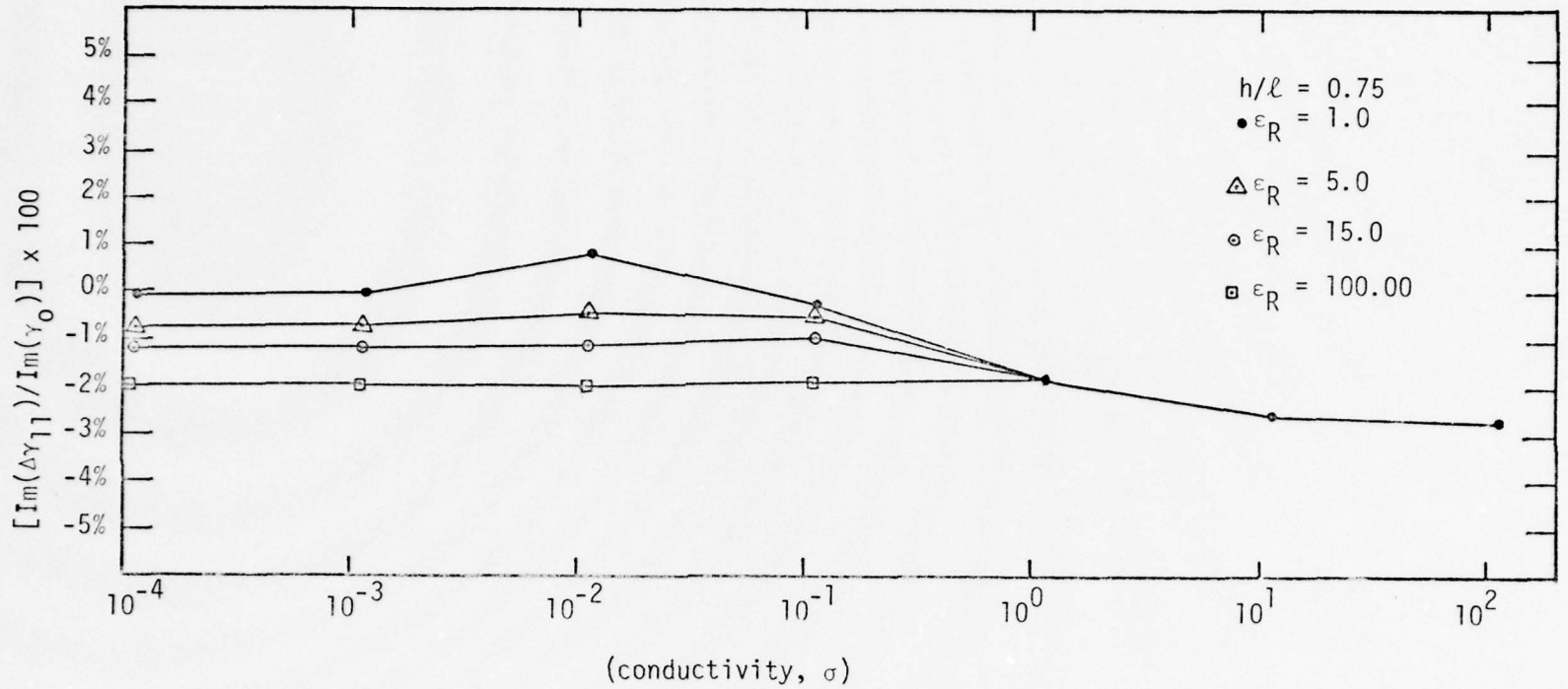


Figure 3-21. Plot of the percent change of the fundamental resonant frequency relative to the free space resonant frequency, shown as a function of permittivity, $\varepsilon_R\varepsilon_o$, and conductivity, σ, for fixed spacing, $h/\ell = 0.75$.

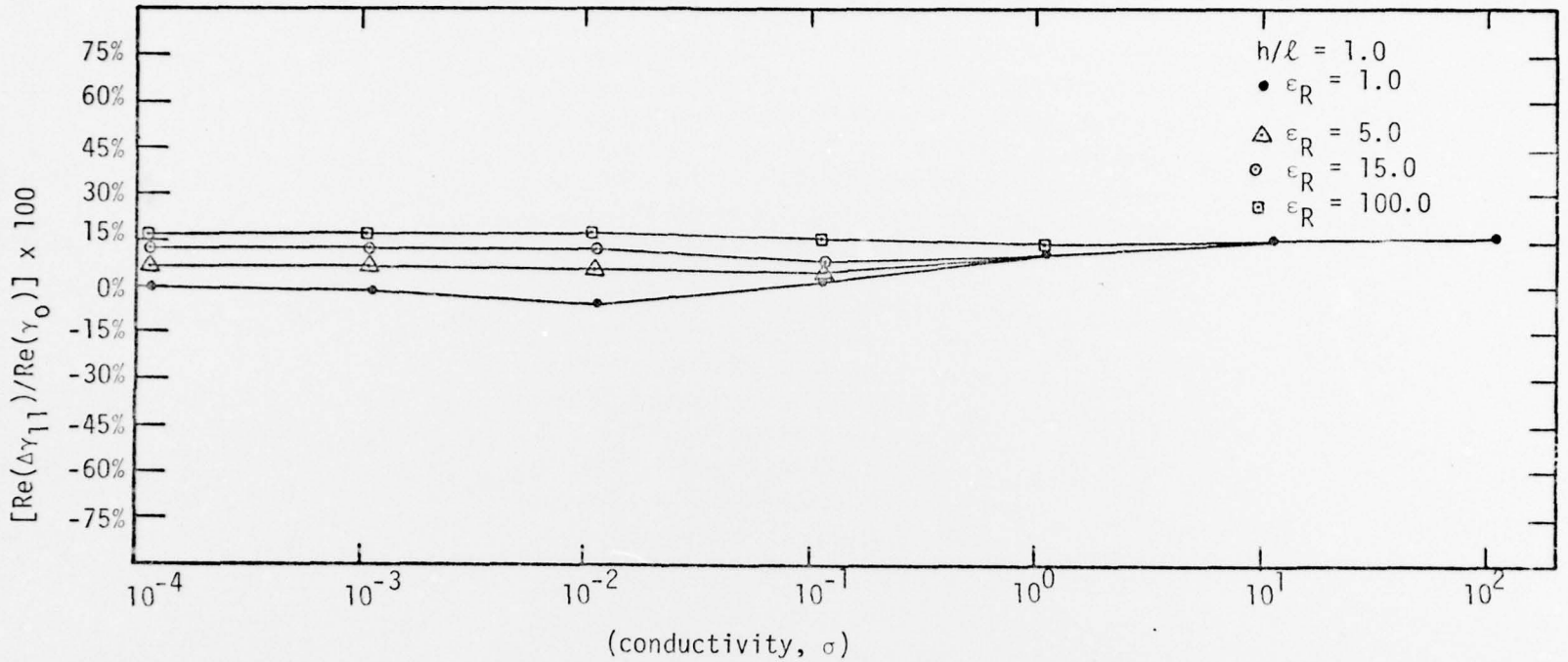


Figure 3-22. Plot of the percent change of the fundamental damping constant relative to the free space damping constant, shown as a function of permittivity, $\varepsilon_R\varepsilon_o$, and conductivity, σ, for fixed spacing, h/ℓ = 1.0.

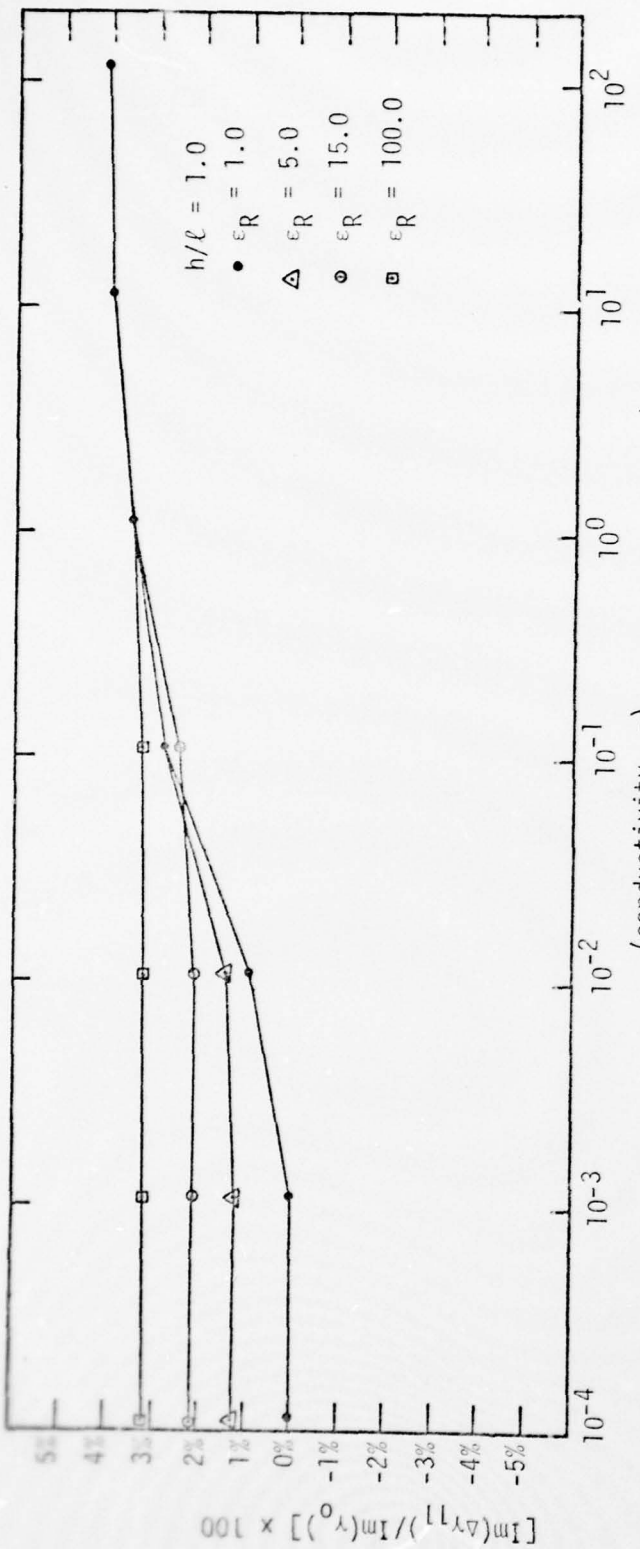


Figure 3-23. Plot of the percent change of the fundamental resonant frequency relative to the free space resonant frequency, shown as a function of permittivity, $\varepsilon_R\varepsilon_o$, and conductivity, σ, for fixed spacing $h/\ell = 1.0$.

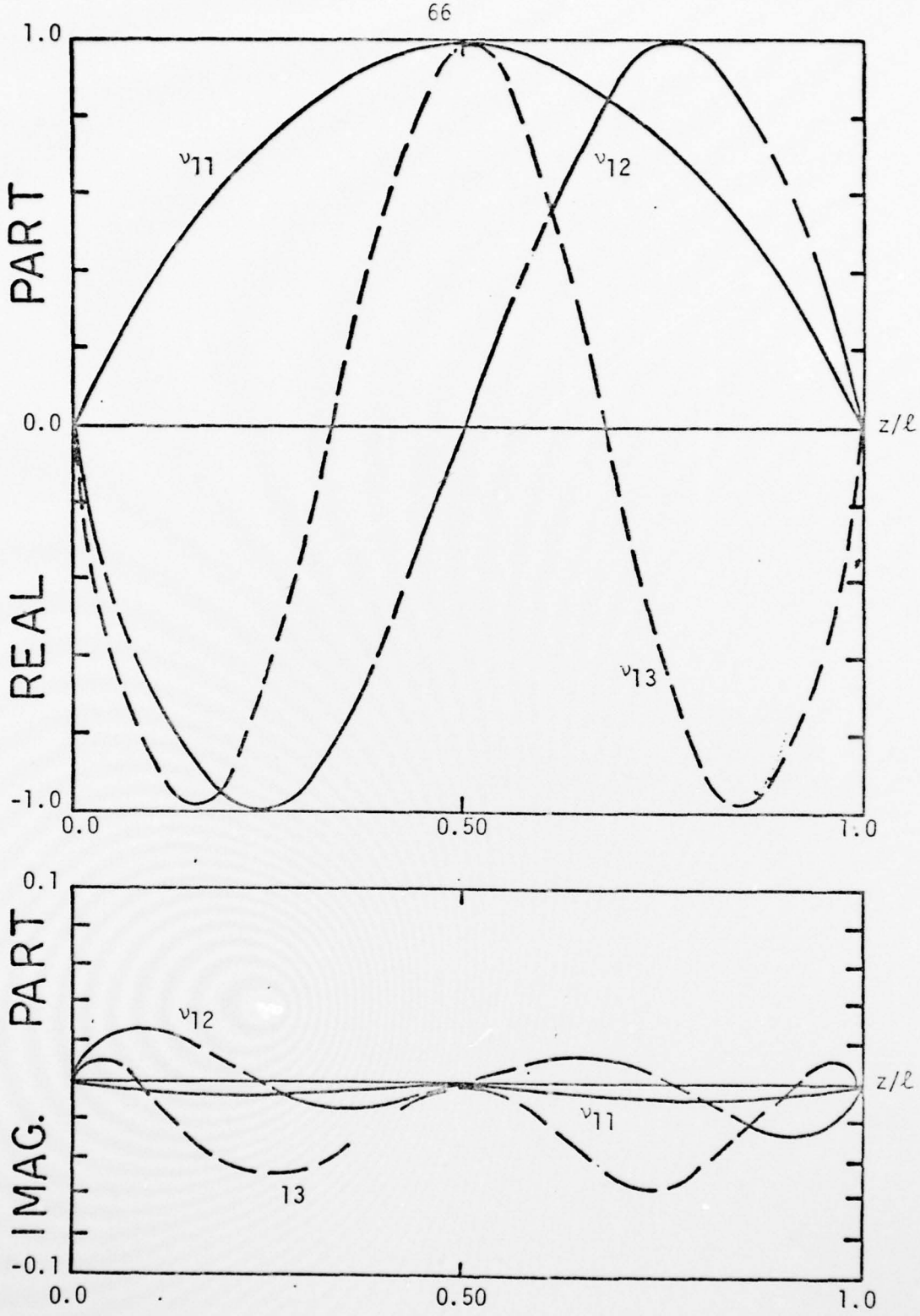


Figure 3-24. Real and imaginary part of normalized natural modal current distribution for resonant frequencies γ_{11}, γ_{12}, γ_{13}, $h/\ell = 0.5$, $\varepsilon_R = 1.0$, $\sigma = 120.0$, $\Omega = 10.6$.

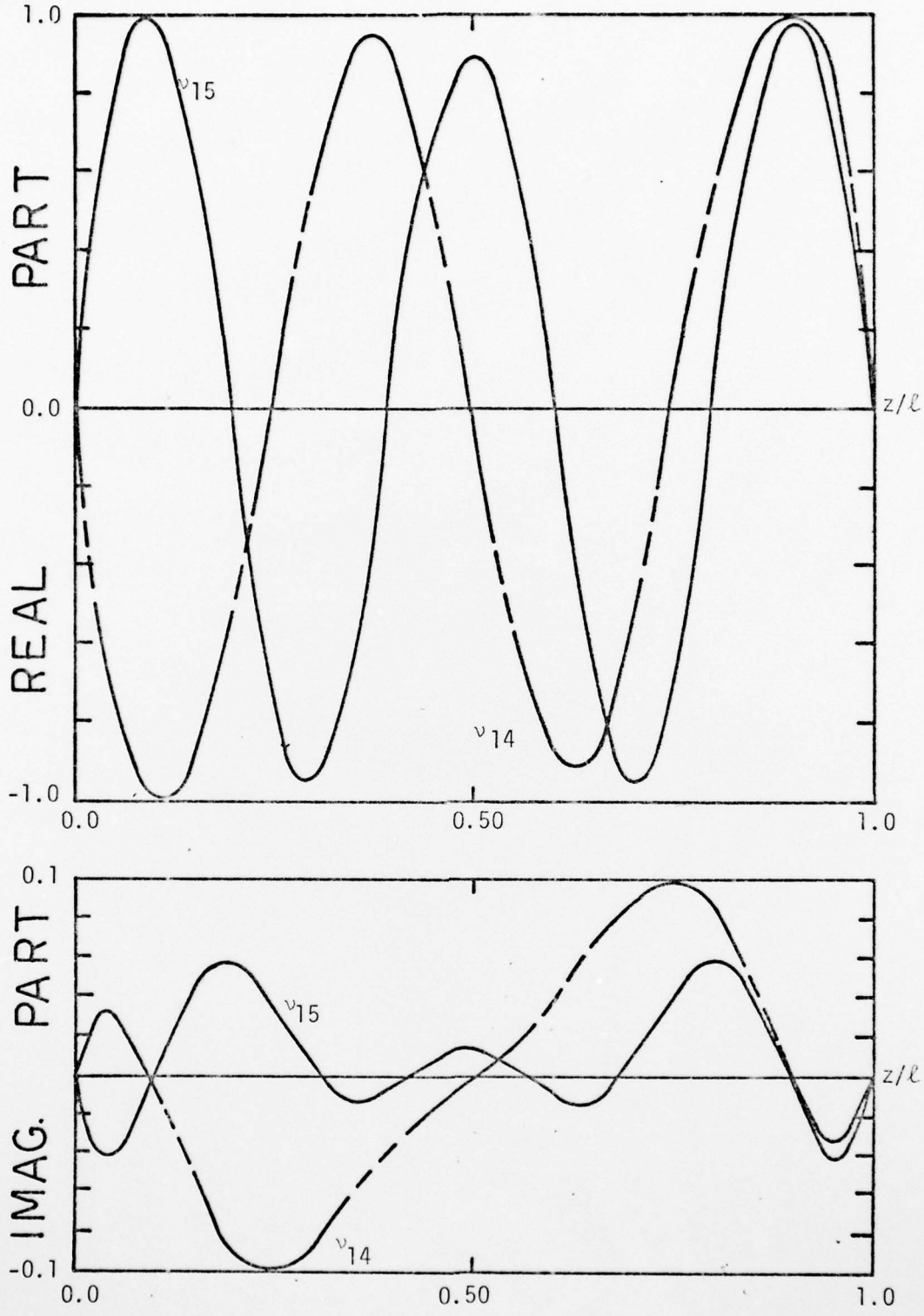


Figure 3-25. Real and imaginary part of normalized natural modal current distributions for resonant frequencies γ_{14} and γ_{15}, $h/\ell = 0.5$, $\varepsilon_R = 1.0$, $\sigma = 120.0$, $\Omega = 10.6$.

IV. Conclusions

The Singularity Expansion Method (SEM) coupled with the reflection coefficient approximation seems to be an appropriate technique for analyzing a cylindrical scatterer over a finitely conducting ground. Pole locations of the cylinder over perfect ground calculated by investigators were found to be identical to those calculated in this analysis when the ground conductivity is large. Also, when the ground conductivity is reduced with the relative permittivity held at unity, calculated pole locations agree with those of the free space problem. These facts add credence to the reflection coefficient technique. In general, it is found that displacement of the singularities from their free space position is a function of discontinuity in the ground plane. The mechanism for discontinuity is seen to be somewhat inmaterial. Mode vectors corresponding to first layer singularities show little or no dependence on the parameters of the problem.

The greatest value of this work lies in the fact that a relatively complicated problem has been solved within acceptable engineering accuracy over a wide range of parameters.

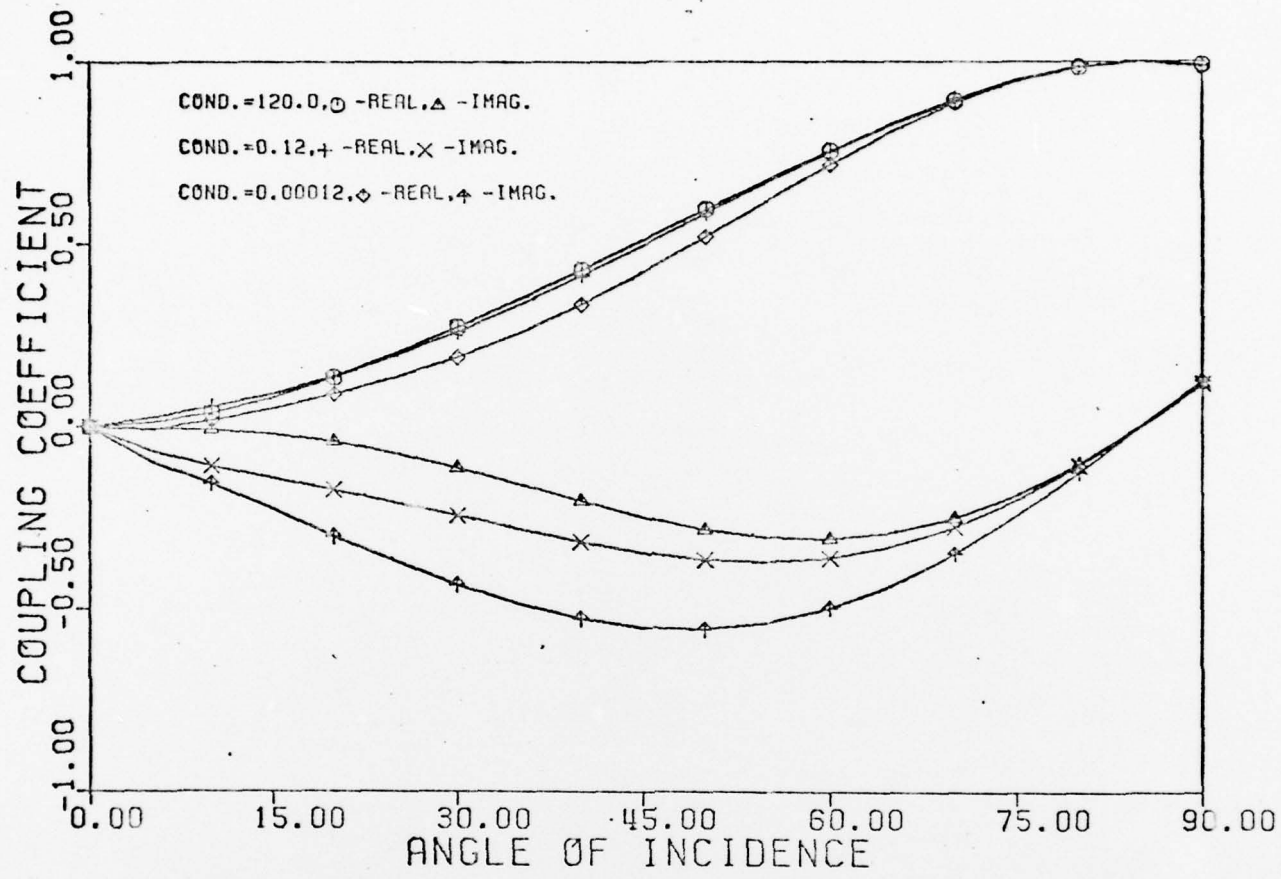


Figure 3-26. Coupling coefficient for fundamental self-resonant singularity, γ_{11}, as a function of conductivity, σ, and incident angle θ. The scatterer height-to-length ratio, h/ℓ, is 0.25, and the relative permittivity, ε_R, is unity

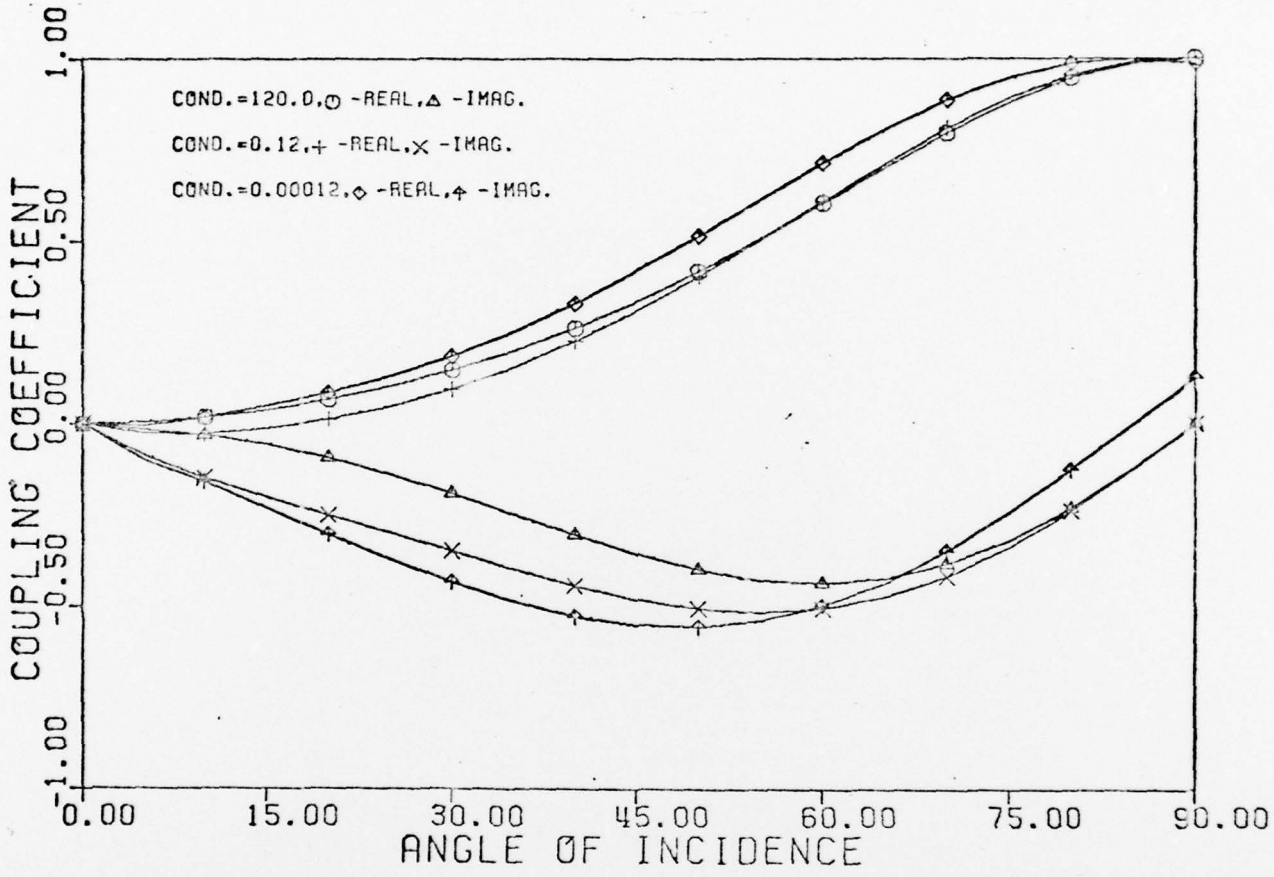


Figure 3-27. Coupling coefficient for fundamental self-resonant singularity, γ_{11}, as a function of conductivity, σ, and incident angle θ. The scatterer height-to-length ratio, h/ℓ, is 0.50, and the relative permittivity, ε_R, is unity

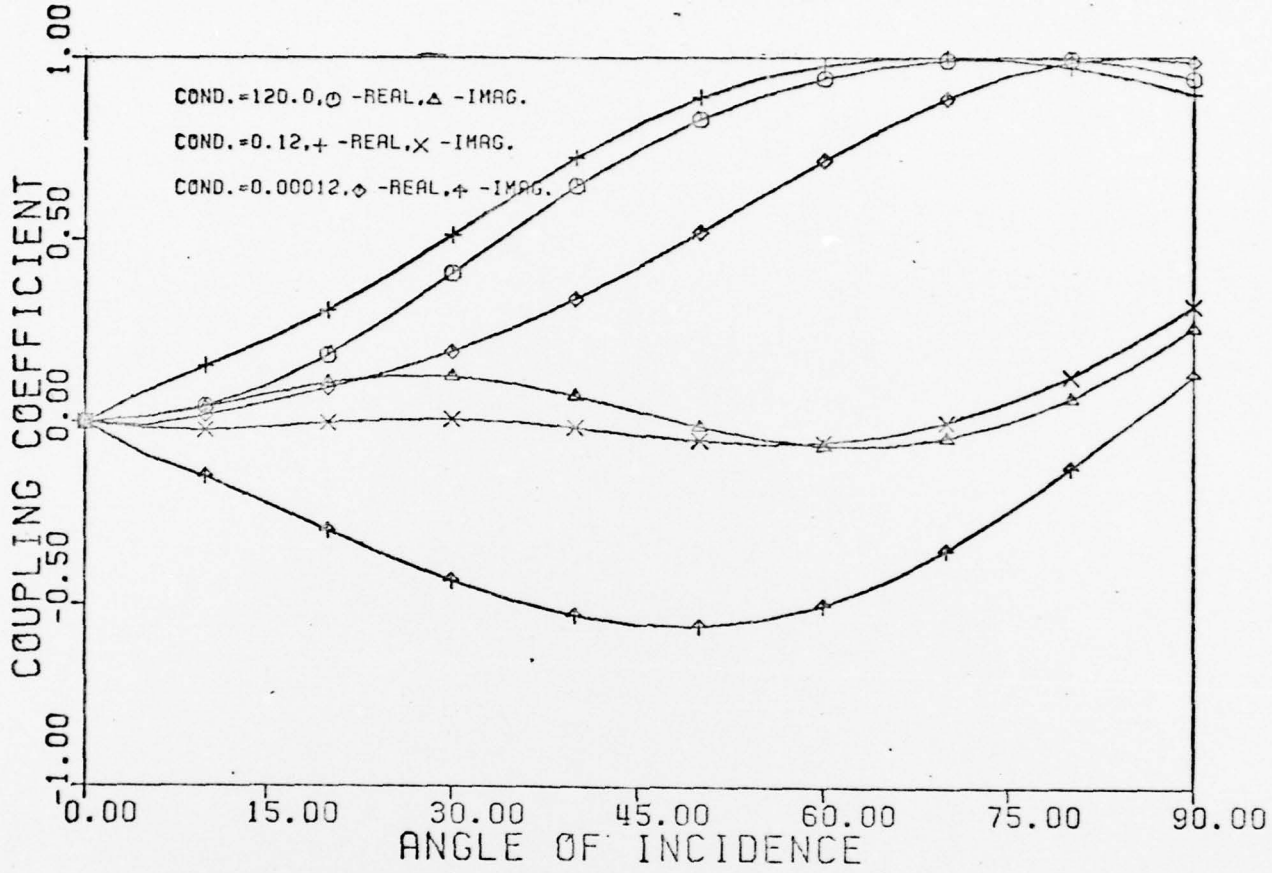


Figure 3-28. Coupling coefficient for fundamental self-resonant singularity, γ_{11}, as a function of conductivity, σ, and incident angle θ. The scatterer height-to-length ratio, h/ℓ, is 0.75, and the relative permittivity, ε_R, is unity

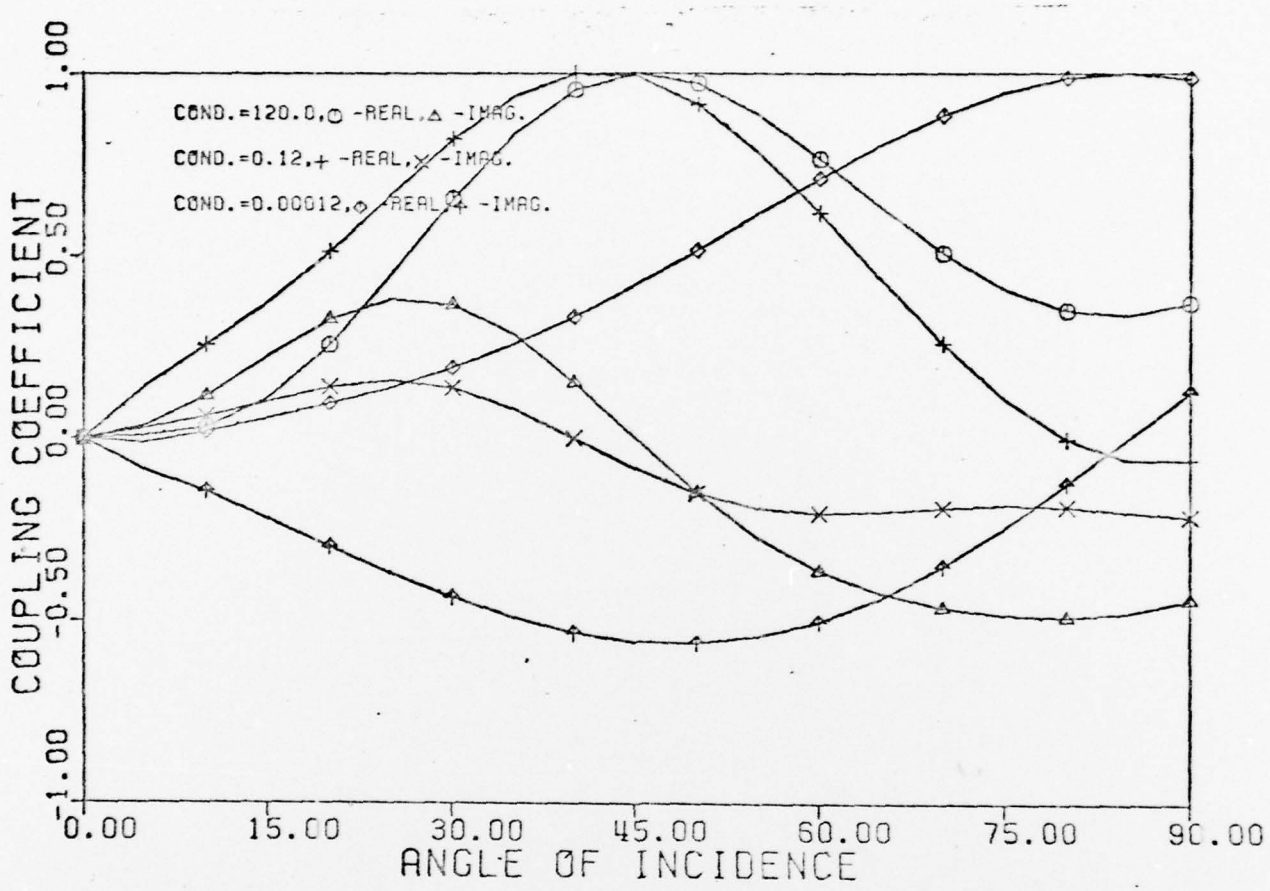


Figure 3-29. Coupling coefficient for fundamental self-resonant singularity, γ_{11}, as a function of conductivity, σ, and incident angle θ. The scatterer height-to-length ratio, h/ℓ, is 1.00, and the relative permittivity, ε_R, is unity

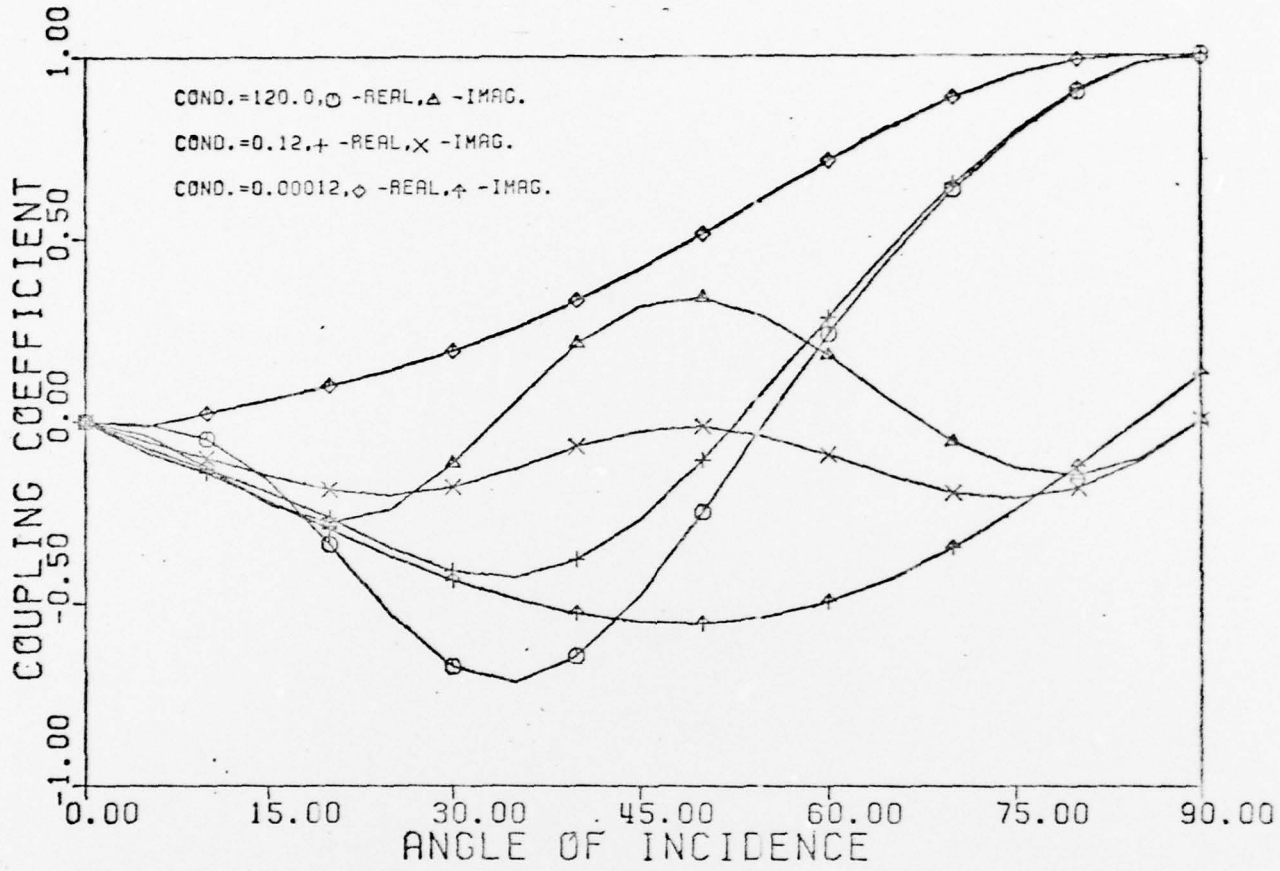


Figure 3-30. Coupling coefficient for fundamental self-resonant singularity, γ_{11}, as a function of conductivity, σ, and incident angle θ. the scatterer height-to-length ratio h/ℓ, is 1.25, and the relative permittivity, ε_R, is unity

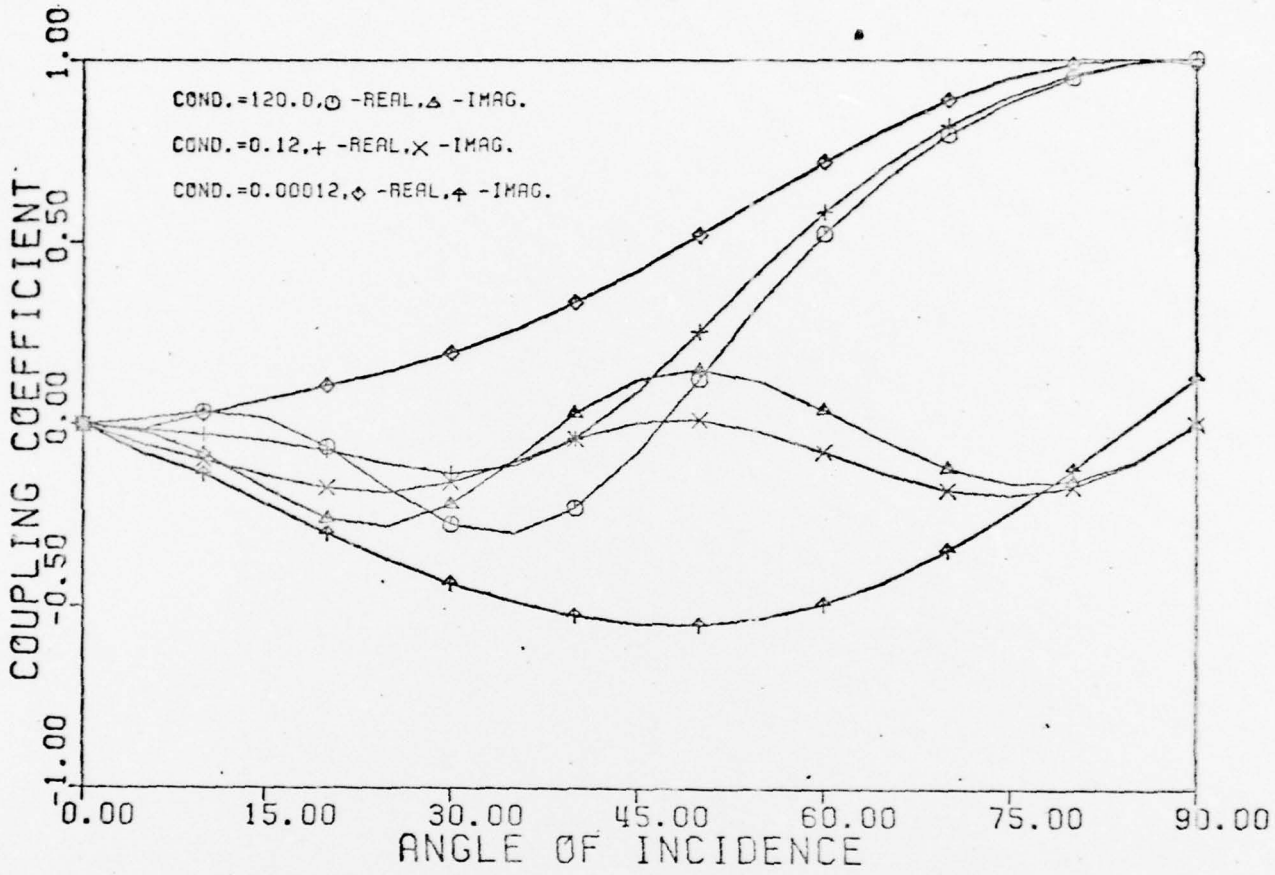


Figure 3-31. Coupling coefficient for fundamental self-resonant singularity, γ_{11}, as a function of conductivity, σ, and incident angle θ. The scatterer height-to-length ratio, h/ℓ, is 1.50, and the relative permittivity, ε_R, is unity

Table 3-1. Predicted angle of incidence for maximum coupling using the "standing wave analogy." The table applies to Figure 3-26 through 3-31 for large couductivity, (σ = 120.0), and unity permittivity, (ε_R = 1.0)

FIGURE	h/ℓ	$I_m(\gamma_{11}) = \frac{\omega \ell}{c}$	$\beta h = \frac{2\pi h}{\lambda}$	cosθ=0	$\tan[\beta h \sin\theta] + \beta h \sin\theta = 0$
3-26	0.25	2.850	0.713	90°	NO SOLUTION
3-27	0.50	2.775	1.388	90°	NO SOLUTION
3-28	0.75	2.825	2.119	90°	73.0°<θ<73.5°
3-29	1.00	3.025	3.025	90°	42.0°<θ<42.5°
3-30	1.25	2.975	3.719	90°	33.0°<θ<33.5°
3-31	1.50	2.850	4.275	90°	28.0°<θ<28.5°

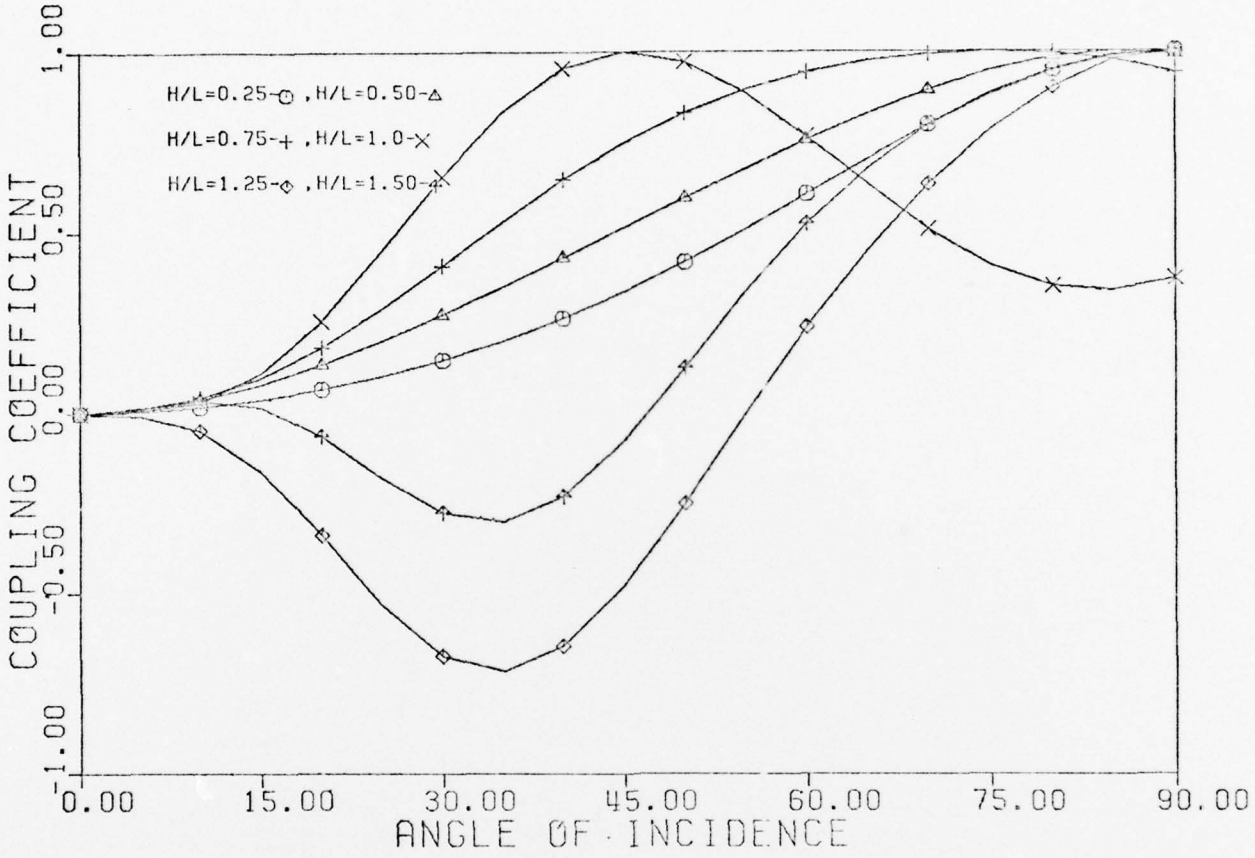


Figure 3-32. Real part of coupling coefficient for fundamental self-resonant singularity, γ_{11}, as a function of scatterer height-to-length ratio, h/ℓ, and incident angle θ. The ground conductivity, σ, is 120.0, and the relative permittivity, ε_R, is unity

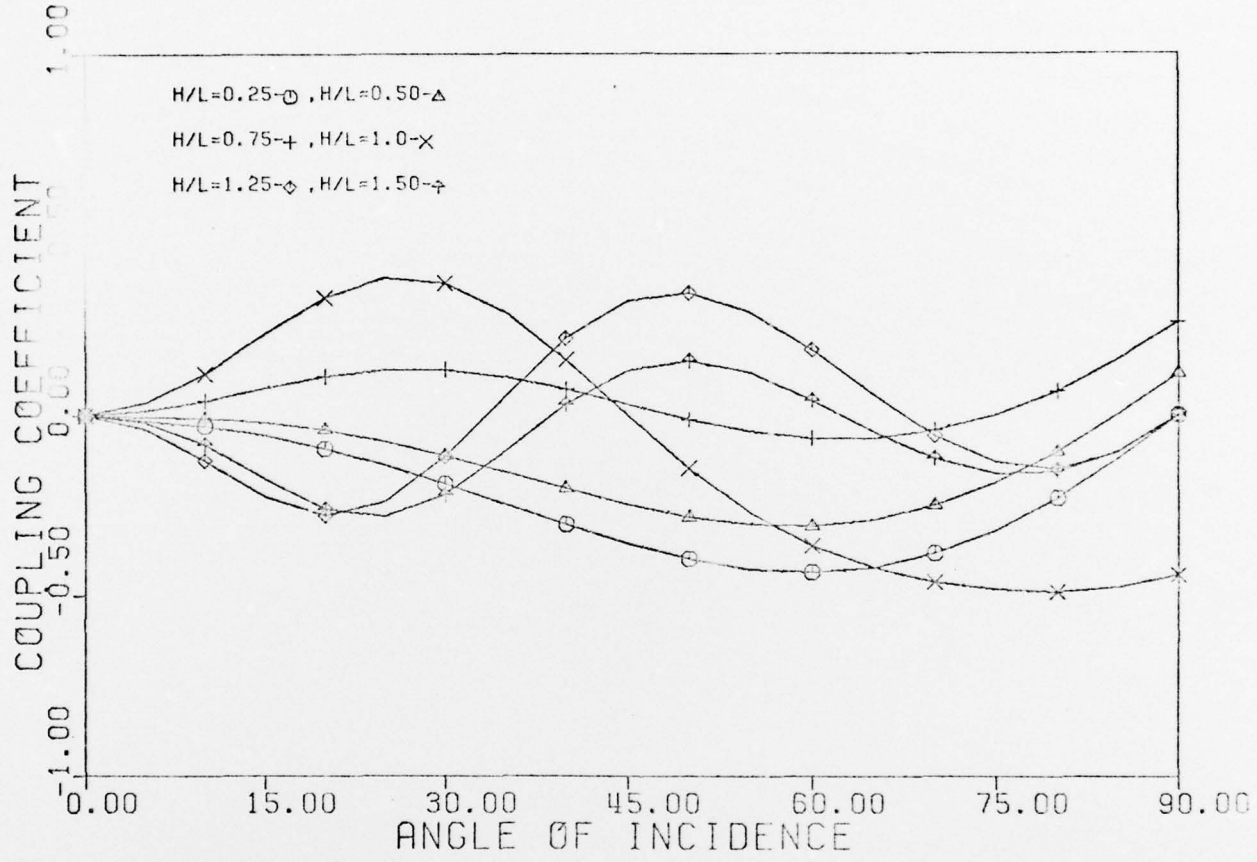


Figure 3-33. Imaginary part of coupling coefficient for fundamental self-resonant singularity, Y_{11}, as a function of scatterer height-to-length ratio, h/ℓ, and incident angle θ. The ground conductivity, σ, is 120.0, and the relative permittivity, ε_R, is unity

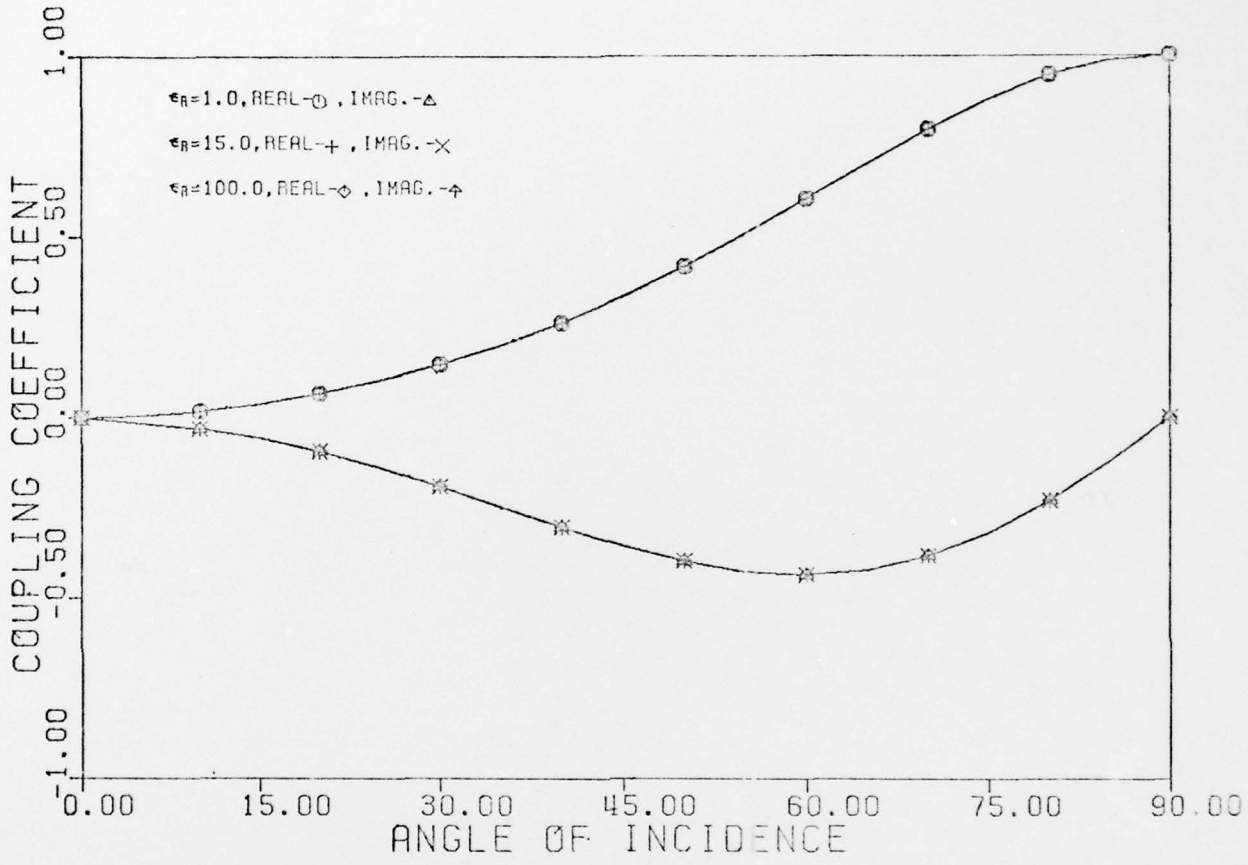
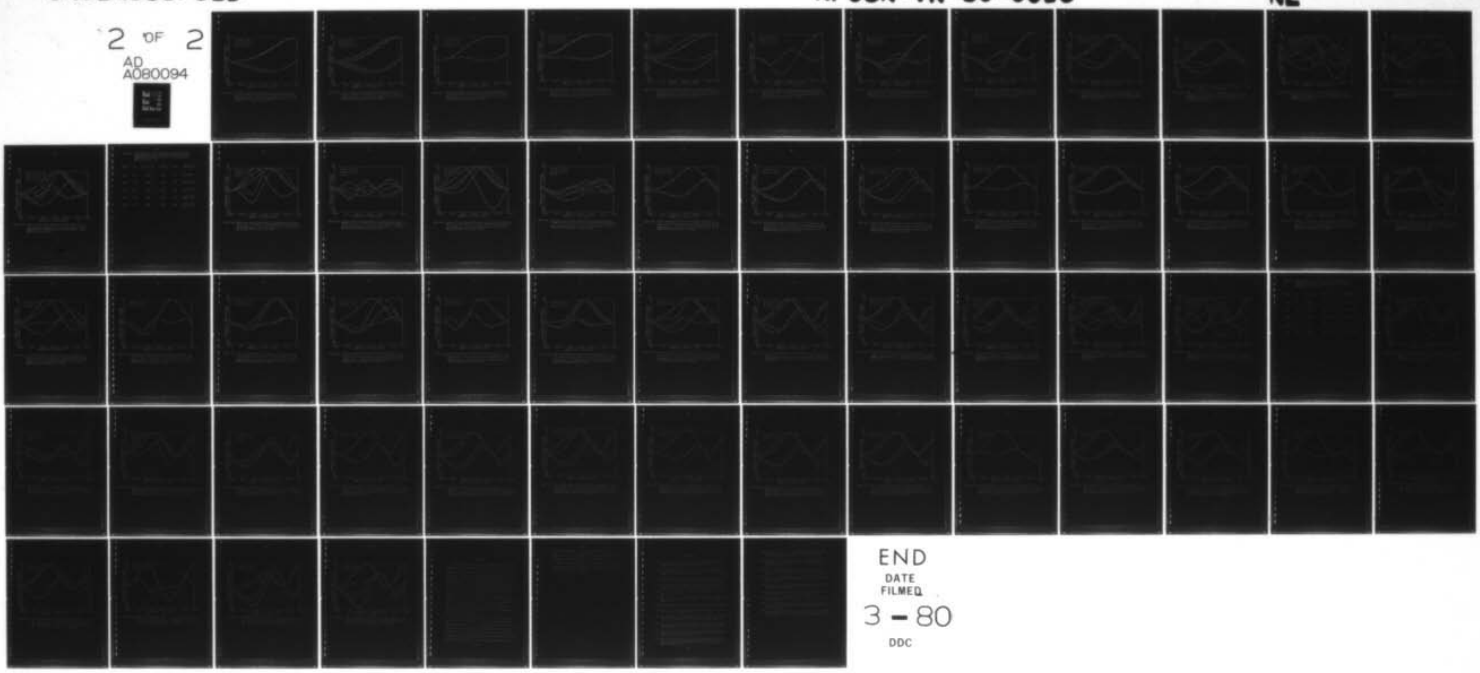


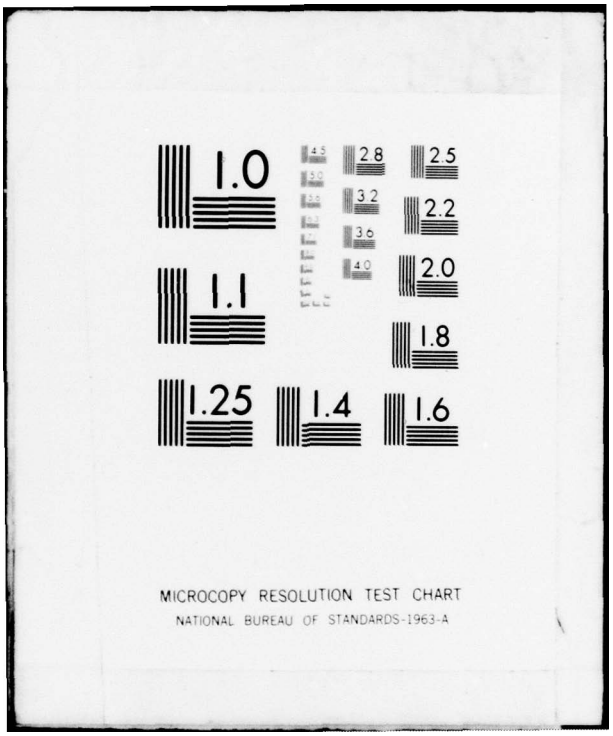
Figure 3-34. Coupling coefficient for fundamental self-resonant singularity, γ_{11}, as a function of the ground plane relative permittivity, ϵ_R, and incident angle θ. The scatterer height-to-length ratio, h/ℓ, is 0.25, and the conductivity, σ, is 120.0

AD-A080 094 AUBURN UNIV ALA ENGINEERING EXPERIMENT STATION F/G 20/3
SINGULARITIES, COUPLING COEFFICIENTS, AND MODE VECTORS FOR A TH--ETC(U)
DEC 79 T H SHUMPERT AFOSR-79-0017
UNCLASSIFIED AFOSR-TR-80-0013 NL

2 OF 2
AD
A080094



END
DATE
FILMED
3 - 80
DDC


1.0
1.1
1.25
1.4
1.6
1.8
2.0
2.2
2.5
2.8
3.2
3.6
4.0
4.5
5.0
MICROCOPY RESOLUTION TEST CHART
NATIONAL BUREAU OF STANDARDS-1963-A

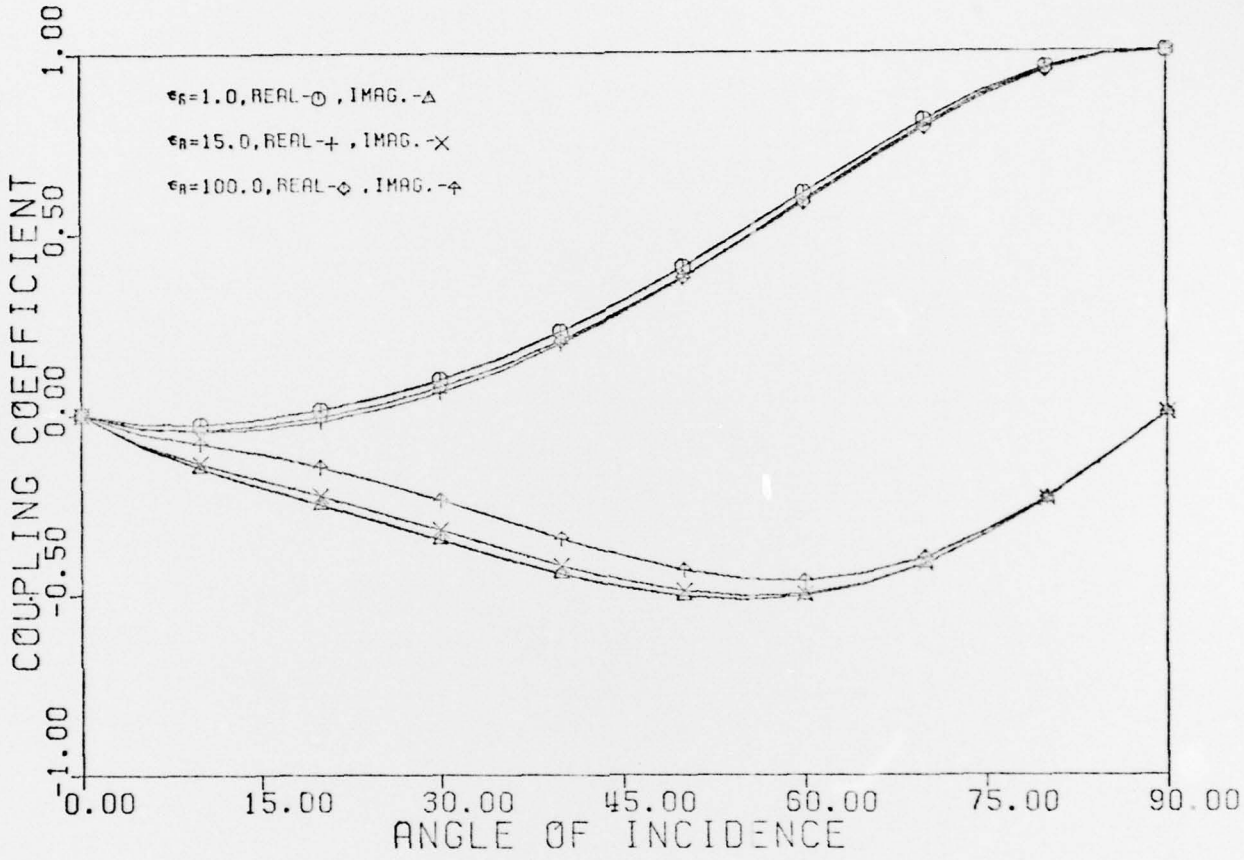


Figure 3-35. Coupling coefficient for fundamental self-resonant singularity, γ_{11}, as a function of the ground plane relative permittivity, ε_R, and incident angle θ. The scatterer height-to-length ratio, h/ℓ, is 0.25, and the conductivity, σ, is 0.12

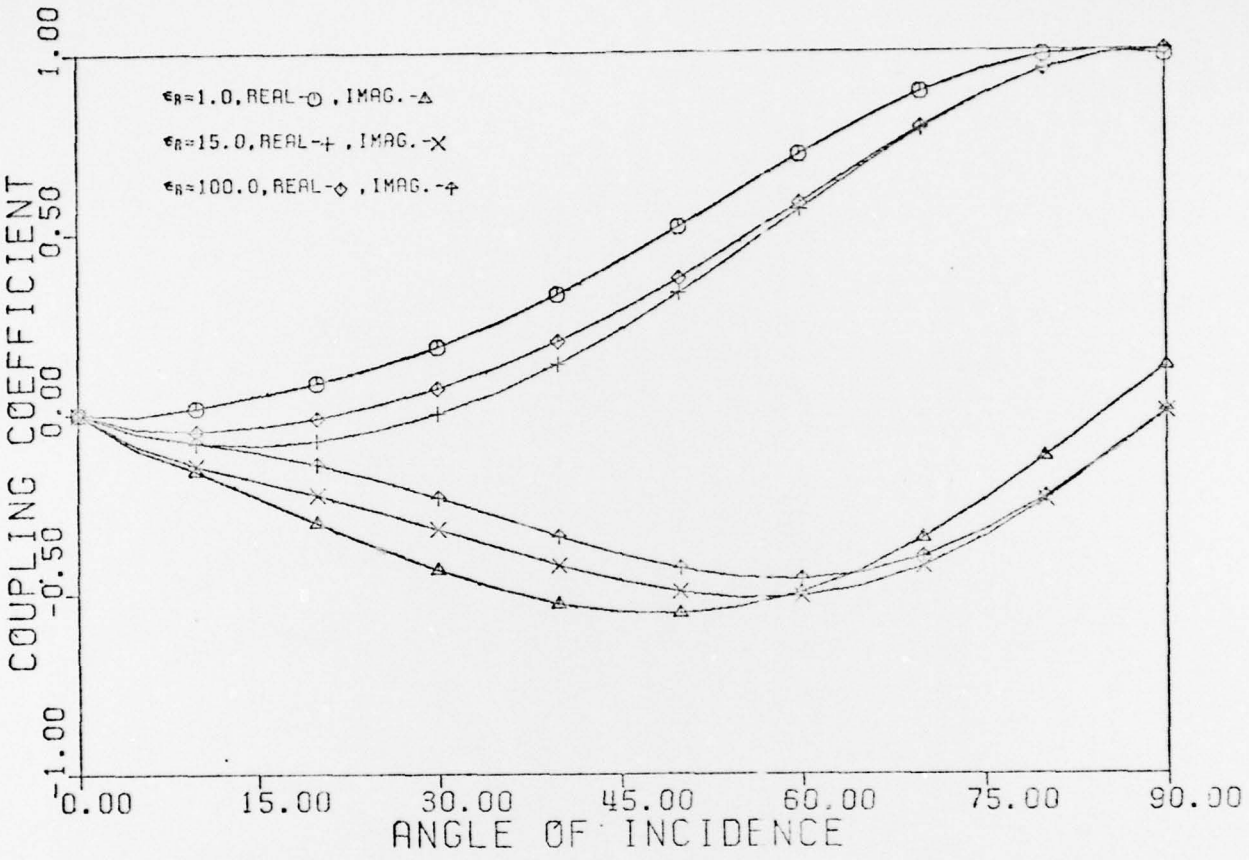


Figure 3-36. Coupling coefficient for fundamental self-resonant singularity, γ_{11}, as a function of the ground plane relative permittivity, ϵ_R, and incident angle θ. The scatterer height-to-length ratio, h/ℓ, is 0.25, and the conductivity, σ, is 0.00012

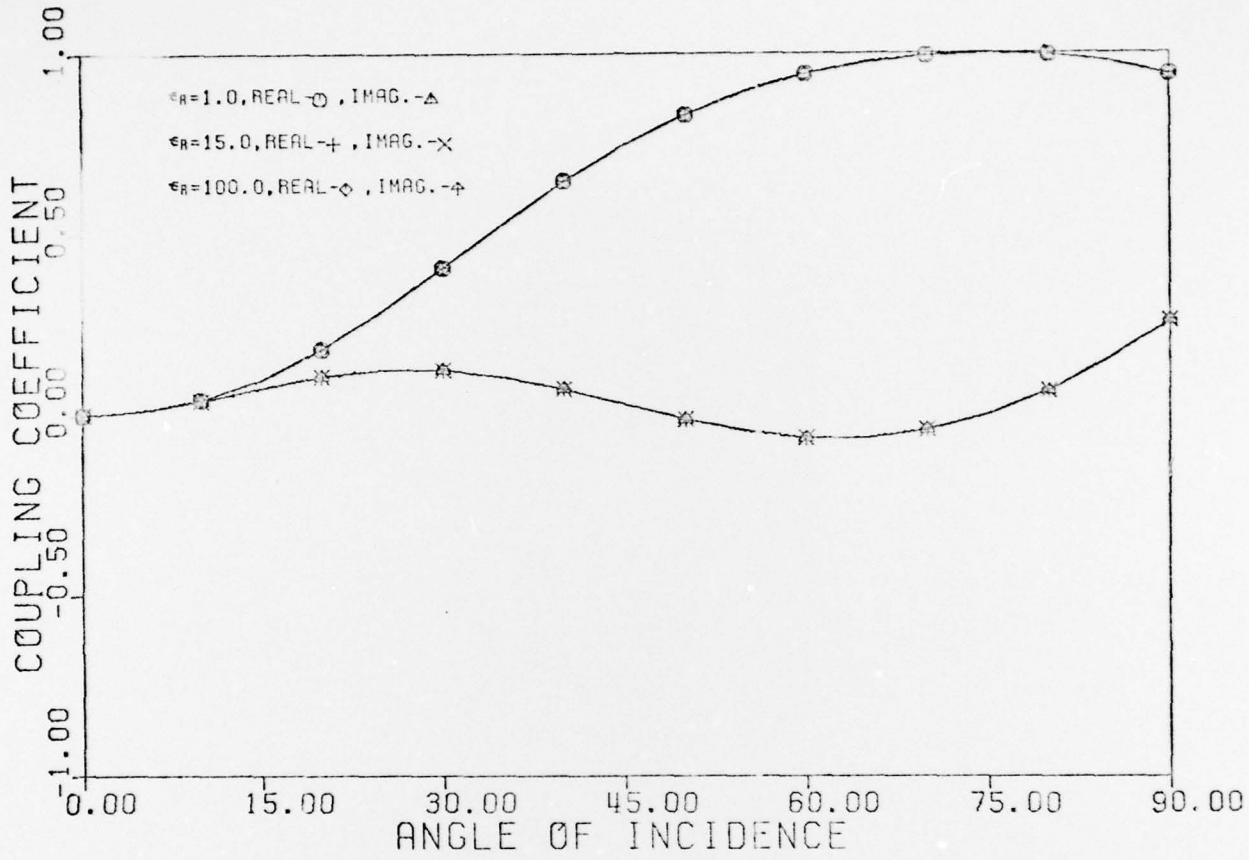


Figure 3-37. Coupling coefficient for fundamental self-resonant singularity, γ_{11}, as a function of the ground plane relative permittivity, ϵ_R, and incident angle θ. The scatterer height-to-length ratio, h/ℓ, is 0.75, and the conductivity, σ, is 120.0

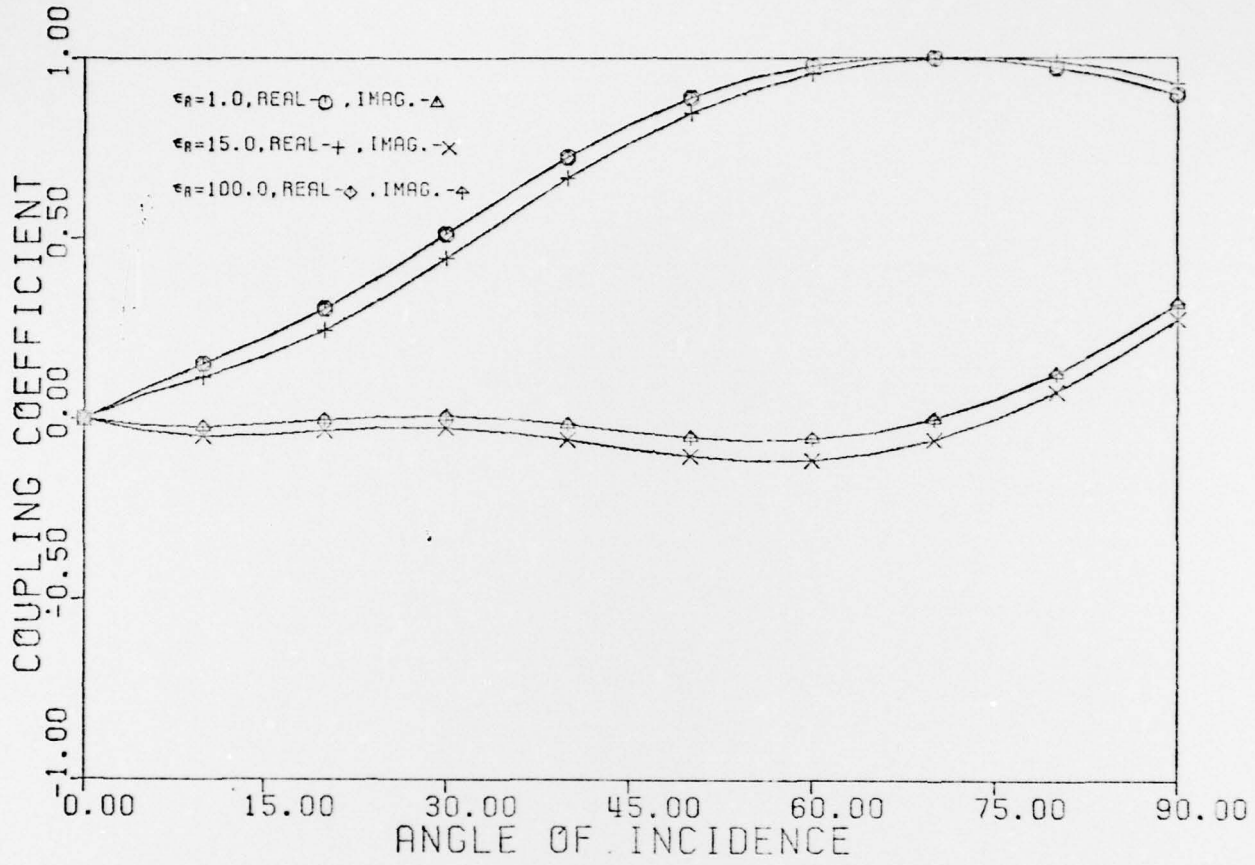


Figure 3-38. Coupling coefficient for fundamental self-resonant singularity, Y_{11}, as a function of the ground plane relative permittivity, ϵ_R, and incident angle θ. The scatterer height-to-length ratio, h/ℓ, is 0.75, and the conductivity, σ, is 0.12

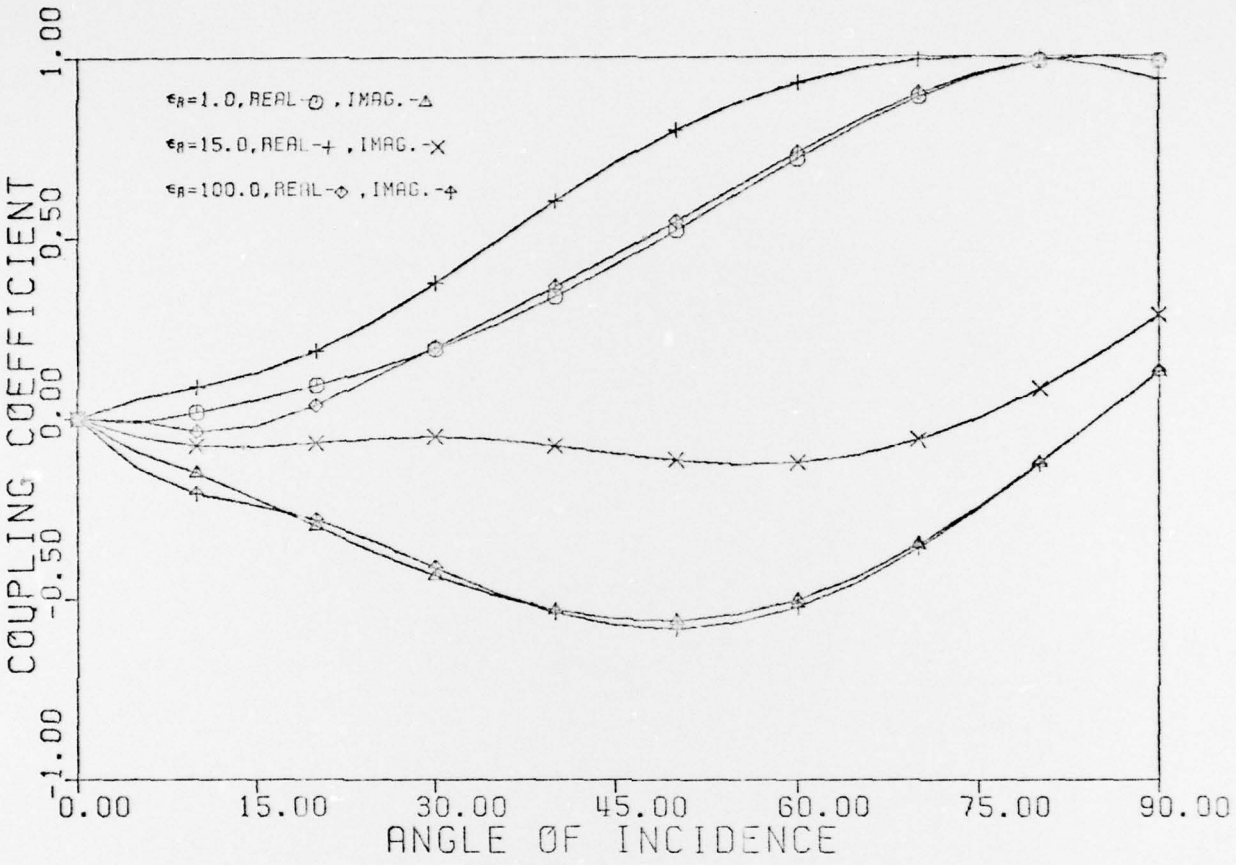


Figure 3.39. Coupling coefficient for fundamental self-resonant singularity, γ_{11}, as a function of the ground plane relative permittivity, ϵ_R, and incident angle θ. The scatterer height-to-length ratio, h/ℓ, is 0.75, and the conductivity, σ, is 0.00012

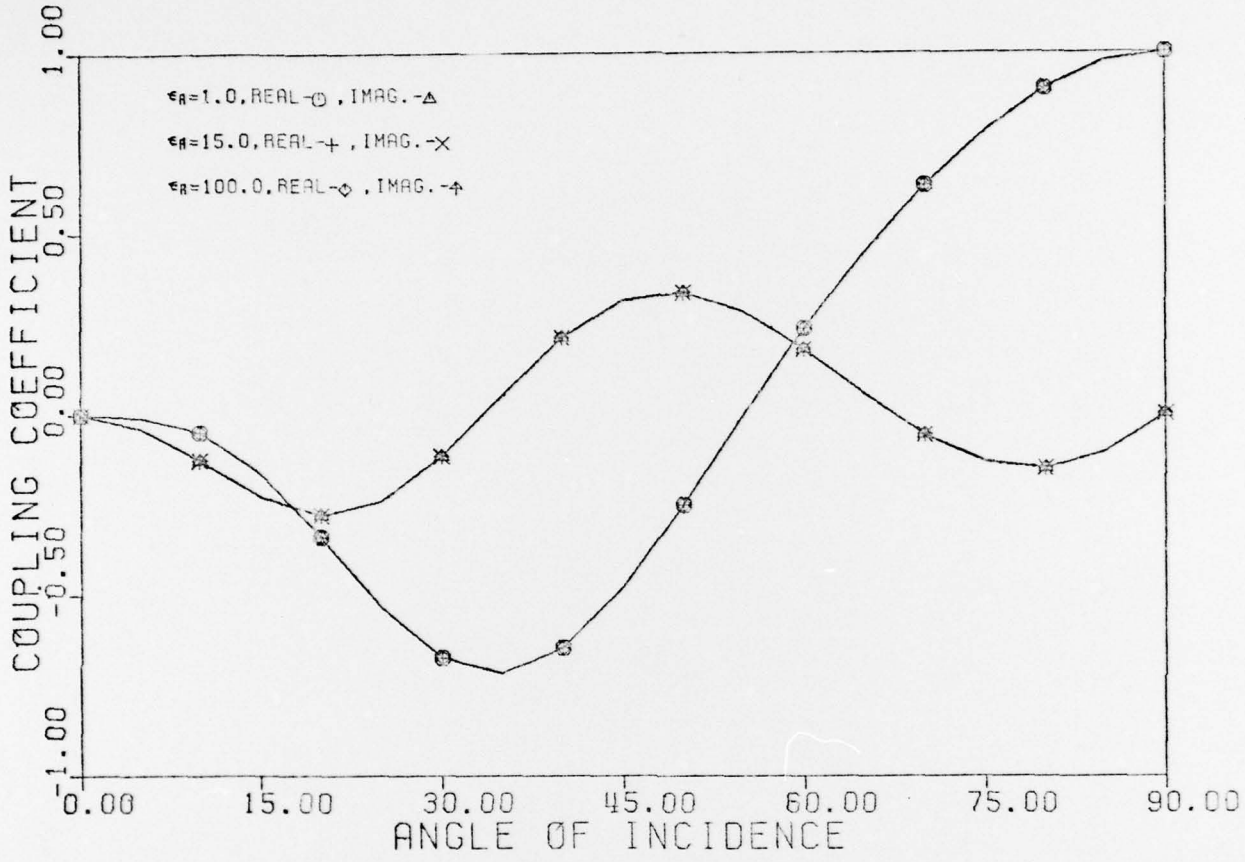


Figure 3-40. Coupling coefficient for fundamental self-resonant singularity, γ_{11}, as a function of the ground plane relative permittivity, ϵ_R, and incident angle θ. The scatterer height-to-length ratio, h/ℓ, is 1.25, and the conductivity, σ, is 120.0

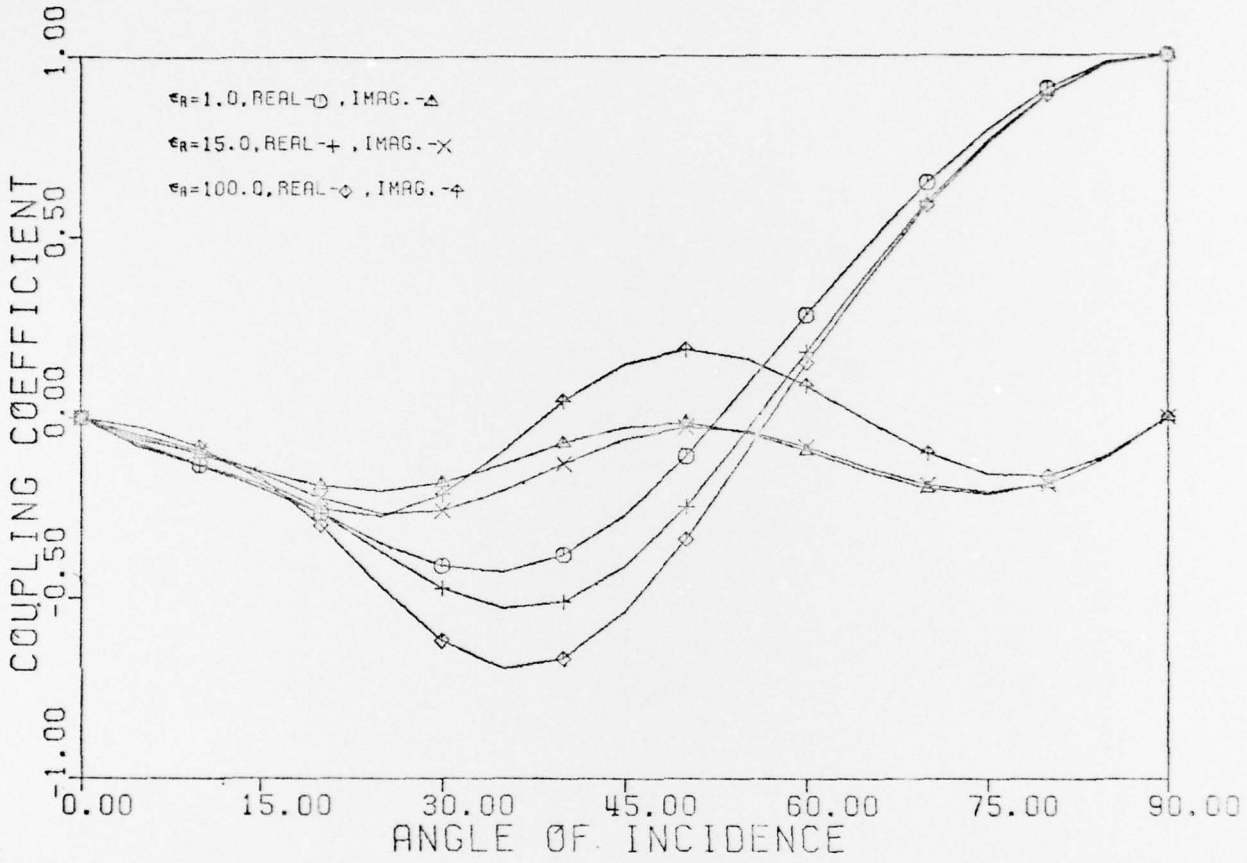


Figure 3-41. Coupling coefficient for fundamental self-resonant singularity, γ_{11}, as a function of the ground plane relative permittivity, ϵ_R, and incident angle θ. The scatterer height-to-length ratio, h/ℓ, is 1.25, and the conductivity, σ, is 0.12

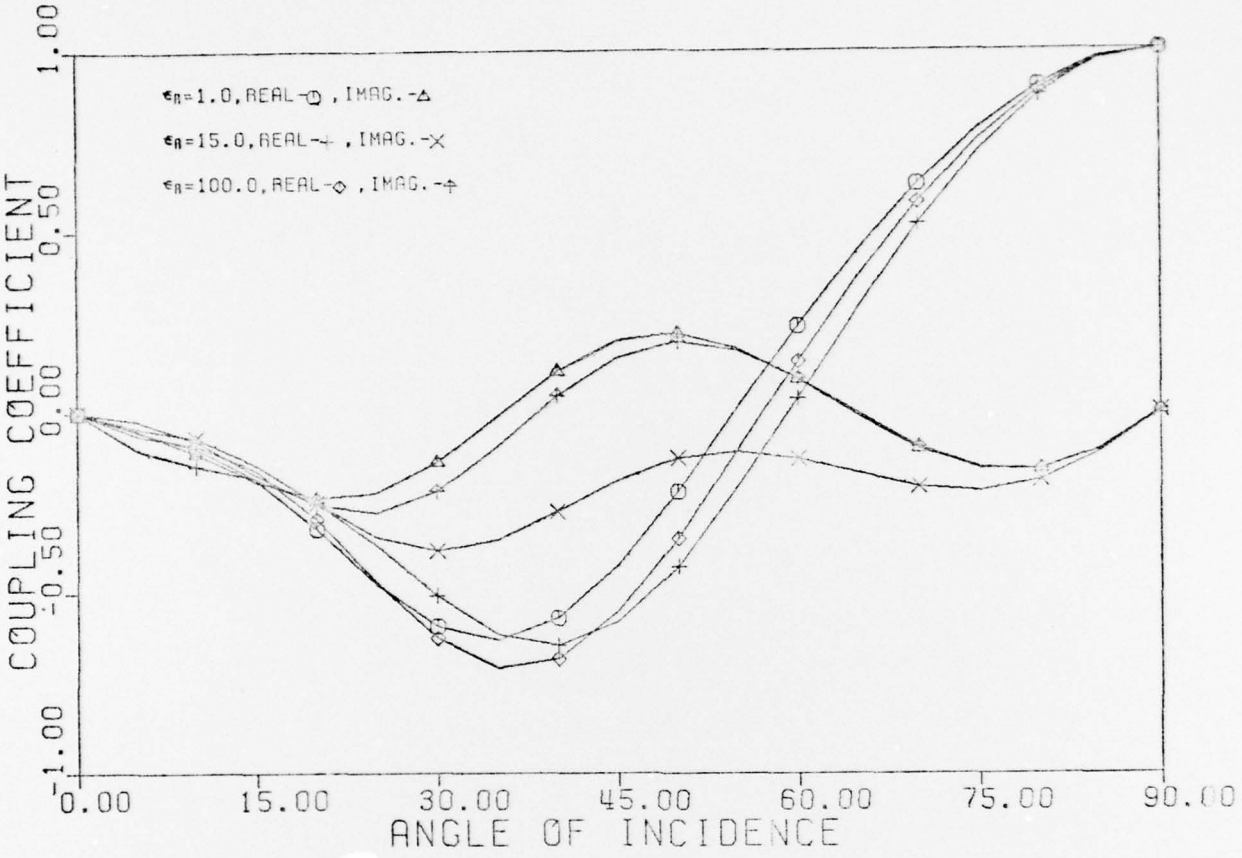


Figure 3-42. Coupling coefficient for fundamental self-resonant singularity, γ_{11}, as a function of the ground plane relative permittivity, ϵ_R, and incident angle θ. The scatterer height-to-length ratio, h/ℓ, is 1.25, and the conductivity, σ, is 0.00012

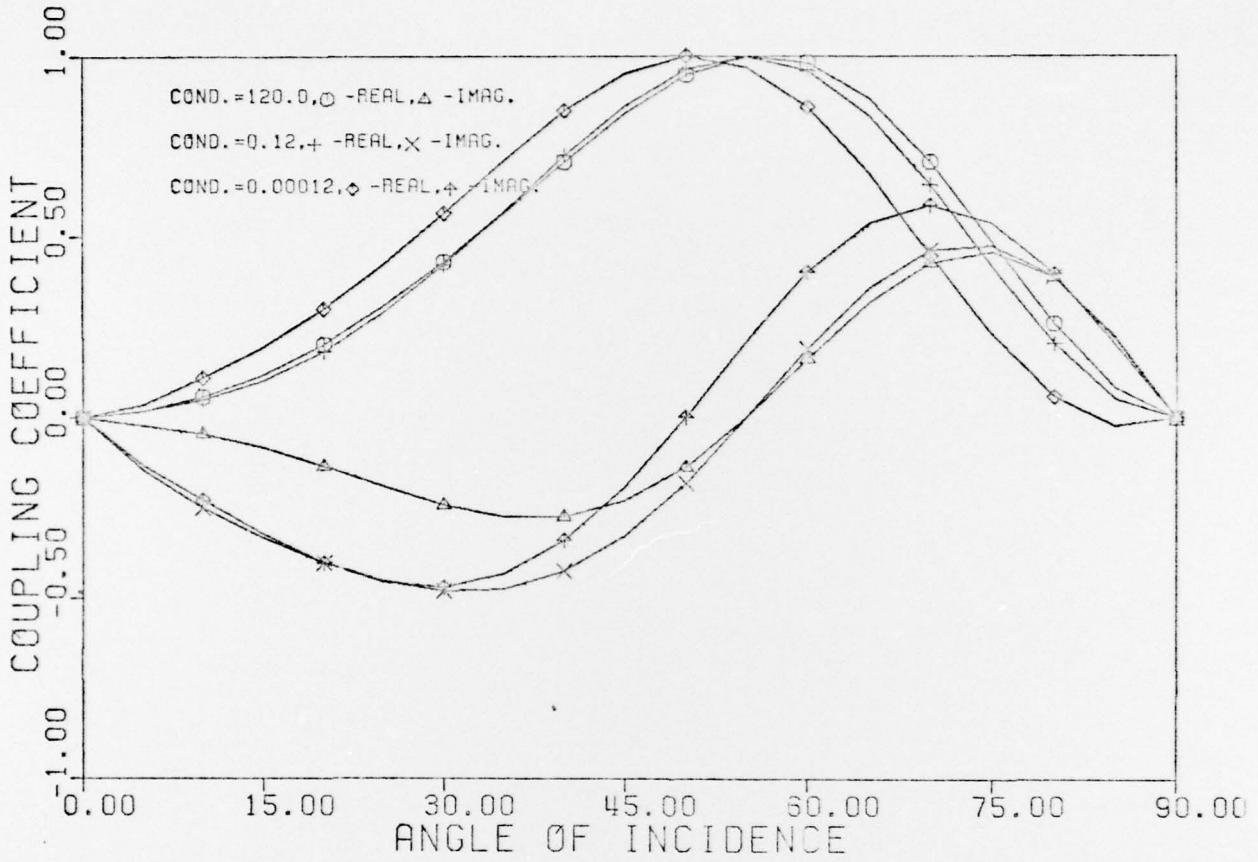


Figure 3-43. Coupling coefficient for second self-resonant singularity, ν_{12}, as a function of conductivity, σ, and incident angle θ. The scatterer height-to-length ratio, h/ℓ, is 0.20, and the relative permittivity, ε_R, is unity

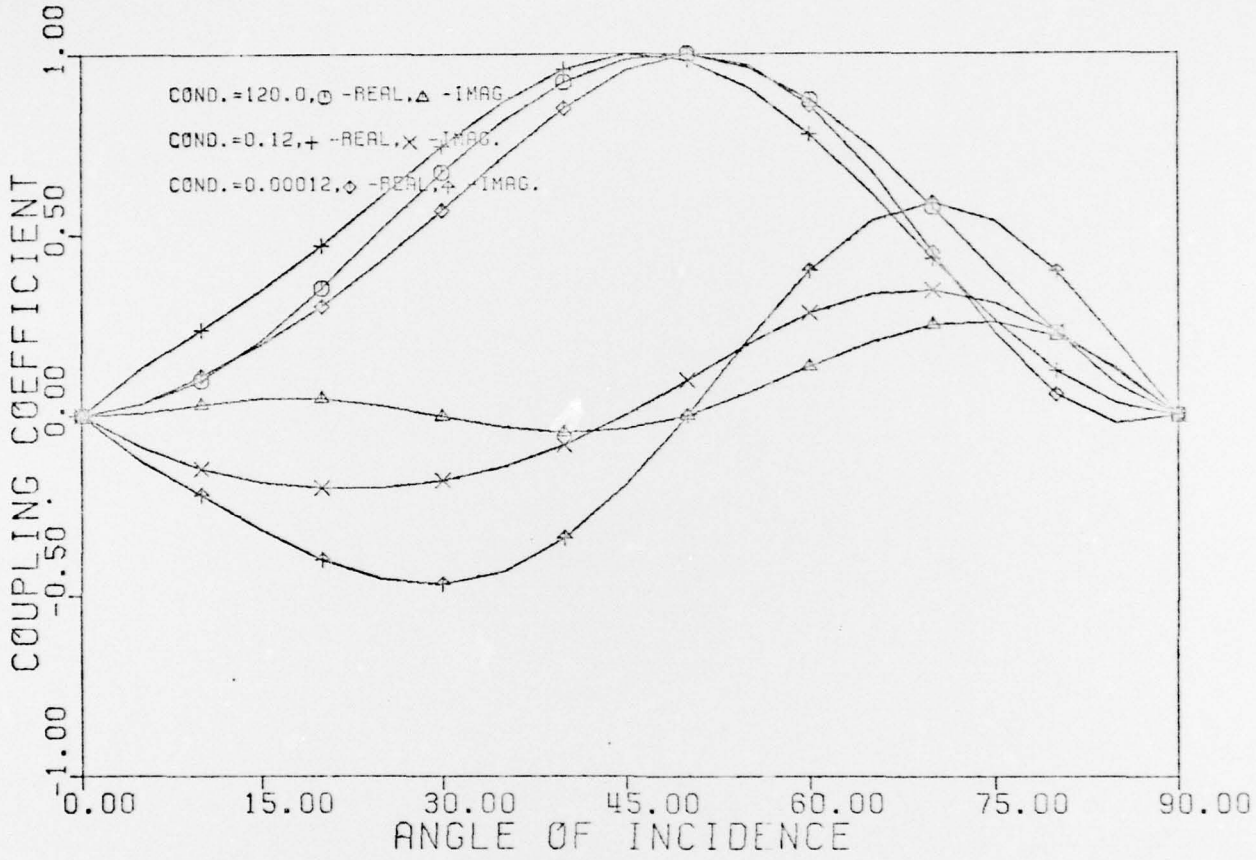


Figure 3-44. Coupling coefficient for second self-resonant singularity, γ_{12}, as a function of conductivity, σ, and incident angle θ. The scatterer height-to-length ratio, h/ℓ, is 0.40, and the relative permittivity, ε_R, is unity

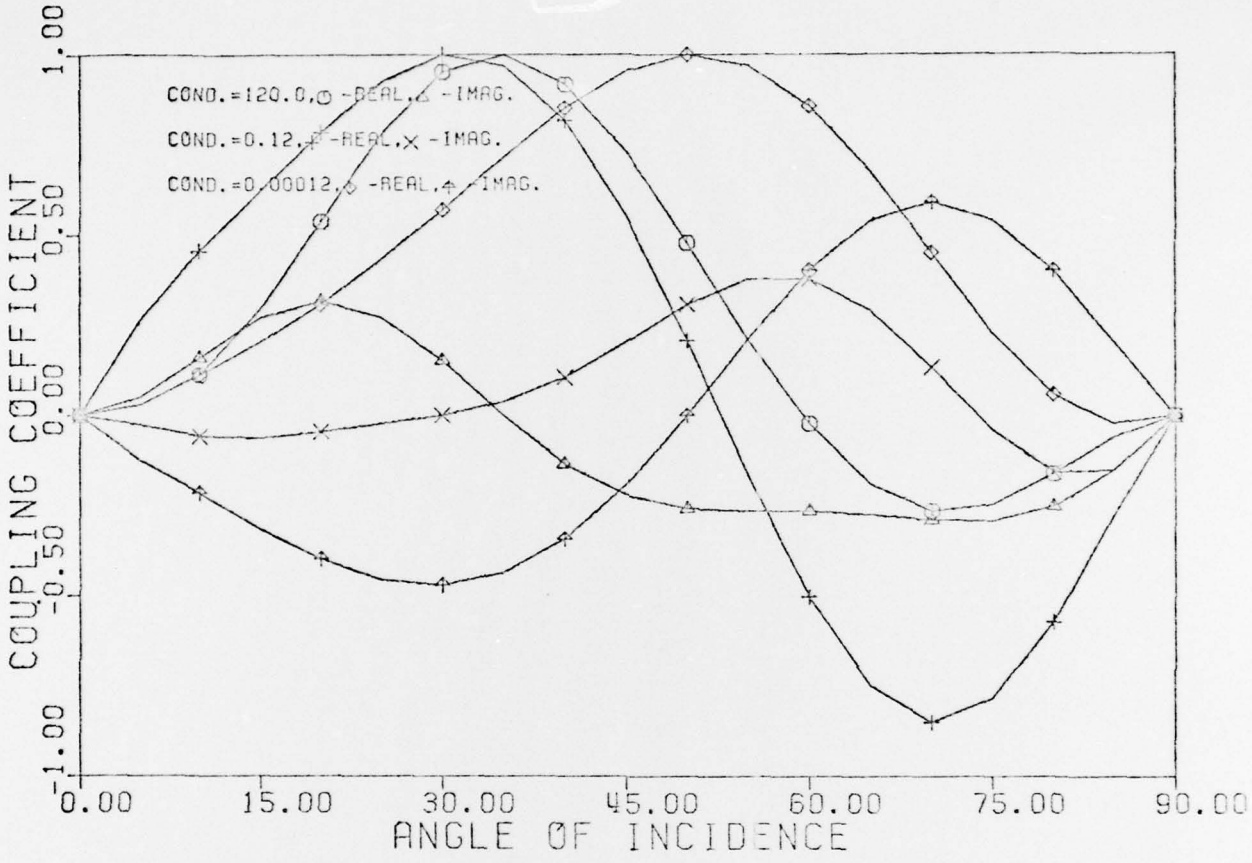


Figure 3-45. Coupling coefficient for second self-resonant singularity, γ_{12}, as a function of conductivity, σ, and incident angle θ. The scatterer height-to-length ratio, h/ℓ, is 0.60, and the relative permittivity, ε_R, is unity

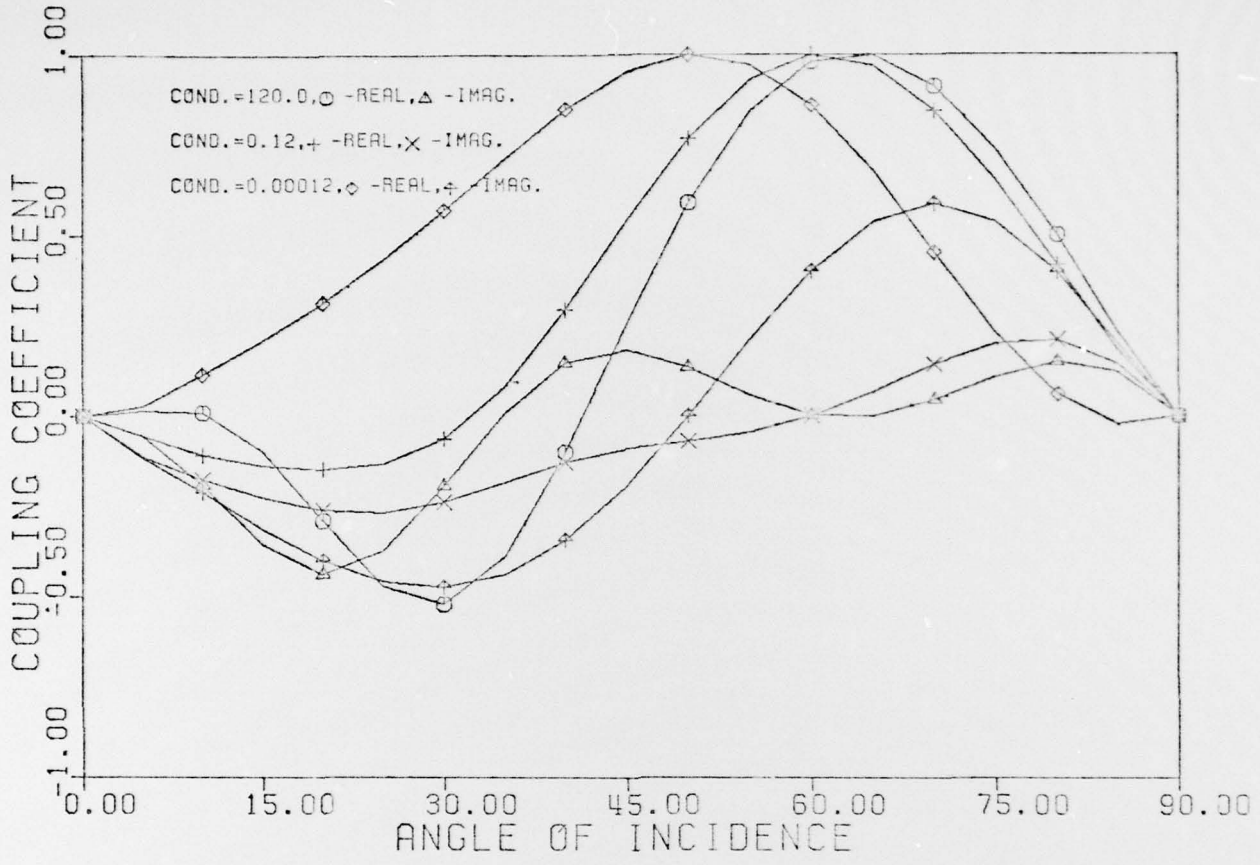


Figure 3-46. Coupling coefficient for second self-resonant singularity, γ_{12}, as a function of conductivity, σ, and incident angle θ. The scatterer height-to-length ratio, h/ℓ, is 0.80, and the relative permittivity, ϵ_R, is unity

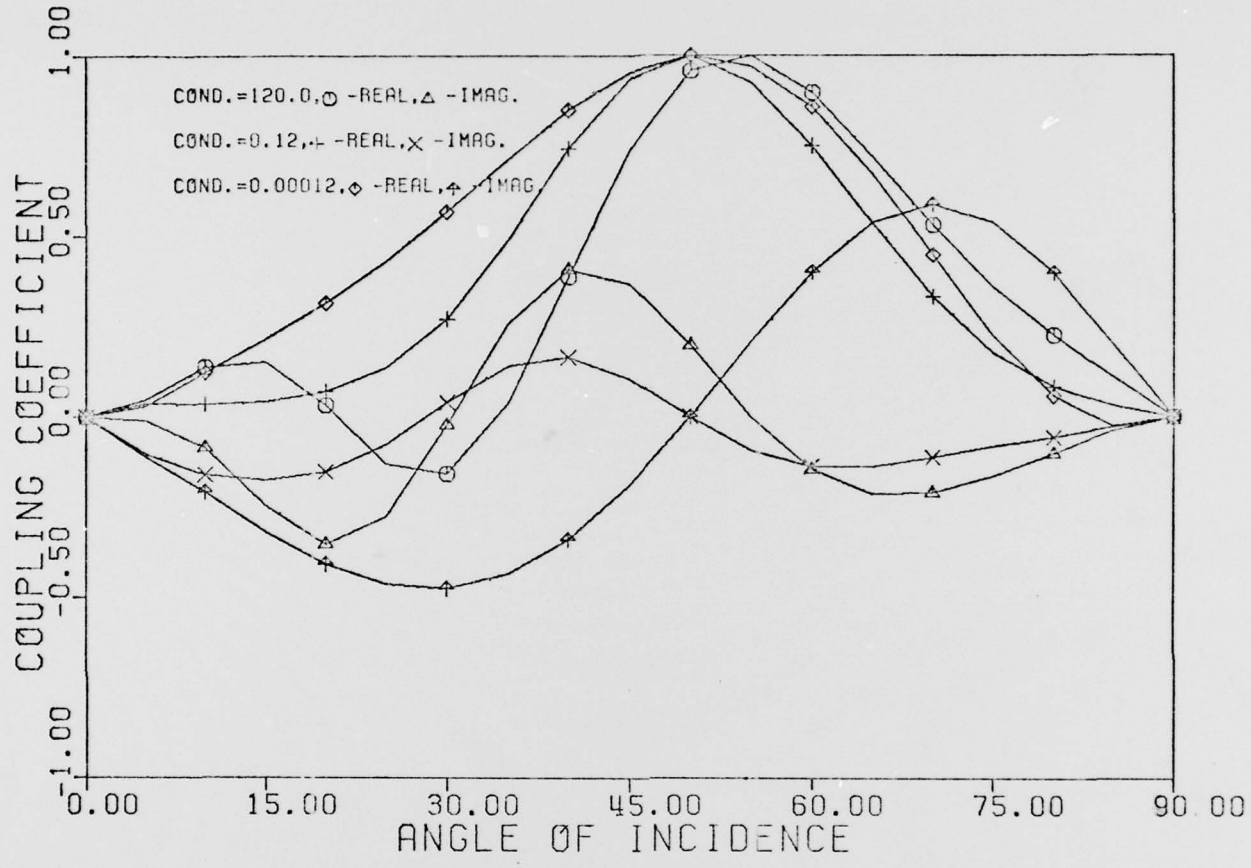


Figure 3-47. Coupling coefficient for second self-resonant singularity, γ_{12}, as a function of conductivity, σ, and incident angle θ. The scatterer height-to-length ratio, h/ℓ, is 1.0, and the relative permittivity, ε_R, is unity

Table 3-2. Predicted angle of incidence for maximum coupling using the "standing wave analogy." The table applies to Figure 3-43 through 3-47 for large conductivity, (σ = 120.0), and unity permittivity, (ε_R = 1.0)

FIGURE	h/ℓ	$I_m(\gamma_{12}) = \frac{\omega\ell}{c}$	$\beta h = \frac{2\pi h}{\lambda}$	$\cos\theta=0$	$\tan[\beta h \sin\theta] + \beta h \sin\theta = 0$
3-43	0.2	5.800	1.38	90°	NO SOLUTION
3-44	0.4	5.825	2.70	90°	48.5°<θ<42.0°
3-45	0.6	6.025	3.90	90°	31.0°<θ<31.5°
3-46	0.8	5.900	5.34	90°	22.0°<θ<22.5° 66.5°<θ<67.0°
3-47	1.0	5.900	6.66	90°	17.5°<θ<18.0° 47.5°<θ<48.0°

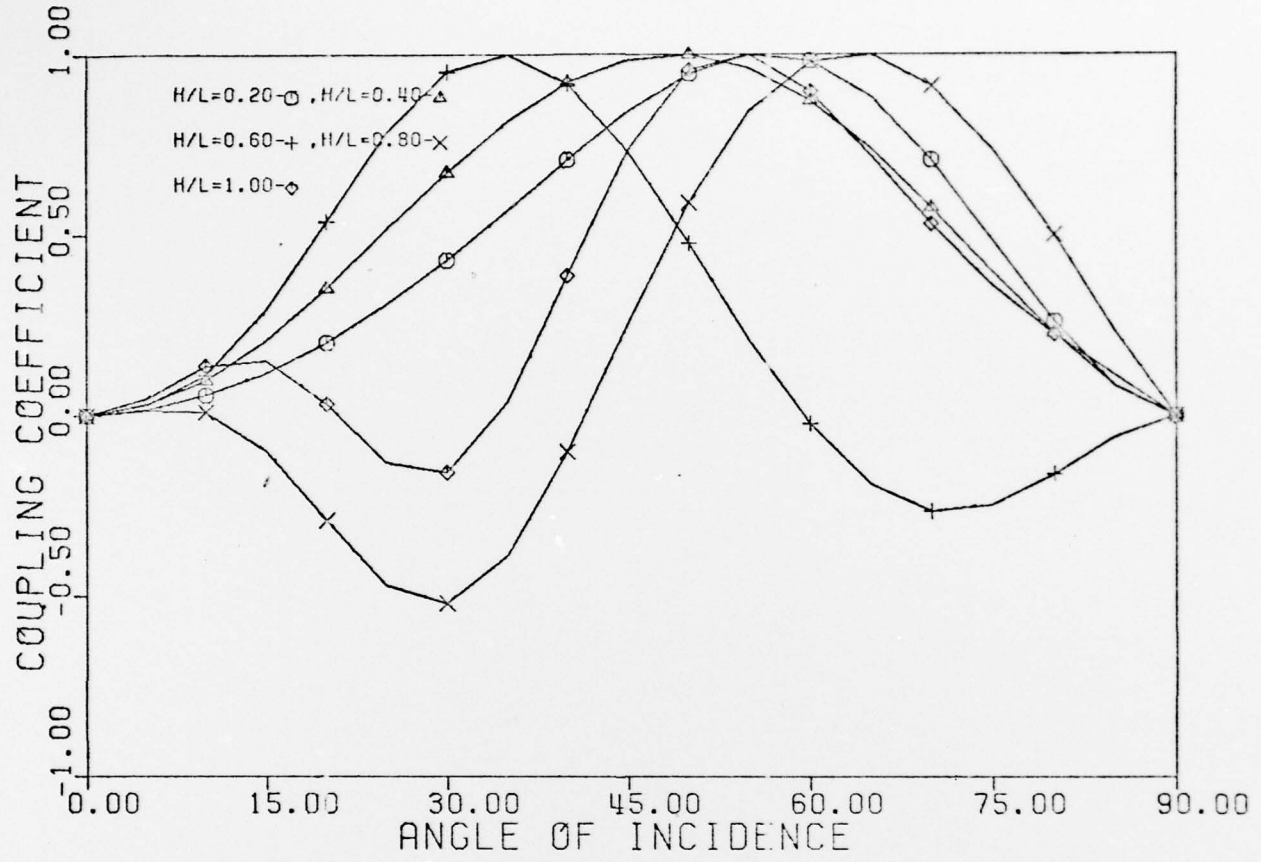


Figure 3-48. Real part of coupling coefficient for second self-resonant singularity, Y_{12}, as a function of scatterer height-to-length ratio, h/ℓ, and incident angle θ. The ground conductivity, σ, is 120.0, and the relative permittivity, ϵ_R, is unity

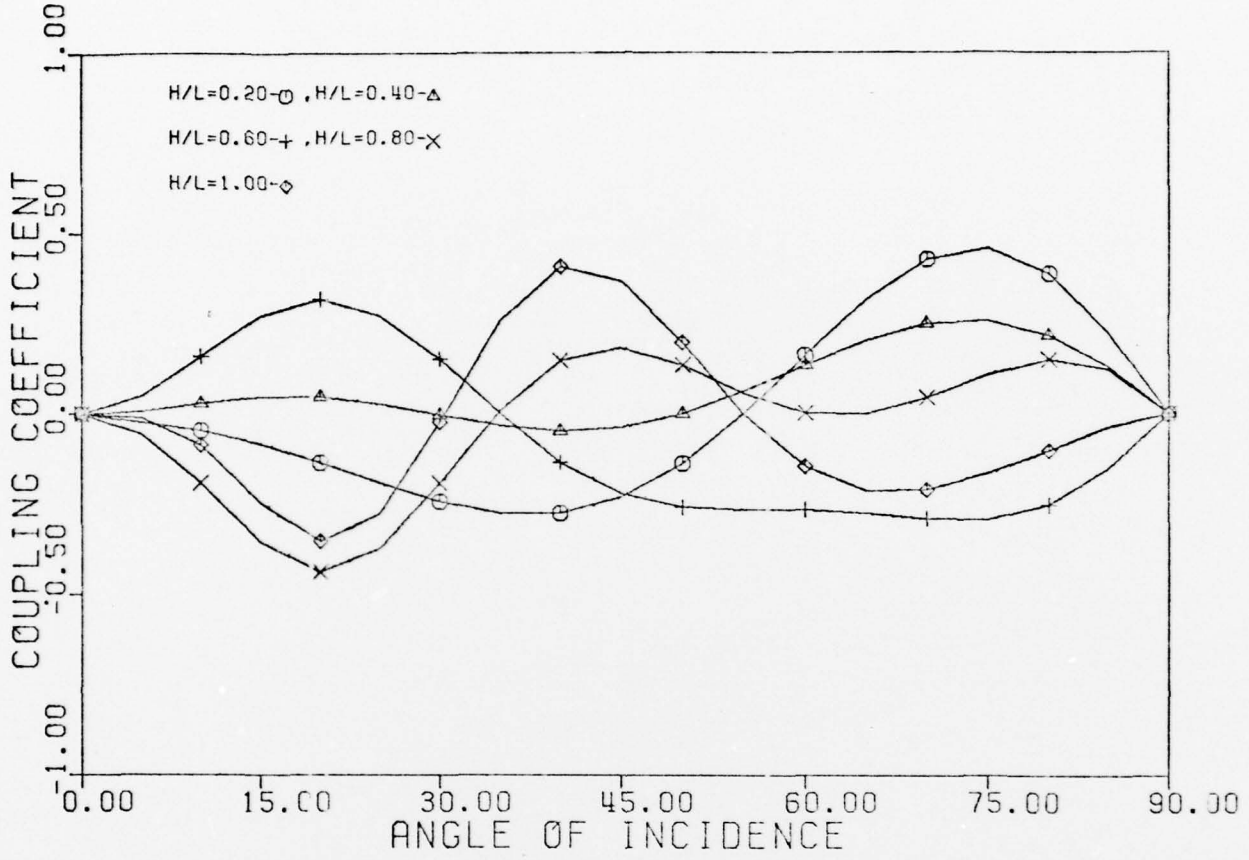


Figure 3-49. Imaginary part of coupling coefficient for second self-resonant singularity, γ_{12}, as a function of scatterer height-to-length ratio, h/ℓ, and incident angle θ. The ground conductivity, σ, is 120.0, and the relative permittivity, ε_R, is unity

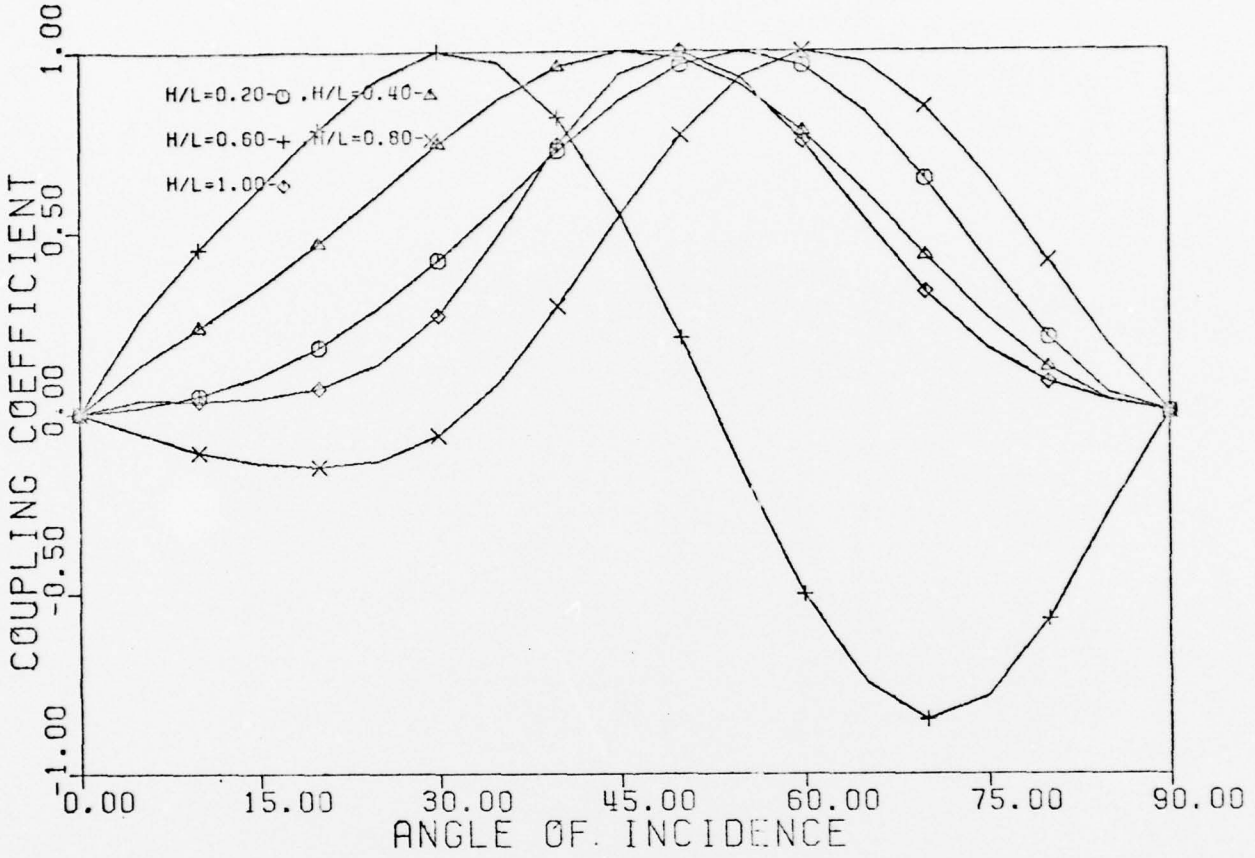


Figure 3-50. Real part of coupling coefficient for second self-resonant singularity, γ_{12}, as a function of scatterer height-to-length ratio, h/ℓ, and incident angle θ. The ground conductivity, σ, is 0.12, and the relative permittivity, ε_R, is unity

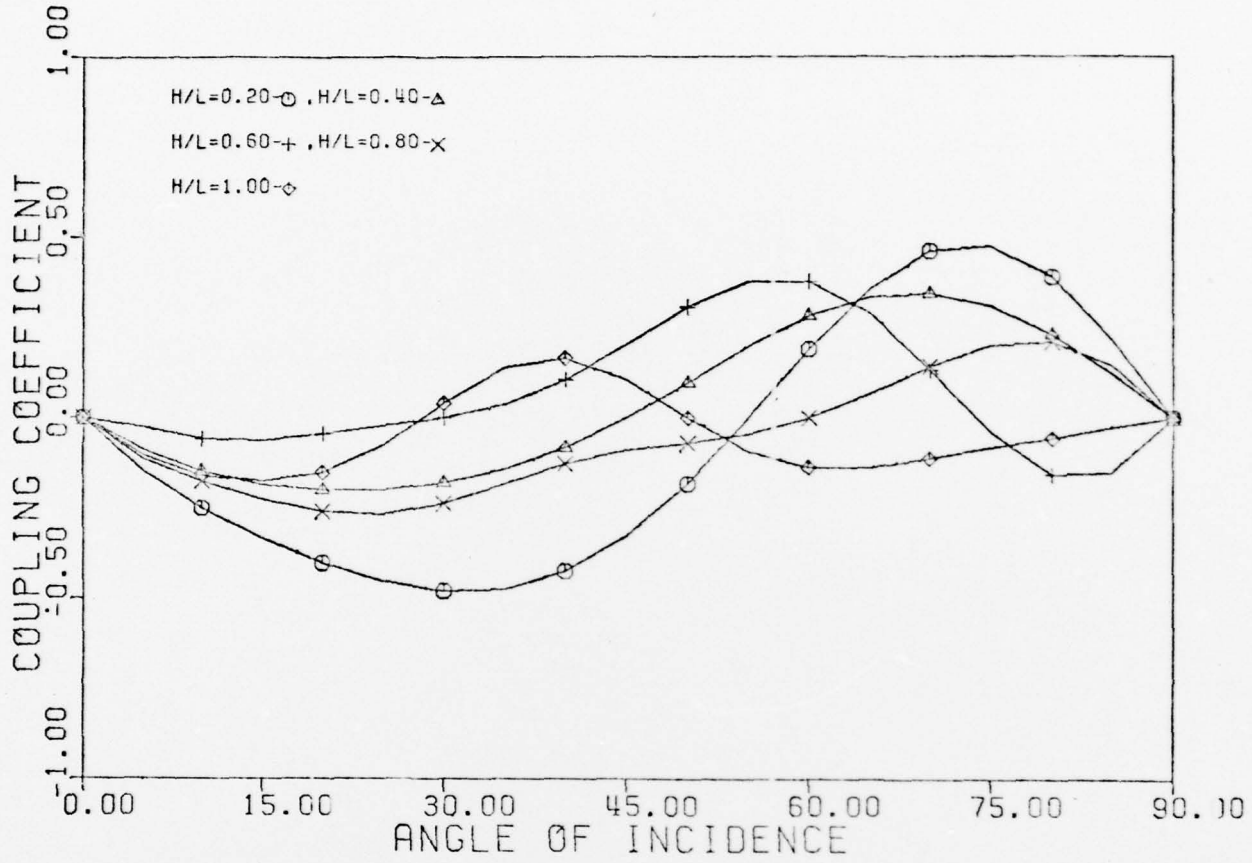


Figure 3-51. Imaginary part of coupling coefficient for second self-resonant singularity, γ_{12}, as a function of scatterer height-to-length ratio, h/ℓ, and incident angle θ. The ground conductivity, σ, is 0.12, and the relative permittivity, ε_R, is unity

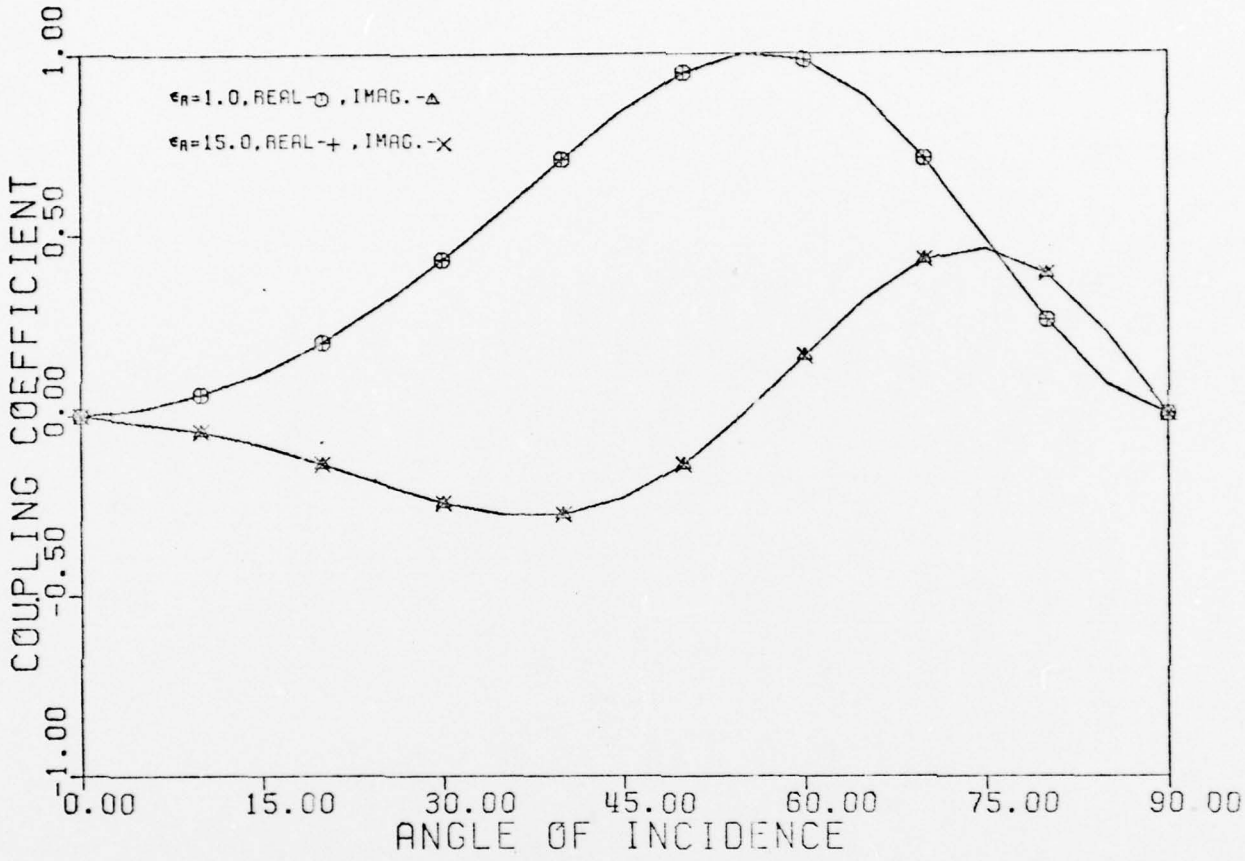


Figure 3-52. Coupling coefficient for second self-resonant singularity, γ_{12}, as a function of the ground plane relative permittivity, ϵ_R, and incident angle θ. The scatterer height-to-length ratio, h/ℓ, is 0.20, and the conductivity, σ, is 120.0

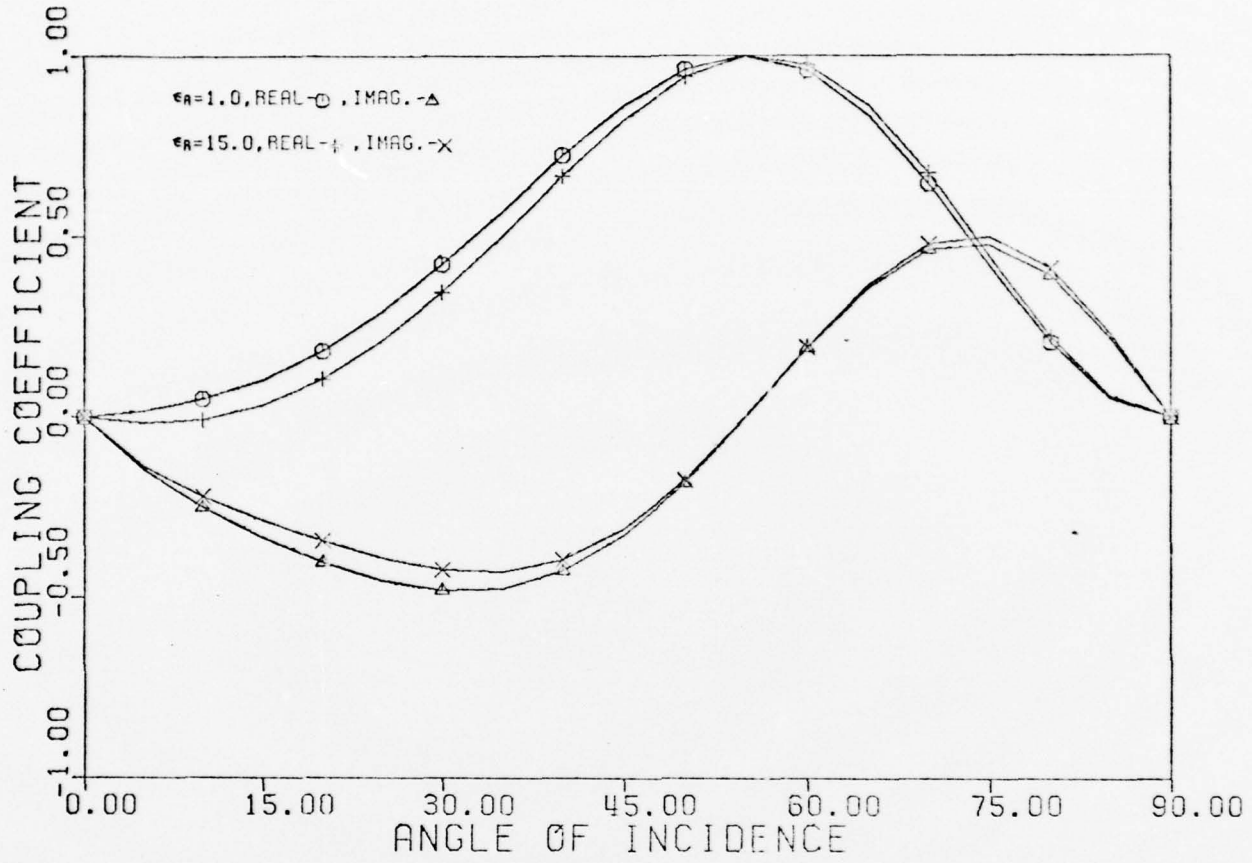


Figure 3-53. Coupling coefficient for second self-resonant singularity, γ_{12}, as a function of the ground plane relative permittivity, ε_R, and incident angle θ. The scatterer height-to-length ratio, h/ℓ, is 0.20, and the conductivity, σ, is 0.12

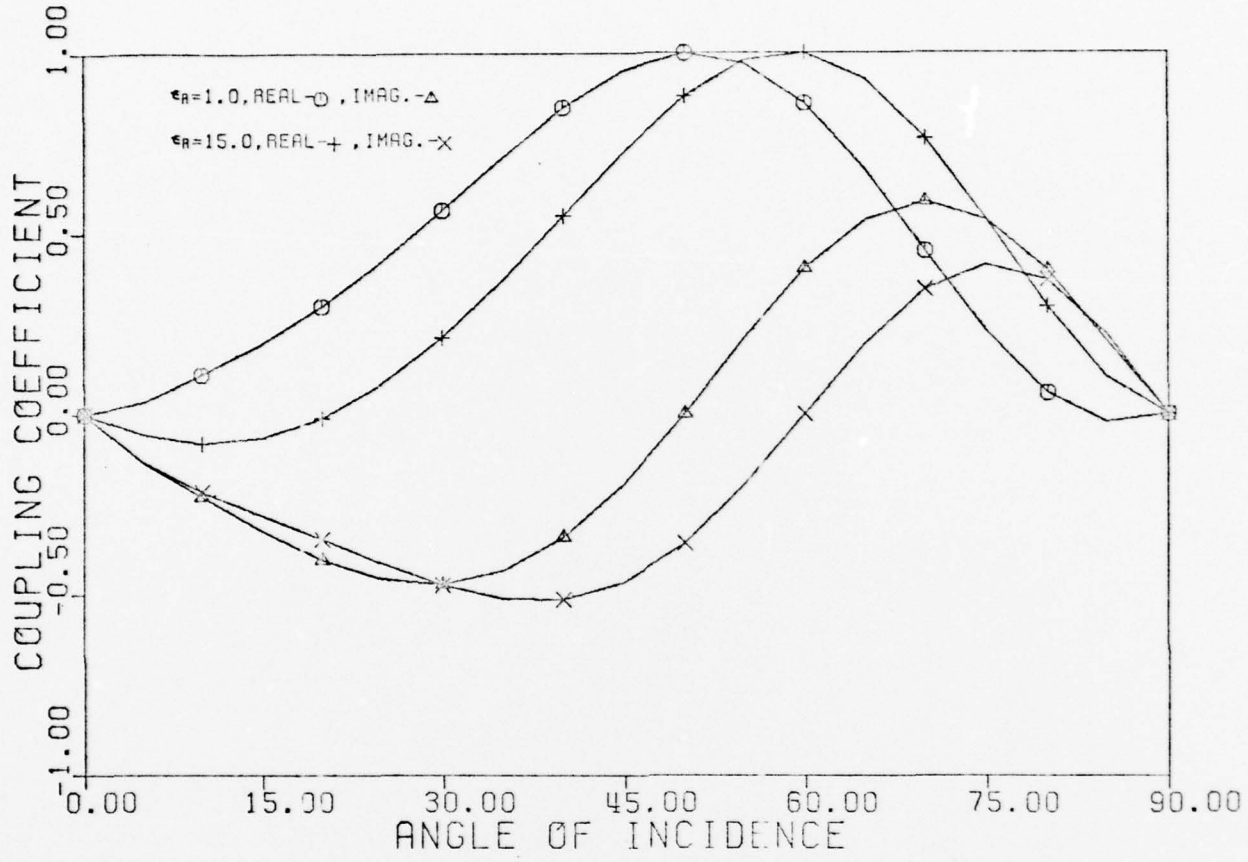


Figure 3-54. Coupling coefficient for second self-resonant singularity, γ_{12}, as a function of the ground plane relative permittivity, ϵ_R, and incident angle θ. The scatterer height-to-length ratio, h/ℓ, is 0.20, and the conductivity, σ, is 0.00012

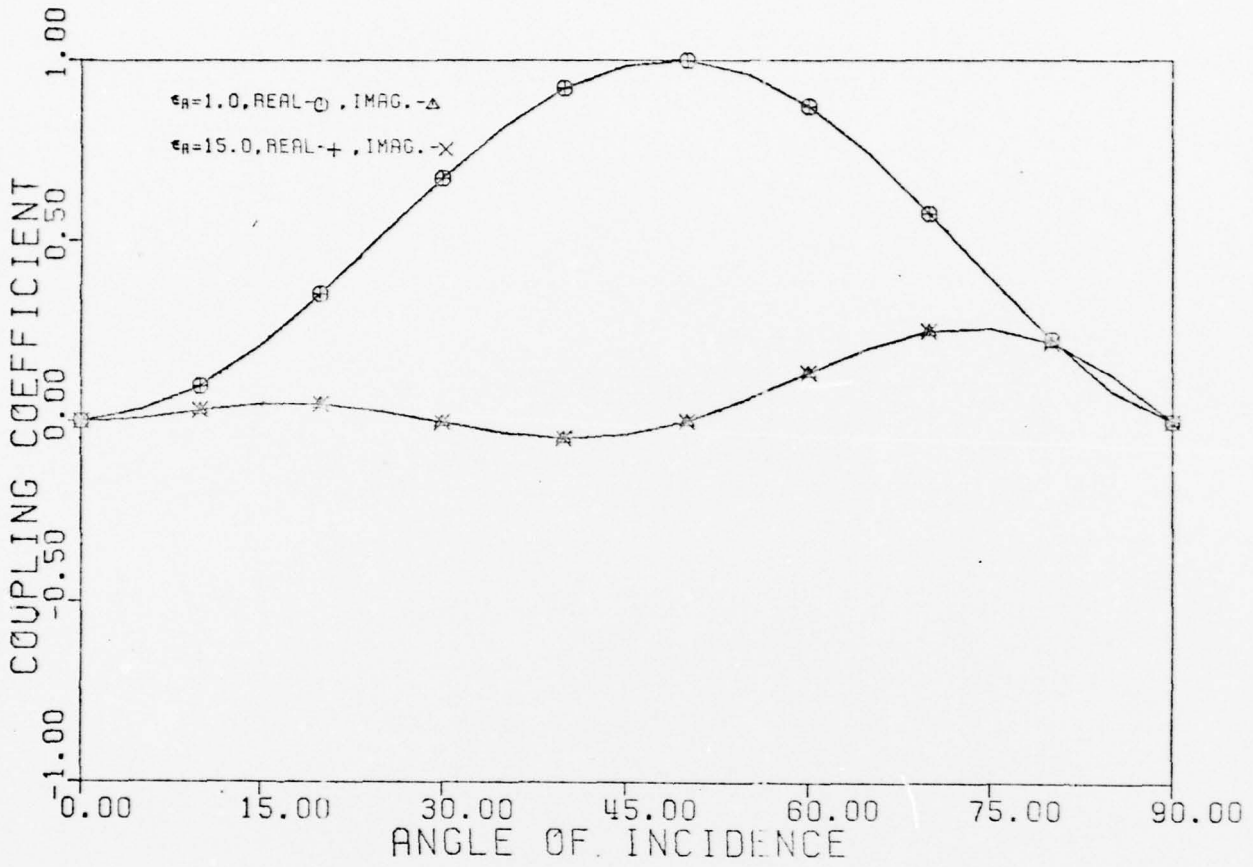


Figure 3-55. Coupling coefficient for second self-resonant singularity, γ_{12}, as a function of the ground plane relative permittivity, ε_R, and incident angle θ. The scatterer height-to-length ratio, h/ℓ, is 0.40, and the conductivity, σ, is 120.0

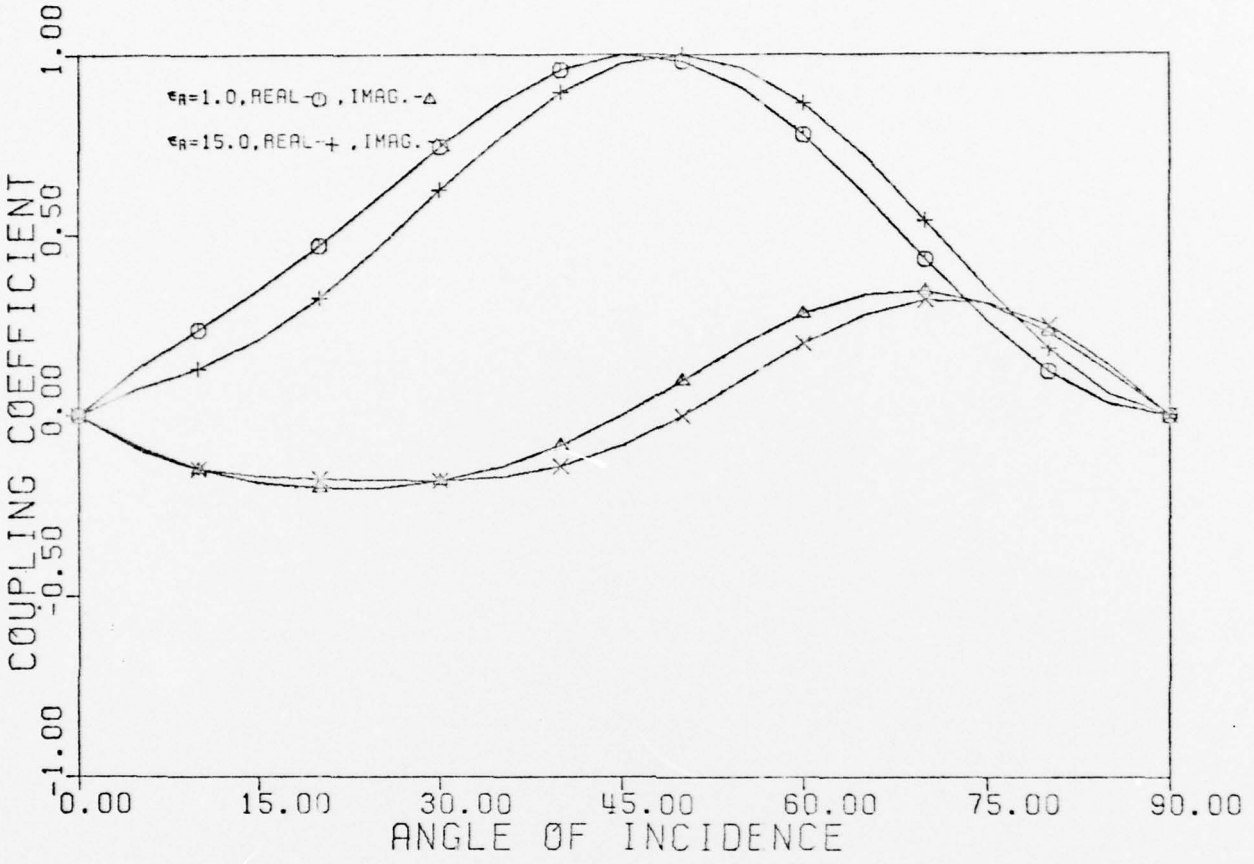


Figure 3-56. Coupling coefficient for second self-resonant singularity, γ_{12}, as a function of the ground plane relative permittivity, ε_R, and incident angle θ. The scatterer height-to-length ratio, h/ℓ, is 0.40, and the conductivity, σ, is 0.12

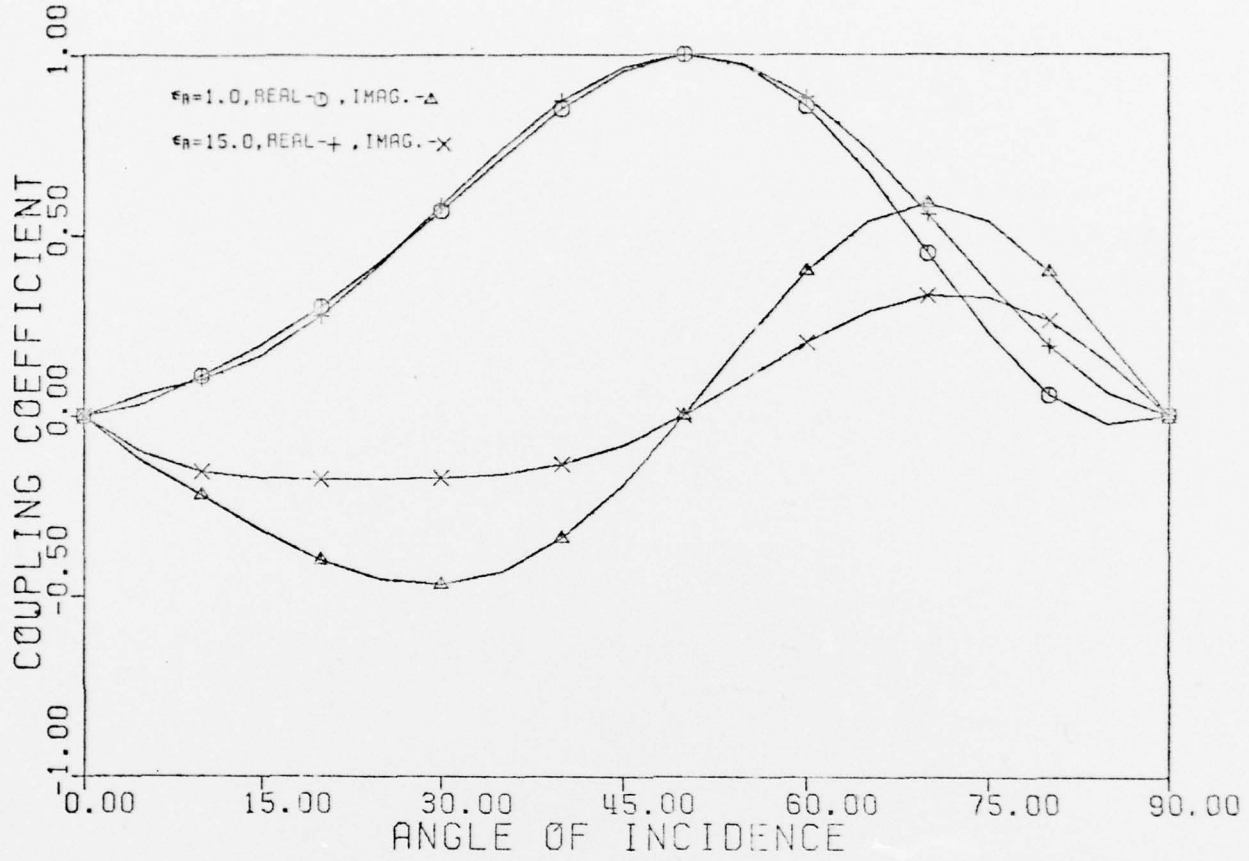


Figure 3-57. Coupling coefficient for second self-resonant singularity, γ_{12}, as a function of the ground plane relative permittivity, ϵ_R, and incident angle θ. The scatterer height-to-length ratio, h/ℓ, is 0.40, and the conductivity, σ, is 0.00012

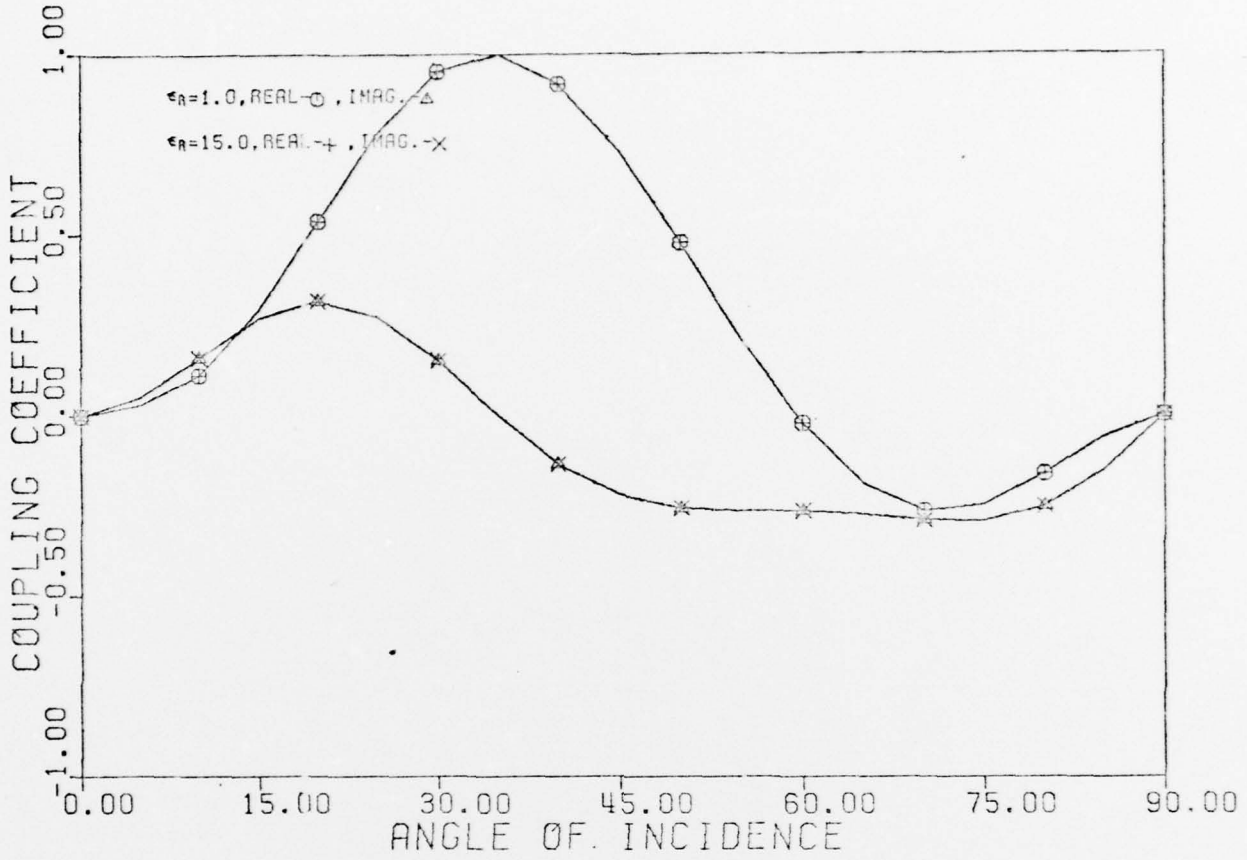


Figure 3-58. Coupling coefficient for second self-resonant singularity, γ_{12}, as a function of the ground plane relative permittivity, ϵ_R, and incident angle θ. The scatterer height-to-length ratio, h/ℓ, is 0.60, and the conductivity, σ, is 120.0

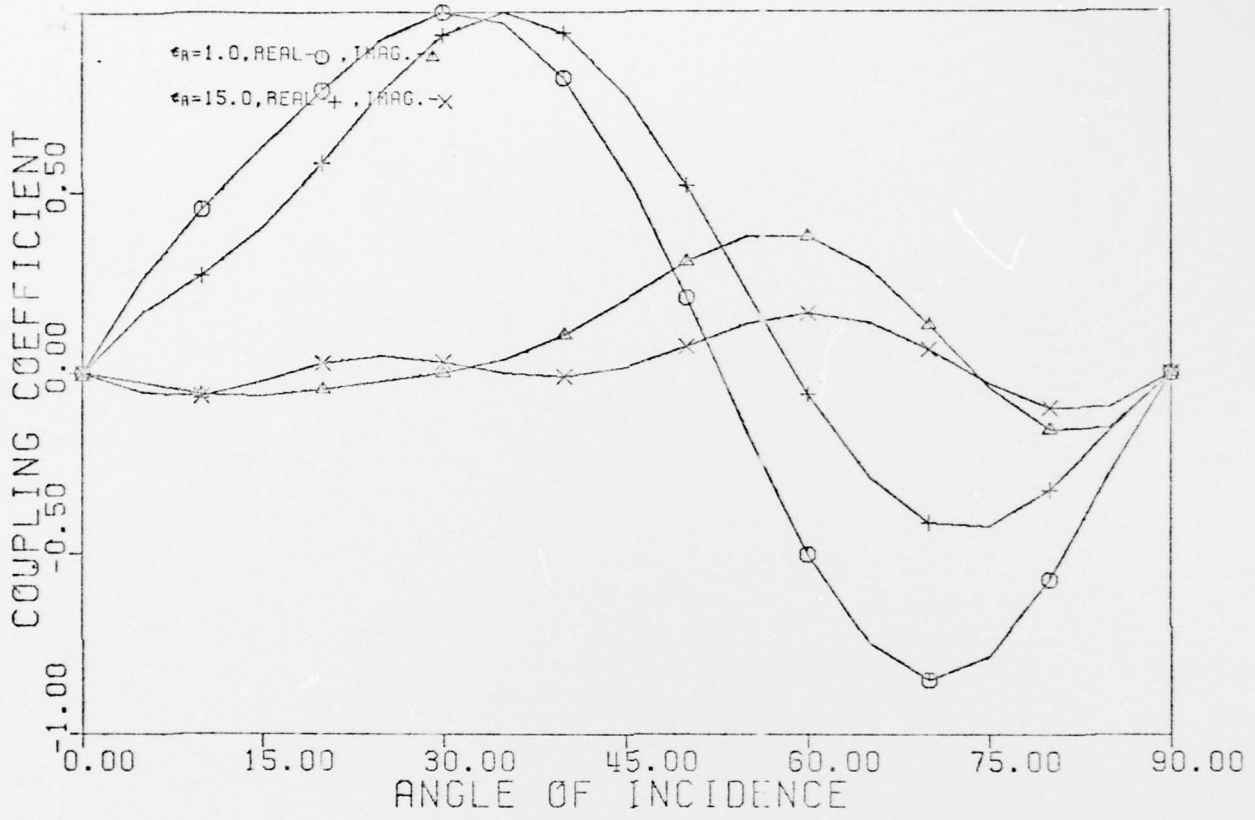


Figure 3-59. Coupling coefficient for second self-resonant singularity, Y_{12}, as a function of the ground plane relative permittivity, ϵ_R, and incident angle θ. The scatterer height-to-length ratio, h/ℓ, is 0.60, and the conductivity, σ, is 0.12

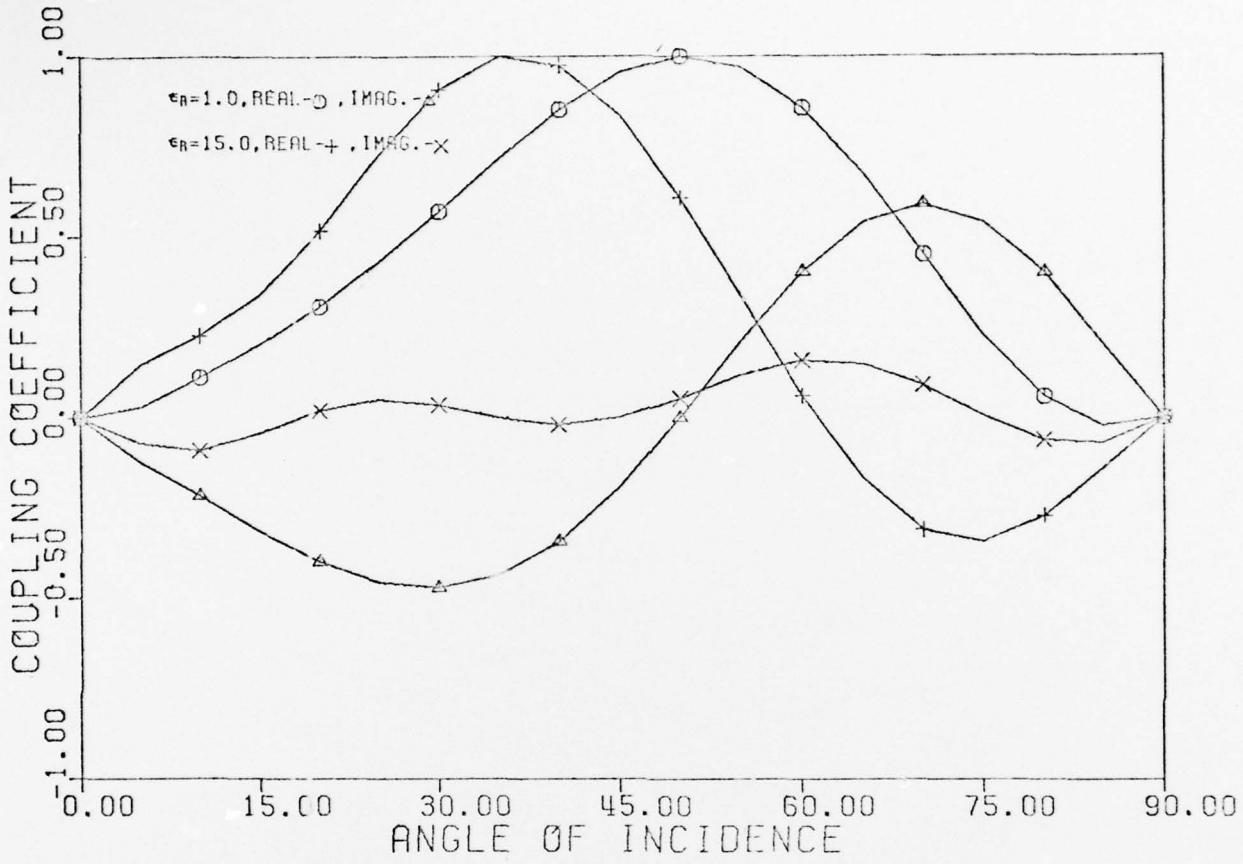


Figure 3-60. Coupling coefficient for second self-resonant singularity, γ_{12}, as a function of the ground plane relative permittivity, ε_R, and incident angle θ. The scatterer height-to-length ratio, h/ℓ, is 0.60, and the conductivity, σ, is 0.00012

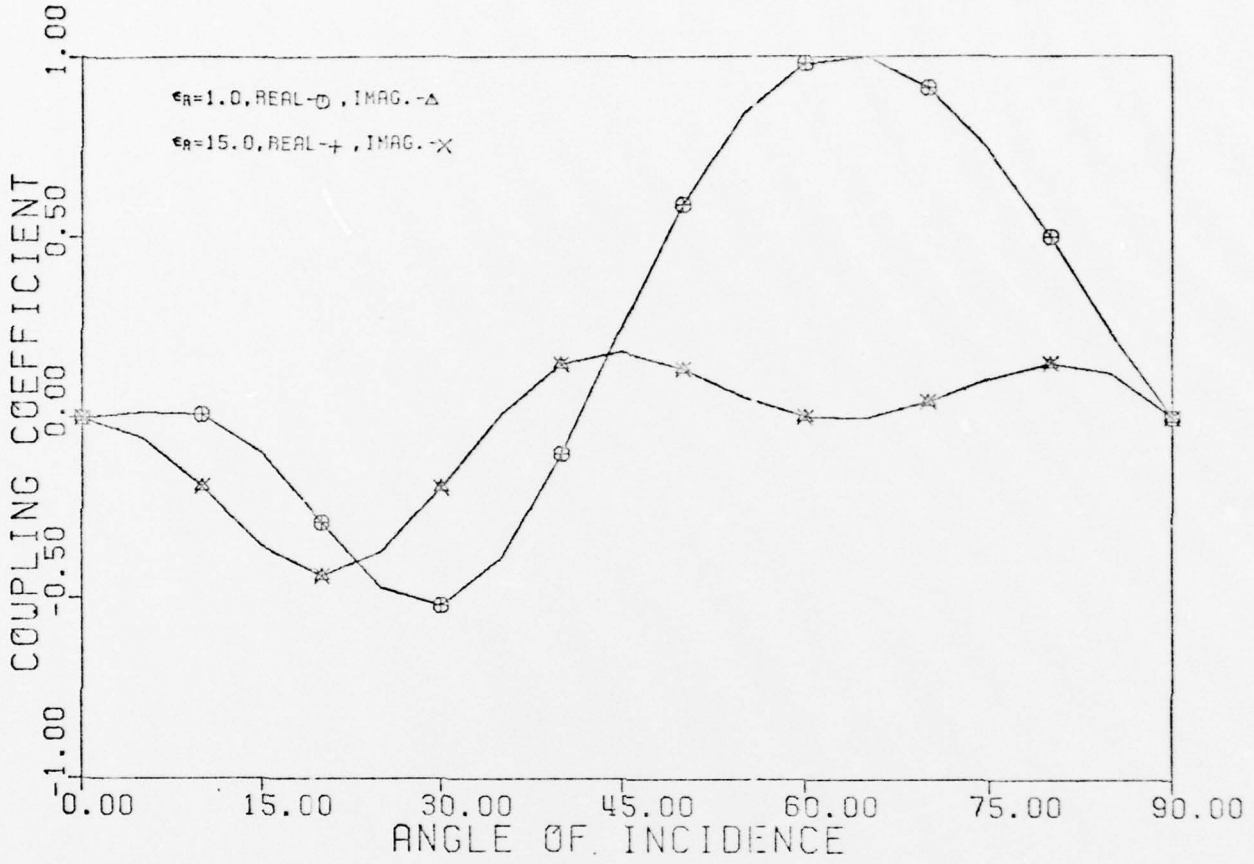


Figure 3-61. Coupling coefficient for second self-resonant singularity, γ_{12}, as a function of the ground plane re ative permittivity, ε_R, and incident angle θ. The scatterer height-to-length ratio, h/ℓ, is 0.80, and the conductivity, σ, is 120.0

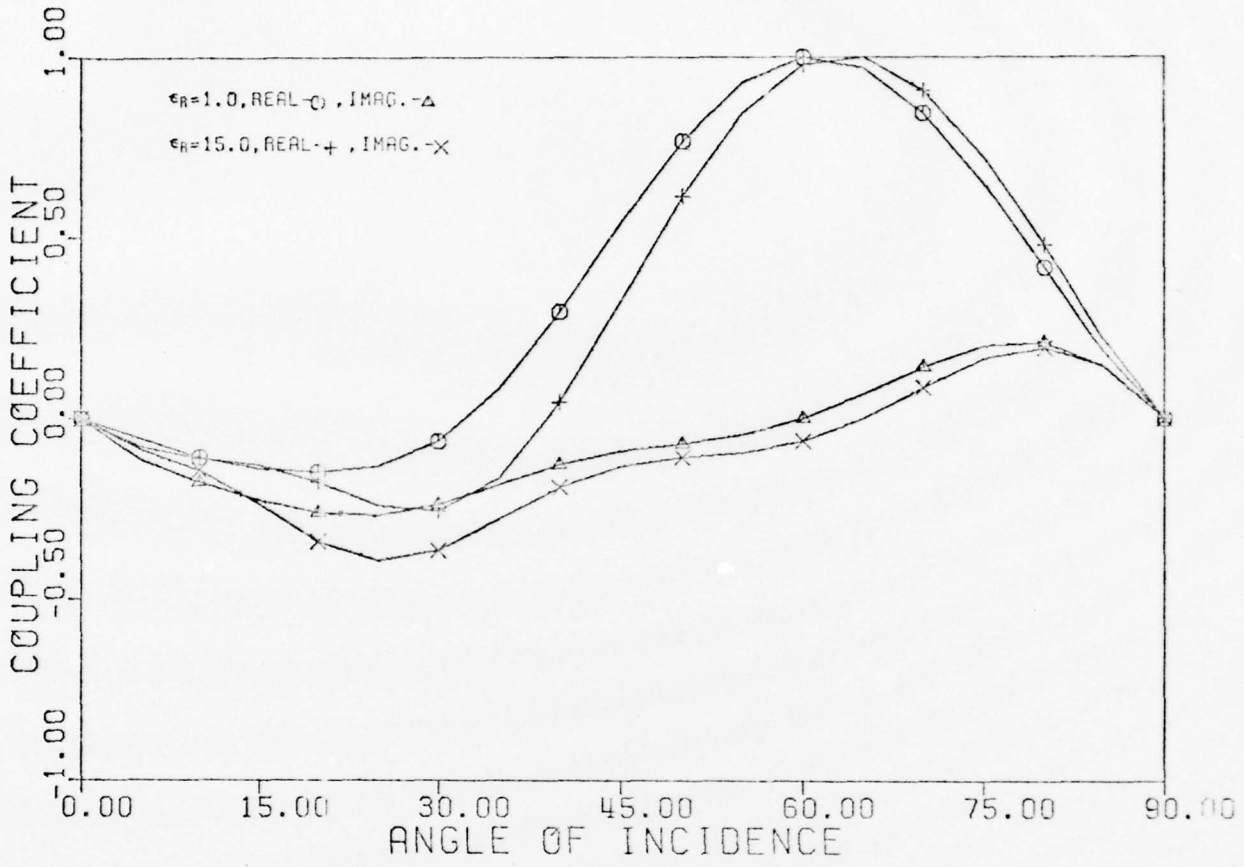


Figure 3-62. Coupling coefficient for second self-resonant singularity, γ_{12}, as a function of the ground plane relative permittivity, ϵ_R, and incident angle θ. The scatterer height-to-length ratio, h/ℓ, is 0.80, and the conductivity, σ, is 0.12

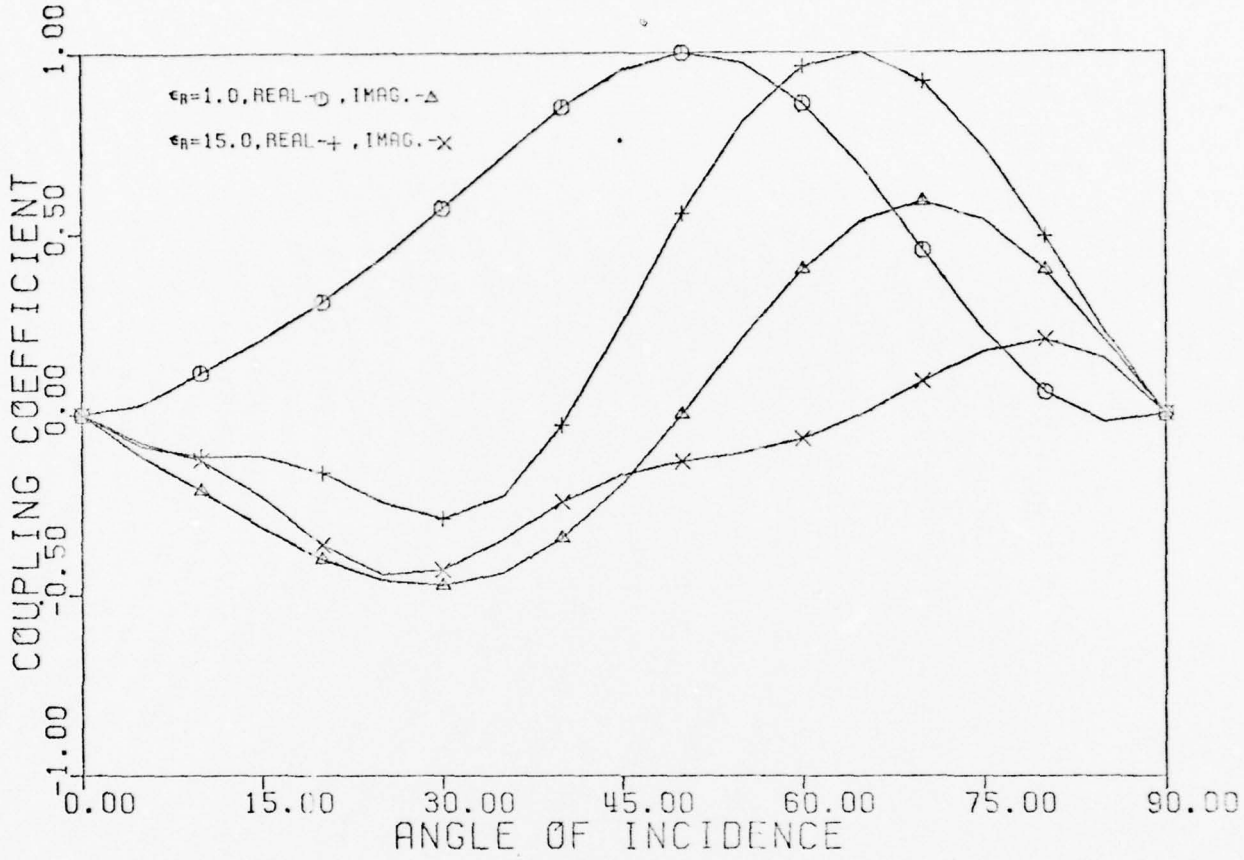


Figure 3-63. Coupling coefficient for second self-resonant singularity, γ_{12}, as a function of the ground plane relative permittivity, ε_R, and incident angle θ. The scatterer height-to-length ratio, h/ℓ, is 0.80, and the conductivity, σ, is 0.00012

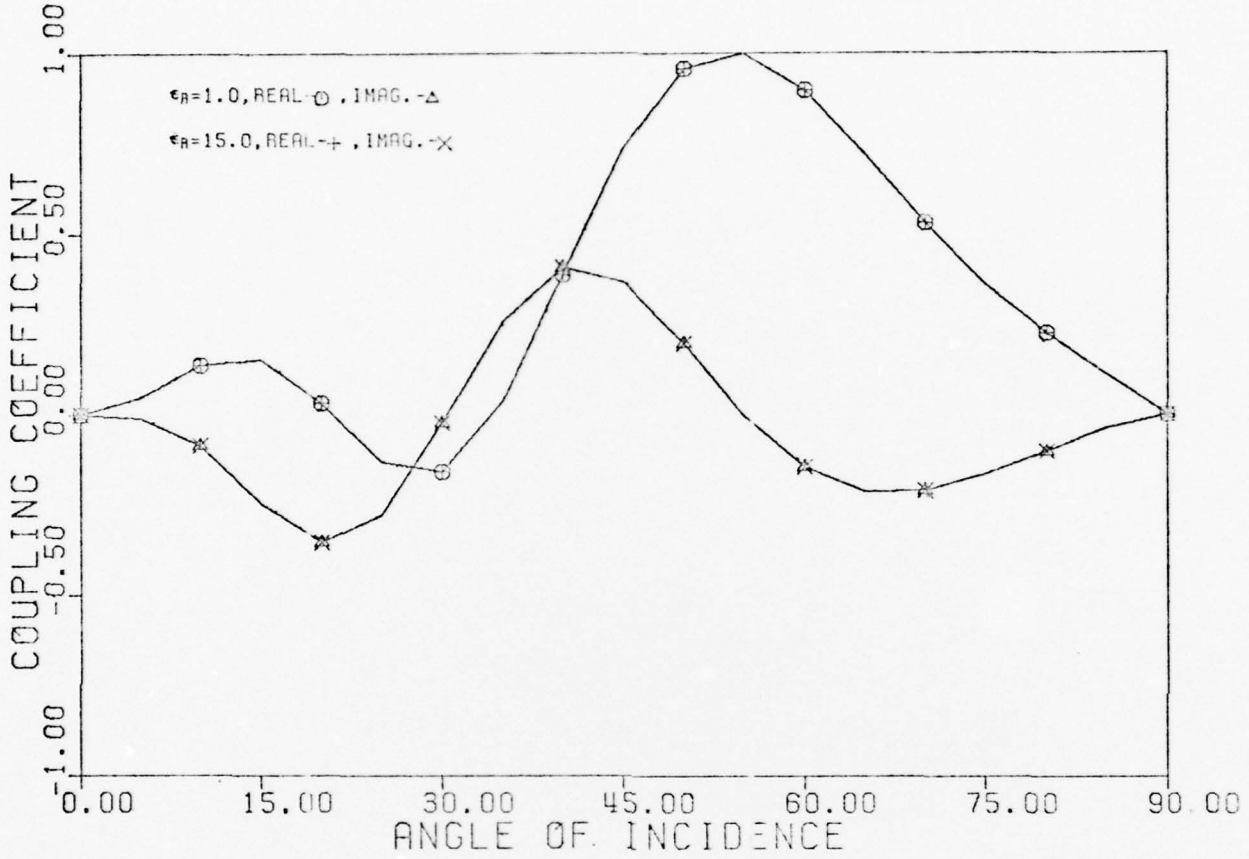


Figure 3-64. Coupling coefficient for second self-resonant singularity, Y_{12}, as a function of the ground plane relative permittivity, ϵ_R, and incident angle θ. The scatterer height-to-length ratio, h/ℓ, is 1.0, and the conductivity, σ, is 120.0

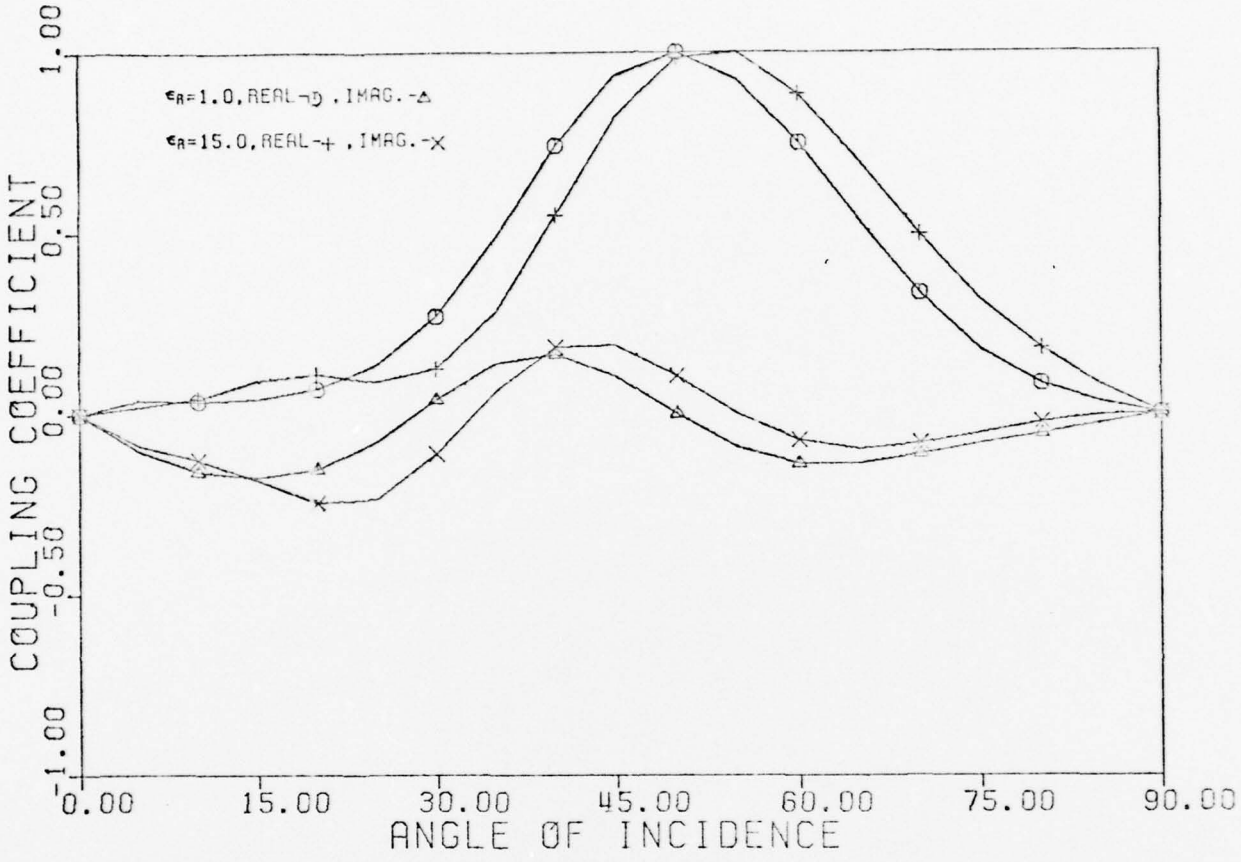


Figure 3-65. Coupling coefficient for second self-resonant singularity, γ_{12}, as a function of the ground plane relative permittivity, ϵ_R, and incident angle θ. The scatterer height-to-length ratio, h/ℓ, is 1.0, and the conductivity, σ, is 0.12

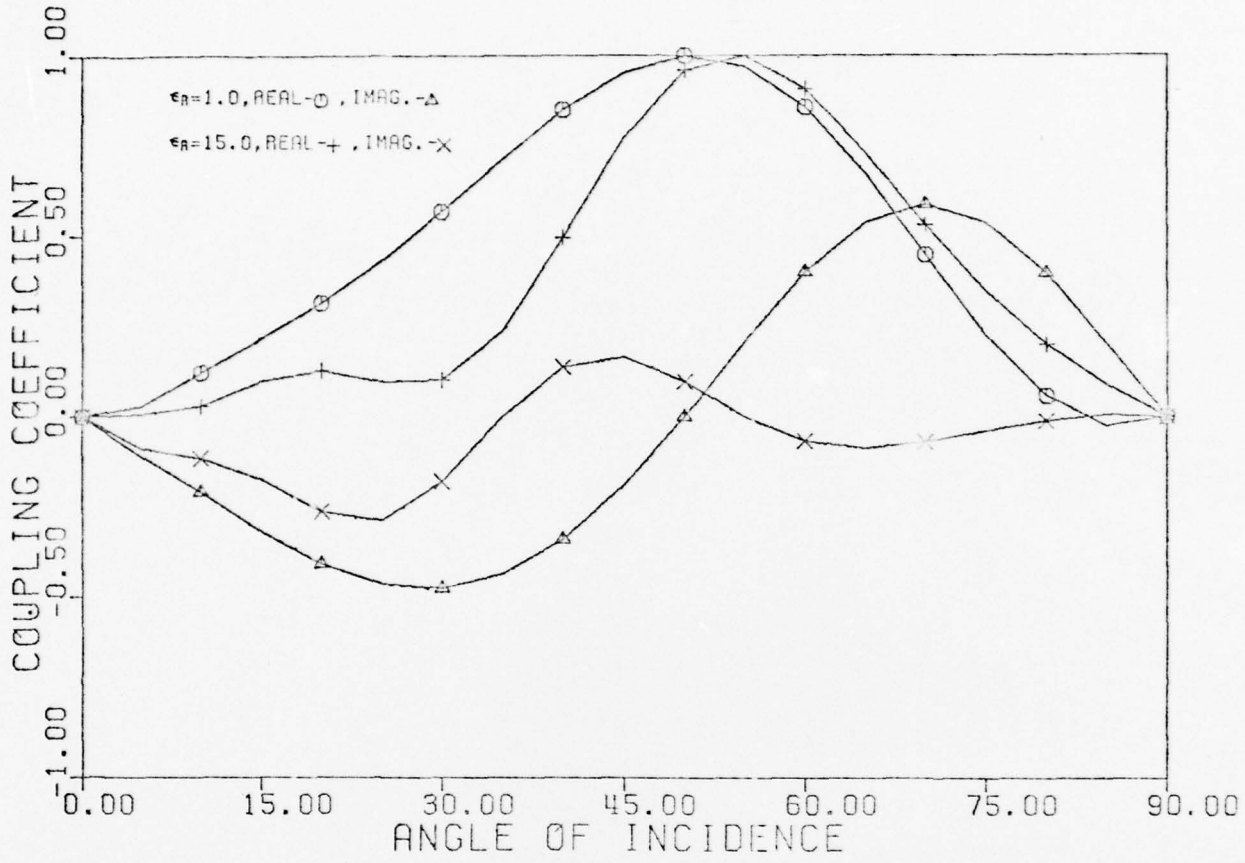


Figure 3-66. Coupling coefficient for second self-resonant singularity, γ_{12}, as a function of the ground plane relative permittivity, ϵ_R, and incident angle θ. The scatterer height-to-length ratio, h/ℓ, is 1.0, and the conductivity, σ, is 0.00012

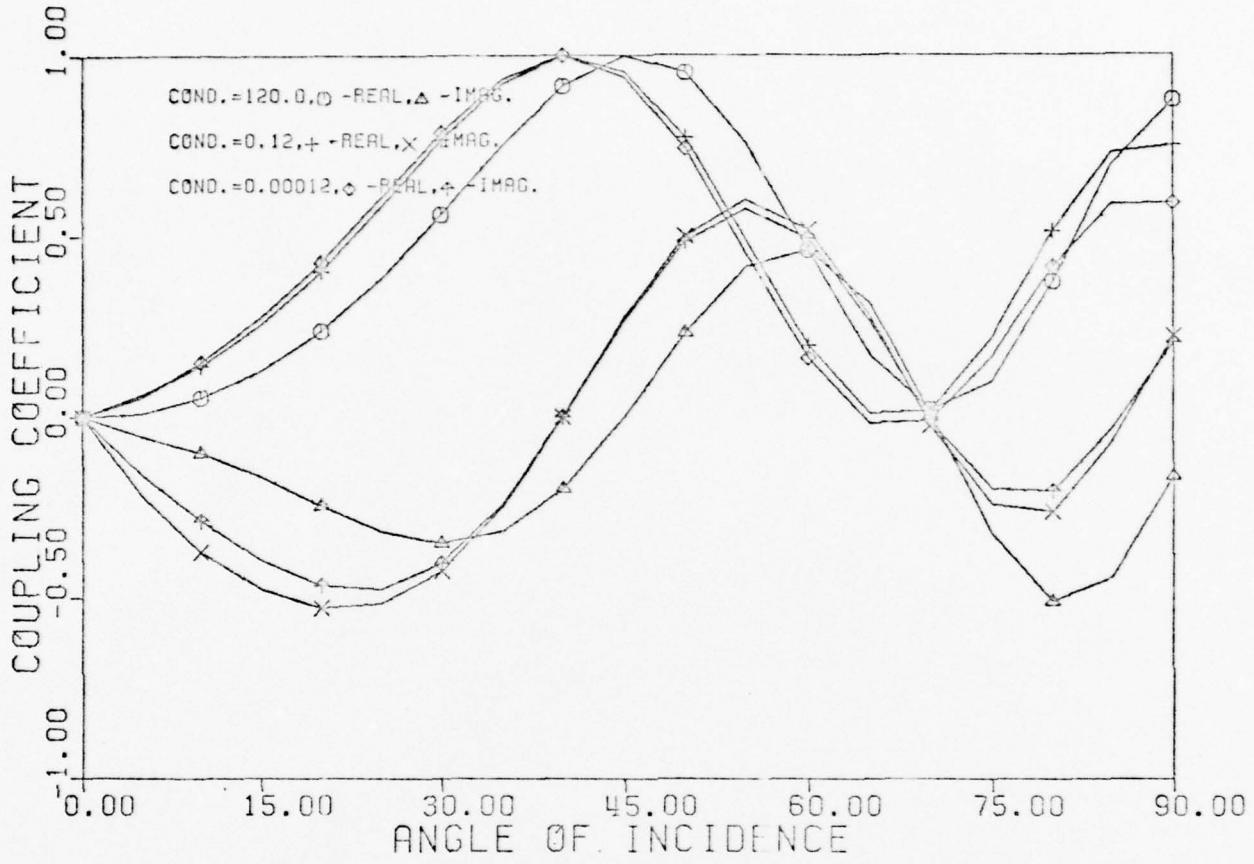


Figure 3-67. Coupling coefficient for third self-resonant singularity, γ_{13}, as a function of conductivity, σ and incident angle θ. The scatterer height-to-length ratio, h/ℓ, is 0.10, and the relative permittivity, ϵ_R, is unity

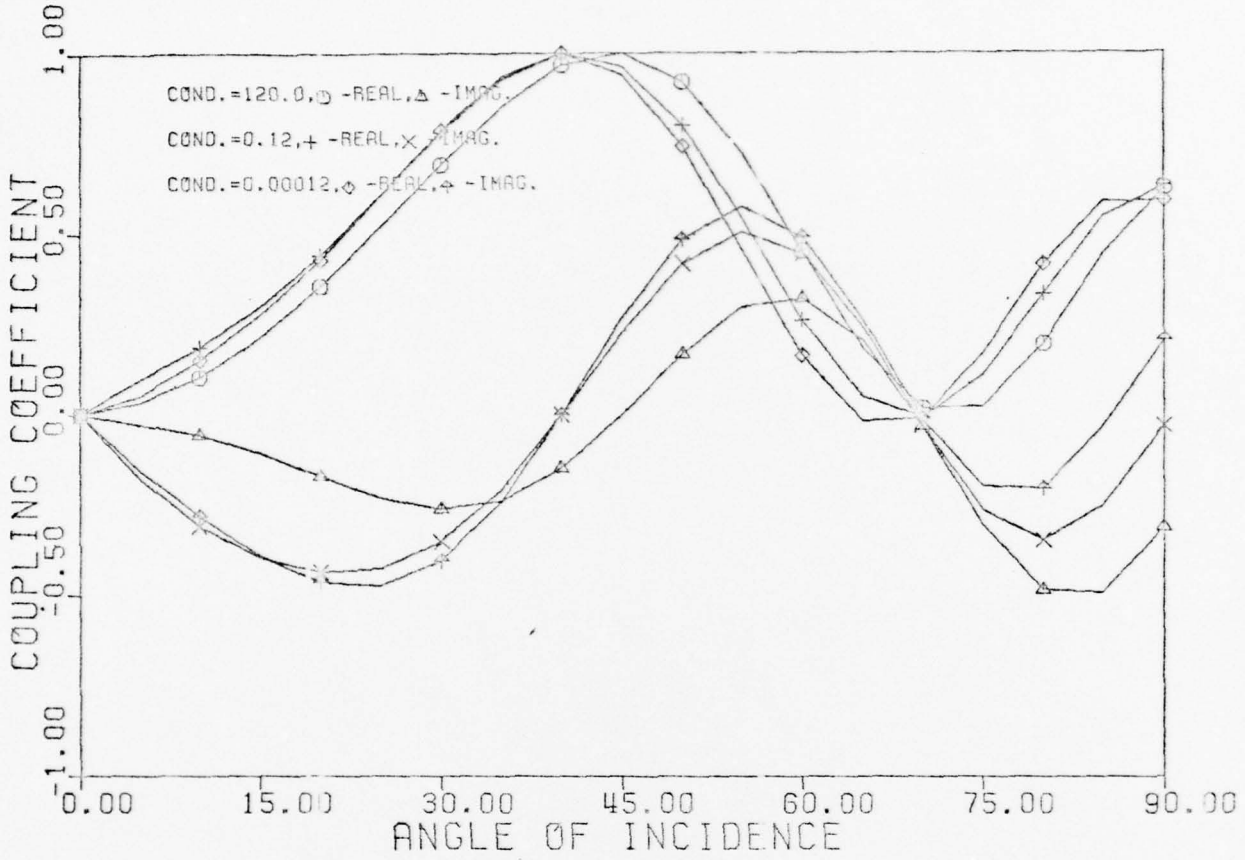


Figure 3-68. Coupling coefficient for third self-resonant singularity, γ_{13}, as a function of conductivity, σ, and incident angle θ. The scatterer height-to-length ratio, h/ℓ, is 0.20, and the relative permittivity, ϵ_R, is unity

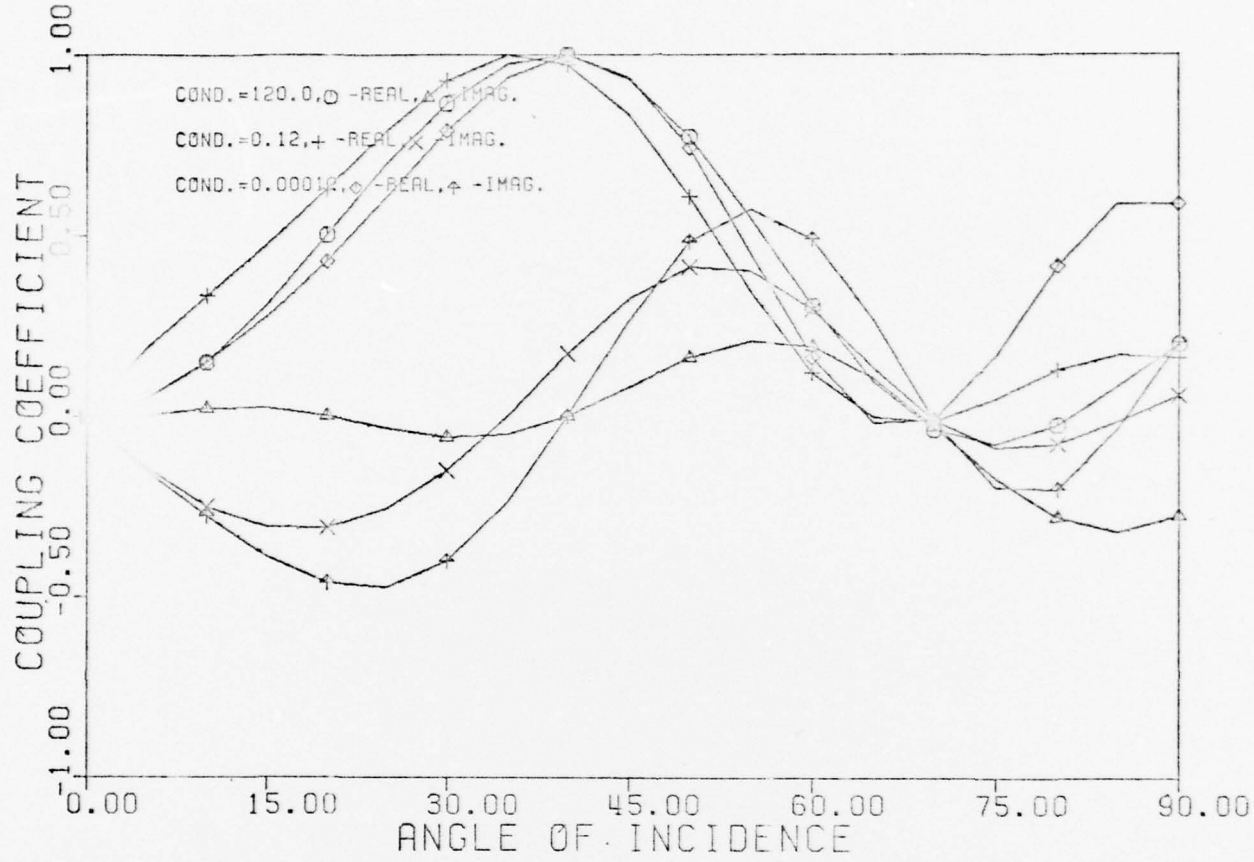


Figure 3-69. Coupling coefficient for third self-resonant singularity, γ_{13}, as a function of conductivity, σ, and ircident angle θ. The scatterer height-to-length ratio, h/ℓ, is 0.30, and the relative permittivity, ε_R, is unity

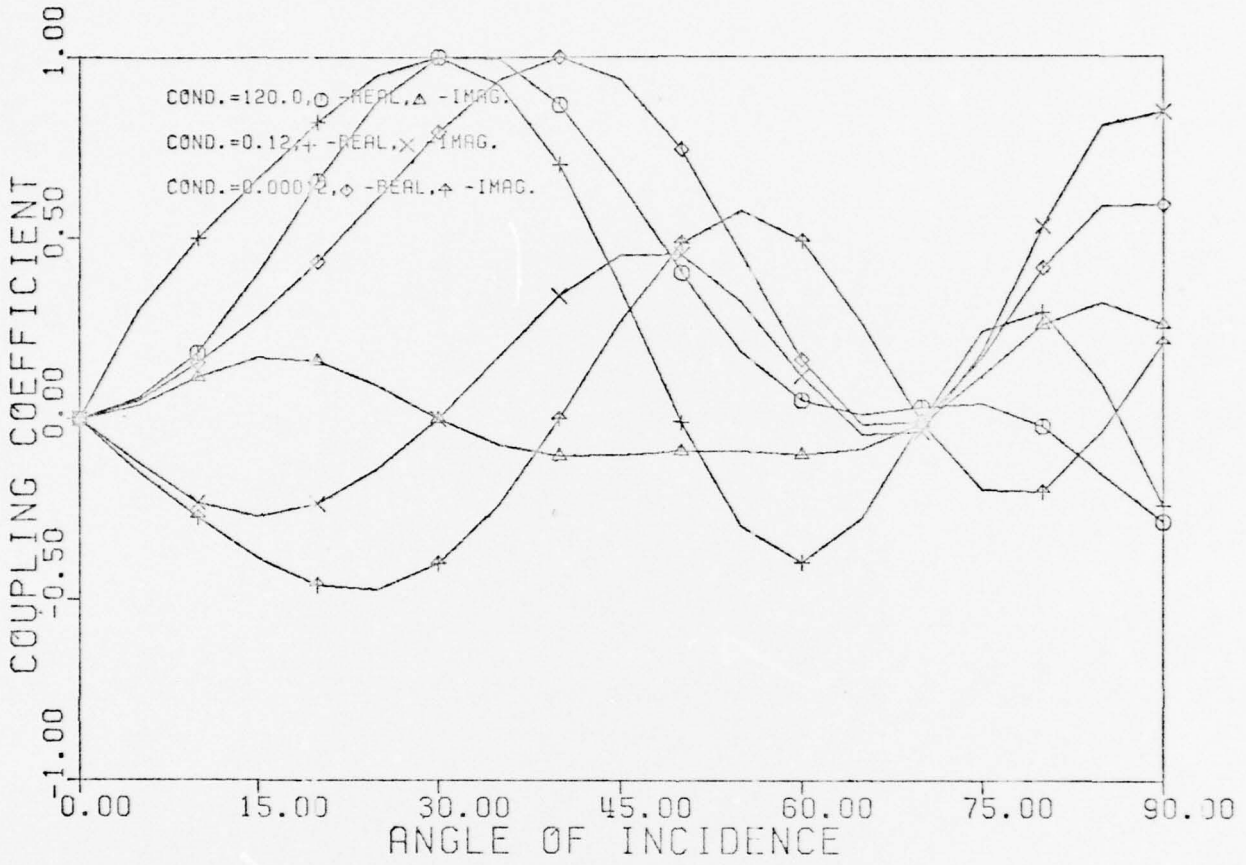


Figure 3-70. Coupling coefficient for third self-resonant singularity, γ_{13}, as a function of conductivity, σ, and incident angle θ. The scatterer height-to-length ratio, h/ℓ, is 0.40, and the relative permittivity, ϵ_R, is unity

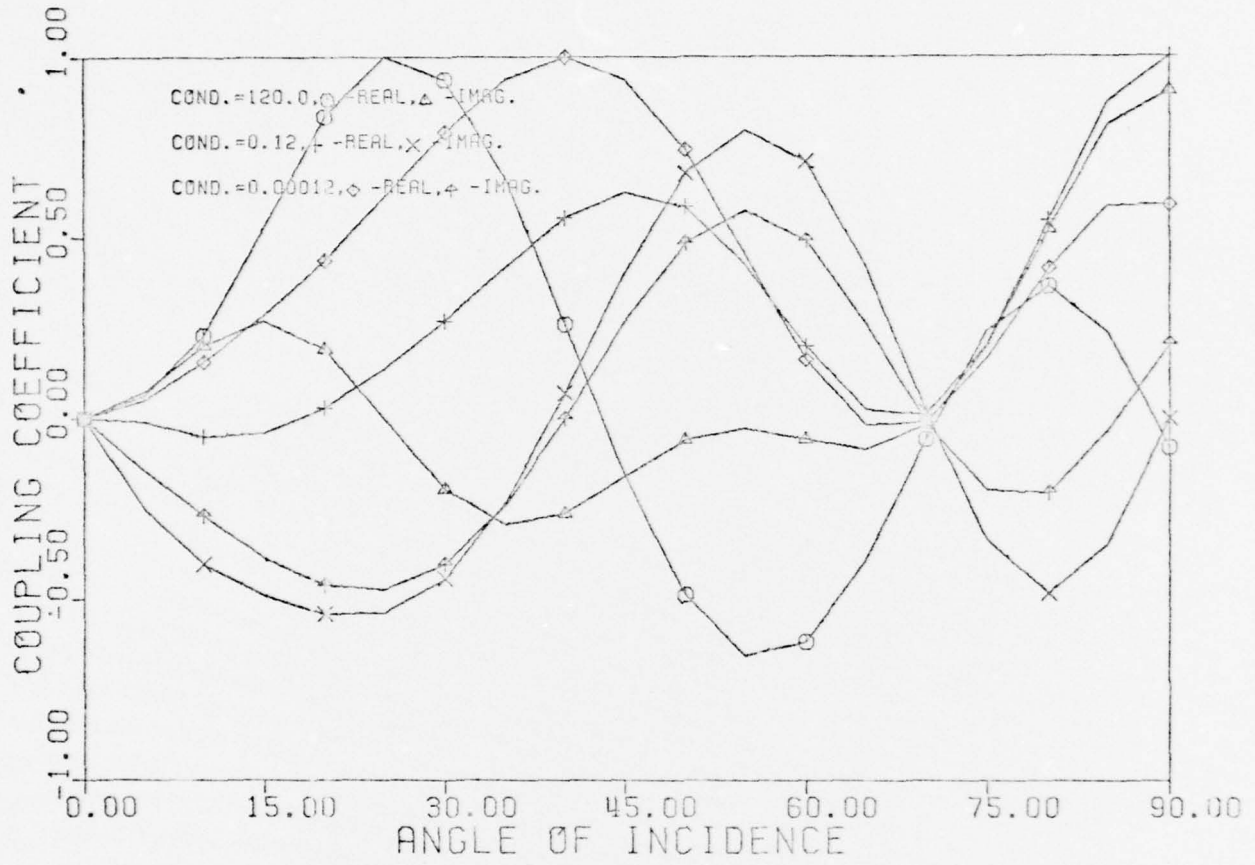


Figure 3-71. Coupling coefficient for third self-resonant singularity, γ_{13}, as a function of conductivity, σ, and incident angle θ. The scatterer height-to-length ratio, h/ℓ, is 0.50, and the relative permittivity, ε_R, is unity

Table 3-3. Predicted angle of incidence for maximum coupling using the "standing wave analogy." The table applies to Figures 3-67 through 3-71 for large conductivity, (σ = 120.0), and unity permittivity, (ε_R = 1.0)

FIGURE	h/ℓ	$Im(\gamma_{11}) = \frac{\omega \ell}{C}$	$\beta h = \frac{2\pi h}{\lambda}$	cosθ=0	$\tan[\beta h \sin\theta] + \beta h \sin\theta = 0$
3-67	0.1	8.725	0.873	90°	NO SOLUTION
3-68	0.2	8.675	1.730	90°	NO SOLUTION
3-69	0.3	8.775	2.630	90°	50.0°<θ<50.5°
3-70	0.4	8.875	3.550	90°	34.5°<θ<35.0°
3-71	0.5	8.875	4.440	90°	27.0°<θ<27.5°

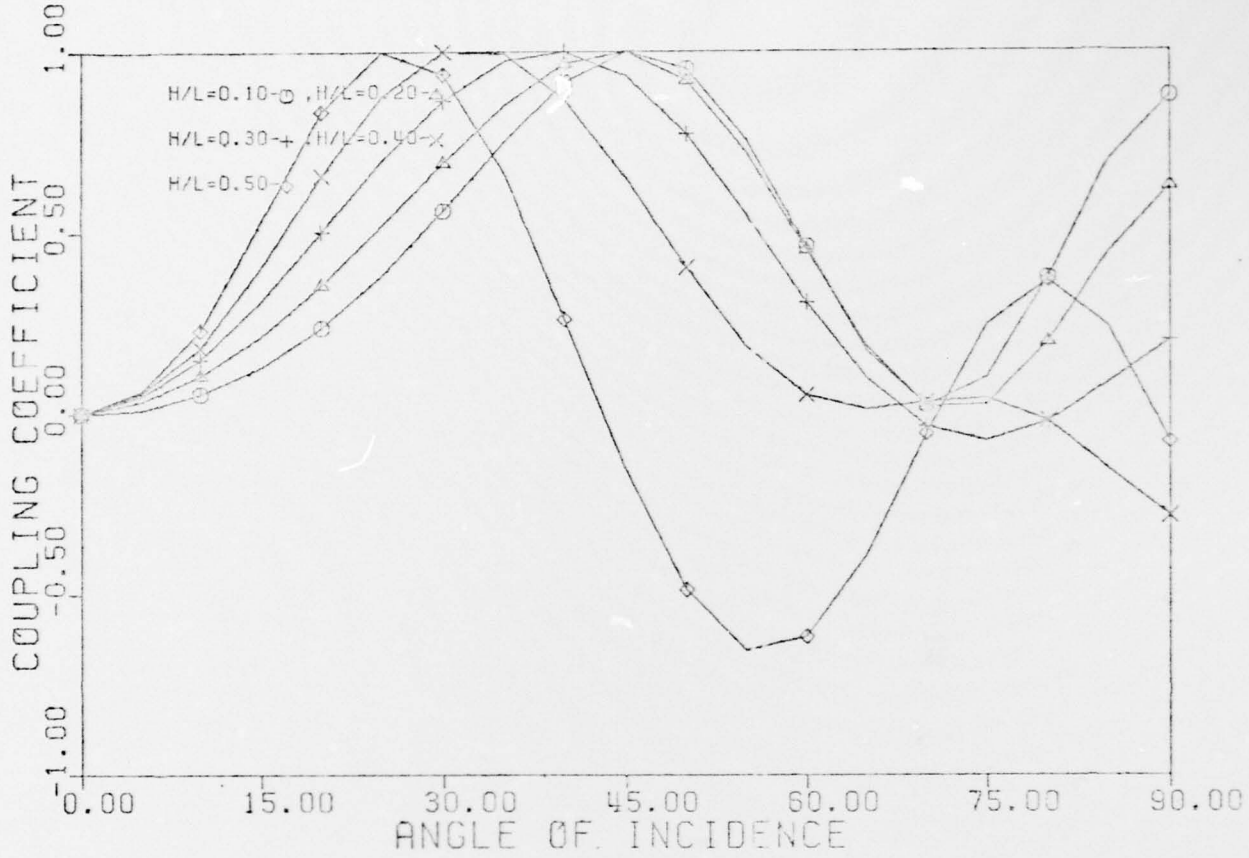


Figure 3-72. Real part of coupling coefficient for third self-resonant singularity, γ_{13}, as a function of scatterer height-to-length ratio, h/ℓ, and incident angle θ. The ground conductivity, σ, is 120.0, and the relative permittivity, ε_R, is unity

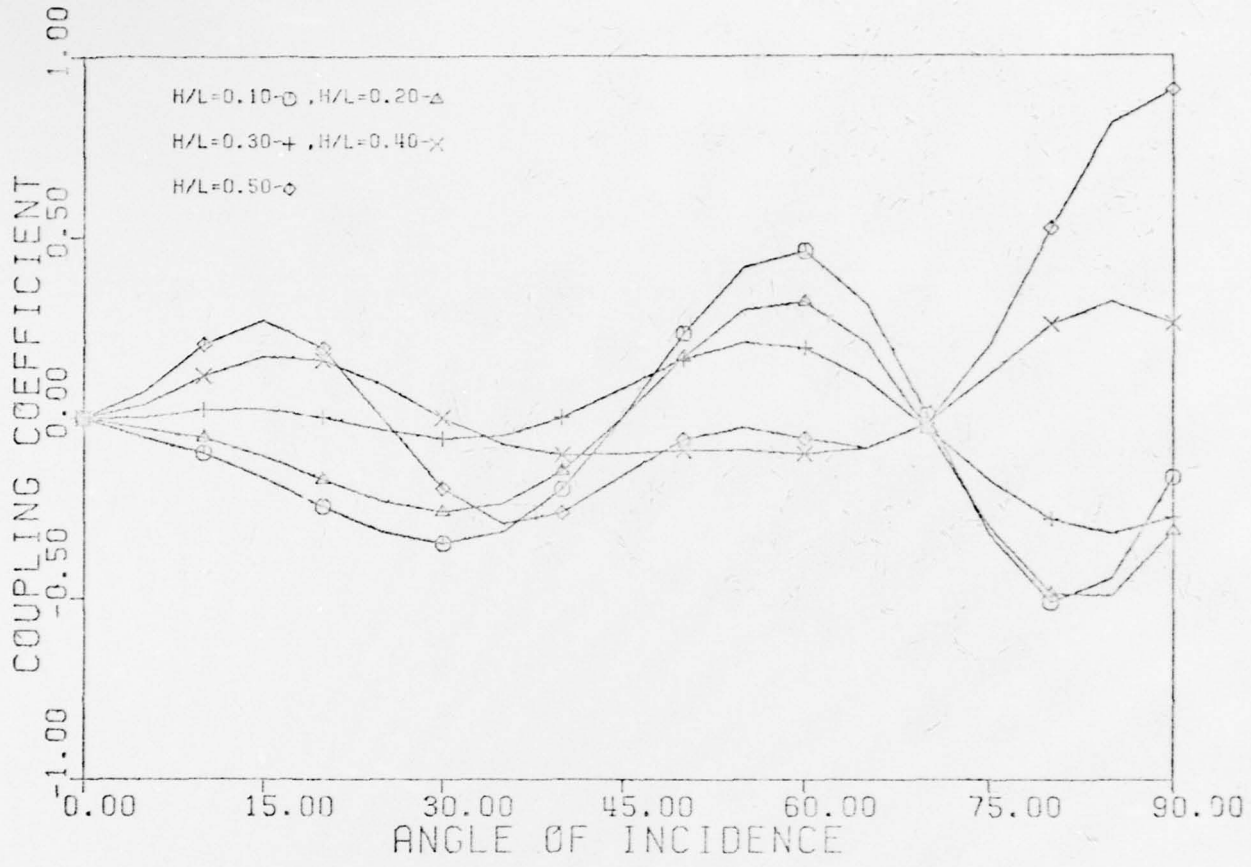


Figure 3-73. Imaginary part of coupling coefficient for third self-resonant singularity, γ_{13}, as a function of scatterer height-to-length ratio, h/ℓ, and incident angle θ. The ground conductivity, σ, is 120.0, and the relative permittivity, ε_R, is unity

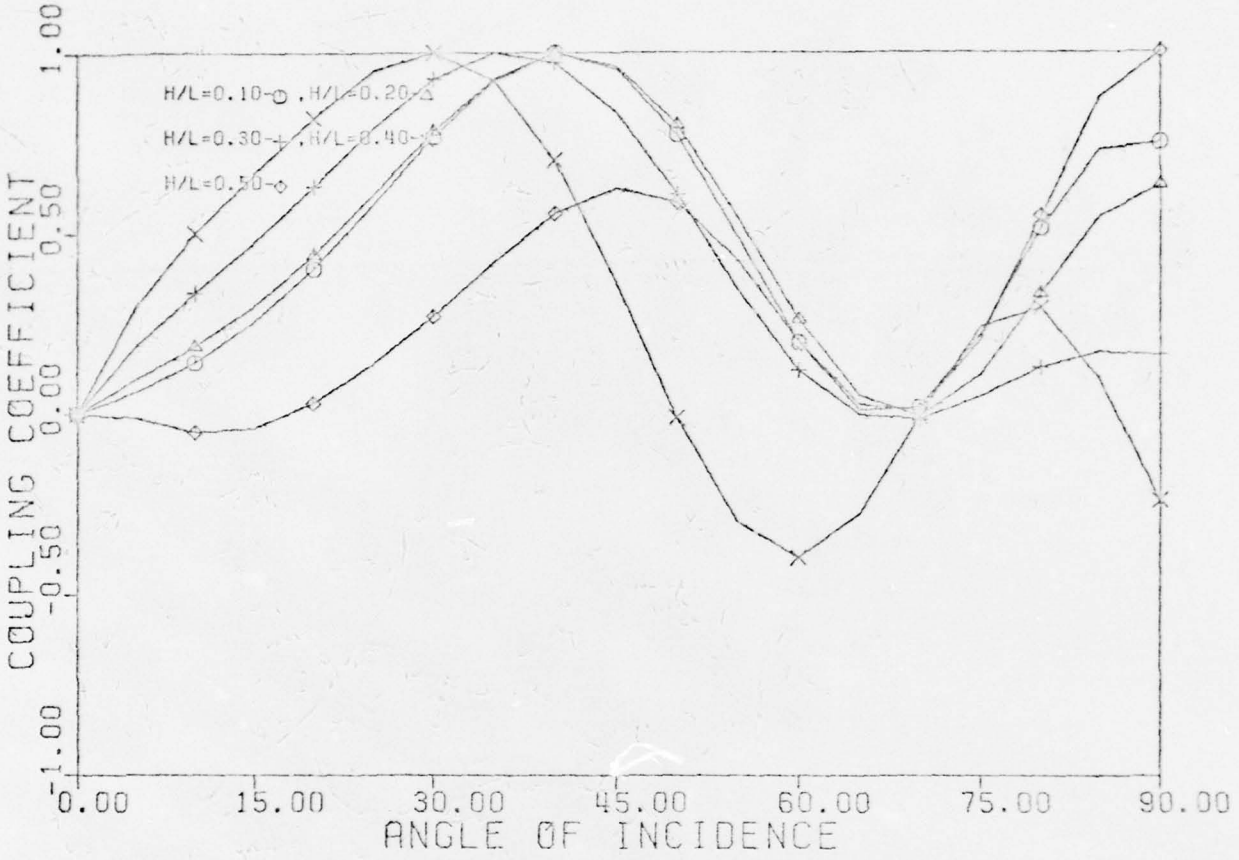


Figure 3-74. Real part of coupling coefficient for third self-resonant singularity, γ_{13}, as a function of scatterer height-to-length ratio, h/ℓ, and incident angle θ. The ground conductivity, σ, is 0.12, and the relative permittivity, ε_R, is unity

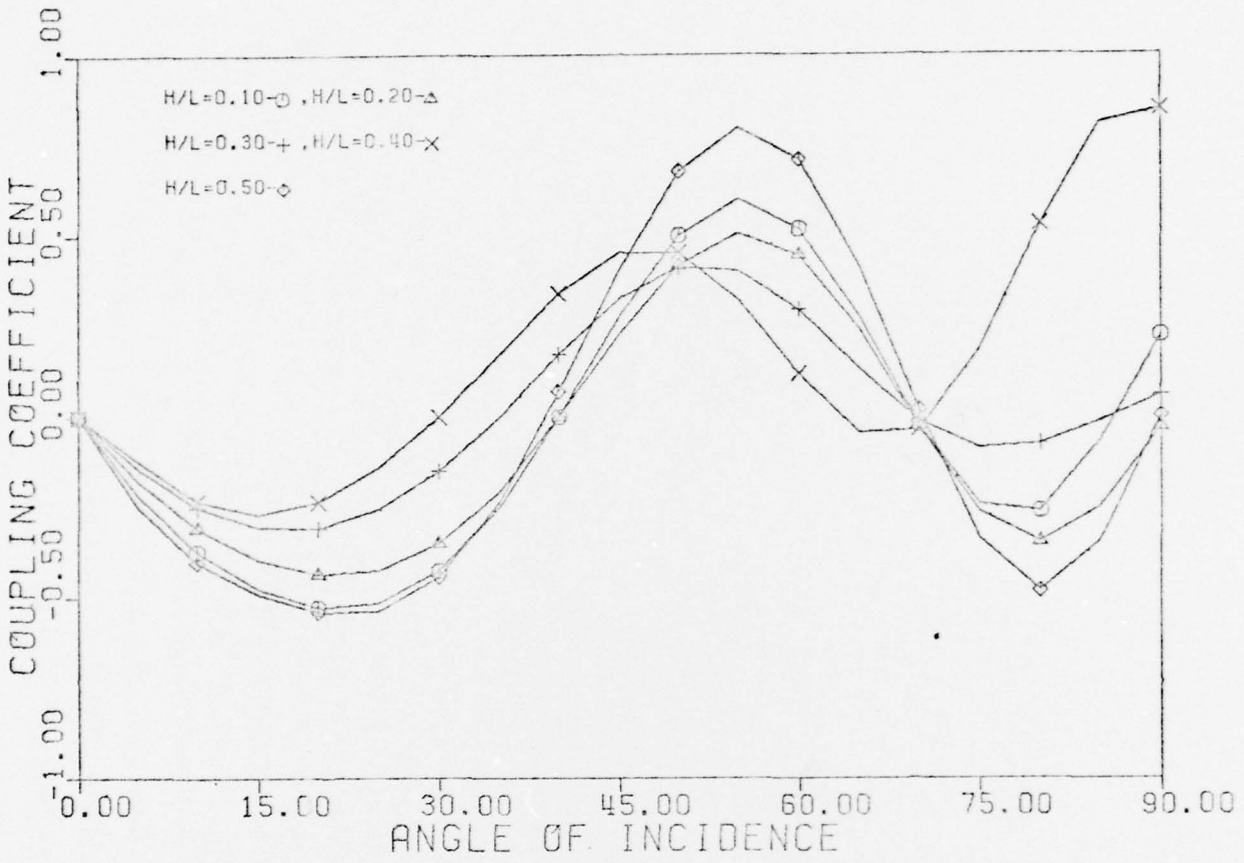


Figure 3-75. Imaginary part of coupling coefficient for third self-resonant singularity, γ_{13}, as a function of scatterer height-to-length ratio, h/ℓ, and incident angle θ. The ground conductivity, σ, is 0.12, and the relative permittivity, ε_R, is unity

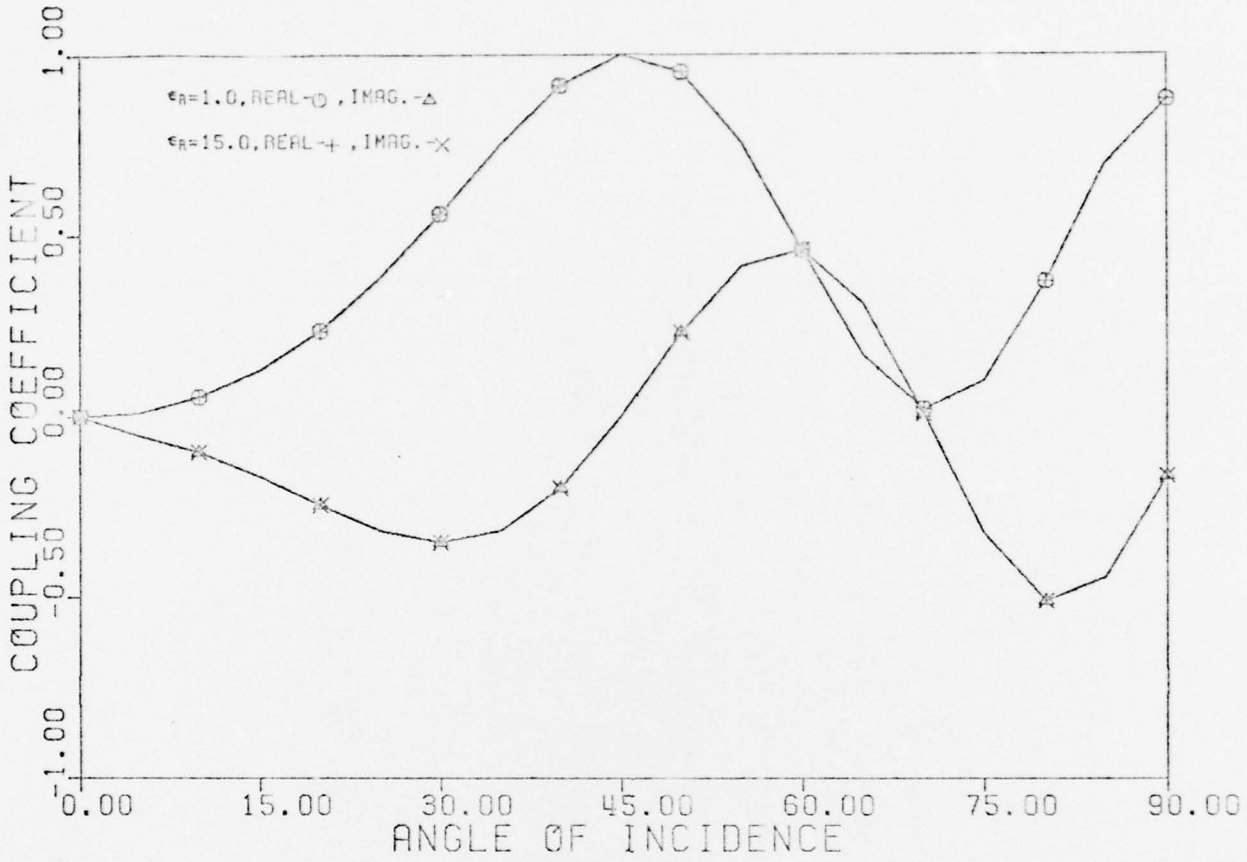


Figure 3-76. Coupling coefficient for third self-resonant singularity, γ_{13}, as a function of the ground plane relative permittivity, ϵ_R, and incident angle θ. The scatterer height-to-length ratio, h/ℓ, is 0.10, and the conductivity, σ, is 120.0

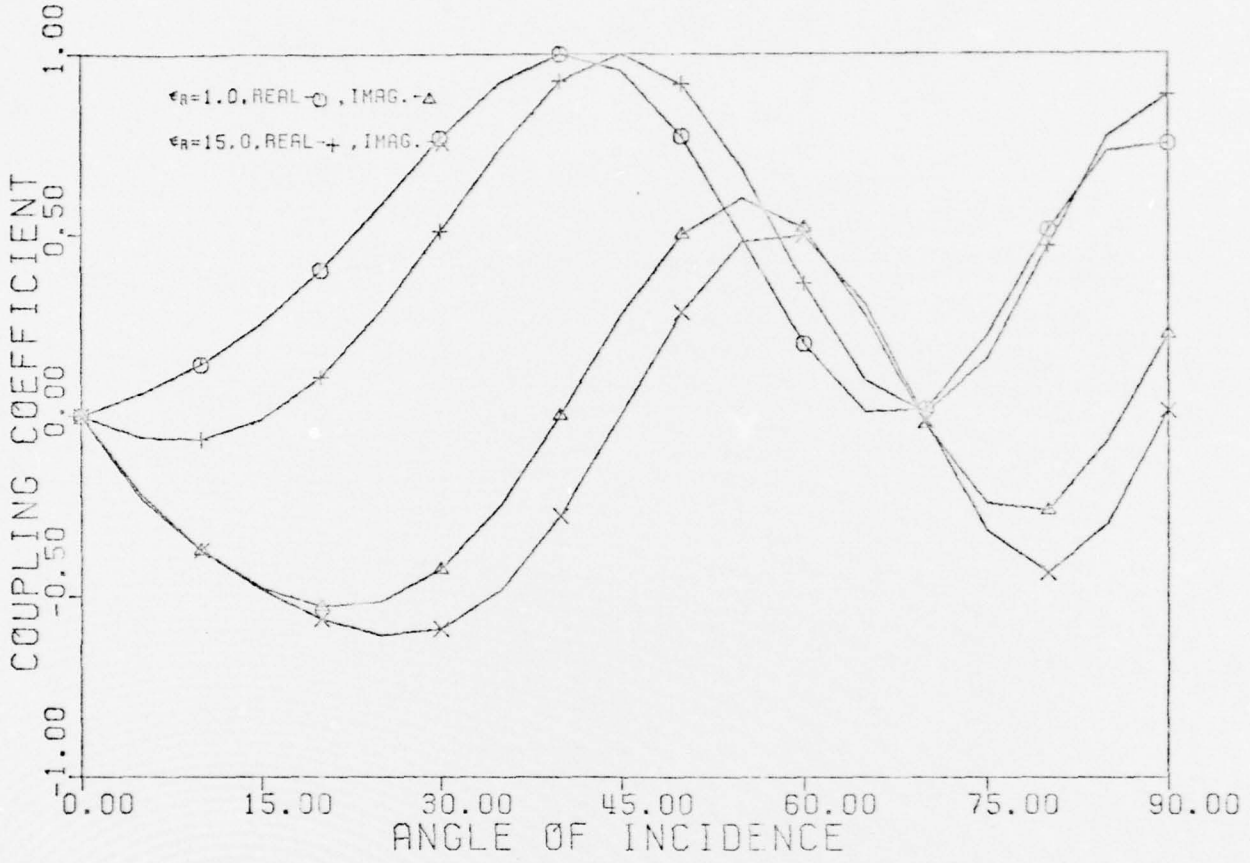


Figure 3-77. Coupling coefficient for third self-resonant singularity, γ_{13}, as a function of the ground plane relative permittivity, ϵ_R, and incident angle θ. The scatterer height-to-length ratio, h/ℓ, is 0.10, and the conductivity, σ, is 0.12

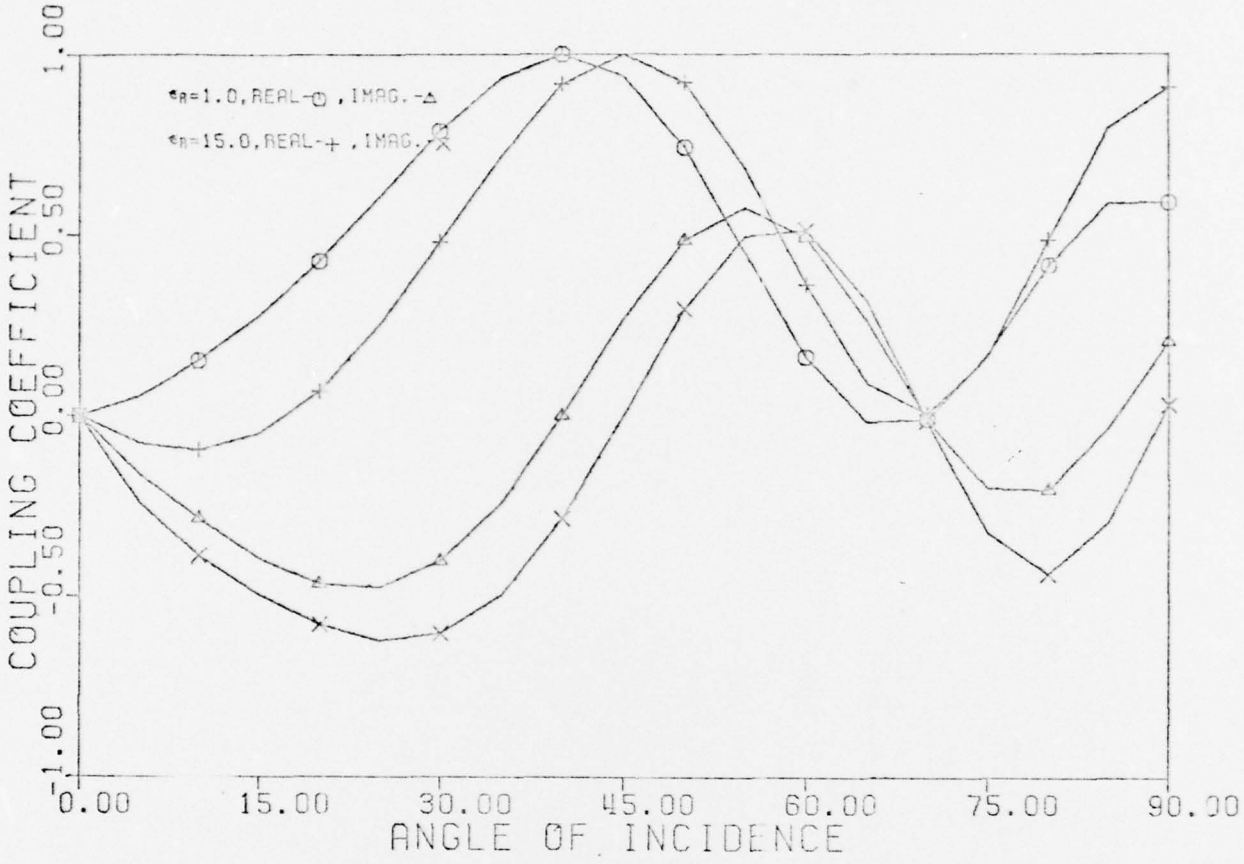


Figure 3-78. Coupling coefficient for third self-resonant singularity, γ_{i3}, as a function of the ground plane relative permittivity, ε_R, and incident angle θ. The scatterer height-to-length ratio, h/ℓ, is 0.10, and the conductivity, σ, is 0.00012

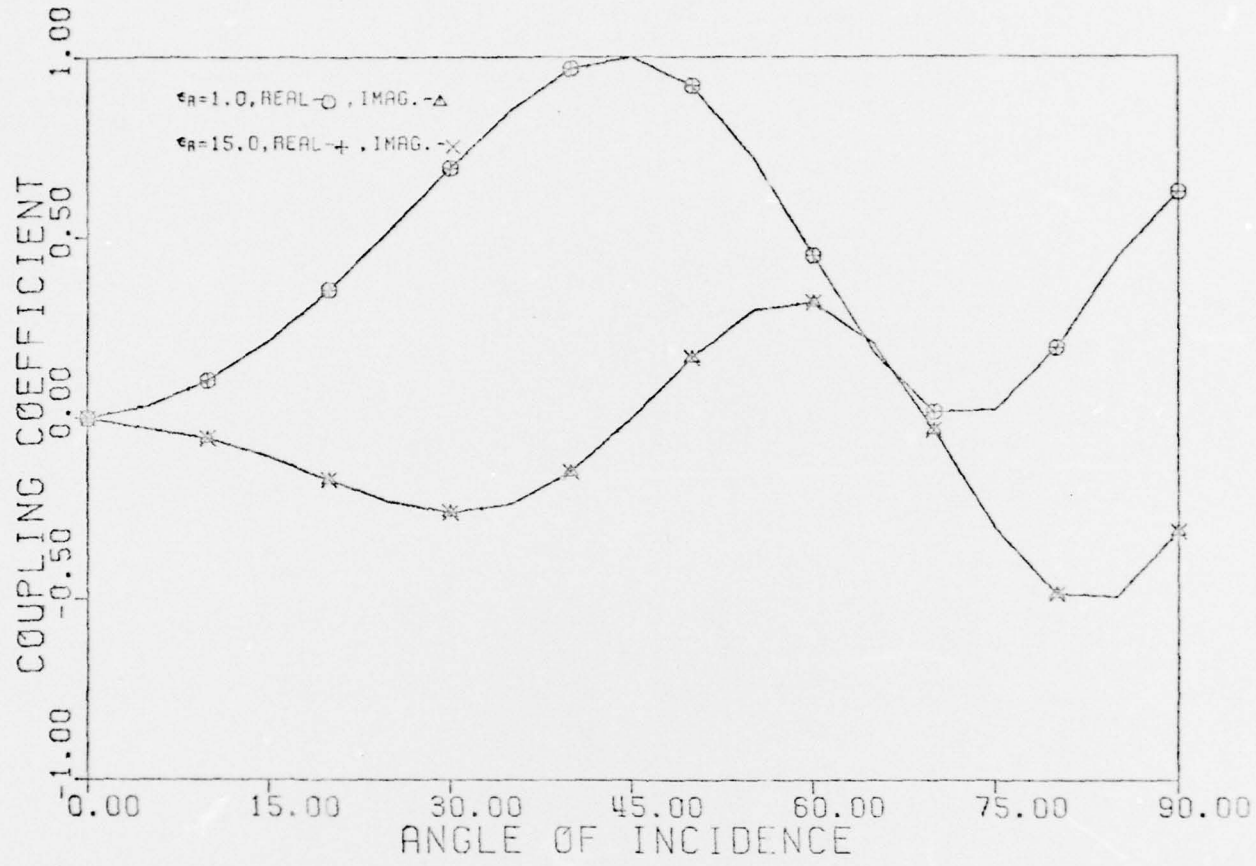


Figure 3-79. Coupling coefficient for third self-resonant singularity, γ_{13}, as a function of the ground plane relative permittivity, ε_R, and incident angle θ. The scatterer height-to-length ratio, h/ℓ, is 0.20, and the conductivity, σ, is 120.0

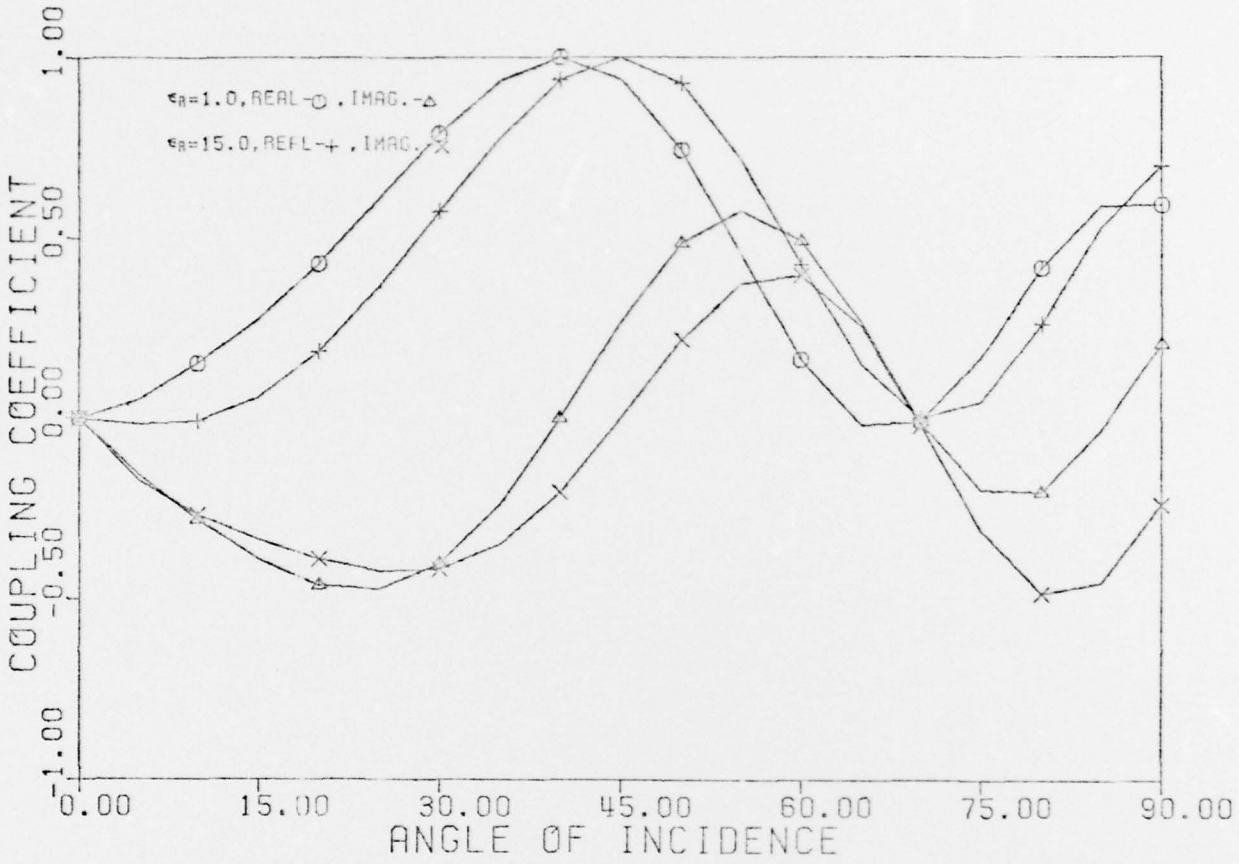


Figure 3-80. Coupling coefficient for third self-resonant singularity, γ_{13}, as a function of the ground plane relative permittivity, ϵ_R, and incident angle θ. The scatterer height-to-length ratio, h/ℓ, is 0.20, and the conductivity, σ, is 0.12

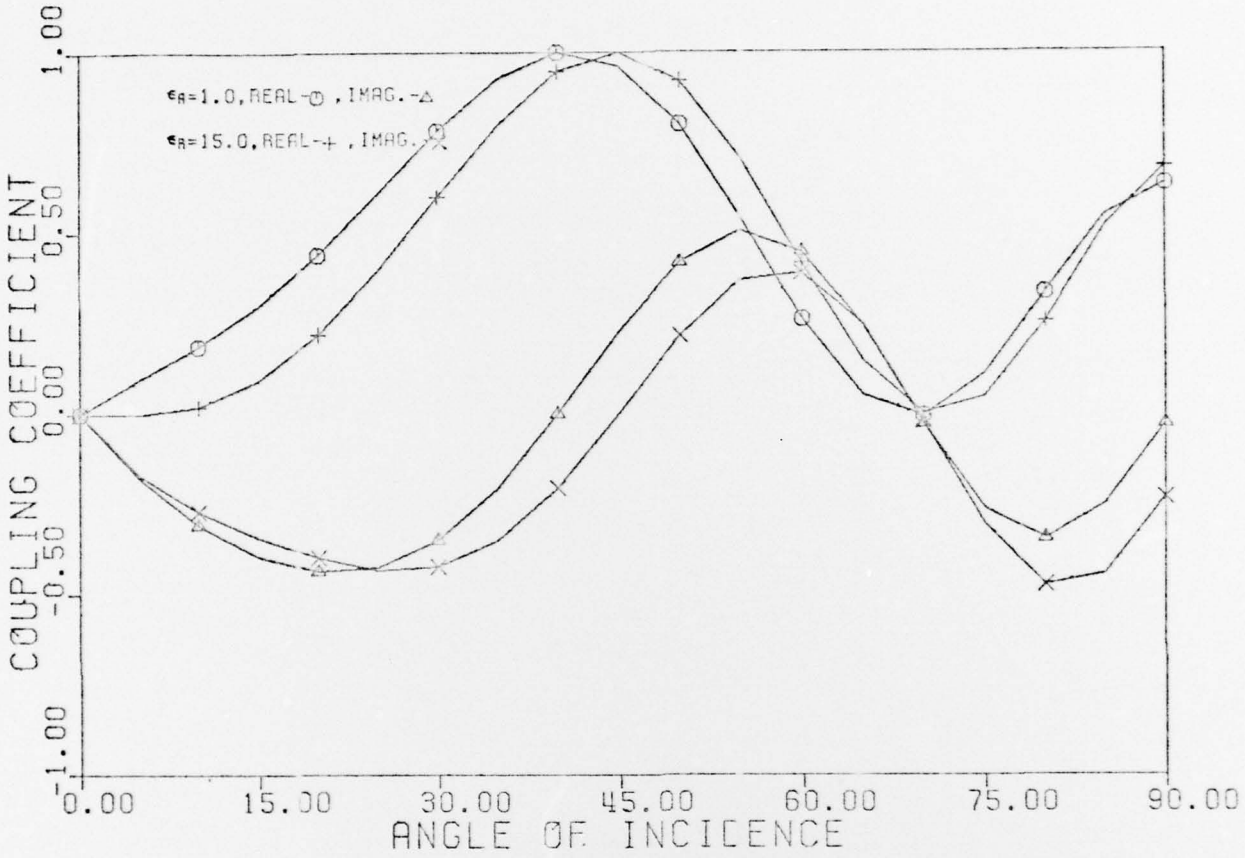


Figure 3-81. Coupling coefficient for third self-resonant singularity, γ_{13}, as a function of the ground plane relative permittivity, ϵ_R, and incident angle θ. The scatterer height-to-length ratio, h/ℓ, is 0.20, and the conductivity, σ, is 0.00012

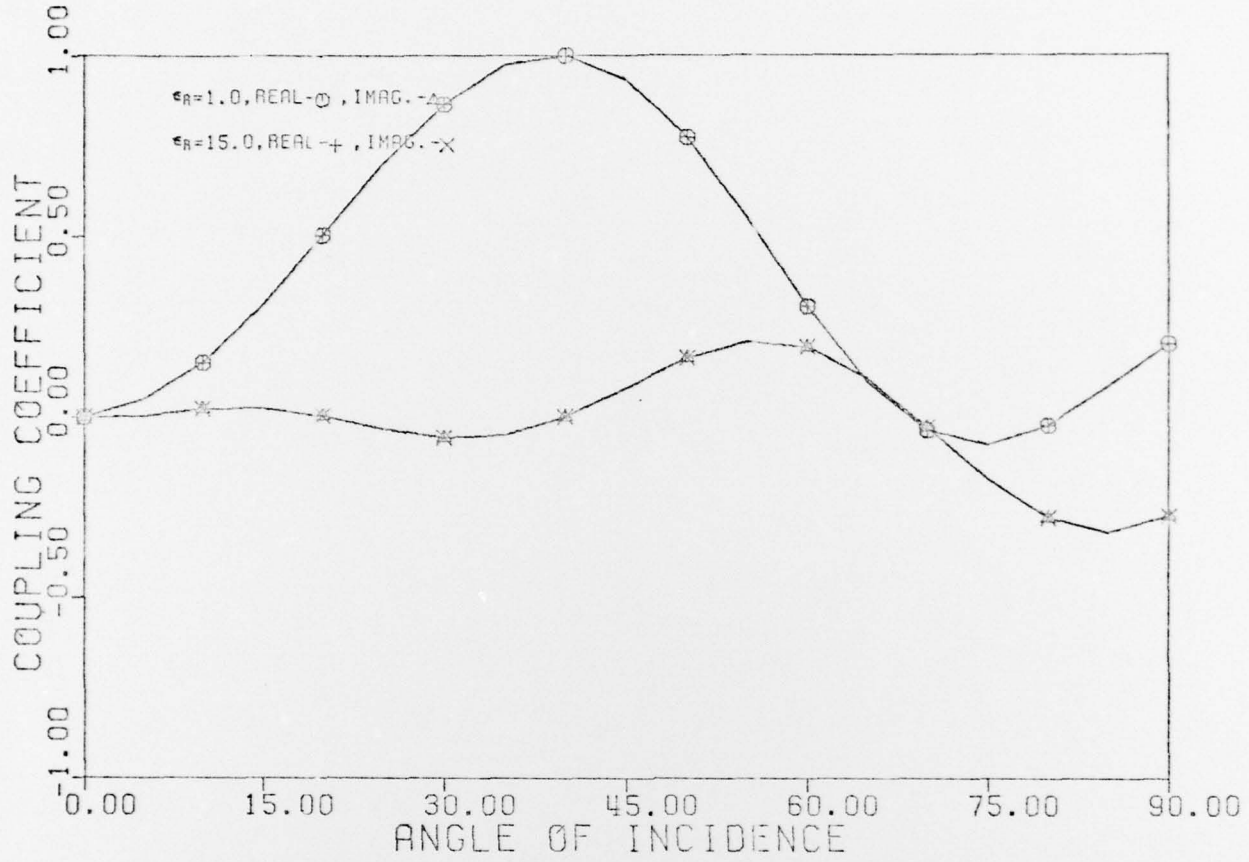


Figure 3-82. Coupling coefficient for third self-resonant singularity, γ_{13}, as a function of the ground plane relative permittivity, ϵ_R, and incident angle θ. The scatterer height-to-length ratio, h/ℓ, is 0.30, and the conductivity, σ, is 120.0

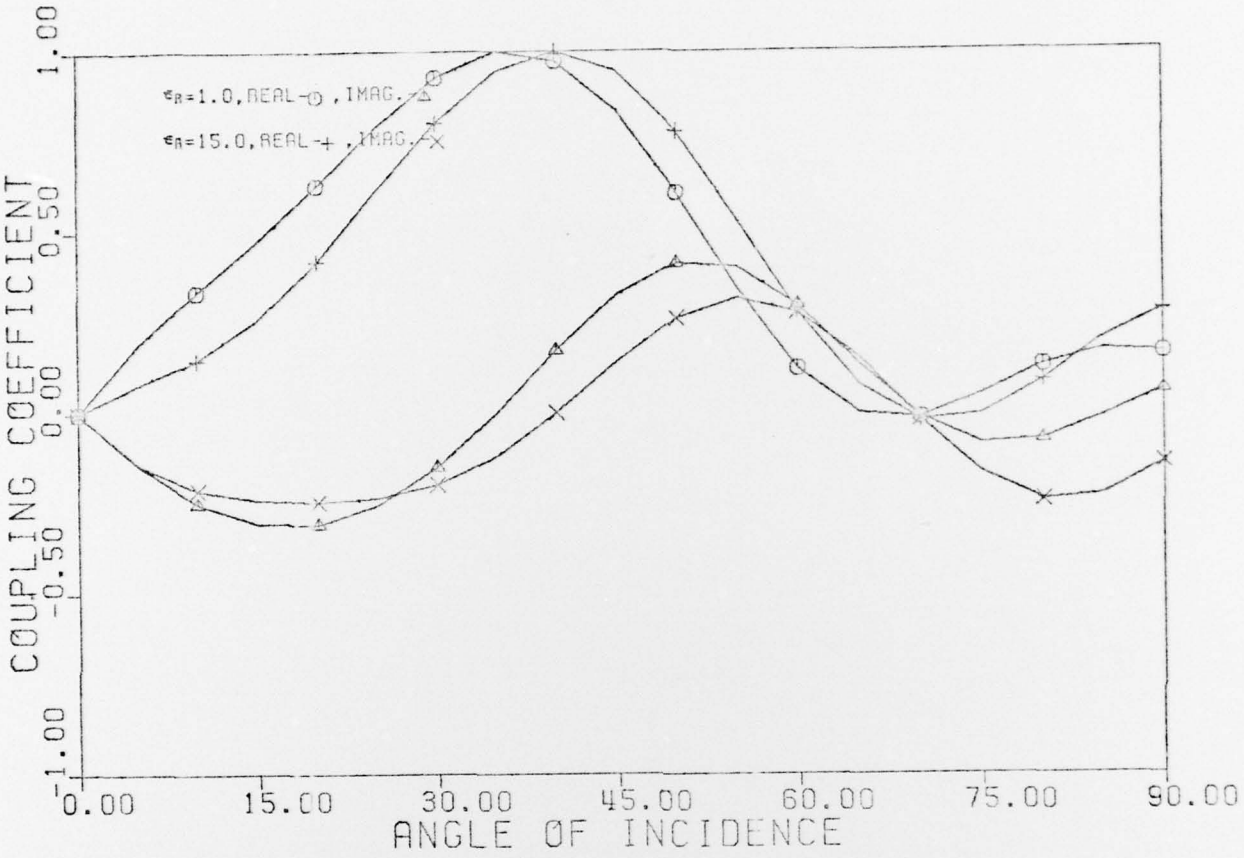


Figure 3-83. Coupling coefficient for third self-resonant singularity, Y_{13}, as a function of the ground plane relative permittivity, ϵ_R, and incident angle θ. The scatterer height-to-length ratio, h/ℓ, is 0.30, and the conductivity, σ, is 0.12

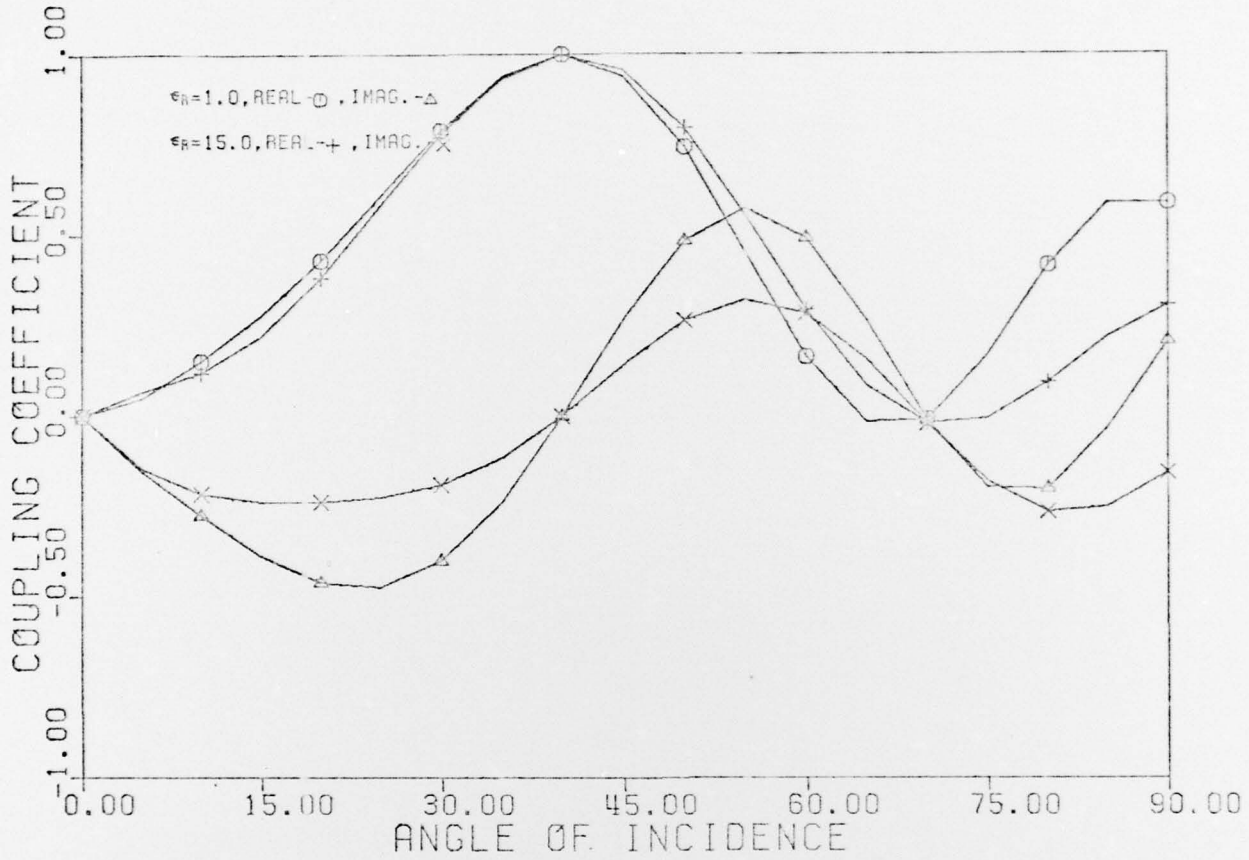


Figure 3-84. Coupling coefficient for third self-resonant singularity, γ_{13}, as a function of the ground plane relative permittivity, ϵ_R, and incident angle θ. The scatterer height-to-length ratio, h/ℓ, is 0.30, and the conductivity, σ, is 0.00012

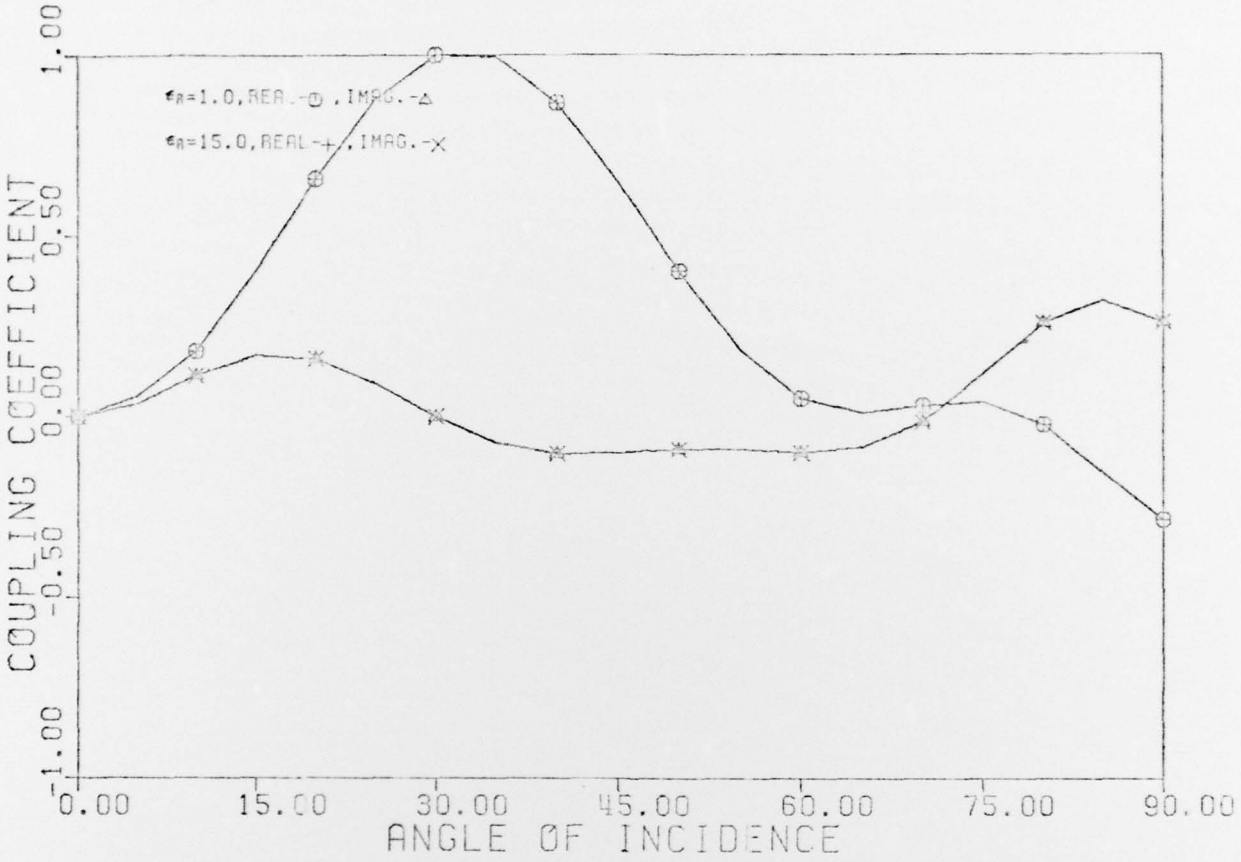


Figure 3-85. Coupling coefficient for third self-resonant singularity, γ_{13}, as a function of the ground plane relative permittivity, ϵ_R, and incident angle θ. The scatterer height-to-length ratio, h/ℓ, is 0.40, and the conductivity, σ, is [illegible]0

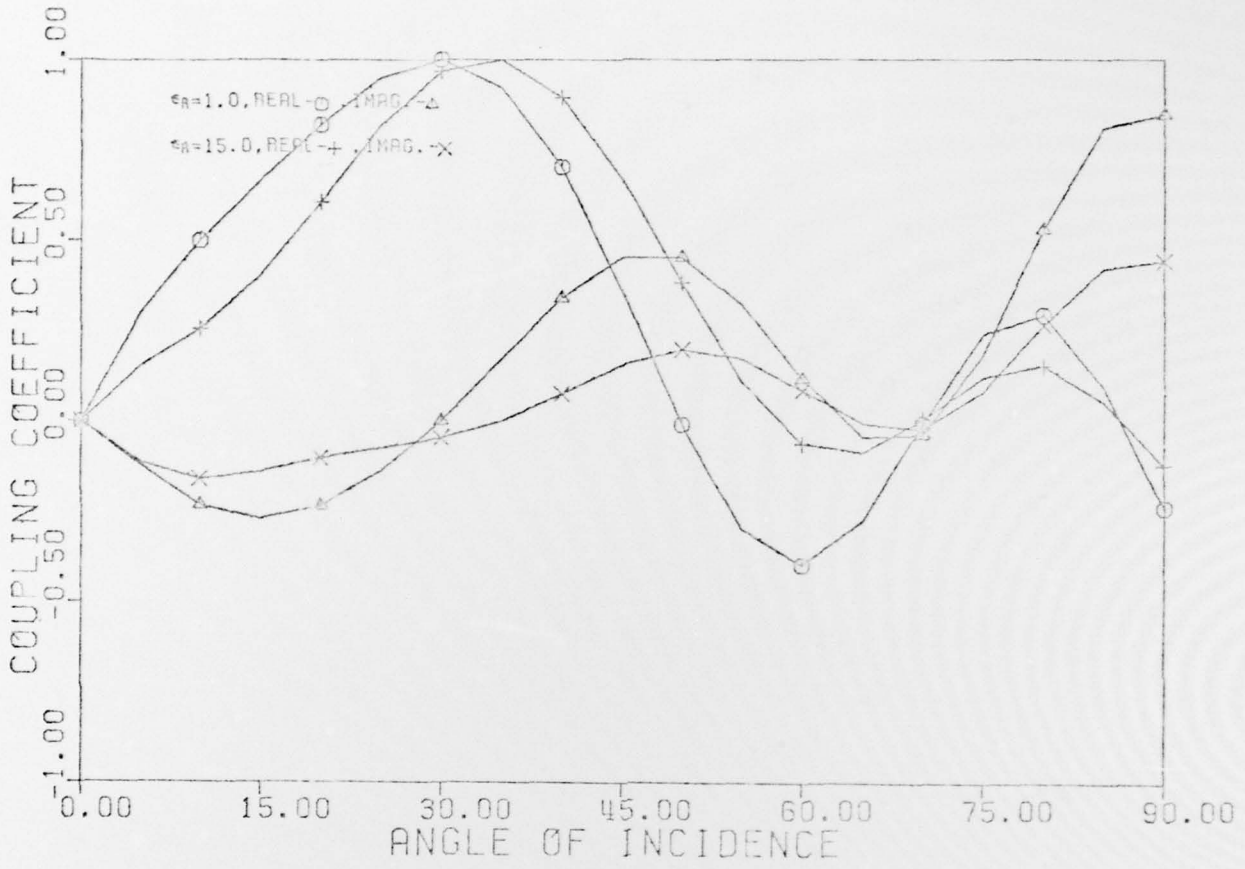


Figure 3-86. Coupling coefficient for third self-resonant singularity, γ_{13}, as a function of the ground plane relative permittivity, ε_R, and incident angle θ. The scatterer height-to-length ratio, h/ℓ, is 0.40, and the conductivity, σ, is 0.12

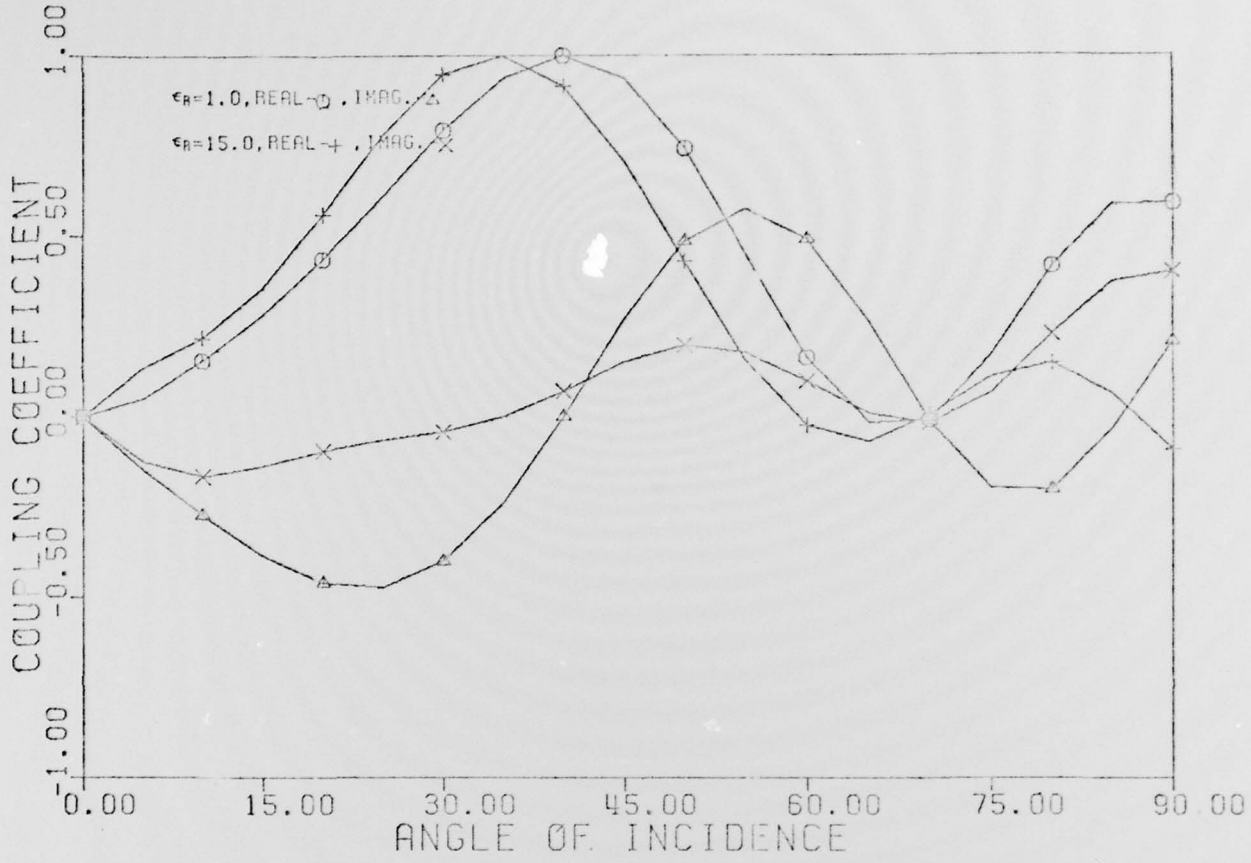


Figure 3-87. Coupling coefficient for third self-resonant singularity, γ_{13}, as a function of the ground plane relative permittivity, ϵ_R, and incident angle θ. The scatterer height-to-length ratio, h/ℓ, is 0.40, and the conductivity, σ, is 0.00012

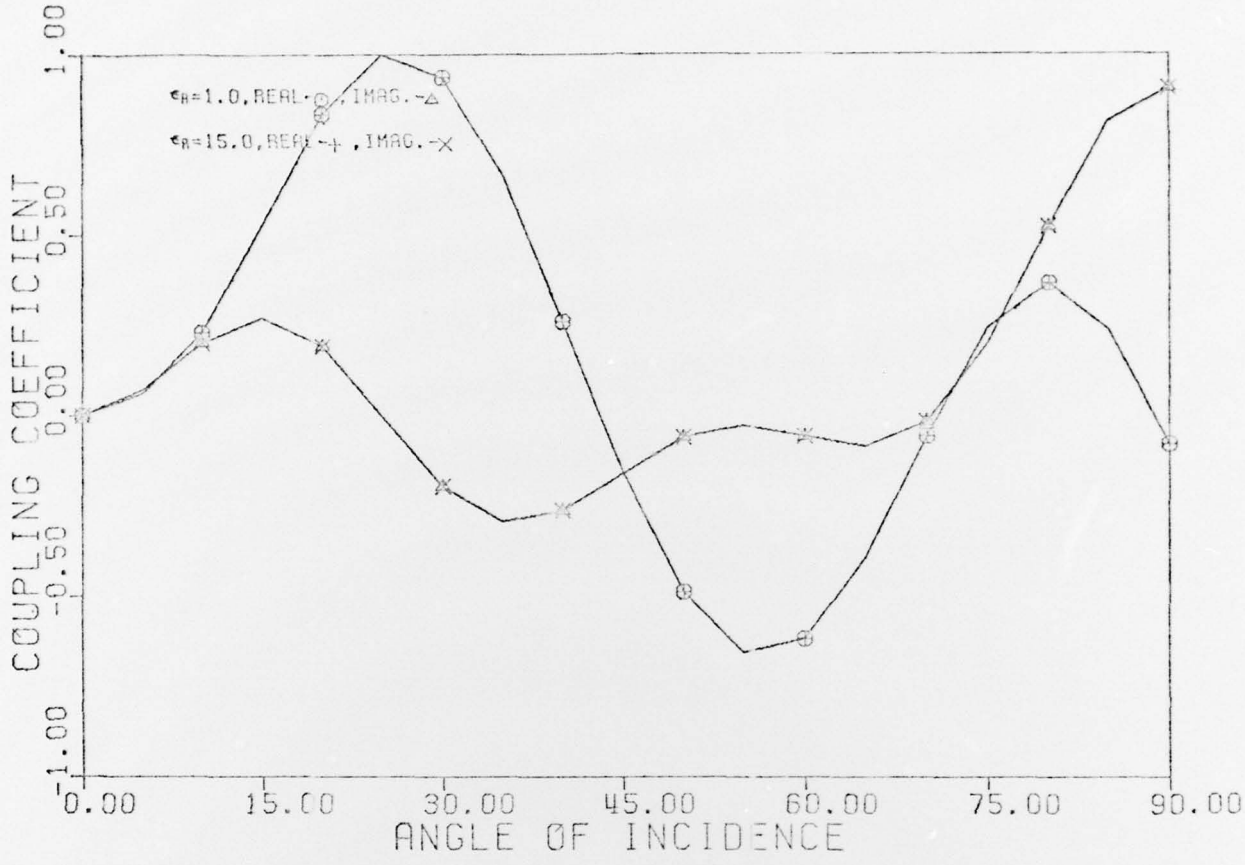


Figure 3-88. Coupling coefficient for third [illegible] f-resonant singulatiry, γ_{13}, as a function of the ground pla[illegible] relative permittivity, ϵ_R, h/ℓ, is 0.50, and the conductivity, σ, is 120.0

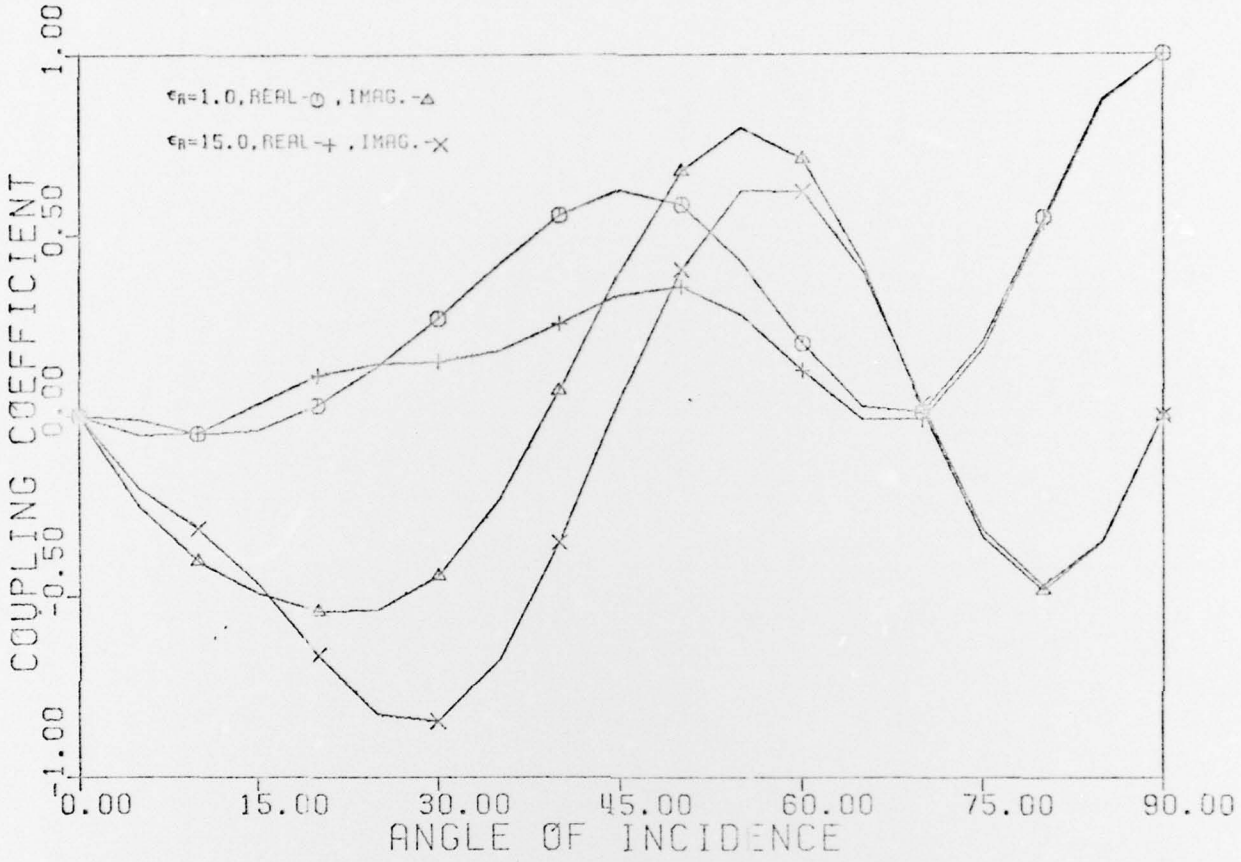


Figure 3-89. Coupling coefficient for third self-resonant singularity, Y_{13}, as a function of the ground plane relative permittivity, ε_R, h/ℓ, is 0.50, and the conductivity, σ, is 0.12

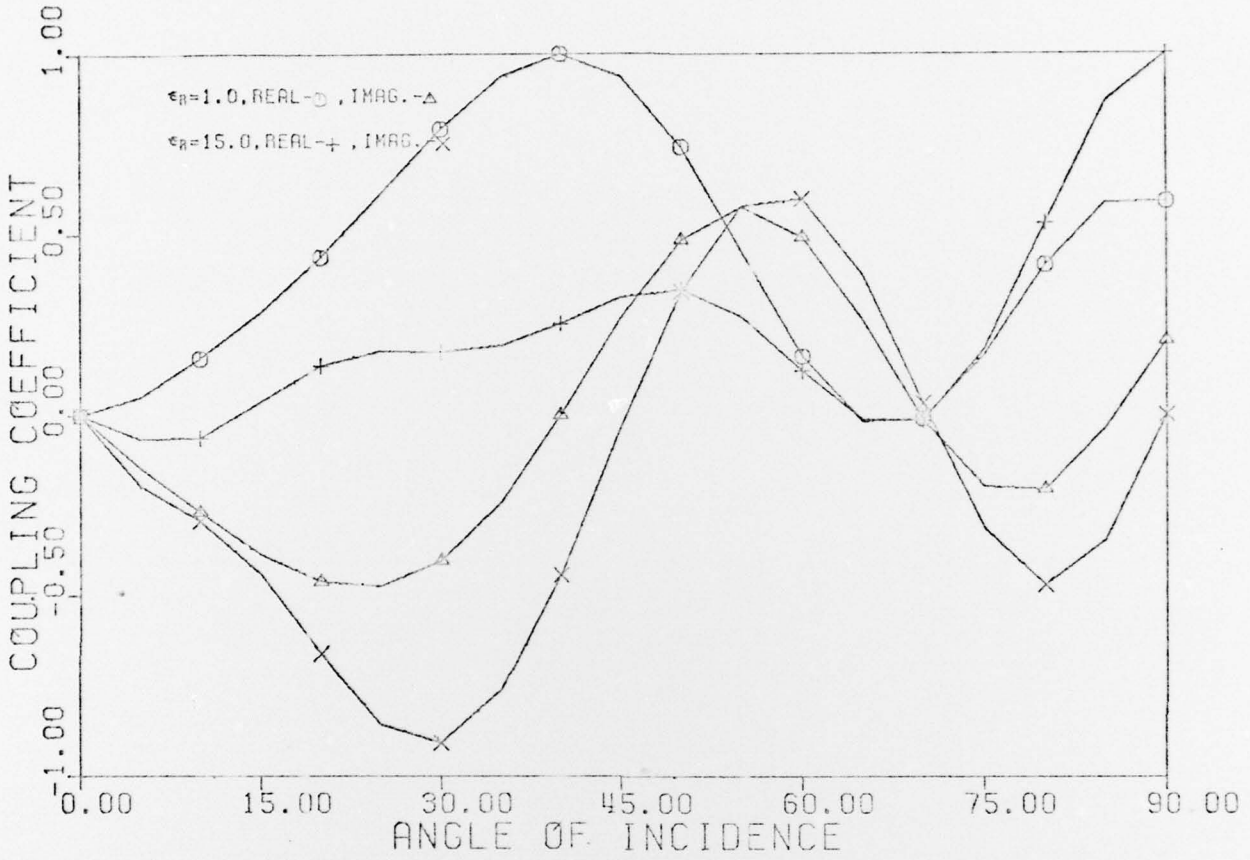


Figure 3-90. Coupling coefficient for third self-resonant singularity, Y_{13}, as a function of the ground plane relative permittivity, ϵ_R, h/ℓ, is 0.50, and the conductivity, σ, is 0.00012

IV. Conclusiors

The Singularity Expansion Method (SEM) coupled with the reflection coefficient approximation seems to be an appropriate technique for analyzing a cylindrical scatterer over a firitely conducting ground. Pole locations of the cylinder over perfect ground calculated by investigators were found to be identical to those calculated in this analysis when the ground conductivity is large. Also, wher the ground conductivity is reduced with the relative permittivity held at unity, calculated pole locations agree with those of the free space problem. These facts add credence to the reflection coefficient technique. In general, it is found that displacement of the singularities from their free space position is a function of discontinuity in the ground plane. The mechanism for discontinuity is seen to be somewhat immaterial. Mode vectors corresponding to first layer singularities show little or no dependence on the parameters of the problem.

Coupling coefficients corresponding to the first three fundamental resonances have been presented as a function of the parameters of the thin wire-lossy ground problem. For the case when the ground plane is nearly perfectly conducting the "standing wave analogy" as discussed in the numerical results section predicts, relatively accurately, the angle of incidence which results in maximum coupling to the scatterer. Although the "standing wave analogy" is obviously not completely rigorous, the

point of view taken here is that the physical insight provided by this technique and its apparent accuracy in predicting maximum coupling are sufficient to compensate for the lack of mathematical rigor.

The greatest value of this work lies in the fact that a relatively complicated problem has been solved within acceptable engineering accuracy over a wide range of parameters.

REFERENCES

[1] F. M. Tesche. "On the Analysis of Scattering and Antenna Problem Using the Singularity Expansion Technique," IEEE Trans. Antennas Propagat., Vol. AP-21, pp. 53-62, Jan., 1973.

[2] K. R. Umashankar, T. H. Shumpert, and D. R. Wilton, "Scattering by a Thin Wire Parallel to a Ground Plane Using the Singularity Expansion Method," IEEE Trans. Antennas Propagat., Vol. AP-23, pp. 178-134, March, 1975.

[3] Dennis J. Galloway, "Cylindrical Scatterer Near Perfectly Conducting Ground, Master's Thesis, Auburn University, Auburn, Alabama, 1976.

[4] T. K. Sarkar and B. J. Strait, "Analysis of Arbitrarily Oriented Thin Wire Antenna Arrays Over Imperfect Ground Planes," Syracuse University, Syracuse, New York, Technical Report TR-75-15, December, 1975.

[5] E. C. Jordon, Electromagnetic Waves and Radiating Systems, Prentice-Hall, Englewood Cliffs, N.J., 1950.

[6] Donnie Horace Herndon, "Finite Cylindrical Scatterer Near Imperfectly Conducting Ground," Master's Thesis, Auburn University, Auburn, Alabama, 1976.

[7] R. F. Harrington, Time-Harmonic Electromagnetic Fields, McGraw-Hill, New York, N.Y., 1961.

[8] R. F. Harrington, Field Computation by Moment Methods, McMillan Co., New York, N.Y., pp. 62-81, 1966.

[9] T. H. Shumpert, "EMP Interaction with a Thin Cylinder Above a Ground Plane Using the Singular Expansion Method," Air Force Weapons Laboratory, Albuquerque, N.M., Interaction Note 182, June, 1973.

[10] Carl E. Baum, "On the Singularity Expansion Method for the Solution of Electromagnetic Interaction Problems," Air Force Weapons Laboratory, Albuquerque, N.M., Interaction Note 88, December, 1971.

[11] Carl E. Baum, "On the Singularity Expansion Method for the Case of First Order Poles," Air Force Weapons Laboratory, Albuquerque, N.M., Interaction Note 129, October, 1972.

[12] K. R. Umashankar, "The Calculation of Electromagnetic Transient Currents on Thin Perfectly Conducting Bodies Using the Singularity Expansion Method," Ph.D. Dissertation, University of Mississippi, University, Mississippi.

[13] L. Marin and R. W. Latham, "Representation of Transient Scattered Fields in Terms of Free Oscillations of Bodies," Proc. IEEE (Lett.), pp. 640-641, May, 1972.

[14] C. E. Baum, "Electromagnetic Transient Interaction with Objects with Emphasis on Finite Size Objects, and some Aspects of Transient Pulse Production," presented at the 1972 Spring URSI Meeting, Washington, D.C.

[15] Cheng C. Kao, "Measurements of Surface Currents on a Finite Circular Tube Illuminated by Electromagnetic Wave," IEEE Trans. Antennas Propagat. (Commun.), Vol. AP-18, pp. 569-573, July, 1970.

[16] Cheng C. Kao, "Electromagnetic Scattering from a Finite Tubular Cylinder: Numerical Solutions," Radio Sci., Vol. 5, pp. 617-624, March, 1970.

[17] Cheng C. Kao, "Three-Dimensional Electromagnetic Scattering from a Circular Tube of Finite Length," J. App. Phys., Vol. 40, pp. 4723-2740, November, 1969.

[18] W. E. Williams, "Diffraction By a Cylinder of Finite Length," Proc. Cambridge Phil. Soc., Vol. 52, pp. 322-335, 1956.

[19] A. N. Sommerfeld, Partial Differential Equations, Academic Press, New York, 1949.

[20] K. A. Norton, "The Physical Reality of Space and Surface Waves in the Radiation Field of Radio Antennas," Proc. IRE, Vol. 25, pp. 1192-1202, September, 1937

[21] Jerry D. McCannon, "Comparative Numerical Study of Several Methods for Analyzing a Vertical Thin-Wire Antenna Over a Lossy Half-Space", Ph.D. Dissertation, University of Illinois at Urbana-Champaign, 1974.